ISSN 2074-272X

науково-практичний журнал 2024/2

Електротехніка і Електромеханіка

Electrical Engineering & Electromechanics

Електричні машини та апарати
Електротехнічні комплекси та системи
Промислова електроніка
Інженерна електрофізика.
Техніка сильних електричних та магнітних полів
Електричні станції, мережі і системи

Журнал включено до найвищої категорії «А»
Переліку фахових видань України

З 2019 р. журнал індексується у Scopus

З 2015 р. журнал індексується
у Web of Science Core Collection:
Emerging Sources Citation Index

Electrical Engineering & Electromechanics

Scientific Journal was founded in 2002
Founder – National Technical University «Kharkiv Polytechnic Institute» (Kharkiv, Ukraine)

From no. 1 2019 Journal «Electrical Engineering & Electromechanics» is indexing in **Scopus** and from no. 1 2015 Journal is indexing in **Web of Science Core Collection: Emerging Sources Citation Index (ESCI)**.

Also included in DOAJ (Directory of Open Access Journals), in EBSCO's database, in ProQuest's databases – Advanced Technologies & Aerospace Database and Materials Science & Engineering Database, in Gale/Cengage Learning databases.

Editorial office address:
National Technical University «Kharkiv Polytechnic Institute», Kyrpychova Str., 2, Kharkiv, 61002, Ukraine
phones: +380 57 7076281, +380 67 3594696, **e-mail:** a.m.grechko@gmail.com (**Grechko O.M.)**

ISSN (print) 2074-272X
ISSN (online) 2309-3404

Printed 28 February 2024. Format 60 × 90 ⅛. Paper – offset. Laser printing. Edition 50 copies.
Printed by Printing house «Madrid Ltd» (18, Gudanova Str., Kharkiv, 61024, Ukraine)

Electrical Engineering & Electromechanics
Scientific Journal

no. 2, 2024

Table of Contents

UDC 621.314.332 https://doi.org/10.20998/2074-272X.2024.2.01

A.A. Stavynskyi, O.A. Avdeeva, D.L. Koshkin, R.A. Stavynskyi, O.M. Tsyganov

Technical solutions to reduce losses in magnetic cores and material consumption of three-phase transformer and reactor equipment

Purpose. *The increase in energy costs and the need for further energy saving lead to an increase in requirements for reducing losses in the magnetic cores of transformers and reactors.* ***Problem.*** *The improvement of transformer and reactor equipment is traditionally carried out by applying the achievements of electrical materials science and new technologies to traditional designs and structures of electromagnetic systems. The basis of modern transformers is made up of laminated and twisted magnetic cores. The disadvantage of laminated magnetic cores is large additional losses in corner zones due to the texture of anisotropic steel. Disadvantage of twisted three-phase three-contour magnetic cores is large additional losses caused by the lack of magnetic coupling of three separate magnetic flux contours. The disadvantages of combined joint tape-plate magnetic cores are the unsatisfactory use of the active volume and increased losses, which are determined by the uneven distribution of the magnetic field and the negative impact of steel texture in the corner zones of the twisted parts.* ***Aim.*** *To determine the possibility of improving three-phase transformers and reactors.* ***Methodology****. The improvement is achieved by geometrical and structural transformations of the outer contours and elements of the varieties of magnetic cores.* ***Results****. The possibility of eliminating additional losses of a planar laminated magnetic core by a combination of anisotropic and isotropic steels at the appropriate location in the yoke-rod and corner sections is determined. With an octagonal outer contour of the combined magnetic core, a reduction in mass is achieved without an increase in losses. The mutually orthogonal position of the steel layers or the elements of the joint twisted and combined three-phase planar and spatial magnetic cores achieves magnetic coupling and elimination of additional losses of individual twisted contour sections. The hexagonal configurations of the inner contours of the twisted yoke-corner parts and the cross-sections of the laminated rods of the variants of the axial spatial joint magnetic core improve the magnetic flux density distribution and reduce the main losses of the yokes, as well as reduce the complexity of manufacturing rods from identical rectangular steel layers.* ***Originality.*** *The paper presents constructive and technological proposals and features of varieties of non-traditional planar and spatial, laminated, twisted and combined tape-plate joint magnetic cores, which differ in the combination of anisotropic, isotropic and amorphous steels, as well as the multifaceted geometric shape of contours and the spatial arrangement of elements. Based on the identity of the optimal geometric ratios of the variants of electromagnetic systems of transformers and reactors, with joint planar and spatial twisted and combined and tape-plate magnetic cores, the unification of the structure of transformer and reactor equipment with a capacity of I-III dimensions.* References 29, figures 8.

Key words: **three-phase transformer, reactor, laminated twisted magnet core, transformer construction.**

Розглянуто стан розвитку трансформаторобудування. Визначена недостатня ефективність застосування відомих способів зниження втрат у магнітопроводах для задоволення нових вимог енергоресурсозбереження. Показана можливість удосконалення і уніфікації трифазних трансформаторів та реакторів на основі комбінацій анізотропної, ізотропної і аморфної сталей, багатогранних геометричних конфігурацій контурів та зміни положень в просторі шарів сталі, а також елементів планарних і просторових шихтованих, витих та комбінованих навито-пластинчастих магнітопроводів. Бібл. 29, рис. 8.

Ключові слова: **трифазний трансформатор, реактор, шихтований витий магнітопровід, трансформаторобудування.**

Problem definition. The increase in the cost of energy and the need for further energy conservation lead to an increase in requirements and regulations for increasing the efficiency of transformers. In particular, the Standards ND 428 and ND 538 for oil and dry transformers have been replaced by the more demanding European Standard EN 50464-1 and the International Standard IEC 60034-30. It is necessary to significantly reduce idle losses, first of all, in the most mass production range of power distribution three-phase transformers (TTs) with power of 25-2500 kV·A and a voltage of 6-10 kV. In addition to the main contribution to the total losses of power systems by the specified TTs, the energy efficiency of the power supply is additionally affected by the losses in the magnetic cores of three-phase reactors (TRs) of a similar power range. In this regard, the reduction of losses in magnetic cores of TTs and TRs of sizes I-III is an important current task [1-4].

Analysis of the latest research. For more than 20 years, in works analyzing the development of transformer and reactor equipment, innovative structures have been classified based on the achievements of electrical materials science. The main innovations are reduced to the development of «dry» transformers with «encapsulated» and «cable» windings [5, 6]. Amorphous electrical steels (ESs), superconducting windings, and cryogenic technology are also used [7, 8]. Instead of toxic oil for cooling, the use of organosilicon liquid and elegas begins [9-11]. In addition, an important factor in increasing the technical level of TTs and TRs is the use of optimization methods in their design [12, 13].

About 50 % of the losses at the nominal load of the transformers are due to losses during idle operation. The costs of their compensation many times exceed the costs of short-circuit losses. Due to the real partial average load of transformers, reduction of idle losses is a priority.

In the past decades, losses in magnetic cores have been reduced due to the use of ESs with improved specific characteristics. The production of cold-rolled anisotropic and amorphous ESs has been mastered. In general, meeting the requirements of the new Standards is achieved by reducing electromagnetic loads or using a strip amorphous ES, which involves an increase in material capacity (in amorphous and anisotropic ES, the saturation magnetic flux density is 1.6 T and above 2 T, respectively). In addition, the filling factor of the

amorphous ES cross-section of the rod is 0.8-0.85 in comparison with the similar coefficient of 0.96-0.97 when using a crystal ES. TTs with composite windings and «high-temperature» superconductivity are being created [8, 9, 14]. However, distribution TTs of the main power range with technologies of closed high-temperature cryogenic cooling systems have no advantages over conventional TTs, which is due to the complexity of the cryogenic structural part. There is a need for cooling during commissioning and return of superconductivity after protective switching off.

In general, «amorphous» and «superconducting» TTs differ in their increased cost. The fragility of amorphous ES and superconducting composite «high-temperature» windings precludes their use in transport and other special TTs.

There are methods of comprehensive assessment of the technical condition of functioning transformers and recommendations for their further use [15]. However, fines are provided for the operation of operational transformers that do not meet the above Standards.

The structural and constructive basis of TT and TR consists of charged and twisted magnetic cores. The texture of the anisotropic ES creates a multiple increase in losses in the zones of magnetic flux reversal relative to the rolling direction of the layers of the laminated magnetic core. The volumes of these zones are reduced by using oblique joints in the corners and in two-frame (divided by width into sections) magnetic cores [16, 17]. Complex equipment for the formation of oblique joints with a change in size and a small shift of the joints of adjacent layers during the assembly of magnetic cores (Step-lap, Malty step-lap technologies) was created [4]. The shift is achieved by applying the initial configuration of the smaller sides of the plates (Fig. 1,*a*) or by reducing the areas of oblique joints and forming the angular protrusions of «whiskers» (Fig. 1,*b*), which are actually hidden waste.

According to [18], oblique joints are not an effective solution for improving laminated magnetic cores of TTs of I-II dimensions. Also, the increase in the losses of ready-made planar laminated magnetic cores relative to the specific losses of anisotropic ES along the rolling stock reaches 37-58 %, regardless of the shape of the joints. This is a well-known problematic issue of modern TTs (TRs).

The production of magnetic cores with laminated stacking is complemented by ES tape (roll) winding technologies. Such technologies are used for the manufacture of sections (contours) of three-contour continuous and joint twisted and combined magnetic cores [9, 16, 19-21]. The production of twisted three-phase three-section planar and spatial magnetic cores is increasing in connection with the expansion of the use of amorphous ES [19, 20]. In recent times, twisted split contact magnetic cores have been replaced by analogs with the formation of covering layers by separation and bending of sections of the ES tape. Conditionally oblique connections of parts of magnetic corers are formed with a small shift of the joints of adjacent layers. A reduction in contact losses and magnetization current is achieved (Unicore – magnetic cores) [20]. However, the absence of a magnetic connection of the twisted sections determines the vector composition of the action in the core sections of the sectional magnetic fluxes. The consequence of the magnetic separation of the sections is the third harmonics of the indicated fluxes and additional 30-35 % losses, which do not depend on the texture and brand of ES. This is another well-known problematic issue of transformer and reactor equipment.

On the basis of the above, the task of reducing idle losses and losses in the magnetic cores of TTs and TRs without increasing their mass and cost indicators is difficult and has not yet been resolved.

The goal of the work is to reduce the losses of TTs' and TRs' magnetic cores while reducing their material consumption.

Research method and results. Presented in [1-11] as new developments, electromagnetic systems (EMSs) of TTs and TRs are made in the same technical solutions of magnetic cores for more than a century. These developments in the structural and constructive sense have reached a certain limit of development. The trends of structural and technological inertia of electromechanical engineering have also been preserved recently. Further improvement of TTs and TRs with stacked and twisted magnetic cores is possible by the methods of their structural and geometric transformations and the use of combinations of ES brands [18, 22, 23].

The outer «conventional» rectangular contour of a planar laminated magnetic core [24-26] forms a significant unevenness of the magnetic flux density distribution in the range of 0.01-2.1 T in the corners (Fig. 1,*c*). The outer sections of the corners with height h_c (Fig. 1,*a*,*b*) are underloaded and are practically a useless weight supplement of the magnetic core.

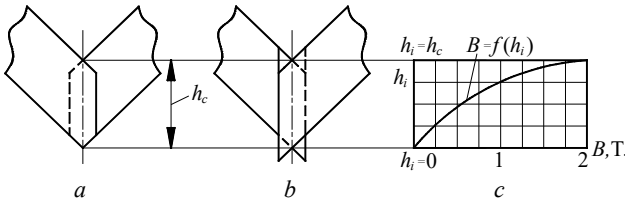

Fig. 1. Schemes of variants of the rod's and yoke's plate structures with two-plane (*a*) and oblique (*b*) separations of the steel strip and the dependence of the distribution of magnetic flux density (*c*) on the height of the corner zone of the laminated rectangular magnetic core

Unconventional proposals for reducing losses include magnetic cores with a combination of ES brands. To reduce losses by reducing the unevenness of the distribution of the magnetic field in the cross section and corners, the outer part of the two-frame laminated magnetic core is proposed to be made with improved magnetic properties relative to the inner part [27].

Other proposals for the improvement of the planar laminated magnetic core are options with a combination of isotropic and anisotropic ESs. In a magnetic core with direct junctions (Fig. 2,*a*,*b*), the combination of the specified ESs alternates in adjacent layers [28]. Corner zones contain only isotropic ES, which completely eliminates significant additional losses in corner zones. However, approximately half of each variant of the

combined magnetic core [28] contains an isotropic ES with increased specific losses, which reduces the efficiency of this innovation.

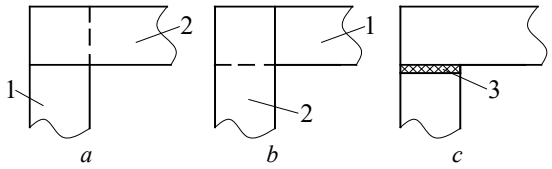

Fig. 2. Schemes of variants of corner zones of a planar laminated magnetic core with direct joints of adjacent layers of the transformer (*a*, *b*) and the reactor's magnetic core (*c*): 1 – anisotropic steel; 2 – isotropic steel; 3 – insulating gasket

A general drawback of traditional TTs' and TRs' structures is the disunification of internal structures, i.e., connections of rod's and yoke's sections of planar magnetic corers. With the general identity of the variants of the external configuration, the TTs' magnetic cores are stacked with shift of oblique (Fig. 1,*a*,*b*) or straight (Fig. 2,a,*b*) joints, and the TRs' magnetic cores contain structural gaps between the rods with insulating gaskets (Fig. 2,*c*).

The further development of the offer of non-conventional combinations of elements of the laminated magnetic core is the installation of plates of anisotropic ES in the zones of orthogonal change of the flux direction relative to the texture. Plates of chevron-shaped isotropic ETS with opposite sides of different widths are used. In the side corners of the planar magnetic core, these plates are installed in adjacent layers with the opposite direction. In the opposite middle corners (T-shaped sections), chevron plates are installed with the orthogonal position of the middle corners (Fig. 3,*a*). The chevron plates of the anisotropic ES of the side sections can be made with rounding of the axial corners to reduce the uneven distribution of the field. The rounding radius corresponds to the insulating gap h_i between the magnetic core and the winding (Fig. 3,*b*).

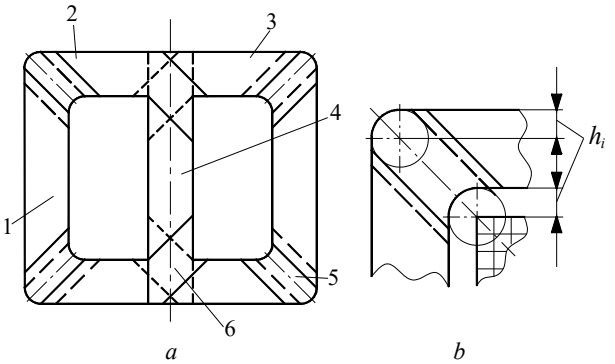

Fig. 3. Scheme of (a) three-phase with rounded corners (*b*) magnetic core with plates 1-4 of anisotropic and plates 5, 6 of isotropic electrical steels

Inseparable connection of anisotropic and isotropic sections of chevron plates in the joints by welding reduces the current and losses of idle. Eliminating the significant complication of the production of magnetic cores with the connection of the joints of isotropic and anisotropic ESs is possible by integral welding and transverse separation of strip blanks.

ES tandem blanks for cross-sectioning into combined plates (Fig. 4) are formed by combining and connecting along the lines of joints of anisotropic (Fig. 4,*a*) and isotropic (Fig. 4,*b*) ES strips. One, two or more fragments of isotropic ETC strips can be welded to the fragment(s) of the anisotropic ETC strip. Before connecting the fragments, the anisotropic components are located with the direction of the texture, which is parallel to the lines of separation (Fig. 4,*c*). Separated sections of fragments with two or several seams are cut at given angles into plates (Fig. 4,*d*,*e*) with a combination of ESs [29]. Fragments can be connected by one of the methods of welding (laser, electron beam, diffusion, etc.). Determining the method and process of such welding is a separate research task.

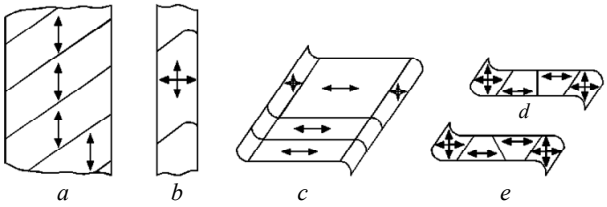

Fig. 4. Schematic diagrams of cutting and connecting components of the combined magnetic core: transverse divisions of the package of anisotropic (◄►) (*a*) and isotropic (▲▼◄►) (*b*) ESs into fragments; welding fragments along the lines of joints to the blank and its division into sections (*c*); separation of fragments into combined plates (*d*, *e*)

One of the directions of structural and geometric transformations of static EMSs is the replacement of conventional rectangular and circular forming contours of active elements with non-conventional ones, in particular octagonal and hexagonal contours [22, 23, 29]. In addition to the proposals for designs and methods (Fig. 3, 4), reducing the mass of isotropic components relative to analogs [27, 28] while reducing the total mass and losses is possible by replacing the rectangular outer contour of the planar magnetic core with an octagonal one. Rod and yoke areas (Fig. 5,*a*) are formed by plates of trapezoidal anisotropic ES.

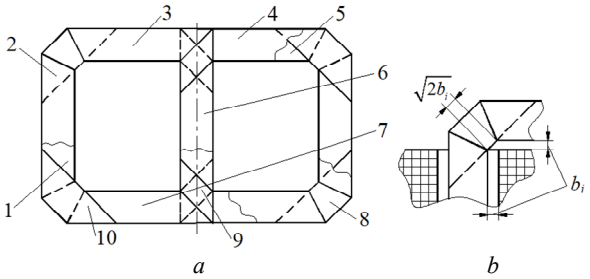

Fig. 5. Schemes of the structure (*a*) and the side corner zone (*b*) of a planar rod magnetic core of reduced mass with plates 1-7 of anisotropic and plates 8-10 of isotropic steels

Trapezoidal plates of adjacent layers differ in length and angles. The short bases of the long plates are equal to the long bases of the short plates and these bases are opposite. The sides of the anisotropic plates connect to the plates of the isotropic ES located in the side corners (Fig. 5,*a*). In this way, an octagonal external contour of the magnetic core is formed. At the same time, the uniformity of the field distribution increases and the

unused mass of the corner zones is removed (Fig. 5,*b*). The middle angular (T-shaped) sections are divided by smaller and larger sides of the parallelogram plates of the isotropic ES, which are oppositely located in the middle layers. Trapezoidal or parallelogram plates of the anisotropic ES are installed on the axis of the central rod part of the magnetic corer (Fig. 5,*a*). In the corners, in the absence of an insulating gap b_i (Fig. 5,*b*), triangular plates can also be installed between trapezoidal plates.

It is possible to eliminate losses from the third contour harmonics of the magnetic field of a three-phase planar three-section magnetic core with twisted components in a structure with an orthogonal position of the layers of the middle and side elements (Fig. 6,*a*). Lateral C-shaped elements are made by cutting a twisted blank or of curved strips of anisotropic ES. The middle element for extracting additional losses of orthogonal rotation of the flux and reducing additional losses of phase asymmetry can be made of the best brands of isotropic ES. The transverse section of the strip (Fig. 6,*b*) makes it possible to form oblique joints of the middle and side elements.

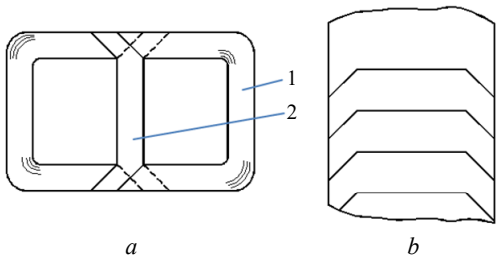

Fig. 6. Structural scheme (*a*) of a planar joint magnetic corer with twisted side 1 and laminated 2 middle elements and separation of the strip (*b*) of steel on the plates of the middle element

Sectioning of the magnetic core by width (Fig. 6,*a*) in addition to oblique connections, reduces the magnetic resistance of the joints by reversing the sections in each pair of adjacent middle and side elements.

In addition to the combined strip-plate one, it is possible to manufacture a twisted variant of the scheme of the magnetic core (Fig. 6,*a*). It is possible to make two identical twisted magnetic cores from sections of two twisted cut blanks. The blanks with the same heights h_m and identical cross-sections differ in the lengths l_1 and l_2 of the internal rectangular contours:

$$l_1 = h_m + 2b_v + 2b_i; \quad l_2 = 2b_v + b_t,$$

where b_v and b_t are the width of the winding window and the thickness of the technological waste layer of the ES (cutting disc).

The winding coils are wound on insulating frames covering the side and middle elements of the magnetic core (Fig. 6,*a*). Such frames make up the supporting base of EMS with fragile amorphous ES. Mutually orthogonal layers of ES of butt joints of the middle and side sections of the magnetic core of TTs' schemes (Fig. 6,*a*) should be insulated by applying a thin, durable heat-resistant coating.

Another variant of the technical solution containing C-shaped parts of twisted blanks is a T-shaped EMS spatial design (Fig. 7,*a*). For the coincidence of the directions of the ES layers, under the condition that the joints are coplanar, one of the C-shaped sections of the magnetic core is connected to the other two with the arrangement of the side surfaces in orthogonal planes (Fig. 7,*b*).

Losses from the third harmonics of the contour fluxes are also absent in the variants of the spatial EMS mentioned above with a common magnetic connection of the rods and yoke parts of the contact magnetic core when the primary winding is connected by a triangle. However, such EMSs are made in traditional circular forming contours of winding coils and rods. The circular contours of the rods of the specified options are filled, if there are central technological holes, with concentric turns of isotropic or involutely curved sheets of anisotropic ES. Rods made of ES packages of different widths are also used (Fig. 8,*a*). The indicated types of sections and structures of the rods fill the contour circles by 80-90 % and are installed between twisted jugular-angled end parts with triangular internal contours.

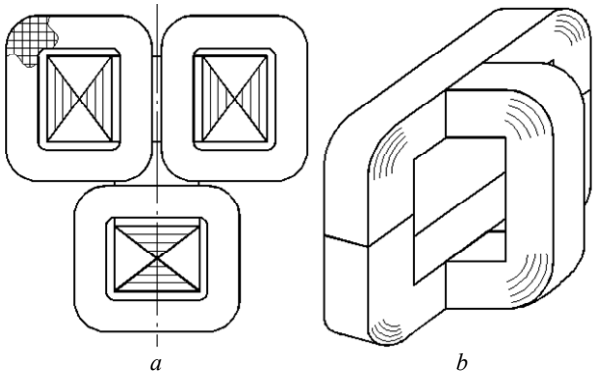

Fig. 7. Design scheme (*a*) and magnet core (*b*) of spatial EMS with T-shaped orthogonal location of twisted areas

The indicated circular and triangular contours of parts of the magnetic core have a negative effect on the use of the active volume of the EMS and increase losses in ES of TTs (TRs) with a magnetic core (Fig. 8,*a*). There is a significant uneven distribution of the magnetic field along the radial length l_a of a rectangular cross-sectional yokes with zero values of magnetic flux density on the inner and outer winding layers of the ES. This increases the magnetic flux density in the middle parts of the yokes and corners and causes an increase in losses, which is taken into account depending on the magnetic flux density by the corresponding coefficients. At the same time, the increase in losses when using anisotropic ES is also caused by the mismatch of the directions of the field lines in the corners with the direction of the texture of the twisted parts. Therefore, it is advisable to make the yoke-corner and rod parts of the combined butt-wound-plate magnetic core of isotropic or amorphous and anisotropic ES.

Improvement of the EMS with a tape/roll-plate magnetic core is possible by replacing the circular and triangular contours of parts of the magnetic core with hexagonal ones (Fig. 8,*b*,*c*). The mentioned transformations lead to a decrease in the unevenness of the field in the radial direction of the yoke, that is, along the length l_a (Fig. 8,*a*,*b*). At the given average value of the

amplitude of the magnetic flux density of the yoke B_{am}, distribution 1 changes to distribution 2 (Fig. 8,*d*). In this way, the magnetic flux densities in the main average volumes of the ES of the yokes and corners are reduced and the losses are reduced.

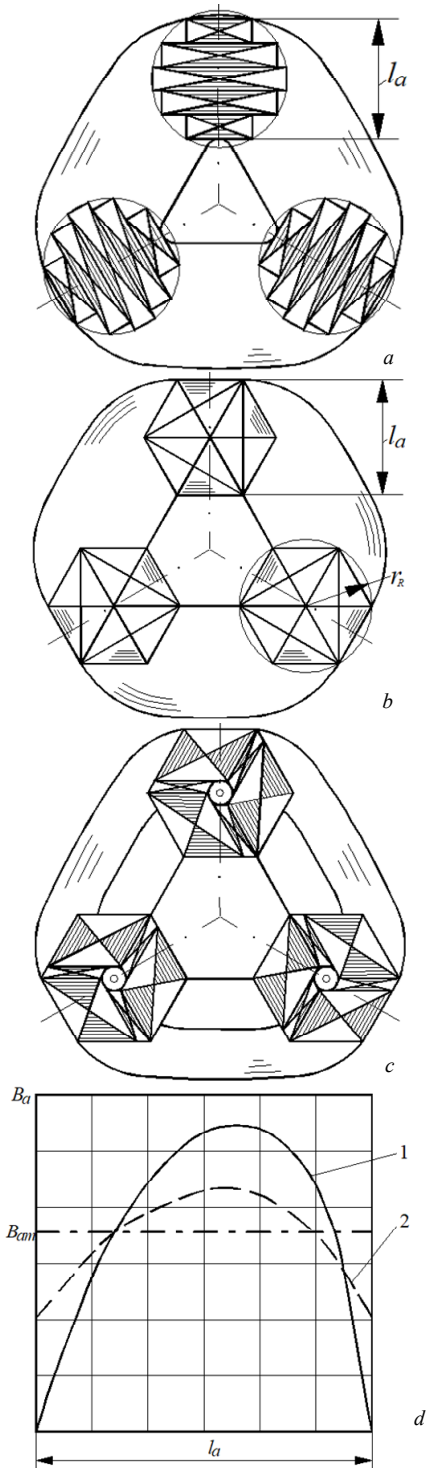

Fig. 8. Structural and geometrical features of three-phase tape-plate magnetic core variants with circular and triangular (*a*) and hexagonal (*b*, *c*) contours of rods and yoke-cirner parts and options for distribution of the magnetic flux density in yokes (*d*) with triangular (1) and hexagonal (2) internal contours

Identical rectangular plates of ES of rods (Fig. 8,*b*) almost completely fill ES hexagonal contours and fill the circumscribed circle with a coefficient of 0.826. In connection with the ratio of the lengths of the circle of the radius r_R (Fig. 8,*b*) and the inscribed hexagon 1.047, by replacing the circular configurations of the turns with the hexagonal ones, some reduction in the mass and losses of the winding is achieved for a given cross-sectional area of the rod. The presence of the central holes of the hexagonal rods reduces the mass and losses of the magnetic core using double-contour joint-corner parts and the structure of the rods from identical ES plates (Fig. 8,*c*).

Reasoned selection of a certain technical solution from the available options for new design or proof of the advantages of newly created innovations requires solving the problem of structural or structural-parametric optimization. Mathematical models of the specified problems must satisfy the conditions of invariance. The first is the availability of mathematical models with objective functions of a universal type and assembly order with the same set of controlled variables for any known and new proposals of a technical object. The second is the compliance of mathematical models with the requirements of comparison of measurement units, that is, the results of calculations of optimization criteria must be determined in dimensionless or specific (relative) units.

Such conditions are met by the method of universal target functions of dimensionless indicators of the technical level and relative geometric and electromagnetic controlled variables [22-24]. When applying the specified method, the identity of the general type of target functions of transformers, reactors and induction machines [22, 23] was revealed which corresponds to the general electromagnetic principle of their action. Objective functions k – the individual optimization criteria (masses k = 1, costs k = 2, losses k = 3), ij – the EMS option of TTs and TRs are determined by the equations:

$$F_{KTTij} = K_{MK}\left(\Pi_{TT}\right)^{3/4}\Pi^{*}_{KTTij};$$

$$F_{KTRij} = K_{MK}\left(\Pi_{TR}\right)^{3/4}\Pi^{*}_{TRij},$$

where K_{MK} is the component of the specific characteristics of one of the EMS active materials; $\Pi_{TT(TR)}$ and $\Pi^{*}_{KTT(TR)ij}$ is the indicator of output data and electromagnetic loads and dimensionless optimization component ij – variant of the EMS of the TTs (TRs), which corresponds to k – the optimization criterion.

The components $\Pi^{*}_{KTT(TR)ij}$ are nonlinear equations with relative controlled variables. Their extrema $\Pi^{*}_{TT(TR)e}$ represent indicators of technical level of ij – EMS variants [22-24].

When applying the mentioned method, the identity of the indicators of the technical level and, accordingly, the optimal geometric ratios of the same constructions and structures of TTs and TRs were revealed [22]. This makes it possible to manufacture on the basis of the same twisted or combined butt magnetic cores schemes (Fig. 6,*a*; Fig. 8,*b*,*c*) of unified optimized EMS of TTs and TRs, which differ in the number of winding coils in the winding window. Such unification will lead to a significant effect in the production of TTs and TRs of I-III dimensions.

Conclusions.

1. Oblique and double-contour (frame) connections of corner, rod and yoke sections, respectively, used in

laminated textured magnetic cores do not provide a significant reduction in additional losses during idle operation of conventional variants of three-phase transformers (TTs) and reactors (TRs).

2. Utilization instead of anisotropic one of strip amorphous electrical steel (ES) is limited by the technological limit of the power of TTs (TRs) with twisted magnetic cores and significantly worsens their mass and cost performance. At the same time, the issue of reducing significant additional losses of twisted three-phase three-contour magnetic cores remains problematic.

3. The improvement of TTs (TRs) with laminated textured planar magnetic cores is ensured by the location in the zones of change in the flow direction of the fragments of the isotropic ES with the rounding of right angles or the octagonal configuration of the external contours.

4. Elimination of losses from the third harmonics of contour currents is achieved by replacing twisted three-phase magnetic cores with separate cores with planar and spatial butt-joint magnetic cores with magnetic connection of rod and yoke-corner parts.

5. On the basis of the identity of the optimal geometric ratios of the same general structures of TTs and TRs, it seems appropriate to develop their unified electromagnetic systems with variants of joint planar and spatial twisted and strip-plate magnetic cores, which differ, respectively, in the orthogonal arrangement of the ES layers or the position in space of the middle and side sections and hexagonal configurations of rod contours and internal yoke contours.

6. The construction of spatial strip-plate contact magnetic cores should be based on a combination of brands of isotropic and anisotropic ESs in yoke-corner parts and rods.

Conflict of interest. The authors declare no conflict of interest.

REFERENCES

1. Targosz R., Topalis F.V. Energy efficiency of distribution transformers in Europe. *2007 9th International Conference on Electrical Power Quality and Utilisation*, 2007, pp. 1-5. doi: https://doi.org/10.1109/EPQU.2007.4424121.

2. De Almeida A., Santos B., Martins F. Energy-efficient distribution transformers in Europe: impact of Ecodesign regulation. *Energy Efficiency*, 2016, vol. 9, no. 2, pp. 401-424. doi: https://doi.org/10.1007/s12053-015-9365-z.

3. Charalampopoulos C., Psomopoulos C.S., Ioannidis G.Ch., Kaminaris S.D. Implementing the EcoDesign Directive in distribution transformers: First impacts review. *AIMS Energy*, 2017, vol. 5, no. 1, pp. 113-124. doi: https://doi.org/10.3934/energy.2017.1.113.

4. Ilo A. Behavior of transformer cores with multistep-lap joints. *IEEE Power Engineering Review*, 2002, vol. 22, no. 3, pp. 43-47. doi: https://doi.org/10.1109/MPER.2002.989193.

5. Yuen D.C.M., Choi V., Liu Zhi Gao, Jun Han. The first 110 kV /35 kV - 31.5 MVA cast resin transformer. *Conference Record of the 2004 IEEE Industry Applications Conference, 2004. 39th IAS Annual Meeting*, 2004, vol. 2, pp. 763-767. doi: https://doi.org/10.1109/IAS.2004.1348500.

6. Gao Yingna, Wang Shishan, Gao Hong. A new type of dry power transformer based on XLPE cable winding. *2005 International Conference on Electrical Machines and Systems*, 2005, vol. 3, pp. 1771-1774 doi: https://doi.org/10.1109/ICEMS.2005.202864.

7. Najafi A., Iskender I. Comparison of core loss and magnetic flux distribution in amorphous and silicon steel core transformers. *Electrical Engineering*, 2018, vol. 100, no. 2, pp. 1125-1131. doi: https://doi.org/10.1007/s00202-017-0574-7.

8. Hu D., Li Z., Hong Z., Jin Z. Development of a single-phase 330kVA HTS transformer using GdBCO tapes. *Physica C: Superconductivity and Its Applications*, 2017, vol. 539, pp. 8-12. doi: https://doi.org/10.1016/j.physc.2017.06.002.

9. Puilo G.V., Kuzmenko I.S., Tongaluk V.V. State-of-the-art trends in distribution transformers perfection. *Electrical Engineering & Electromechanics*, 2008, no. 2, pp. 48-52. (Rus).

10. Vani A., Sree Rama Chandra Murthy P. An automated tool for analyzing dissolved gases in power transformers and SF6 in switch gears using Artificial Intelligence approaches. *Journal of Electrical Engineering*, 2015, vol. 15, no. 2, pp. 262-274.

11. Ozgonenel O., Font A., Ilhan S. SF6 gaz yalitimli dagitim transformatörünün elektrostatik alan analizi. *2016 National Conference on Electrical, Electronics and Biomedical Engineering, ELECO 2016*, pp. 359-362. (Tur).

12. Blume S., Biela J. Optimal Transformer Design for Ultraprecise Solid State Modulators. *IEEE Transactions on Plasma Science*, 2013, vol. 41, no. 10, pp. 2691-2700. doi: https://doi.org/10.1109/TPS.2013.2280429.

13. Chen B., Liang X., Wan N. Design Methodology for Inductor-Integrated Litz-Wired High-Power Medium-Frequency Transformer With the Nanocrystalline Core Material for Isolated DC-Link Stage of Solid-State Transformer. *IEEE Transactions on Power Electronics*, 2020, vol. 35, no. 11, pp. 11557-11573. doi: https://doi.org/10.1109/TPEL.2020.2987944.

14. Puilo G.V., Nasypannaya E.P. Efficiency of windings with high-temperature superconductivity application in power transformers. *Electrotechnic and Computer Systems*, 2014, no. 14 (90), pp. 43-52. (Rus).

15. Bardyk E.I., Bolotnyi N.P. Development of fuzzy classifier for technical condition ranking of power transformer. *Electrical Engineering & Electromechanics*, 2023, no. 5, pp. 3-13. doi: https://doi.org/10.20998/2074-272X.2023.5.01.

16. Flanagan W.M. *Handbook of transformers design and application*. Boston, Mc Grow Hill, 1993. 232 p.

17. Marketos P., Meydan T. Novel Transformer Core Design Using Consolidated Stacks of Electrical Steel. *IEEE Transactions on Magnetics*, 2006, vol. 42, no. 10, pp. 2821-2823. doi: https://doi.org/10.1109/TMAG.2006.879139.

18. Levin M.I., Pentegov I.V., Rymar S.V., Lavreniuk A.V. Analysis of three-phase power transformer laminated magnetic core designs. *Electrical Engineering & Electromechanics*, 2014, no. 1, pp. 40-44. (Rus). doi: https://doi.org/10.20998/2074-272X.2014.1.08.

19. Kefalas T.D., Kladas A.G. Development of Distribution Transformers Assembled of Composite Wound Cores. *IEEE Transactions on Magnetics*, 2012, vol. 48, no. 2, pp. 775-778. doi: https://doi.org/10.1109/TMAG.2011.2172976.

20. Hernandez I., Olivares-Galvan J.C., Georgilakis P.S., Cañedo J.M. Core loss and excitation current model for wound core distribution transformers. *International Transactions on Electrical Energy Systems*, 2014, vol. 24, no. 1, pp. 30-42. doi: https://doi.org/10.1002/etep.1687.

21. Avdieieva O.A., Vakhonina L.V., Sadovoy O.S., Stavinskiy R.A., Tsyganov O.M. Improving the main indicators of transformers with twisted one-piece magnetic cores by changing the technology of circular winding turns formation. *Electrical Engineering & Electromechanics*, 2022, no. 3, pp. 3-7. doi: https://doi.org/10.20998/2074-272X.2022.3.01.

22. Stavinskiy A.A., Stavinskiy R.A., Avdieieva E.A. The method of comparative analyses of static electromagnetic systems that is different in structure and configuration of elements. *Electrotechnic and Computer Systems*, 2014, no. 14 (90), pp. 53-60. (Rus).

23. Stavinskyi A.A., Stavinskyi R.A., Avdeeva E.A., Palchikov O.O. A universal method for the justified selection of technical solutions for the active part of electrical machines and devices. *Bulletin of NTU «KhPI» Series: Electrical Machines and Electromechanical Energy Conversion*, 2016, no. 11 (1183), pp. 70-79. (Rus).

24. Stavynskyi A.A., Avdeeva O.A., Tsyganov O.M., Stavynskyi R.A., Sadovy O.S. Comparison of three-phase transformers with rectangular and circular rod contour of planar laminated magnetic cores (mass and cost indicators). *Bulletin of NTU «KhPI» Series: Electrical Machines and Electromechanical Energy Conversion*, 2019, no. 4 (1329), pp. 38-43. (Ukr). doi: https://doi.org/10.20998/2409-9295.2019.4.05.

25. Poveda-Lerma A., Serrano-Callergues G., Riera-Guasp M., Pineda-Sanchez M., Puche-Panadero R., Perez-Cruz J. Lamination effects on a 3D model of the magnetic core of power transformers. *Open Physics*, 2017, vol. 15, no. 1, pp. 997-1003. doi: https://doi.org/10.1515/phys-2017-0124.

26. Magdaleno-Adame S., Kefalas T.D., Garcia-Martinez S., Perez-Rojas C. Electromagnetic finite element analysis of electrical steels combinations in lamination core steps of single-phase distribution transformers. *2017 IEEE International Autumn Meeting on Power, Electronics and Computing (ROPEC)*, 2017, pp. 1-5. doi: https://doi.org/10.1109/ROPEC.2017.8261585.

27. Magdaleno-Adame S., Melgoza-Vazquez E., Olivares-Galvan J.C., Escarela-Perez R. Loss reduction by combining electrical steels in the core of power transformers. *International Transactions on Electrical Energy Systems*, 2016, vol. 26, no. 8, pp. 1737-1751. doi: https://doi.org/10.1002/etep.2175.

28. Levin M.I., Pentegov I.V., Rymar S.V., Lavreniuk A.V. New approaches at construction of magnetic conductors for mains transformers. *Electrical Engineering & Electromechanics*, 2015, no. 1, pp. 20-24. (Rus). doi: https://doi.org/10.20998/2074-272X.2015.1.04.

29. Stavinskiy A.A., Tsyganov A.M. Design and technological proposals for improving a single-phase transformer with laminated magnetic core. *Electrical Engineering & Electromechanics*, 2020, no. 6, pp. 11-17. doi: https://doi.org/10.20998/2074-272X.2020.6.02.

Received 04.09.2023
Accepted 07.11.2023
Published 02.03.2024

A.A. Stavynskyi[1]*, Doctor of Technical Science, Professor,*
O.A. Avdeeva[2]*, Candidate of Technical Science,*
D.L. Koshkin[1]*, Candidate of Technical Science, Associate Professor,*
R.A. Stavynskyi[2]*, Candidate of Technical Science, Associate Professor,*
O.M. Tsyganov[1]*, Candidate of Technical Science,*
[1] Mykolayiv National Agrarian University,
9, Georgiya Gongadze Str., Mykolaiv, 54020, Ukraine,
e-mail: andrey.stavynskiy@mnau.edu.ua;
Koshkindl@mnau.edu.ua;
potomkinske@gmail.com (Corresponding Author)
[2] Admiral Makarov National University of Shipbuilding,
9, Avenue Heroes of Ukraine, Mykolaiv, 54020, Ukraine,
e-mail: e.avdeeva@ukr.net;
rostyslav.stavynskyi@nuos.edu.ua

How to cite this article:
Stavynskyi A.A., Avdeeva O.A., Koshkin D.L., Stavynskyi R.A., Tsyganov O.M. Technical solutions to reduce losses in magnetic cores and material consumption of three-phase transformer and reactor equipment. *Electrical Engineering & Electromechanics*, 2024, no. 2, pp. 3-9. doi: https://doi.org/10.20998/2074-272X.2024.2.01

UDC 621.3 https://doi.org/10.20998/2074-272X.2024.2.02

K. Abed, H.K.E. Zine

Intelligent fuzzy back-stepping observer design based induction motor robust nonlinear sensorless control

Introduction. *The control algorithm of Induction Motor (IM) is massively dependent on its parameters; so, any variation in these parameters (especially in rotor resistance) gives unavoidably error propagates. To avoid this problem, researches give more than solution, they have proposed Variable Structure Control (VSC), adaptive observers such as Model Reference Adaptive System, Extended Luenberger Observer (ELO) and the Extended Kalman Filter (EKF), these solutions reduce the estimated errors in flux and speed. As* ***novelty*** *in this paper, the model speed observer uses the estimated currents and voltages as state variables; we develop this one by an error feedback corrector. The Indirect Rotor Field Oriented Control (IRFOC) uses the correct observed value of speed; in our research, we improve the observer's labour by using back-stepping Sliding Mode (SM) control.* ***Purpose.*** *To generate the pulse-width modulation inverter pulses which reduce the error due of parameters variations in very fast way.* ***Methods.*** *We develop for reach this goal an exploration of two different linear observers used for a high performance VSC IM drive that is robust against speed and load torque variations. Firstly, we present a three levels inverter chosen to supply the IM; we present its modelling and method of control, ending by an experiment platform to show its output signal. A block diagram of IRFOC was presented; we analyse with mathematic equations the deferent stages of modelling, showed clearly the decoupling theory and the sensorless technique of control. The study described two kinds of observers, ELO and EKF, to estimate IM speed and torque. By the next of that, we optimize the step response using the fuzzy logic, which helps the system to generate the PI controller gains. Both of the two observers are forward by SM current controller, the convergence of SM-ELO and SM-EKF structures is guaranteed by minimizing the error between actual and observed currents to zero.* ***Results.*** *Several results are given to show the effectiveness of proposed schemes.* References 25, table 2, figures 9.

Key words: **induction motor, indirect rotor field oriented control, extended Kalman filter observer, extended Luenberger observer, fuzzy logic control, sliding mode control.**

Вступ. *Алгоритм керування асинхронним двигуном (АД) багато в чому залежить від його параметрів; тому будь-яка зміна цих параметрів (особливо опору ротора) неминуче призводить до поширення помилок. Щоб уникнути цієї проблеми, дослідники пропонують щось більше, ніж просто рішення: вони запропонували управління змінною структурою (VSC), адаптивні спостерігачі, такі як адаптивна система еталонної моделі, розширений спостерігач Люенбергера (ELO) та розширений фільтр Калмана (EKF); ці рішення зменшують передбачувані помилки за потоком та швидкістю.* ***Новизною*** *цієї статті є те, що спостерігач швидкості моделі використовує оцінені струми та напруги як змінні стани; ми розробляємо його за допомогою коректора зворотного зв'язку помилки. Непряме управління з полю ротора (IRFOC) використовує правильне значення швидкості; у нашому дослідженні ми покращуємо роботу спостерігача, використовуючи керування ковзним режимом (SM) зі зворотним кроком.* ***Мета***. *Генерувати імпульси інвертора широтно-імпульсної модуляції, які швидко зменшують помилку, викликану змінами параметрів.* ***Методи***. *Для досягнення цієї мети ми розробляємо дослідження двох різних лінійних спостерігачів, що використовуються для високопродуктивного приводу VSC АД, стійкого до змін швидкості та моменту навантаження. По-перше, ми представляємо трирівневий інвертор, вибраний для живлення АД; ми представляємо його моделювання та метод управління, закінчуючи експериментальною платформою, що демонструє його вихідний сигнал. Представлена блок-схема IRFOC; ми аналізуємо за допомогою математичних рівнянь різні етапи моделювання, наочно демонструючи теорію розв'язки та безсенсорний метод керування. У дослідженні описані два типи спостерігачів, ELO та EKF, для оцінки швидкості та крутного моменту АД. Далі ми оптимізуємо перехідну реакцію, використовуючи нечітку логіку, яка допомагає системі генерувати коефіцієнти посилення ПІ-регулятора. Обидва з двох спостерігачів передаються контролером струму SM, зближення структур SM-ELO та SM-EKF гарантується за рахунок зведення до нуля помилки між фактичним та спостережуваним струмами.* ***Результати***. *Наведено результати, що показують ефективність запропонованих схем.* Бібл. 25, табл. 2, рис. 9.

Ключові слова: **асинхронний двигун, непряме керування по полю ротора, розширений спостерігач фільтра Калмана, розширений спостерігач Люенбергера, керування нечіткою логікою, керування ковзним режимом.**

Introduction. Recently, in the literature researches develop Induction Motor (IM) control in modern methods, taking in consideration IM parameters variations as inputs and signal behaviors as wishes outputs, the implantation of modern observers in control schemes is more than necessary.

In several structures and families, observers take places in linear and non-linear configurations systems as important solution can deals with motors states variations in good manner; for example, in the case when IM parameters was changed, we can see in [1-7] that the researches use adaptive observer as solution to get a speed convergence, in [8-11] researches deal with this problem by using back-stepping control, which gives better results.

We can see also in [12-24] the using of fuzzy logic technique to observe the controller parameters. In [22] the writer gives a model of Sliding Mode (SM) observer powered by fuzzy logic technique in goal of minimizing the error surface. In [22, 24], they use fuzzy logic to esteem the PI or PID parameters (K_p and K_i) which vary with the IM parameters variation during system operation.

Purpose. In our work, we take a new reasoning method to preserve the system divergence when changing motor parameters (rotor resistance in our case). We propose the using of a Variable Structure Control (VSC) methodology in order to improve the system robustness, the application runs by the implementation of SM in two observers structures combining by Extended Luenberger Observer (ELO) and Extended Kalman Filter (EKF) is shown in [12-17] the system is vector-controlled by indirect rotor field control scheme.

Not only the control of parameters variations is reached in our proposed method; but the robustness is also ameliorated by using SM, which we can observe in

lateral conditions of speed and torque variations during system operation.

In addition, in our paper, we made a comparison between SM control and fuzzy logic technique, this comparison allowed us to select our prefer method which plays a role in the improvement of the IM nonlinear sensorless control.

The simulation results, in the end of work, are given to show the effectiveness of proposed control approach. Those results are obtained from a drive control algorithms in the laboratory, with the help of MATLAB tool.

Three levels voltage inverter. We can create Three Levels Inverter (3LI) voltages in complete bridges by collecting three half-bridges using capacitive divider structure (Fig. 1).

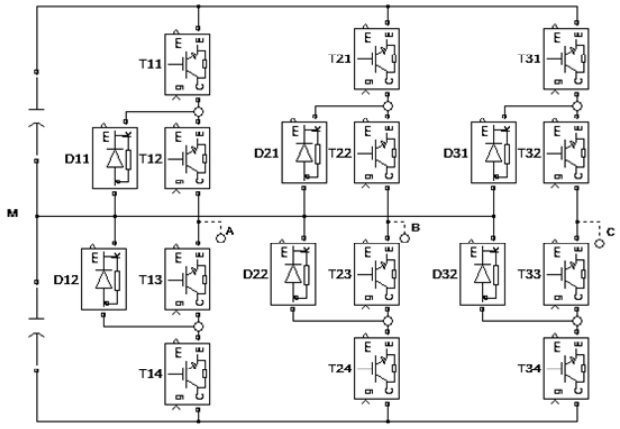

Fig. 1. Three Levels inverter Neutral Point Clamped (3LI-NPC)

1. Inverter's command strategy. The output voltages of 3LI are given in:

$$\begin{bmatrix} V_A \\ V_B \\ V_c \end{bmatrix} = \frac{1}{3}\begin{bmatrix} 2 & -1 & -1 \\ -1 & 2 & -1 \\ -1 & -1 & 2 \end{bmatrix} \cdot \left\{ \begin{bmatrix} B_{11}^b \\ B_{21}^b \\ B_{31}^b \end{bmatrix} \cdot U_{c1} - \begin{bmatrix} B_{10}^b \\ B_{20}^b \\ B_{30}^b \end{bmatrix} \cdot U_{c2} \right\}, \quad (1)$$

where B_{Ki} is the transistor's base command T_{Ki}.

Researchers have controlled the 3LI with deferent pulse-width modulation (PWM) strategies; in the next (Fig. 2 and Table 1) we present simulation and experimentation comparison between three strategies methods, we found that saw tooth-sinusoidal command is the better one to use; we use it, in this research, with two identical carriers. The experimental results in [18] were raised by using the acquisition card AT-MIO-16X through a current and voltage sensor card.

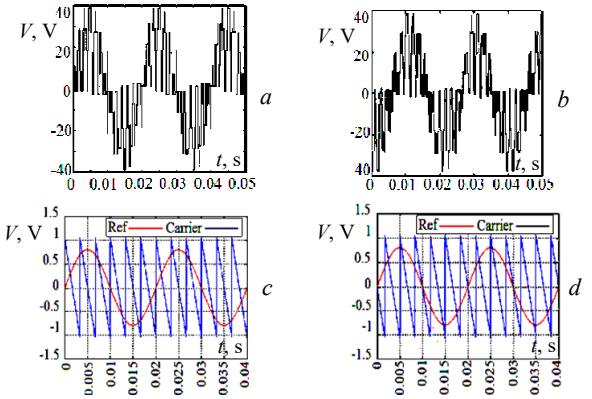

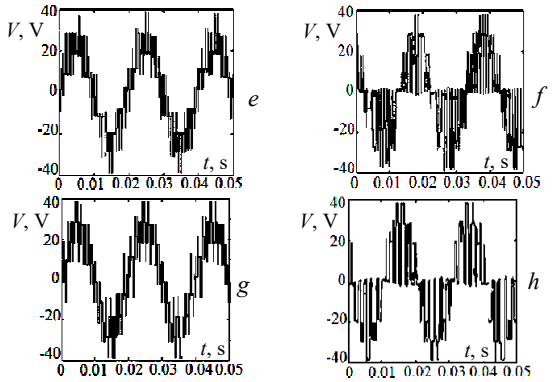

Fig. 2. Output voltage V_a as a function of time:
- triangular-sinusoidal command with one carrier simulation result in (*a*) and experimentation result in (*b*);
- principle of saw tooth-sinusoidal command with two carriers: reference voltage and saw tooth carrier 1 in (*c*) and reference voltage and saw tooth carrier 2 in (*d*);
- saw tooth-sinusoidal command with two carriers simulation result in (*e*) and experimentation result in (*f*);
- vector modulation strategy simulation result in (*g*) and experimentation result in (*h*)

Table 1

Comparison between harmonics of the various command types

Command strategy	THD max	THD min
Triangular-sinusoidal with one carrier	0.671	0.669
Saw-tooth-sinusoidal with two carriers	0.421	0.420
Vector modulation	0.498	0.497

2. Power stage. The IGBT transistor characteristics are: IRFBC40, 3 to 8 kHz, V_{CE} = 600 V, I_C = 49 A, V_{CE} (sat) ≤ 2 V, E_{TS} ≤ 9 mJ.

The commutation diode characteristics: BYT30PI 1000, V_{RRM} = 1 kV, I_F = 30 A, t_{rr} = 55 ns, V_S = 1.47 V.

Command stage:

- PIA card (Parallel Interface Adapter);
- a galvanic insulation card for the PC and card PIA protection;
- an interface card.

Sample of experimental installation is shown in Fig. 3.

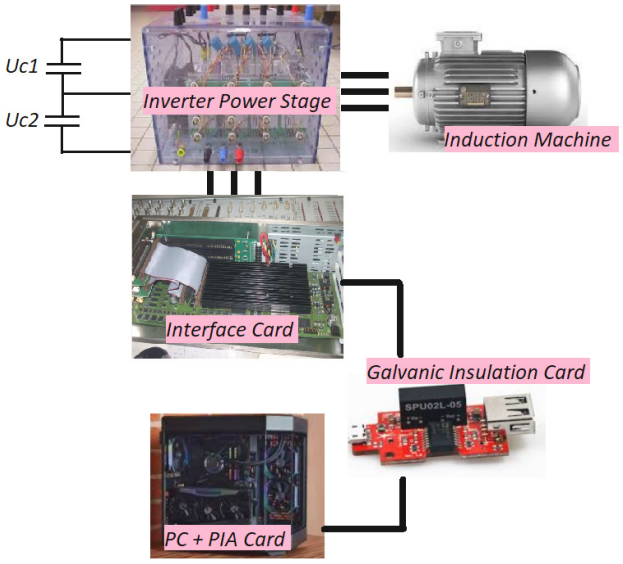

Fig. 3. Experimental installation constituents

Field oriented control structure. This plan uses a more robust strategy (Fig. 4), which exclude all kind of sensors in its algorithm.

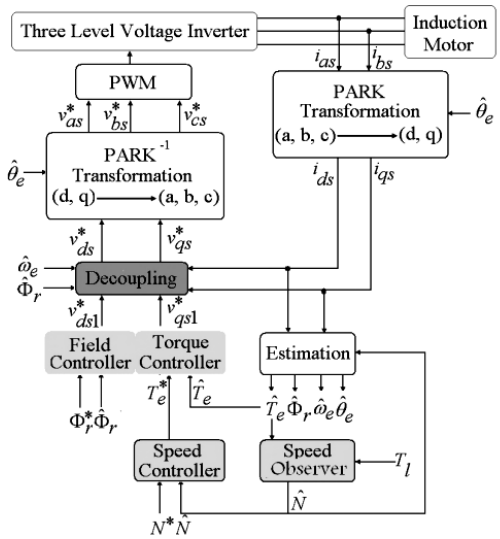

Fig. 4. Field oriented controller block diagram

The Indirect Rotor Field Oriented Control (IRFOC) proposes:

$$\begin{bmatrix} \frac{\mathrm{d}i_{ds}}{\mathrm{d}t} \\ \frac{\mathrm{d}i_{qs}}{\mathrm{d}t} \\ \frac{\mathrm{d}\phi_{dr}}{\mathrm{d}t} \\ \frac{\mathrm{d}\phi_{qr}}{\mathrm{d}t} \end{bmatrix} = \begin{bmatrix} -\gamma & \omega_e & \frac{k}{\tau_r} & p\cdot N\cdot k \\ -\omega_e & -\gamma & -p\cdot N\cdot k & \frac{k}{\tau_r} \\ \frac{L_m}{\tau_r} & 0 & -\frac{1}{\tau_r} & \omega_e - p\cdot N \\ 0 & \frac{L_m}{\tau_r} & -(\omega_e - p\cdot N) & -\frac{1}{\tau_r} \end{bmatrix} \begin{bmatrix} i_{ds} \\ i_{qs} \\ \phi_{dr} \\ \phi_{qr} \end{bmatrix} + \begin{bmatrix} \frac{1}{\sigma L_s} & 0 \\ 0 & \frac{1}{\sigma L_s} \\ 0 & 0 \\ 0 & 0 \end{bmatrix} \begin{bmatrix} v_{ds} \\ v_{qs} \end{bmatrix}, \quad (2)$$

where i_{ds}, i_{qs} are the *d*-*q* axis stator currents; v_{ds}, v_{qs} are the *d*-*q* axis stator applied voltages; ϕ_{dr}, ϕ_{qr} are the *d*-*q* rotor flux linkages; τ_r is the rotor time constant, $\tau_r = L_r/R_r$; ω_e is the synchronous angular speed; $k = M/\sigma L_s L_r$; γ, k are the simplifying constants; $\sigma = 1 - M^2/L_s L_r$; N is the estimated speed; L_s, L_r are the stator and rotor inductances; L_m is the mutual inductance; R_s, R_r are the stator and rotor winding resistances; M is the mutual magnetizing inductance; σ is the leakage coefficient; p is the number of pole pairs.

The decoupling between *d* and *q* axes can be realized by: $\Phi_{qr} = 0$; $\mathrm{d}\Phi_{qr}/\mathrm{d}t = 0$, and $\Phi_{dr} = \Phi_r$, where Φ_r is the rated flux. So:

$$\begin{cases} v_{ds} = \sigma L_s \dfrac{di_{ds}}{dt} + \left(R_s + R_r \dfrac{M^2}{L_r^2} \right) i_{ds} - \omega_e \sigma L_s i_{qs} - \dfrac{M}{L_r^2} R_r \Phi_r; \\ v_{qs} = \sigma L_s \dfrac{di_{qs}}{dt} + \omega_e \sigma L_s i_{qs} + \left(R_s + R_r \dfrac{M^2}{L_r^2} \right) i_{ds} - \dfrac{M}{L_r^2} pN\Phi_r; \\ \tau_r \dfrac{d\Phi_r}{dt} + \Phi_r = M i_{ds}; \\ \omega_e = pN + \dfrac{M}{\tau_r} \dfrac{i_{qs}}{\Phi_r}. \end{cases} \quad (3)$$

The mechanical equations, electromagnetic torque and motor speed are related by:

$$J\frac{\mathrm{d}N}{\mathrm{d}t} + fN = T_e - T_l, \quad (4)$$

where T_e, T_l are the electromagnetic and load torques; f is the friction coefficient; J is the total inertia.

The expression of electromagnetic torque is:

$$T_e = p\frac{M}{L_r}\Phi_r i_{qs}. \quad (5)$$

The decoupled system is given by:

$$\begin{cases} v_{ds}^* = v_{ds1} - e_{ds}; \\ v_{qs}^* = v_{qs1} - e_{qs}, \end{cases} \quad (6)$$

where

$$\begin{cases} e_{ds} = \hat{\omega}_e \sigma L_s i_{qs} + \dfrac{M}{L_r^2} R_r \Phi_r; \\ e_{qs} = -\hat{\omega}_e \sigma L_s i_{ds} - \dfrac{M}{L_r} \hat{\omega}_e \Phi_r + \dfrac{M^2}{L_r \tau_r} i_{qs}, \end{cases} \quad (7)$$

where «^» is the estimated value; «*» is the reference value.

Sensorless speed control design. The estimation of synchronous angular speed is calculated by using the row 4 in (3):

$$\omega_e = pN + \frac{M}{\tau_r}\frac{i_{qs}}{\hat{\Phi}_r + \varepsilon}, \quad (8)$$

where $\hat{\Phi}_r$ is the estimate flux; $\varepsilon = 0.01$ is the constant to avoid the mathematical divergence when $\hat{\Phi}_r \approx 0$.

From the row 3 of (3) we estimate:

$$\hat{\Phi}_r = \frac{M}{1 + \tau_r p} i_{ds}.$$

Speed control. From the synchronous angular speed, we obtained $\theta_e = \int \omega_e \mathrm{d}t$. To estimate the speed, we establish following function:

$$N = \frac{1}{Jp + f}(T_e - T_l). \quad (9)$$

Closed loop Luenberger observer implantation. Several researches use ELO in sensorless control of IM [14, 16, 17], the goal is to remove all mechanical sensors. From (4) and (5) we have:

$$\frac{\mathrm{d}N}{\mathrm{d}t} = -\frac{f}{J}N + \frac{pM\Phi_r}{JL_r} i_{qs} - \frac{1}{J}T_l. \quad (10)$$

The 2nd order ELO is given by: $\begin{cases} \dot{\hat{X}} = A\hat{X} + BU + L(Y - \hat{Y}); \\ \hat{Y} = C\hat{X}, \end{cases}$

where $\hat{X} = \begin{bmatrix} N_{obs} \\ T_{l-obs} \end{bmatrix}$, $L = \begin{bmatrix} l_1 \\ l_2 \end{bmatrix}$, and we have finally:

$$\begin{bmatrix} \frac{\mathrm{d}N_{obs}}{\mathrm{d}t} \\ \frac{\mathrm{d}T_{l-obs}}{\mathrm{d}t} \end{bmatrix} = \begin{bmatrix} -\frac{f}{J} - l & \frac{-1}{J} \\ -l_2 & 0 \end{bmatrix} \begin{bmatrix} N_{obs} \\ T_{l-obs} \end{bmatrix} + \begin{bmatrix} \frac{pM\Phi_r}{JL_r} \\ 0 \end{bmatrix} (i_{qs}) + \begin{bmatrix} l_1 \\ l_2 \end{bmatrix} \cdot N, \quad (11)$$

where N_{obs} is the observed speed; T_{l_obs} is the observed load torque. We put $l_1 = 250$, $l_2 = -600$ to fix the observer dynamics.

Control with extended Kalman filter observer. EKF offers the estimation of the systems states [12, 13]. The forward approximation is used to discretize (2):

$$\begin{cases} x(k+1) = f(x(k), k) + g(u(k), k); \\ y(k) = h(x(k), k), \end{cases} \quad (12)$$

where

$$f(x(k), k) + g(u(k), k) = A_d x(k) + B_d u(k);$$
$$A_d = I + A_c T_s;\ B_d = B_c T_s;$$

$$A_c=\begin{bmatrix} -\gamma & \omega_e & k/\tau_r & pNk \\ -\omega_e & -\gamma & -pNk & k/\tau_r \\ L_m/\tau_r & 0 & -1/\tau_r & \omega_e-pN \\ 0 & L_m/\tau_r & -(\omega_e-pN) & -1/\tau_r \end{bmatrix}; B_c=\begin{bmatrix} \frac{1}{\sigma L_s} & 0 \\ 0 & \frac{1}{\sigma L_s} \\ 0 & 0 \\ 0 & 0 \end{bmatrix}, \quad (13)$$

where $T_s = (t_k - t_{k-1})$ is the sampling time.

The stochastic model of the disturbances is established by adding noise vectors as below:

$$\begin{cases} \hat{x}(k+1) = f(\hat{x}(k),k) + g(u(k),k) + w(k); \\ y(k) = h(\hat{x}(k),k) + v(k), \end{cases} \quad (14)$$

where $u(k)$, $y(k)$ are the input and output signals; $w(k)$ is the process noise; $v(k)$ is the measurement one; $x(k)$ is the state vector, which can be observed by the EKF as:

$$\hat{x}(k+1) = f(\hat{x}(k),k) + g(u(k),k) + K_e\left[y(k) - h(\hat{x}(k),k)\right]. \quad (15)$$

By using Riccati difference equation, we can establish the Kalman gain K_e and we can simplify it as:

$$K_e = \begin{bmatrix} 0 & 0 & 0 \\ k_{e1} & k_{e2} & k_{e3} \end{bmatrix}^T \begin{bmatrix} \cos\hat{\theta}_e & \sin\hat{\theta}_e \\ -\sin\hat{\theta}_e & \cos\hat{\theta}_e \end{bmatrix}, \quad (16)$$

where k_{e1}, k_{e2}, k_{e3} are the adjustable parameters, and:

$$h(x(k)) = \left[\cos\hat{\theta}_e(k) \quad \sin\hat{\theta}_e(k)\right]^T.$$

The output variables of the EKF may be chosen as:

$$\left[y_1(k), y_2(k)\right] = \left[\Phi_{\beta s}, \Phi_{\alpha s}\right], \quad (17)$$

where $\Phi_{\alpha s}$, $\Phi_{\beta s}$ are the α-β stator flux linkages.

When $x = \left[\hat{\theta}_e \quad \hat{w}_e \quad w'\right]^T$ are the state variables with w' as the double integration of noise.

When we put $u(k) = 0$, the model (14) can be written as:

$$\begin{cases} \hat{x}(k+1) = F(\hat{x}(k)) + w(k); \\ y(k) = h(\hat{x}(k)) + v(k), \end{cases} \quad (18)$$

where

$$F = \begin{bmatrix} 1 & T_s & 0 \\ 0 & 1 & 1 \\ 0 & 0 & 1 \end{bmatrix}.$$

So, $\hat{w}_e$ and $\hat{\theta}_e$ can be observed by:

$$\hat{w}_e(p) = \frac{\mathrm{d}\hat{\theta}_e(p)}{\mathrm{d}t} = \frac{\hat{\theta}(k+1) - \hat{\theta}(k)}{T_s} = \hat{w}_e(k) + k_1\varepsilon(k); \quad (19)$$

$$\hat{w}_e(k+1) - \hat{w}_e(k) = w'(k) + k_2\varepsilon(k); \quad (20)$$

$$w'(k+1) - w'(k) = k_3\varepsilon(k); \quad (21)$$

$$\varepsilon(k) = y_2(k)\cos\hat{\theta}_e(k) - y_1(k)\sin\hat{\theta}_e(k). \quad (22)$$

The block diagram of the EKF used is shown in Fig. 5.

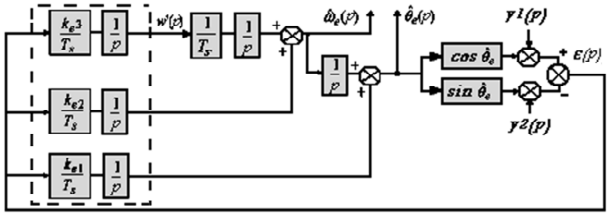

Fig. 5. Simplified EKF observer block diagram

SM current and flux observer design. The application of SM control to IMs has been widespread in [8-11, 22]; we implant it to estimate the speed and rotor time constant, our method guarantees the convergence of the current during control time and produces, as well, fluxes along the *d* and *q* axes. From (2) we can write:

$$\begin{bmatrix} \frac{\partial\hat{i}_{ds}}{\partial t} \\ \frac{\partial\hat{i}_{qs}}{\partial t} \end{bmatrix} = -\gamma\begin{bmatrix} \hat{i}_{ds} \\ \hat{i}_{qs} \end{bmatrix} + k\begin{bmatrix} \Psi_{dr} \\ \Psi_{qr} \end{bmatrix} + \frac{1}{\sigma L_s}\begin{bmatrix} v_{ds} \\ v_{qs} \end{bmatrix}; \quad (23)$$

$$\begin{bmatrix} \frac{\partial\hat{\Phi}_{dr}}{\partial t} \\ \frac{\partial\hat{\Phi}_{qr}}{\partial t} \end{bmatrix} = \frac{M}{\tau_r}\begin{bmatrix} i_{ds} \\ i_{qs} \end{bmatrix} - \begin{bmatrix} \Psi_{dr} \\ \Psi_{qr} \end{bmatrix}, \quad (24)$$

where

$$\Psi_{dr} = -u_{ds}\mathrm{sign}(s_{ds}); \qquad \Psi_{qr} = -u_{qs}sign(s_{qs});$$

$$u_{ds} = \left|-\gamma\bar{i}_{ds} - k\left(\frac{\phi_{dr}}{T_r} + pN\phi_{qr}\right)\right|;$$

$$u_{qs} = \left|-\gamma\bar{i}_{qs} - k\left(\frac{\phi_{qr}}{T_r} + pN\phi_{dr}\right)\right|, \quad (25)$$

where $\bar{i}_{ds} = \hat{i}_{ds} - i_{ds}, \bar{i}_{qs} = \hat{i}_{qs} - i_{qs}$;

$$\begin{bmatrix} \Psi_{dr} \\ \Psi_{qr} \end{bmatrix} = \begin{bmatrix} \frac{1}{\hat{\tau}_r} & p\hat{N}k \\ -p\hat{N}k & \frac{1}{\hat{\tau}_r} \end{bmatrix}\begin{bmatrix} \hat{\Phi}_{dr} \\ \hat{\Phi}_{qr} \end{bmatrix}, \quad (26)$$

and $s_{ds} = \hat{i}_{ds} - i_{ds}$; $s_{qs} = \hat{i}_{qs} - i_{qs}$.

So, speed and real value of the rotor time constant can be calculated by:

$$\begin{bmatrix} \frac{1}{\hat{\tau}_r} \\ p\hat{N}k \end{bmatrix} = \frac{1}{\left|\hat{\Phi}_r\right|}\begin{bmatrix} -\hat{\Phi}_{dr} & -\hat{\Phi}_{qr} \\ -\hat{\Phi}_{qr} & \hat{\Phi}_{dr} \end{bmatrix}\begin{bmatrix} \Psi_{dr} \\ \Psi_{qr} \end{bmatrix}, \quad (27)$$

where $\left|\hat{\Phi}_r\right| = (-\hat{\Phi}_{dr}^2 - \hat{\Phi}_{qr}^2)$.

Fuzzy-PI controller architecture. It has been developed recently in [19-24], we use fuzzy logic algorithm, as a smart attitude, to reconstruct the rotor resistance and load time constant, after their variations. The fuzzy part in the controller adjusts the PI gains, which planned to enhance the step feedback; the improvement of PI observers has been developed in other way by [25].

The speed error and its rate of change are the controller inputs, the K_i and K_p are its outputs, $e(k) = \overset{*}{N} - \hat{N}$ and $\Delta e(k) = e(k) - e(k-1)$

The program uses such linguistic tags: NL (Negative Large), NM (Negative Medium), NS (Negative Short), ZE (Zero), PS (Positive Short), PM (Positive Medium), PL (Positive Large). Every fuzzy tag has a related membership function. «*Set if then*» is the logic sentence, which represents the fuzzy control rules, these rules are formulated as follows: **If** $e(k)$ is NL **and** $\Delta e(k)$ is N **then** $T_e^*(k)$ is ZE. Results for speed control are shown in Table 2 with E is the error, CE is the convergence of error.

Table 2

Control rule base

$\downarrow CE / E\rightarrow$	NL	NM	NS	ZE	PS	PM	PL
N	ZE	S	M	L	M	S	ZE
ZE	ZE	S	M	L	M	S	ZE
P	ZE	M	L	L	L	M	ZE

To produce the inference mechanism, we use Mamdani Max-Min method (Fig. 6). We apply the center of gravity process to crisp the output value in the defuzzification stage:

$$\Delta\mu_0 = \sum_{j=0}^{n} C^0(\Delta\mu_j)\Delta\mu_j \Big/ \sum_{j=0}^{n} C^0(\Delta\mu_j). \quad (28)$$

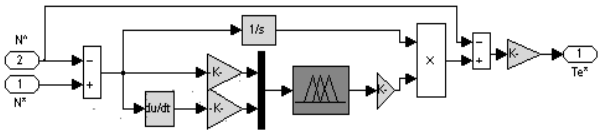

Fig. 6. Synoptic model of fuzzy controller for IM

Results and analysis. We consider the IM as continuous model. The IGBT based inverter is a 3LI-NPC, controlled by an 18 kHz PWM. The robustness of sensorless speed control is verified, in the first, we apply varied load torque values as: +10 N·m in 1 s, –10 N·m in 2.5 s, +10 N·m in 6 s, –10 N·m in 7 s, 0 N·m in 8 s with flux 0.8 Wb. The speed is fixed at 150 then –150 rad/s into 3.5 s.

In Fig. 7,*a* we show, obviously, that the dynamic performances of the speed are very good.

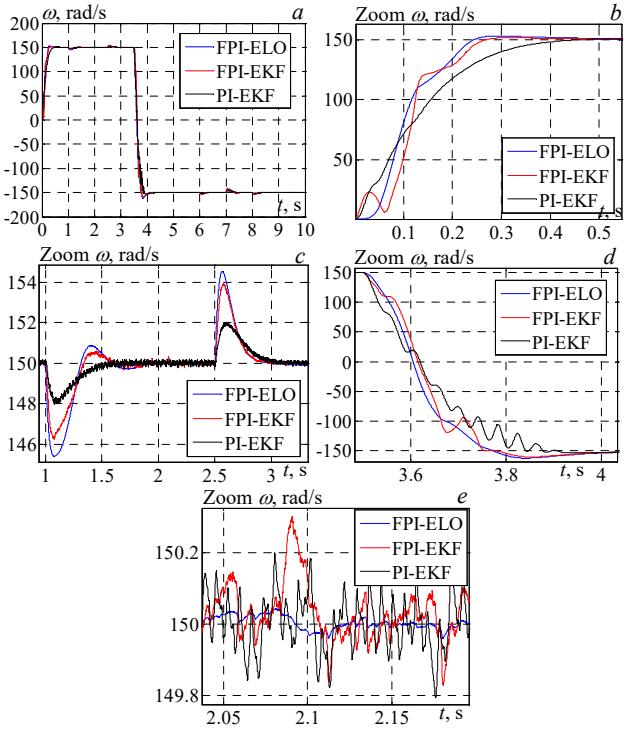

Fig. 7. Simulation results of the improved EKF and ELO observer by FPI controller: IM speed in (*a*); zoom in speed gives a comparison between the observer's time responses in (*b*); zoom in speed during control shows the speed overshoots in (*c*); speed delay time during the change of the speed reference in (*d*); harmonics observed during control in (*e*)

Presented in Fig. 7,*b* the Fuzzy Proportional-Integral FPI-ELO gives the better time response; it is more reliable and less-noise than the FPI-EKF (Fig. 7,*d* and Fig. 7,*e*). But it makes a slightly overshoot as shown in Fig. 7,*c* when step changes take place in the load torque.

Figure 8 shows the superiority of the FPI-EKF controller compared to the traditional Proportional-Integral PI-EKF either in the overshoot or in the harmonic's noises.

In other stage of studying, using VSC with SM, we have tested the strength of our controllers, with load torque applied as the following way: +10 N·m in 1.5 s, 0 N·m in 2.5 s, +10 N·m in 6 s, –10 N·m in 7 s, 0 N·m in 8 s.

The comparison in Fig. 9,*a*,*b*,*c* reveals that the observation by ELO or EKF of the electromagnetic torque.

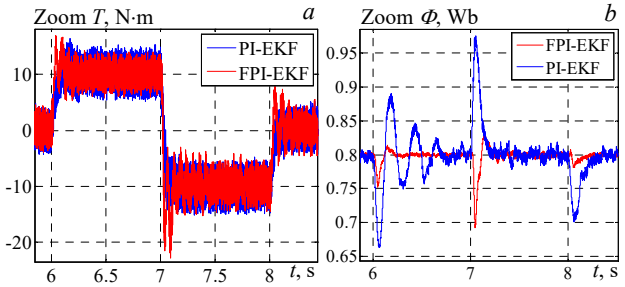

Fig. 8. Estimated electromagnetic torque *T* (*a*); «*d* axe» flux in (*b*)

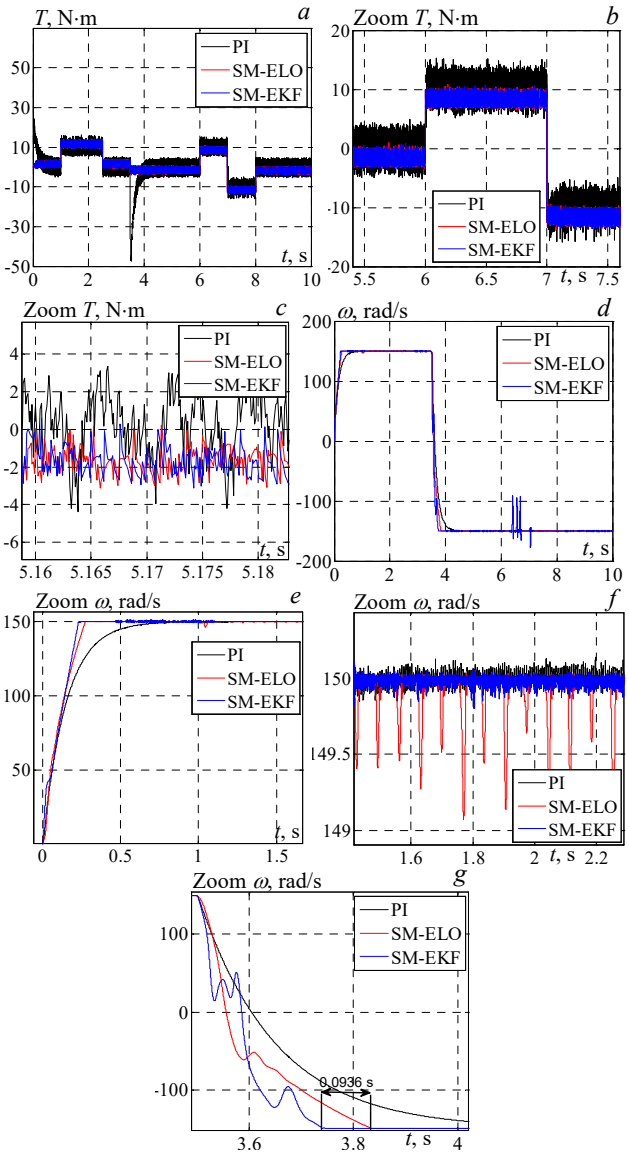

Fig. 9. Simulation results of the improved EKF and ELO observer by SM control: observed electromagnetic torque in (*a* and *b*); harmonics observed during electromagnetic control in (*c*); comparison between SM-ELO and SM-EKF speed in (*d*); comparison between SM-ELO and SM-EKF speed response time in (*e*); harmonics observed during speed control in (*f*); comparison between SM-ELO and SM-EKF speed delay time during speed reference change in (*g*)

Conclusions. The high-performance intelligent sensorless based variable structure control in an indirect rotor field oriented control scheme, of the induction motor drive, using Luenberger and extended Kalman filter observers is discussed in this literature. The robustness of the speed response using two different observers design has been compared, and it has been found to be favorable.

The results investigation confirms that the combination of sliding mode with adaptive observers achieves a pleasing performance even in the presence of noises or variations in the induction motor parameters and drive conditions. Moreover, it can be said from the results that the estimation of rotor speed has been done satisfactorily, and the sliding mode extended Kalman filter has better characteristics than the other observer presented.

Conflict of interest. The authors of the article declare that there is no conflict of interest.

REFERENCES

1. Ren Y., Wang R., Rind S.J., Zeng P., Jiang L. Speed sensorless nonlinear adaptive control of induction motor using combined speed and perturbation observer. *Control Engineering Practice*, 2022, vol. 123, art. no. 105166. doi: https://doi.org/10.1016/j.conengprac.2022.105166.

2. Chen C., Yu H., Gong F., Wu H. Induction Motor Adaptive Backstepping Control and Efficiency Optimization Based on Load Observer. *Energies*, 2020, vol. 13, no. 14, art. no. 3712. doi: https://doi.org/10.3390/en13143712.

3. Ammar A., Benakcha A., Bourek A. Adaptive MRAC-based direct torque control with SVM for sensorless induction motor using adaptive observer. *The International Journal of Advanced Manufacturing Technology*, 2017, vol. 91, no. 5-8, pp. 1631-1641. doi: https://doi.org/10.1007/s00170-016-9840-5.

4. Nguyen N.-D., Nam N.N., Yoon C., Lee Y.Il. Speed Sensorless Model Predictive Torque Control of Induction Motors Using a Modified Adaptive Full-Order Observer. IEEE *Transactions on Industrial Electronics*, 2022, vol. 69, no. 6, pp. 6162-6172. doi: https://doi.org/10.1109/TIE.2021.3094493.

5. Yin S., Huang Y., Xue Y., Meng D., Wang C., Lv Y., Diao L., Jatskevich J. Improved Full-Order Adaptive Observer for Sensorless Induction Motor Control in Railway Traction Systems Under Low-Switching Frequency. *IEEE Journal of Emerging and Selected Topics in Power Electronics*, 2019, vol. 7, no. 4, pp. 2333-2345. doi: https://doi.org/10.1109/JESTPE.2019.2898875.

6. Huang S., Deng X., Xing P., Su C. Improved Design of Feedback Matrix of Adaptive Observer for Induction Motor. *Journal of Physics: Conference Series*, 2023, vol. 2479, no. 1, art. no. 012015. doi: https://doi.org/10.1088/1742-6596/2479/1/012015.

7. Zhao H., Eldeeb H.H., Wang J., Kang J., Zhan Y., Xu G., Mohammed O.A. Parameter Identification Based Online Noninvasive Estimation of Rotor Temperature in Induction Motors. *IEEE Transactions on Industry Applications*, 2021, vol. 57, no. 1, pp. 417-426. doi: https://doi.org/10.1109/TIA.2020.3039940.

8. Pudari M., Arya S.R., Arya R.K. An improved Sliding Mode Observer for parameter estimation in induction motor drive with optimised gains. *Australian Journal of Electrical and Electronics Engineering*, 2023, vol. 20, no. 3, pp. 235-250. doi: https://doi.org/10.1080/1448837X.2023.2174110.

9. Yang Z., Zhang D., Sun X., Ye X. Adaptive Exponential Sliding Mode Control for a Bearingless Induction Motor Based on a Disturbance Observer. *IEEE Access*, 2018, vol. 6, pp. 35425-35434. doi: https://doi.org/10.1109/ACCESS.2018.2851590.

10. Zhang Y., Yin Z., Liu J., Tong X. Design and implementation of an adaptive sliding-mode observer for sensorless vector controlled induction machine drives. *Journal of Electrical Engineering and Technology*, 2018, vol. 13, no. 3, pp. 1304-1316. doi: https://doi.org/10.5370/JEET.2018.13.3.1304.

11. Ye S., Yao X. A Modified Flux Sliding-Mode Observer for the Sensorless Control of PMSMs With Online Stator Resistance and Inductance Estimation. *IEEE Transactions on Power Electronics*, 2020, vol. 35, no. 8, pp. 8652-8662. doi: https://doi.org/10.1109/TPEL.2019.2963112.

12. Mynar Z., Vaclavek P., Blaha P. Synchronous Reluctance Motor Parameter and State Estimation Using Extended Kalman Filter and Current Derivative Measurement. *IEEE Transactions on Industrial Electronics*, 2021, vol. 68, no. 3, pp. 1972-1981. doi: https://doi.org/10.1109/TIE.2020.2973897.

13. Chaabane H., Khodja D.E., Chakroune S., Hadji D. Model reference adaptive backstepping control of double star induction machine with extended Kalman sensorless control. *Electrical Engineering & Electromechanics*, 2022, no. 4, pp. 3-11. doi: https://doi.org/10.20998/2074-272X.2022.4.01.

14. Chaabane H., Eddine K.D., Salim C. Sensorless backstepping control using a Luenberger observer for double-star induction motor. *Archives of Electrical Engineering*, 2020, vol. 69, no. 1, pp. 101-116. doi: https://doi.org/10.24425/aee.2020.131761.

15. Saifi R. Implementation of a new flux rotor based on model reference adaptive system for sensorless direct torque control modified for induction motor. *Electrical Engineering & Electromechanics*, 2023, no. 2, pp. 37-42. doi: https://doi.org/10.20998/2074-272X.2023.2.06.

16. You J., Wu W., Wang Y. An Adaptive Luenberger Observer for Speed-Sensorless Estimation of Induction Machines. *2018 Annual American Control Conference (ACC)*, 2018, pp. 307-312. doi: https://doi.org/10.23919/ACC.2018.8431006.

17. Harini B.W. The Effect of Motor Parameters on the Induction Motor Speed Sensorless Control System using Luenberger Observer. *International Journal of Applied Sciences and Smart Technologies*, 2022, vol. 4, no. 1, pp. 59-74. doi: https://doi.org/10.24071/ijasst.v4i1.4518.

18. Mehdi A., Reama A., Benalla H. Two vector based direct power control of AC/DC grid connected converters using a constant switching frequency. *Journal of Power Electronics*, 2017, vol. 17, no. 5, pp. 1363-1371. doi: https://doi.org/10.6113/JPE.2017.17.5.1363.

19. Ganthia B.P., Barik S.K. Fault Analysis of PI and Fuzzy-Logic-Controlled DFIG-based Grid-Connected Wind Energy Conversion System. *Journal of The Institution of Engineers (India): Series B*, 2022, vol. 103, no. 2, pp. 415-437. doi: https://doi.org/10.1007/s40031-021-00664-9.

20. Mehedi I.M., Saad N., Magzoub M.A., Al-Saggaf U.M., Milyani A.H. Simulation Analysis and Experimental Evaluation of Improved Field-Oriented Controlled Induction Motors Incorporating Intelligent Controllers. *IEEE Access*, 2022, vol. 10, pp. 18380-18394. doi: https://doi.org/10.1109/ACCESS.2022.3150360.

21. Elgbaily M., Anayi F., Packianather M. Performance Improvement Based Torque Ripple Minimization for Direct Torque Control Drive Fed Induction Motor Using Fuzzy Logic Control. *Lecture Notes in Electrical Engineering*, 2022, vol. 921 LNEE, pp. 416-428. doi: https://doi.org/10.1007/978-981-19-3923-5_36.

22. Wogi L., Ayana T., Morawiec M., Jąderko A. A Comparative Study of Fuzzy SMC with Adaptive Fuzzy PID for Sensorless Speed Control of Six-Phase Induction Motor. *Energies*, 2022, vol. 15, no. 21, art. no. 8183. doi: https://doi.org/10.3390/en15218183.

23. Salahuddin H., Imdad K., Chaudhry M.U., Nazarenko D., Bolshev V., Yasir M. Induction Machine-Based EV Vector Control Model Using Mamdani Fuzzy Logic Controller. *Applied Sciences*, 2022, vol. 12, no. 9, art. no. 4647. doi: https://doi.org/10.3390/app12094647.

24. Benbouhenni H. Seven-level NPC Inverter-based Neuronal Direct Torque Control of the PMSM Drives with Regulation Speed Using Neural PI Controller. *International Journal of Intelligent Information Systems*, 2019, vol. 8, no. 5, pp. 85-96. doi: https://doi.org/10.11648/j.ijiis.20190805.11.

25. Chatterjee A. Analysis of a Self-Excited Induction Generator With Fuzzy PI Controller for Supporting Domestic Loads in a Microgrid. *Journal of Fuzzy Systems and Control*, 2023, vol. 1, no. 2, pp. 61-65, doi: https://doi.org/10.59247/jfsc.v1i2.42.

Received 13.08.2023
Accepted 06.11.2023
Published 02.03.2024

Khoudir Abed [1], *Doctor on Electrical Engineering, Professor,*
Hamed Kamel Eddine Zine[1], *PhD Student,*
[1] Laboratory of Electrical Engineering of Constantine (LGEC), Mentouri University, Road Ain El Bey, Constantine, Algeria,
e-mail: khoudir.abed@laposte.net (Corresponding Author);
kamel-eddine.zine-hamed@lec-umc.org

How to cite this article:
Abed K., Zine H.K.E. Intelligent fuzzy back-stepping observer design based induction motor robust nonlinear sensorless control. *Electrical Engineering & Electromechanics*, 2024, no. 2, pp. 10-15. doi: https://doi.org/10.20998/2074-272X.2024.2.02

UDC 621.3 https://doi.org/10.20998/2074-272X.2024.2.03

M. Aissaoui, H. Bouzeria, M. Benidir, M.A. Labed

Harmonics suppression in high-speed railway via single-phase traction converter with an LCL filter using fuzzy logic control strategy

Introduction. *The railway Traction Power Supply System (TPSS) encounters a common challenge related to high-frequency harmonic resonance, especially when employing AC-DC-AC traction drive systems in high-speed trains. This resonance issue arises when the harmonic elements introduced by the traction AC-DC converter on the grid side of trains align with the innate resonance frequency of the TPSS.* ***The novelty*** *the proposed work focuses on the challenges associated with resonance elevation and high-frequency harmonics in high-speed trains, while simultaneously enhancing energy quality. This is achieved by integrating a pulse-width-modulated converter on the grid side with a single-phase configuration and incorporating an LCL filter.* ***Methodology.*** *In order to optimize the system's efficiency, a robust control system is employed, taking advantage of the capabilities of a fuzzy logic controller (FLC). The choice of the FLC is justified by its straightforward design and reliability, emphasizing the dedication to precise control, as fuzzy logic excels in handling complex, nonlinear systems. Through the use of linguistic variables and heuristic reasoning, the FLC adjusts to dynamic changes in the system, demonstrating its efficacy in enhancing both transient and steady-state responses.* ***Practical value.*** *A grid-side LCL filter-based converter was meticulously designed and rigorously simulated using the MATLAB/Simulink platform. The inclusion of an advanced FLC in the system introduced a novel approach to control strategies, surpassing the traditional PI controller. Through a comprehensive comparative analysis, the simulation results showcased the remarkable efficacy of the proposed solution in an effectively mitigating high-frequency resonance within the TPSS. This outcome underscores the potential of FLC as a sophisticated control mechanism for enhancing the performance systems in railway applications, showcasing its superiority over conventional control methods. The study contributes in shedding light on innovative approaches for optimizing the control and efficiency of grid-side LCL filter-based converters in high-speed train systems.* References 33, table 2, figures 16.

Key words: **grid-side converter, LCL filter, harmonics, power quality, fuzzy logic controller, simulation, high-speed rail.**

Вступ. *Система тягового електропостачання залізниць (TPSS) стикається із загальною проблемою, пов'язаною з високочастотним гармонійним резонансом, особливо при використанні систем тягового приводу змінного, постійного та змінного струму у високошвидкісних поїздах. Ця проблема резонансу виникає, коли гармонійні елементи, що вносяться тяговим перетворювачем змінного струму в постійний струм на стороні мережі поїздів, збігаються із внутрішньою резонансною частотою TPSS.* ***Новизна*** *запропонованої роботи зосереджена на проблемах, пов'язаних із підвищенням резонансу та високочастотними гармоніками у високошвидкісних поїздах, при одночасному підвищенні якості енергії. Це досягається за рахунок інтеграції перетворювача з широтно-імпульсною модуляцією на стороні мережі з однофазною конфігурацією і включення фільтра LCL.* ***Методологія***. *Для оптимізації ефективності системи використовується надійна система управління, яка використовує можливості контролера нечіткої логіки (FLC). Вибір FLC виправданий його простою конструкцією та надійністю, що підкреслюють прихильність до точного управління, оскільки нечітка логіка чудово справляється зі складними нелінійними системами. Завдяки використанню лінгвістичних змінних та евристичних міркувань, FLC пристосовується до динамічних змін у системі, демонструючи свою ефективність у посиленні як перехідних, так і стійких реакцій.* ***Практична цінність***. *Перетворювач на основі LCL-фільтра на стороні мережі ретельно спроектований та ретельно змодельований за допомогою платформи MATLAB/Simulink. Включення до системи вдосконаленого FLC представило новий підхід до стратегій управління, що перевершує традиційний ПІ-регулятор. Завдяки всебічному порівняльному аналізу, результати моделювання продемонстрували чудову ефективність запропонованого рішення в ефективному пом'якшенні високочастотного резонансу TPSS. Цей результат підкреслює потенціал FLC як складного механізму управління підвищенням продуктивності систем в залізничних застосуваннях, демонструючи його перевагу над традиційними методами управління. Дослідження сприяє проливанню світла на інноваційні підходи до оптимізації управління та ефективності мережевих перетворювачів на основі LCL-фільтрів у системах високошвидкісних поїздів.* Бібл. 31, табл. 2, рис. 16.

Ключові слова: **мережевий перетворювач, LCL-фільтр, гармоніки, якість електроенергії, контролер нечіткої логіки, моделювання, високошвидкісна залізниця.**

1. Introduction High-speed rail frequently employs AC-DC-AC traction converters featuring Pulse Width Modulation (PWM) within electric units. This is done so as to enhance the energy quality and dynamic performance of railway electric systems [1], nevertheless, the presence of high-order harmonics is a common occurrence in railway electric networks, resulting in the challenge of high-frequency resonances [2, 3]. These harmonics give rise to a range of issues, including increased errors and disturbances, torque surges, thereby affecting the overall performance of the traction network [4]. Two primary strategies are commonly explored to tackle the issue of high-frequency harmonics in high-speed trains: one involves addressing the matter within the traction electrical system, meanwhile, the other aspect concentrates on the drive unit of high-speed trains.

The predominant research emphasis has been on mitigating harmonics within the traction system, with many scholars opting for the use of passive filters to alter the impedance of harmonics in this system [5]. In order to improve power quality, a grid-connected voltage source converter has incorporated an LCL-type filter, renowned for its superior high-frequency harmonic attenuation in comparison to conventional L-type filters. LCL filters find extensive use in grid-connected converters [6, 7] and front-active rectifiers [8, 9].

Comprehensive design procedures for a single-phase converter with an LCL filter were extensively discussed in [10, 11]. In addition, LCL filters often produce resonance peaks that endanger the stability of the grid-connected voltage link converter and impair the reliable operation of the traction power system.

Therefore, developing controllers suitable for LCL type single-phase converters faces huge challenges. Traditional PI linear controllers are usually used for grid-side converters of high-speed railways [12, 13]. However, the process of adjusting the PI parameters in the voltage or current control loop can be a problem, as incorrect settings

may result in undesired low-frequency oscillations in traction networks. In order to overcome this issue, various advanced nonlinear control techniques like model predictive control [14] and sliding mode control [15] were proposed in order to improve the dynamic behavior of systems. Nonetheless, implementing and adjusting parameters for these controllers in real-world scenarios can be difficult due to the presence of unknown parameters, complex structures and intricate mathematical models.

Fuzzy logic-based control has demonstrated effectiveness in various industrial applications [16, 17], owing to its heuristic nature, simplicity and efficiency for the utilization of fuzzy logic-based control has shown effectiveness in diverse industrial applications [16, 17], due to its simplicity, heuristic nature and efficiency for both linear and nonlinear systems. By utilizing linguistic variable knowledge, an intelligent fuzzy controller can be developed without the need for a complex mathematical model of the system. This not only reduces computation time but also improves the transient response characteristics of the system [18, 19]. However, designing an effective fuzzy controller in order to enhance the performance of a plant remains a challenging task, often requiring multiple trial-and-error procedures based on computer simulations.

As a solution, a proposed approach involves a simplified structure for the Fuzzy Logic Controller (FLC). Previous studies on line-side converters in high-speed railways have mainly focused on various aspects of controller design, including dynamic performance, stability analysis, and the mitigation of high-order harmonics [20-24].

Introducing a model predictive control for line-side traction rectifiers has demonstrated superior performance in suppressing high-order harmonics compared to traditional PI controllers. Another innovative method involves utilizing a nonlinear controller with active disturbance rejection control, aiming at optimizing the load characteristics of the train rectifier and reducing harmonics [25].

The application of the harmonic transfer function was employed to examine the stability of oscillating voltage fluctuation and controller performance [26]. Additionally, a combined predictive and extended state observer-based control system was proposed to mitigate voltage oscillations and reducing current distortions on both the train and network sides [27]. Some researchers have suggested a passivity-based control model for traction rectifiers so as to enhance both dynamic and static characteristics [28].

While these analytical methods have exhibited certain enhancements in controller performance, they heavily rely on precise mathematical models and a multitude of unknown parameters, often challenging to ascertain in practical applications. Despite the challenges associated with modern intelligent controller design, it is evident that existing control methods possess limitations. Specifically, they struggle to eradicate high-frequency harmonics, attain optimal system performance, and adjust control parameters. This limitation may impede the broader adoption of single-phase traction converters with LCL filters, consequently hindering advancements in railway electric systems. Notably, only a few endeavors have been made to explore the effectiveness of a fuzzy logic-based controller in electric drive applications [29, 30].

For high-speed railway line-side converters, the FLC emerges as a promising solution, eliminating the necessity for a detailed mathematical model of the system. Furthermore, it introduces a transparent physical approach to the control base in the closed loop, deviating from the use of cumbersome rings by others, implying an improvement in computational efficiency.

The goal of the paper is to devise a precise controller utilizing fuzzy logic control for a single-phase traction converter equipped with an LCL filter, with the aim of enhancing energy quality and mitigating undesired harmonic distortions within the railway traction power supply system.

2. System topology. A standard configuration for a high-speed railway traction power supply system is visually depicted in Fig. 1, offering a clear representation of the system. In this diagram the three-phase 220 kV utility undergoes a step-down transformation within an electrical substation to become two single-phase 27.5 kV feeders. This transformation is crucial for providing power to the all-parallel autotransformer-fed network through a V/x structure traction transformer.

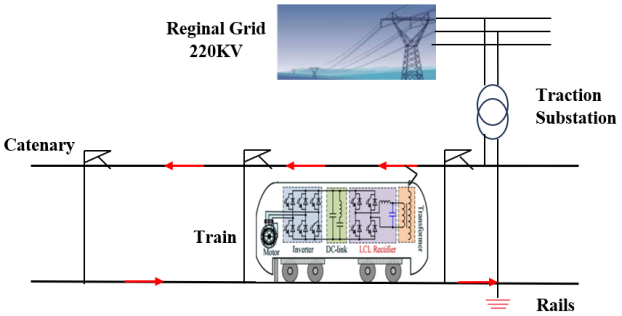

Fig. 1. Typical power-supply system for high-speed railway

Figure 2 illustrates a simplified diagram that showcases the positioning of the electrical train within the traction network system, in which: Z_{ss} is the feeder substation's equivalent impedance; i_T is the electric train's current; l_1 is the separation or gap between the electric train and the substation; l_2 is the distance between the electric train and endpoint of the feeder section.

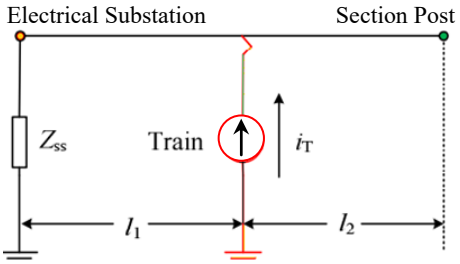

Fig. 2. The electrical train location diagram in the traction network system

This diagram incorporates various components such as communication wires, feeders, protection wires, rail and integrated grounding wires. The methodology used to create this diagram has been described in [31]. In this representation, the electrical train load is conceptually equated to a current source that contains harmonics.

Using the equivalent π-circuit model for multi-conductor transmission lines, Fig. 3 depicts the traction power network, in which: $Z_{T'1}$ and $Y_{T'1}$ are the impedance and admittance from the train to the substation; $Z_{T'2}$ and $Y_{T'2}$ are the impedance and admittance toward the supplying segment termination. The expressions for these values are:

$$\begin{cases} Z_{T'1} = \dfrac{Z_0(\cos\gamma l_1 - 1)}{\sin\gamma l_1}; \quad Y_{T'1} = \dfrac{\sin\gamma l_1}{Z_0}; \\ Z_{T'2} = \dfrac{Z_0(\cos\gamma l_2 - 1)}{\sin\gamma l_2}; \quad Y_{T'2} = \dfrac{\sin\gamma l_2}{Z_0}, \end{cases} \tag{1}$$

where γ, Z_0 are the unit-length propagation constant and characteristic impedance of the contact line, respectively. These parameters can be mathematically expressed as:

$$\begin{cases} Z_0 = \sqrt{Z'/Y'}; \\ \gamma = \sqrt{Z'Y'}, \end{cases} \tag{2}$$

where Z', Y' illustrate the impedance and admittance per unit length for the contact line, respectively.

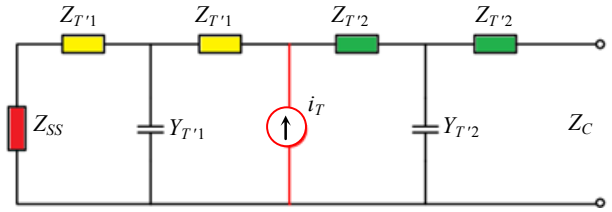

Fig. 3. Representation of equivalent traction network using topology of a π-circuit

When viewed from the train's electric system within the traction network, the parallel input impedance (Z_{pa}) formulation for the traction network can be expressed as:

$$Z_{Pa} = \frac{Z_0 \cos\gamma(l - l_1)(Z_{ss}\cos\gamma l_1 + Z_0 \sin\gamma l_1)}{Z_{ss}\sin\gamma l + Z_0 \cos\gamma l}. \tag{3}$$

The overall extent of the contact line, denoted as l (sum of l_1 and l_2), influences the parallel resonance in the traction network. The system exhibits parallel resonance when the denominator in (3) becomes 0, leading to the maximum impedance (Z_{pa}). The resonance condition is expressed as follows:

$$Z_{ss}\sin\gamma l + Z_0 \cos\gamma l = 0. \tag{4}$$

Given that γl is significantly less than 1, it is valid to approximate tanh(γl) as ≈l, leading to the simplification as:

$$j\omega L_{ss} = \frac{-1}{j\omega C_c l} = \frac{-1}{j\omega C}, \tag{5}$$

where L_{ss} is the internal equivalent inductance of the electrical supply substation (Z_{ss}=$j\omega L_{ss}$); C_c is the distributed capacitance per unit extent of the contact line; C is the overall capacitance along the contact line.

The frequency of parallel resonance f_{pr} is:

$$f_{pr} = \frac{1}{2\pi\sqrt{L_{ss}C}}. \tag{6}$$

The resonance in the traction power network is a parallel resonance involving the equivalent inductor of the electric supply substation and the distributed capacitance across the multi-conductor transmission line. The resonance frequency is determined by the inherent properties of the traction network and remains unaffected by the electric train's location [32].

3. The LCL-type converter analysis. Figure 4 illustrates the unit equivalent to the traction drive for a high-speed locomotive, featuring a single-phase LCL-type converter topology on the grid side. In each power unit, line-side converters connect to the DC-link and incorporate an LCL-type passive filter. The traction transformer is idealized; L_g is the comparable leakage inductance on the secondary side; C_d is the DC-link capacitor; V_{dc} is the voltage on DC-link; R_L is the load equivalent for the traction inverter-motor drive system.

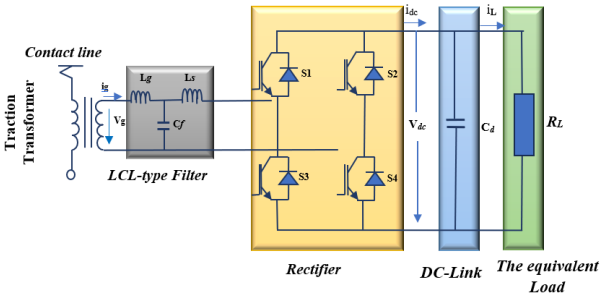

Fig. 4. Equivalent circuit of LCL-type rectifiers on the single-phase line side in every propulsion unit of a high-speed train

3.1. Designing and modeling LCL filters and their parameters. The inductance on the converter side L_s is usually determined based on the acceptable maximum converter current ripple ($\Delta i_{\max}$), typically ranging from 30-40 % of the rated current level. Therefore, the constraint condition for the inductance L_s can be expressed as:

$$L_s \geq \frac{u_{dc}}{8 f_s \Delta i_{\max}}, \tag{7}$$

where f_s is the switching frequency of the converter guides the selection of filter capacitance C_f.

Balancing high-frequency harmonics suppression and managing reactive power at the primary frequency is crucial [33]. To meet allowable reactive power, capacitance C_f can be calculated using (8), particularly at the primary frequency:

$$C_f \leq \beta \frac{P_n}{2\pi f_n U_s^2}, \tag{8}$$

where P_n is the specified power of the converter; β is the coefficient constrained to be under 5 %; f_n is the primary frequency of the grid voltage.

The design of the grid-side inductor L_g involves leveraging the proportion of high-order current on the converter side to that on the grid side. Due to unipolar PWM in a single-phase converter, emphasis is on high-order harmonics around double the switching frequency. Assuming no high-frequency components in the grid voltage, the LCL filter at double the switching frequency is addressed, as illustrated in Fig. 5.

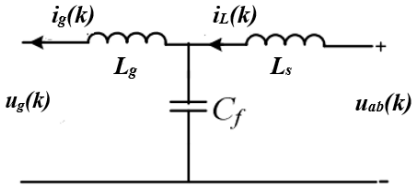

Fig. 5. Model of LCL filter

In Fig. 5 the transfer functions describing the relationship between u_{ab} and i_L, as well as i_g, can be articulated as:

$$\begin{cases} \dfrac{u_{ab}(k)}{i_L(k)} = \dfrac{j\omega_k L_s + j\omega_k L_g C_f - j\omega_k^3 L_f L_g C_f}{1 - j\omega_k^2 L_g C_f}; \\ \dfrac{u_{ab}(k)}{i_g(k)} = j\omega_k L_s - j\omega_k L_g - j\omega_k^3 L_s L_g C_f, \end{cases} \tag{9}$$

where ω_k is the twice angular frequency of switching.

Consequently, the calculation of the ratio between harmonic components on the grid-side current and high-order harmonic current on the inverter side can be determined as:

$$\sigma = \frac{i_g(k)}{i_L(k)} = \frac{1}{\left|1-\omega_k^2 L_g - C_f\right|}, \quad (10)$$

where the permissible ripple amplitude in the converter current set between 30 % to 40 % of the rated current, choosing σ at 15 % magnitude ensures a maximum fluctuation in grid-side current of around 5 %.

Consequently, the potential range for L_g can be inferred as:

$$L_g > \frac{23}{12\omega_k^2 C_f}. \quad (11)$$

In conclusion, the values of the inductor and capacitor need recalibration so as to align with the permissible design parameter range for the resonant frequency f_r. This study ensures that the resonant frequency f_r of the LCL filter is confined within the specified range:

$$5f_n < f_r < f_s. \quad (12)$$

The filter parameters specified in Table 1.

4. Control block diagram. Figures 6, 7 depict the control diagrams using a PI controller and a FLC, respectively. Table 1 presents the values for the single-phase traction converter with LCL filter parameters.

Table 1

System parameters

Parameters	Value
Contact-line voltage V_g, V	1550
Voltage across the DC-link $V_{dc\text{-}link}$, V	3000
Capacitor of the DC-link C_d, μF	3000
Frequency of switching f_s, Hz	550
Primary frequency f, Hz	50
LCL-type filter L_g, mH	1.3
Inductance on the converter side L_s, mH	1.6
Filter capacitance C_f, μF	125
Load resistor R_L, Ω	20

4.1. Control diagram with PI controller. Figure 6 shows the control scheme of the LCL rectifier based on PI controller, in which V_{dc} is the output voltage across the DC-link, where the initial block denotes V_{ref}. The regulator calculates the discrepancy between the reference and actual voltages, forming the input for the PI control unit. The output current from the PI regulator, combined with $\cos\omega t$ from the phase-locked loops (PLL) block, serves as the input for the 2nd block. The 3rd block represents the error from comparing the previous two values.

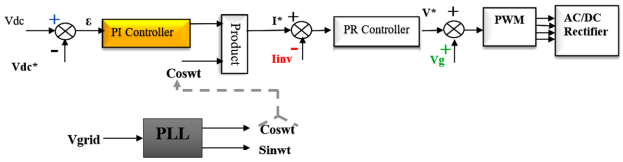

Fig. 6. Control scheme of the LCL rectifier based on PI controller

The output value (PR) from the proportional resonant controller (PR) unit becomes the voltage reference V_{ref}, added to V_{grid}. This resultant value is used in PWM generation for driver signals in the power electronic IGBT rectifier with a LCL filter, as shown in Fig. 6. The summarized mathematical equation for the system is:

$$I_{ref} = K_p(V_{dcref} - V_{dc}) + K_I \int (V_{dcref} - V_{dc})\mathrm{d}t. \quad (13)$$

4.2. Control diagram with FLC. Figure 7 shows the control scheme of the LCL rectifier based on FLC.

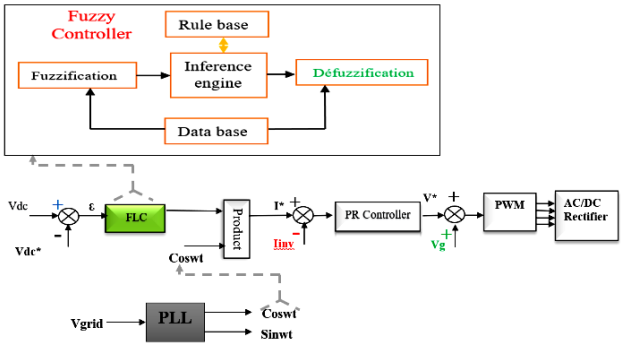

Fig. 7. Control scheme of the LCL rectifier based on FLC

A fuzzy control system leveraging fuzzy logic, evaluates input values in analog form using Boolean variables with continuous values ranging from 0 to 1. This contrasts with classical or digital logic, which operates on discrete values of either 1 or 0. The fuzzy controller consists of 3 stages: fuzzification, where inputs are converted into fuzzy representations using predefined membership functions; the rule-based inference system, which generates a fuzzy response based on linguistically defined rules; and defuzzification, converting the fuzzy response back into a crisp output. The design employs the Fuzzy Logic Toolbox in MATLAB/Simulink.

The inference engine in fuzzy logic, using Mamdani's method, connects membership functions to rules, generating fuzzy output. Defuzzification is the reverse process, transforming a fuzzy quantity into a precise value. In this application, the centroid method computed the result of the FLC, particularly the reference current in Table 2.

Table 2

Rule base of FLC

↓de/e→	NB	NS	Z	PS	PB
NB	NB	NB	NB	NS	Z
NS	NB	NB	NS	Z	PS
Z	NB	NS	Z	PS	PB
PS	NS	Z	PS	PB	PB
PB	Z	PS	PB	PB	PB

The inference engine is crucial in fuzzy logic, linking membership functions and fuzzy rules to generate the fuzzy output using Mamdani method. Defuzzification is the reverse process, transforming a fuzzy quantity into a precise value. In this application, the center of gravity method determined the output of the FLC, particularly the reference V, as shown in Fig. 8, illustrating the surface of fuzzy rules.

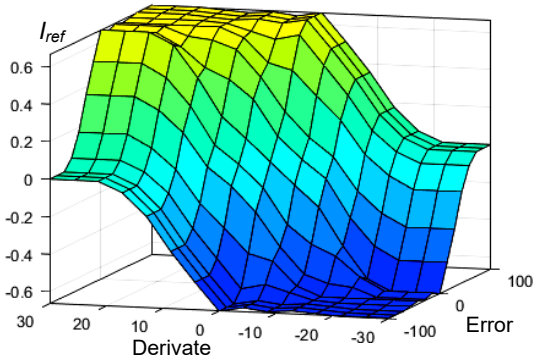

Fig. 8. Fuzzy rules surface

5. Results and comparison. Figures 9, 10 depict simulated waveforms of the DC-link voltages (V_{dc}), utilizing both the PI controller and the FLC, respectively. The observation highlights that the FLC reduces ripples and distortions in the capacitor voltage to a certain extent, while reducing the stabilization time to a value of $t = 0.1$ s compared to the PI controller, where the stabilization time is higher ($t = 0.6$ s), hindering the system's performance.

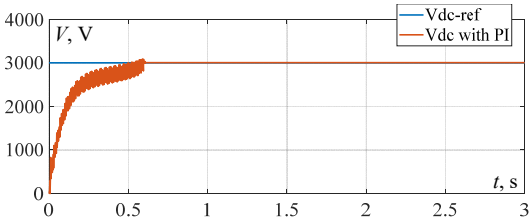

Fig. 9. The simulated waveforms of DC-link voltages based on PI controller

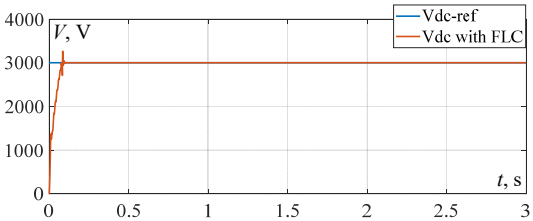

Fig. 10. The simulated waveforms of DC-link voltages based on FLC

This result indicates that the FLC brings a significant improvement in reducing fluctuations and distortions in the capacitor voltage, contributing to a faster and more stable system response. In comparison, the PI controller exhibits inferior performance with a longer stabilization time, which may compromise the overall system performance. These findings underscore the effectiveness of the FLC in enhancing dynamic response and the quality of the voltage across the DC-link in the considered converter.

Figures 11, 12 unveil the simulated voltage waveforms V_g of grid-side voltage during the functioning of a single-phase LCL rectifier using PI and FLCs, respectively. Examination of these figures reveals a significant disparity in the high-order harmonic components in the LCL rectifier with both controllers.

It is clearly evident that under the regulation by the PI controller, the voltage V_g exhibits more pronounced high-order harmonic components compared to those observed in the LCL rectifier operating with the FLC. This observation highlights the remarkable ability of the LCL converter topology with the FLC to significantly attenuate high-order harmonic resonance.

It is crucial to note that this enhanced harmonic attenuation capability offers substantial advantages in the context of power quality, thereby contributing to the stability of the traction power system. These results underscore the notable effectiveness of the FLC in reducing harmonics in comparison to the PI controller, suggesting that the adoption of the FLC could constitute a significant improvement in LCL rectifier applications, especially when it is crucial to effectively suppress high-order harmonic resonance.

Figures 13, 14 depict simulated waveforms of the grid-side current I_g of the LCL-type converter with PI and FLCs, respectively. The ability to eliminate high-frequency harmonics proves to be a crucial factor in the evaluation of filters and control systems. Following the comparison between Fig. 13, 14 it is noticed that the grid-side current is distorted, especially during the period 0–0.2 s, with higher harmonics from the PI controller compared to the FLC.

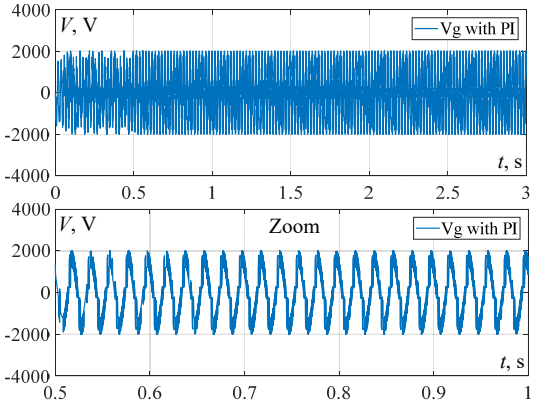

Fig. 11. The simulated waveforms of the grid-side voltage V_g using the PI controller

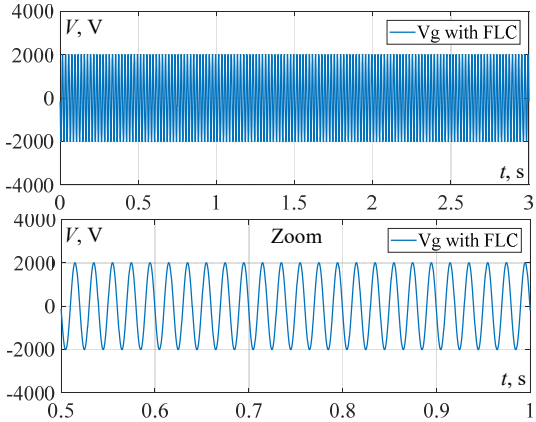

Fig. 12. The simulated waveforms of the grid-side voltage V_g using the FLC

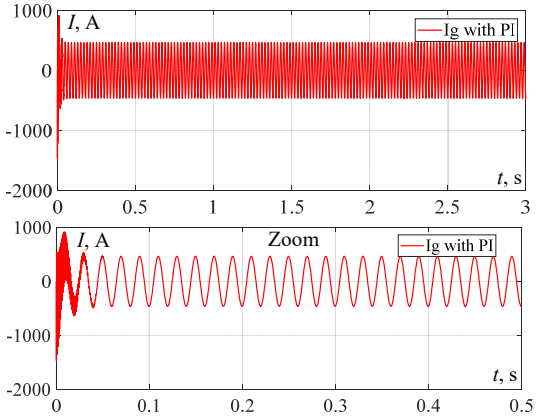

Fig. 13. The simulated waveforms of the grid-side current (I_g) using the PI controller

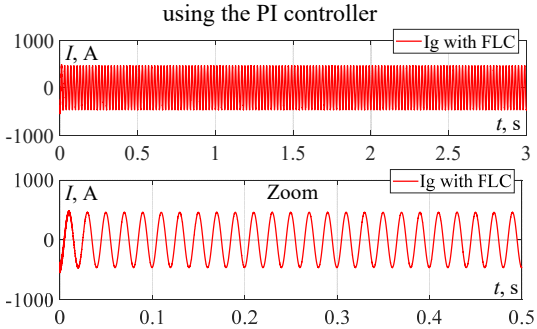

Fig. 14. The simulated waveforms of the grid-side current (I_g) using the FLC

This observation suggests that the attenuation of low-order harmonics operates effectively for the FLC, and low-order harmonics exhibit no significant impact influencing the grid-side current. This conclusion is corroborated by the results obtained from Fast Fourier Transform (FFT) analysis.

An examination of the results highlights the superior performance of the FLC in terms of harmonic reduction and waveform maintenance of the grid-side current, particularly during the critical period 0–0.2 s. These observations indicate that the choice of the FLC could represent a significant improvement in LCL-type converter applications, demonstrating increased effectiveness in suppressing harmonic distortions.

FFT algorithm is employed to assess the harmonic order within the grid-side current and THD of said current in a single-phase LCL converter utilizing PI and FLCs. THD measurements are contrasted for the PI and FLCs, as illustrated in Fig. 15, 16.

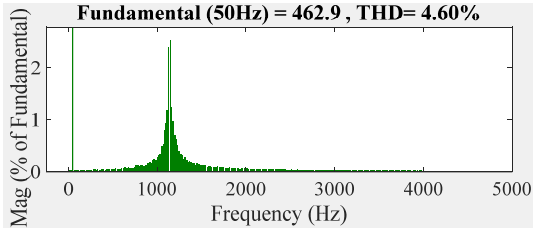

Fig. 15. The harmonic spectrum of the simulated grid-side current utilizing the PI controller

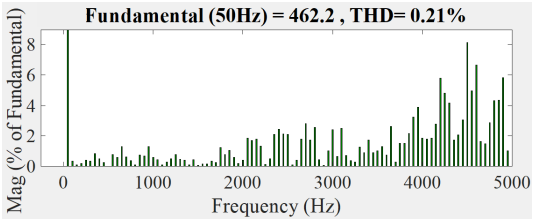

Fig. 16. The harmonic spectrum of the simulated grid-side current utilizing the FLC

Figure 15 displays the THD measurement results for the PI controller, yielding a value of 4.6 %. Conversely, Fig. 16 illustrates the corresponding results for the FLC, showing a notably reduced value of 0.21 %. These values fall well below the critical threshold of 5 %, aligning with harmonic standards.

This analysis demonstrates that the LCL filter ensures satisfactory compliance with harmonic standards, guaranteeing that the THD is below 5 %. Specifically, the results highlight the enhanced effectiveness of the FLC in harmonic suppression, particularly for high-frequency switching sub-harmonics. These findings underscore the notion that the implementation of the FLC represents a significant improvement for the LCL converter, notably ensuring a substantial reduction in THD.

Conclusions. A topological investigation and a mathematical model have been undertaken for the traction power supply system and the circuitry of single-phase line-side LCL-type rectifiers in each power unit of a high-speed train.

The control system aims at addressing high-order harmonic resonance in traction converter systems, particularly focusing on attenuating high-order harmonics in single-phase LCL PWM rectifiers. When guided by a Fuzzy Logic Controller (FLC), these rectifiers efficiently eliminate high-order harmonics in train traction drive systems. This approach, unlike conventional control units with a PI controller, effectively avoids stimulating high-frequency resonance.

The proposed method exhibits notable characteristics such as heightened robustness and autonomy from intricate system parameters. The simplicity and efficiency of the FLC distinguish it, suitable for both linear and nonlinear systems. Its intelligent control implementation does not require an intricate system model, reducing computation time and enhancing response dynamics.

The study conducts a comprehensive comparative analysis of harmonic suppression performance in the LCL converter, comparing its performance with a traditional PI controller to the proposed FLC. Analytical scrutiny and a THD study emphasize the efficacy of the FLC-controlled transformer, affirming its role in ensuring high-quality dynamic performance in traction systems.

Conflict of interest. The authors of the article declare that there is no conflict of interest.

REFERENCES

1. Liu Y., Xu J., Shuai Z., Li Y., Cui G., Hu S., Xie B. Passivity-based decoupling control strategy of single-phase LCL-type VSRs for harmonics suppression in railway power systems. *International Journal of Electrical Power & Energy Systems*, 2020, vol. 117, art. no. 105698. doi: https://doi.org/10.1016/j.ijepes.2019.105698.

2. Djazia K., Sarra M. Improving the quality of energy using an active power filter with zero direct power command control related to a photovoltaic system connected to a network. *Electrical Engineering & Electromechanics*, 2023, no. 5, pp. 20-25. doi: https://doi.org/10.20998/2074-272X.2023.5.03.

3. Aissaoui M., Benidir M., Bouzeria H., Berroum F., Ras A.C., Mammeri I. Analysis of harmonic resonance in traction power supply system. *2022 2nd International Conference on Advanced Electrical Engineering (ICAEE)*, 2022, pp. 1-5. doi: https://doi.org/10.1109/ICAEE53772.2022.9962039.

4. Lv X., Wang X., Che Y., Fu R. Eigenvalue-Based Harmonic Instability Analysis of Electrical Railway Vehicle-Network System. *IEEE Transactions on Transportation Electrification*, 2019, vol. 5, no. 3, pp. 727-744. doi: https://doi.org/10.1109/TTE.2019.2929406.

5. Balakishan P., Chidambaram I.A., Manikandan M. Improvement of power quality in grid-connected hybrid system with power monitoring and control based on internet of things approach. *Electrical Engineering & Electromechanics*, 2022, no. 4, pp. 44-50. doi: https://doi.org/10.20998/2074-272X.2022.4.06.

6. Han Y., Yang M., Li H., Yang P., Xu L., Coelho E.A.A., Guerrero J.M. Modeling and Stability Analysis of LCL-Type Grid-Connected Inverters: A Comprehensive Overview. *IEEE Access*, 2019, vol. 7, pp. 114975-115001. doi: https://doi.org/10.1109/ACCESS.2019.2935806.

7. Gurrola-Corral C., Segundo J., Esparza M., Cruz R. Optimal LCL-filter design method for grid-connected renewable energy sources. *International Journal of Electrical Power & Energy Systems*, 2020, vol. 120, art. no. 105998. doi: https://doi.org/10.1016/j.ijepes.2020.105998.

8. Jiang S., Liu Y., Liang W., Peng J., Jiang H. Active EMI Filter Design With a Modified LCL-LC Filter for Single-Phase Grid-Connected Inverter in Vehicle-to-Grid Application. *IEEE Transactions on Vehicular Technology*, 2019, vol. 68, no. 11, pp. 10639-10650. doi: https://doi.org/10.1109/TVT.2019.2944220.

9. Tang W., Ma K., Song Y. Critical Damping Ratio to Ensure Design Efficiency and Stability of LCL Filters. *IEEE Transactions on Power Electronics*, 2021, vol. 36, no. 1, pp. 315-325. doi: https://doi.org/10.1109/TPEL.2020.3000897.

10. Rasekh N., Hosseinpour M. LCL filter design and robust converter side current feedback control for grid-connected Proton Exchange Membrane Fuel Cell system. *International Journal of Hydrogen Energy*, 2020, vol. 45, no. 23, pp. 13055-13067. doi: https://doi.org/10.1016/j.ijhydene.2020.02.227.
11. Milbradt D.M.C., Hollweg G.V., de Oliveira Evald P.J.D., da Silveira W.B., Gründling H.A. A robust adaptive One Sample Ahead Preview controller for grid-injected currents of a grid-tied power converter with an LCL filter. *International Journal of Electrical Power & Energy Systems*, 2022, vol. 142, art. no. 108286. doi: https://doi.org/10.1016/j.ijepes.2022.108286.
12. Al-Barashi M., Meng X., Liu Z., Saeed M.S.R., Tasiu I.A., Wu S. Enhancing power quality of high-speed railway traction converters by fully integrated T-LCL filter. *IET Power Electronics*, 2023, vol. 16, no. 5, pp. 699-714. doi: https://doi.org/10.1049/pel2.12415.
13. Dey P., Sumpavakup C., Kirawanich P. Optimal Control of Grid Connected Electric Railways to Mitigate Low Frequency Oscillations. *2022 Research, Invention, and Innovation Congress: Innovative Electricals and Electronics (RI2C)*, 2022, pp. 70-75. doi: https://doi.org/10.1109/RI2C56397.2022.9910283.
14. Xue J.-Z., Zhao T., Bu N., Chen X.-L., Zhang B. Speed tracking control of high-speed train based on adaptive control and linear active disturbance rejection control. *Transactions of the Institute of Measurement and Control*, 2023, vol. 45, no. 10, pp. 1896-1909. doi: https://doi.org/10.1177/01423312221146600.
15. Tasiu I.A., Liu Z., Wu S., Yu W., Al-Barashi M., Ojo J.O. Review of Recent Control Strategies for the Traction Converters in High-Speed Train. *IEEE Transactions on Transportation Electrification*, 2022, vol. 8, no. 2, pp. 2311-2333. doi: https://doi.org/10.1109/TTE.2022.3140470.
16. Zhao L., Yin Z., Yu K., Tang X., Xu L., Guo Z., Nehra P. A Fuzzy Logic-Based Intelligent Multiattribute Routing Scheme for Two-Layered SDVNs. *IEEE Transactions on Network and Service Management*, 2022, vol. 19, no. 4, pp. 4189-4200. doi: https://doi.org/10.1109/TNSM.2022.3202741.
17. Woźniak M., Zielonka A., Sikora A. Driving support by type-2 fuzzy logic control model. *Expert Systems with Applications*, 2022, vol. 207, art. no. 117798. doi: https://doi.org/10.1016/j.eswa.2022.117798.
18. Kambalimath S., Deka P.C. A basic review of fuzzy logic applications in hydrology and water resources. *Applied Water Science*, 2020, vol. 10, no. 8, art. no. 191. doi: https://doi.org/10.1007/s13201-020-01276-2.
19. Paranchuk Y.S., Shabatura Y.V., Kuznyetsov O.O. Electromechanical guidance system based on a fuzzy proportional-plus-differential position controller. *Electrical Engineering & Electromechanics*, 2021, no. 3, pp. 25-31. doi: https://doi.org/10.20998/2074-272X.2021.3.04.
20. Ali Moussa M., Derrouazin A., Latroch M., Aillerie M. A hybrid renewable energy production system using a smart controller based on fuzzy logic. *Electrical Engineering & Electromechanics*, 2022, no. 3, pp. 46-50. doi: https://doi.org/10.20998/2074-272X.2022.3.07.
21. Muthubalaji S., Devadasu G., Srinivasan S., Soundiraraj N. Development and validation of enhanced fuzzy logic controller and boost converter topologies for a single phase grid system. *Electrical Engineering & Electromechanics*, 2022, no. 5, pp. 60-66. doi: https://doi.org/10.20998/2074-272X.2022.5.10.
22. Khatir A., Bouchama Z., Benaggoune S., Zerroug N. Indirect adaptive fuzzy finite time synergetic control for power systems. *Electrical Engineering & Electromechanics*, 2023, no. 1, pp. 57-62. doi: https://doi.org/10.20998/2074-272X.2023.1.08.
23. Gopal Reddy S., Ganapathy S., Manikandan M. Power quality improvement in distribution system based on dynamic voltage restorer using PI tuned fuzzy logic controller. *Electrical Engineering & Electromechanics*, 2022, no. 1, pp. 44-50. doi: https://doi.org/10.20998/2074-272X.2022.1.06.
24. Ikhe A., Pahariya Y. Voltage regulation using three phase electric spring by fuzzy logic controller. *Electrical Engineering & Electromechanics*, 2023, no. 4, pp. 14-18. doi: https://doi.org/10.20998/2074-272X.2023.4.02.
25. Goyal D.K., Birla D. A comprehensive control strategy for power quality enhancement in railway power system. *International Journal of Advanced Technology and Engineering Exploration*, 2023, vol. 10, no. 106, pp. 1123-1137. doi: https://doi.org/10.19101/IJATEE.2023.10101018.
26. Liu Y., Yang Z., Wu X., Lan L., Lin F., Su H., Huang J. Adaptive Threshold Adjustment Strategy Based on Fuzzy Logic Control for Ground Energy Storage System in Urban Rail Transit. *IEEE Transactions on Vehicular Technology*, 2021, vol. 70, no. 10, pp. 9945-9956. doi: https://doi.org/10.1109/TVT.2021.3109747.
27. Alekhya G.B.S., Shashikanth K., Prasad M.A. Risk assessment of cost overrun using fuzzy logic model. *Materials Today: Proceedings*, 2022, vol. 62, pp. 1803-1810. doi: https://doi.org/10.1016/j.matpr.2021.12.415.
28. Moaveni B., Rashidi Fathabadi F., Molavi A. Fuzzy control system design for wheel slip prevention and tracking of desired speed profile in electric trains. *Asian Journal of Control*, 2022, vol. 24, no. 1, pp. 388-400. doi: https://doi.org/10.1002/asjc.2472.
29. Pradhan R.K., Sahu C.K. Single-input Fuzzy PI Controller for Traction Line-Side Converter of High Speed Railway. *2021 12th International Conference on Computing Communication and Networking Technologies (ICCCNT)*, 2021, pp. 1-6. doi: https://doi.org/10.1109/ICCCNT51525.2021.9579548.
30. Al-Faris M., Chiverton J., Ndzi D., Ahmed A.I. Vision Based Dynamic Thermal Comfort Control Using Fuzzy Logic and Deep Learning. *Applied Sciences*, 2021, vol. 11, no. 10, art. no. 4626. doi: https://doi.org/10.3390/app11104626.
31. Liu Y., Xu J., Shuai Z., Li Y., Peng Y., Liang C., Cui G., Hu S., Zhang M., Xie B. A Novel Harmonic Suppression Traction Transformer with Integrated Filtering Inductors for Railway Systems. *Energies*, 2020, vol. 13, no. 2, art. no. 473. doi: https://doi.org/10.3390/en13020473.
32. Song W., Jiao S., Li Y.W., Wang J., Huang J. High-Frequency Harmonic Resonance Suppression in High-Speed Railway Through Single-Phase Traction Converter With LCL Filter. *IEEE Transactions on Transportation Electrification*, 2016, vol. 2, no. 3, pp. 347-356. doi: https://doi.org/10.1109/TTE.2016.2584921.
33. Gervasio F.A., Bueno E., Mastromauro R.A., Liserre M., Stasi S. Voltage control of microgrid systems based on 3lnpc inverters with LCL-filter in islanding operation. *2015 International Conference on Renewable Energy Research and Applications (ICRERA)*, 2015, pp. 827-832. doi: https://doi.org/10.1109/ICRERA.2015.7418527.

Received 22.09.2023
Accepted 03.11.2023
Published 02.03.2024

M. Aissaoui[1], *PhD Student,*
H. Bouzeria[1], *Doctor, Associate Professor,*
M. Benidir[1], *Professor,*
M.A. Labed[2], *PhD Student,*
[1] LITE Laboratory, Transportation Engineering Department, University of Constantine 1, Algeria,
e-mail: meryem.aissaoui@umc.edu.dz (Corresponding Author); bouzeria.hamza@umc.edu.dz; mohamed.benidir@umc.edu.dz
[2] LGEC Research Laboratory, Department of Electrical Engineering,
University of Constantine 1, Algeria,
e-mail: mohamedamir.labed@student.umc.edu.dz

How to cite this article:
Aissaoui M., Bouzeria H., Benidir M., Labed M.A. Harmonics suppression in high-speed railway via single-phase traction converter with an LCL filter using fuzzy logic control strategy. *Electrical Engineering & Electromechanics*, 2024, no. 2, pp. 16-22. doi: https://doi.org/10.20998/2074-272X.2024.2.03

UDC 621.3 https://doi.org/10.20998/2074-272X.2024.2.04

A. Chaib Ras, R. Bouzerara, H. Bouzeria

An adaptive controller for power quality control in high speed railway with electric locomotives with asynchronous traction motors

Introduction. *Power quality in an electric railway system pertains to the dependability, consistency, and purity of the electrical power provided to different components and systems within the railway infrastructure. Assessing power quality offers considerable opportunities to improve the efficiency of railway systems.* ***Problem.*** *Managing the flow of active and reactive power effectively, decreasing harmonic currents, and addressing the negative sequence component are all critical parts of improving power quality for electrified rail systems. As a result, flexible AC transmission systems are the major means of minimizing or decreasing these difficulties.* ***Purpose.*** *This study describes a half-bridge reactive power railway power conditioner (HB-RPC) with a novel Ynev balancing transformer. HB-RPC is made up of four switching devices and two DC capacitors and the compensator's stability is determined by the operating voltage of the DC-link. Any variations or imbalances in the DC voltage might cause the compensator to operate in an unstable manner.* ***Novelty.*** *Of a novel balanced transformer with HB-RPC in a high-speed railway system with two scenarios.* ***Methods.*** *The study utilized MATLAB/Simulink software for simulation purposes. The system integrates a fuzzy logic controller (FLC) and a PI controller to optimize DC voltage, ensuring its constancy and balance, with the objective of improving the overall stability of the system.* ***Results.*** *The simulation outcomes illustrate the efficacy of the control approach. Through a comparison of results between scenarios (two and four trains) with the PI-based-HB-RPC and the FLC-based-HB-RPC, the system exhibits enhanced stability for the proposed railway system when employing the FLC-based-HB-RPC, compared to a controller based on PI.* ***Practical value.*** *The proposed configuration elucidates its role in enhancing both the dynamic performance of the system and the power quality of the three-phase rail traction chain.* References 21, table 6, figures 21.
Key words: **railway power conditioner, Ynev transformer, fuzzy logic controller, PI controller, asynchronous motor, power quality, electric railway system.**

Вступ. *Якість електроенергії в системі електричних залізниць відноситься до надійності, сталості та чистоти електроенергії, що подається різним компонентам та системам залізничної інфраструктури. Оцінка якості електроенергії відкриває значні можливості підвищення ефективності залізничних систем.* ***Проблема***. *Ефективне керування потоками активної та реактивної потужності, зниження гармонійних струмів та усунення компонента зворотної послідовності – все це важливі частини покращення якості електроенергії для електрифікованих залізничних систем. В результаті гнучкі системи передачі змінного струму є основним засобом мінімізації чи зменшення цих труднощів.* ***Мета***. *У цьому дослідженні описується напівмостовий стабілізатор реактивної потужності залізниці (HB-RPC) з новим балансуючим трансформатором Ynev. HB-RPC складається з чотирьох перемикаючих пристроїв та двох конденсаторів постійного струму, а стабільність компенсатора визначається робочою напругою ланки постійного струму. Будь-які зміни або дисбаланс напруги постійного струму можуть призвести до нестабільної роботи компенсатора.* ***Новизна***. *Стосується нового балансного трансформатора з HB-RPC у системі високошвидкісних залізниць із двома сценаріями.* ***Методи***. *У дослідженні використовувалося програмне забезпечення MATLAB/Simulink з метою моделювання. Система поєднує контролер нечіткої логіки (FLC) та ПІ-регулятор для оптимізації напруги постійного струму, забезпечення його сталості та балансу з метою покращення загальної стабільності системи.* ***Результати***. *Результати моделювання ілюструють ефективність підходу до управління. За допомогою порівняння результатів сценаріїв (два та чотири поїзди) з HB-RPC на основі ПІ та HB-RPC на основі FLC система демонструє підвищену стабільність для запропонованої залізничної системи при використанні HB на основі FLC-RPC, у порівнянні з контролером з застосуванням ПІ.* ***Практична цінність***. *Запропонована конфігурація пояснює її роль у підвищенні як динамічних характеристик системи, так і якості електроенергії трифазного залізничного тягового кола.* Бібл. 21, табл. 6, рис. 21.
Ключові слова: **залізничний стабілізатор напруги, Ynev трансформатор, контролер нечіткої логіки, ПІ-регулятор, асинхронний двигун, якість електроенергії, електрична залізнична система.**

Introduction. The configuration and utilization of electrified railways are well-established [1]. With the surge in rail traffic and widespread adoption of modern traction vehicles equipped with sinusoidal current absorption rectifiers, electric transport systems have become substantial single-phase loads for the traction supply system. Additionally, they function as nonlinear loads, consuming reactive power and giving rise to power factor and stability issues. Consequently, electric trains contribute to imperfections in the railway supply, including negative sequence current (NSC), reactive power and harmonics [1].

Enhancing energy efficiency and ensuring high-quality performance have become imperative across various technical domains today. The prevalent power quality issues typically fall into two main categories: voltage irregularities and harmonic distortion [2]. The traction power system can be segmented into four components, namely the upstream power system (three-phase power system), the traction power substation, the overhead contact line system, and the electric train, as illustrated in Fig. 1 [1].

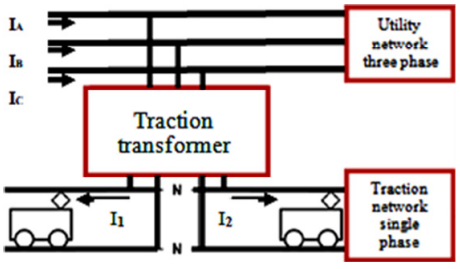

Fig. 1. Synoptic of traction chain system

The high-voltage network faces challenges due to the uncertainty, non-linearity, and asymmetry introduced by traction loads, resulting in the presence of NSC and harmonics. The asymmetry and non-linearity within the traction power supply system contribute to more significant issues for the power grid, including imbalances and harmonic disturbances. The characteristics of locomotives,

utilizing power electronics techniques to adjust speed, make them non-linear loads. In this scenario, these loads act as sources of harmonics while also operating as single-phase loads. This is the reason why the traction system can extract two single-phase electric powers from a three-phase power supply [3, 4], introducing a lot of power quality challenges to the three-phase power system, ultimately impacting the operation of electrical equipment and the network.

Various methods have been used to improve the power quality of three-phase power systems in order to maintain the dependability and balance of electrical railway power systems. This entails reducing the impacts of nonlinear traction loads on three-phase power systems [5] through the use of Flexible AC Transmission Systems (FACTS) [6]. In particular, the use of balance transformers (such as Scott, YNvd, Leblanc, and others) has been a prominent technique to addressing this difficulty [7, 8]. Balancing transformers possess the capability to transform a three-phase system into a two-phase system, thereby reducing NSC on the secondary side under equal load conditions [9].

However, it is important to note that employing balancing transformers alone is insufficient to enhance power quality in the railway traction system. Consequently, the integration of a compensator into the traction system has become essential.

Enhancing the efficiency and rapid control features of these technologies has spurred research into various FACTS devices [10-12]. The selection of specific FACTS devices depends on the intended purpose, leading to their connection in configurations such as shunt, series, series-series and series-shunt [13, 14]. The compensator's overall performance is fundamentally shaped by the configuration of the controller being manipulated.

The aim of this study is to implement a control method for the suggested half-bridge reactive power railway power conditioner (HB-RPC) with Ynev. Consequently, a fuzzy logic controller (FLC) with 49 rules based on HB-RPC is developed to govern the outputs of two power switching legs, thereby enhancing the overall performance of the power system. Subsequently, the achieved outcomes are contrasted with those obtained using a PI controller. This comparison aims to elucidate which controller exerts a more significant influence on the dynamic stability of the traction system under different loads. The paper provides a detailed description of the traction power substation, the transformer connections, and the structure of the HB-RPC.

The system operation and the control method for the compensator under Ynev are described. Trains (asynchronous motors) are used as loads to validate the performance of the system. The most important power quality issues in electrified railways have been investigated here. Results and discussion are analyzed and concluded in this study.

Modeling of proposed system. For studying the performance of our system, an electrified railway system as illustrated in Fig. 2 is proposed.

The Ynev transformer principles. The traction loads operate as single-phase loads within a three-phase system. Consequently, balanced transformers are employed in the power supply system to generate two-phase output from the three-phase system, effectively addressing power quality issues such as the elimination of zero sequence current and reduction of NSC. In [7, 8], various connection configurations are illustrated, each transformer possessing distinct advantages and disadvantages. The selection of a specific configuration is contingent on three key factors: Transformer Utilization Factor (TUF), Line Utilization Factor (LUF), and the current unbalance ratio ε.

$$TUF \equiv SR/ST\,; \tag{1}$$

$$LUF \equiv SR/SL\,; \tag{2}$$

$$\varepsilon \equiv \left|I^-\right| \Big/ \left|I^+\right|, \tag{3}$$

where SR, ST, SL are the maximum utilization capacities for the system, transformer and line, respectively; I^-, I^+ are the negative and positive sequence currents.

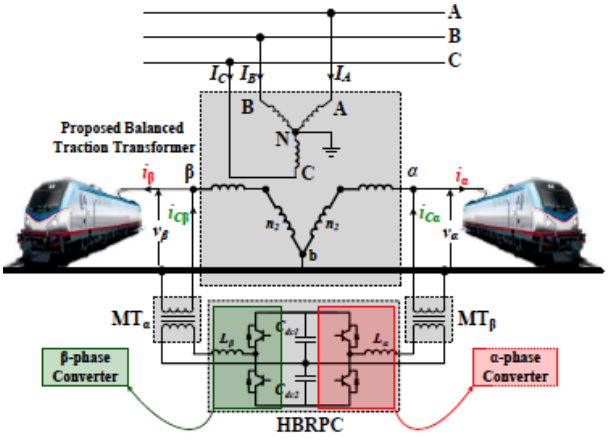

Fig. 2. The proposed electrified railway system

This study involves the transformation of a three-phase system into a single-phase system using a Ynev two-phase balanced transformer (Fig. 3), wherein the primary three-phase winding is interconnected in a star configuration with a grounded neutral point.

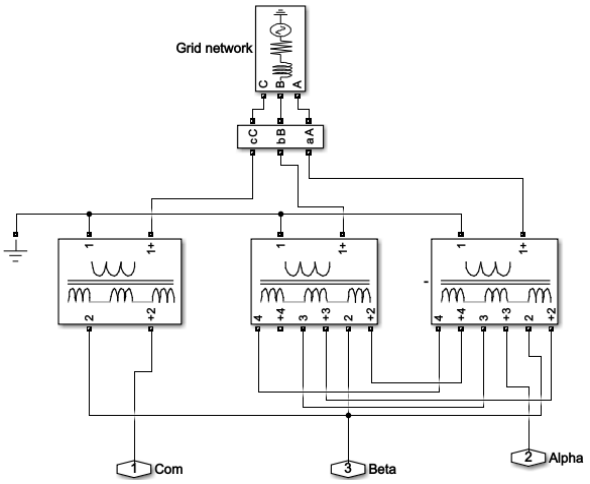

Fig. 3. Ynev transformer wiring diagram

This transformation not only enhances system protection but also involves a secondary winding connected in an open delta configuration [9-15]. The magnitudes of the mathematical voltage expressions on the secondary side are:

$$\left|v_\alpha\right| = \sqrt{3}V\left(N_2^2 + N_3^2 + N_2N_3\right)^{1/3}; \tag{4}$$

$$\left|v_\beta\right| = \sqrt{3}V\left(N_2^2 + N_3^2 + N_2N_3\right)^{1/3}, \tag{5}$$

where N_2, N_3 are the turn ratios associated with the windings of the transformer.

The current relationships can be expressed as:

$$\begin{bmatrix} I_A \\ I_B \\ I_C \end{bmatrix} \equiv \begin{bmatrix} (N_2+N_3) & -N_3 \\ -N_3 & (N_2+N_3) \\ -N_2 & -N_2 \end{bmatrix} \begin{bmatrix} I_\alpha \\ I_\beta \end{bmatrix}, \quad (6)$$

where I_A, I_B, I_C are the primary side's phase currents; I_α, I_β are the secondary side's two-phase currents.

The components of three-phase currents zero sequence I^0, positive sequence I^+, and negative sequence I^- currents are:

$$\begin{bmatrix} I^0 \\ I^+ \\ I^- \end{bmatrix} \equiv \frac{1}{3} \begin{bmatrix} 0 & 0 \\ N_2(1-\alpha^2)+N_3(1-\alpha) & N_2(\alpha-\alpha^2)+N_3(\alpha-1) \\ N_2(1-\alpha)+N_3(1-\alpha^2) & N_2(\alpha^2-\alpha)+N_3(\alpha^2-1) \end{bmatrix}. \quad (7)$$

Load model. In this paper, we model an electric locomotive train, illustrated in Fig. 4, each asynchronous motor driven by two inverters controlled through pulse width modulation. The system incorporates static power converters to transform the physical characteristics, specifically voltage, prior to reaching the traction motor.

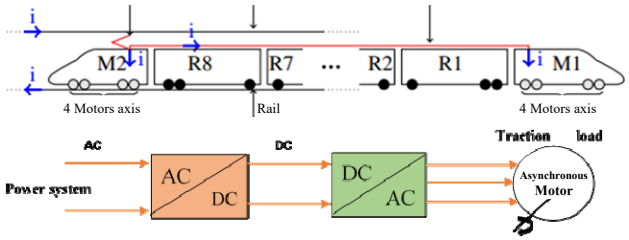

Fig. 4. High speed train's traction circuit schematic diagram

HB-RPC configuration. HB-RPC is one of the FACTS devices that have been specifically designed for railway traction power supply [11]. As illustrated in Fig. 5, HB-RPC is made up of four switching devices and two DC capacitors, which reduces the number of switches compared to a normal railway power conditioner (RPC). As a result, this structure is employed to lower the cost and complexity of the control. It is utilized to manage active and reactive power flow, as well as harmonics suppression.

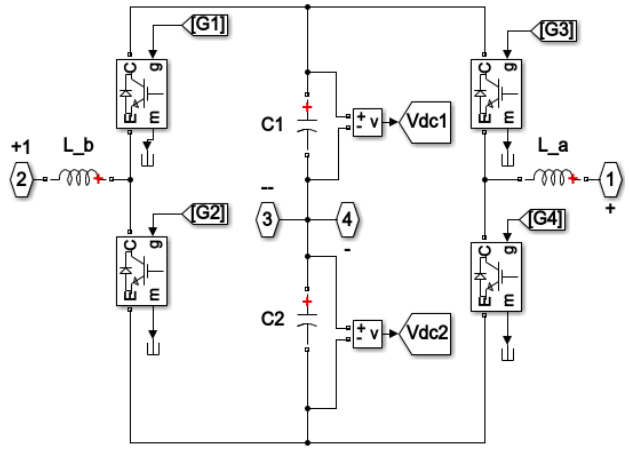

Fig. 5. HB-RPC topology proposed in MATLAB

The Ynev transformer's secondary side is linked to the half-bridge converters through a pair of step-down transformers and inductors. This setup is designed to mitigate the transmission of harmonics and reactive power through the transformer. In this arrangement, each side of the traction power substation accommodates two electric trains (in the 1st case) and four trains (in the 2nd case), with i_α and i_β representing the currents of sections α and β, and denoting the compensating currents.

To address symmetrical and sinusoidal waveforms in the secondary side currents (i_α, i_β), the HB-RPC introduces compensatory currents ($i_{C\alpha}$, $i_{C\beta}$) into the system through interface inductances (L_α, L_β) and step-down transformers.

The load currents can be written as [9-16]:

$$\begin{cases} I_{L\alpha}(t) \equiv \sqrt{2} L_{LP\alpha} \cos(\omega t + \theta_1) + \sum_{h=2} \sqrt{2} I_{h\alpha} \cos(\omega t + \theta_{h\alpha}); \\ I_{L\beta}(t) \equiv -\sqrt{2} I_{LP\beta} \cos(\omega t + \theta_2) + \sum_{h=2} \sqrt{2} I_{h\beta} \cos(\omega t + \theta_{h\beta}), \end{cases} \quad (8)$$

where $I_{h\alpha}$, $I_{h\beta}$ are the h^{th} order harmonic currents of the α and β phases, respectively; $\theta_{h\alpha}$, $\theta_{h\beta}$ are the phases degree of h^{th} order harmonic currents of the α and β phases; θ_1, θ_2 are the phase difference between α and β phases; $I_{LP\alpha}$, $I_{LP\beta}$ are the active components.

The compensation currents ($I_{C\alpha}$, $I_{C\beta}$) for the two half-bridge converters can be expressed as:

$$\begin{cases} I_{C\alpha} = I_\alpha(t) - I_{ref\alpha}(t); \\ I_{C\beta} = I_\beta(t) - I_{ref\beta}(t), \end{cases} \quad (9)$$

where I_α, I_β are the secondary side currents; $I_{ref\alpha}$, $I_{ref\beta}$ are the reference currents.

The connection between the compensation currents and the reference currents can be established as:

$$\begin{cases} I_{ref\alpha}(t) = \sqrt{\frac{2}{3}} I_{mp} \cos \omega t; \\ I_{ref\beta}(t) = \sqrt{\frac{2}{3}} I_{mp} \left(\cos \omega t - \frac{2\pi}{3} \right), \end{cases} \quad (10)$$

where I_{mp} is the DC component:

$$I_{mp} = \frac{1}{2} I_{LP\alpha} + I_{LP\beta}, \quad (11)$$

where $I_{LP\alpha}$, $I_{LP\beta}$ are the active components of two loads currents of traction power arms.

Operation and control method of the system.

A. Operation of the HB-RPC involves the dynamic exchange of power between sides, achieving the transfer and equilibrium of active power, and compensating reactive power to meet the load requirements. This is accomplished by charging or discharging capacitors $C1$, $C2$ as illustrated in Fig. 6, 7, representing the primary goal of the HB-RPC [16-18]. The operations modes of HB-RPC are next:

- when the supply current $i > 0$: the charging mode of the DC-link capacitor, diode $D1$ is conducted and the discharging mode of the DC-link capacitor, power switch $S2$ is conducted (Fig. 6);
- when the supply current $i < 0$: $S1$ is conducted, the capacitor $C1$ is discharging, and $|i|$ starts to increase, when $D2$ is conducted, the capacitor $C2$ is charging, and $|i|$ starts to decrease (Fig. 7).

B. DC-link voltage control. The utilization of two capacitors gives rise to a voltage balance issue. To address this and attain dynamic energy equilibrium, two FLC and PI controllers are suggested. These controllers generate the reference current signals for phases A, B, C along with a compensator to maintain the DC-link voltage stability and minimize power losses.

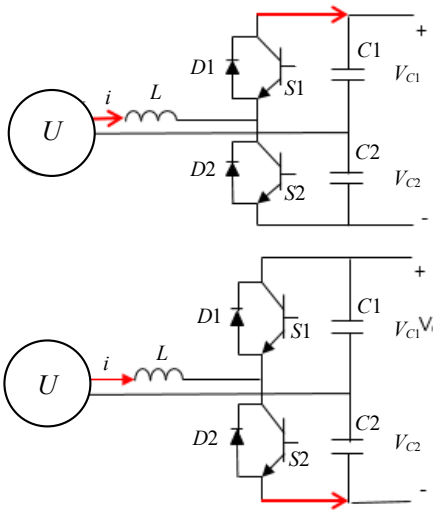

Fig. 6. Charging (above) and discharging (below) mode of HB-RPC for the supply current $i > 0$

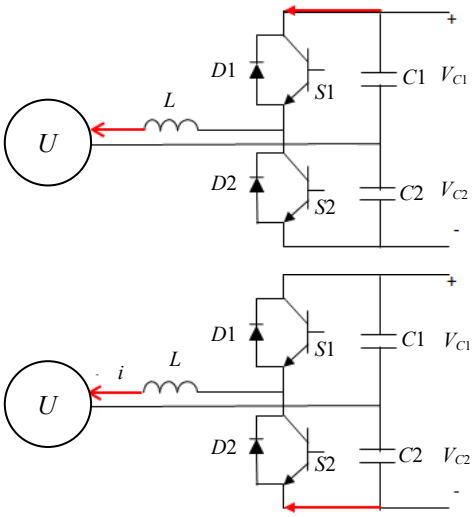

Fig. 7. Charging (above) and discharging (below) mode of HB-RPC for the supply current $i < 0$

Approach utilizing a FLC. It is a mathematical framework designed to assess analog input values in the context of logical variables with continuous values ranging from 0 to 1 [14-19]. FLCs are particularly well-suited for addressing uncertain control problems. The FLC is structured into 3 components: fuzzification, fuzzy inference, and defuzzification (Fig. 8) [20, 21].

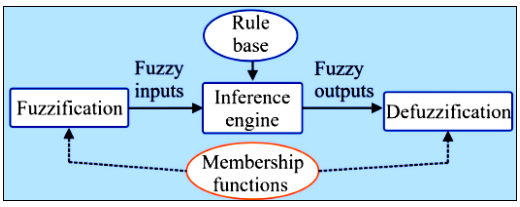

Fig. 8. Architecture of FLC

Fuzzification is the process of transforming crisp inputs values into language values represented by membership functions. FLC's inputs are designated as the error (e) in DC-link voltage and derivate error (de) at simple times t [15]:

$$\begin{cases} e(t) = V_{dc_{ref}}(t) - V_{dc}(t); \\ \mathrm{d}e(t) = e(t) - e(t-1). \end{cases} \quad (12)$$

Common types of input membership functions include triangular, trapezoidal, or exponential shapes.

In our study, we used triangle membership (Fig. 9). Seven linguistic variables for both inputs and output were selected as results there are 49 rules for FLC.

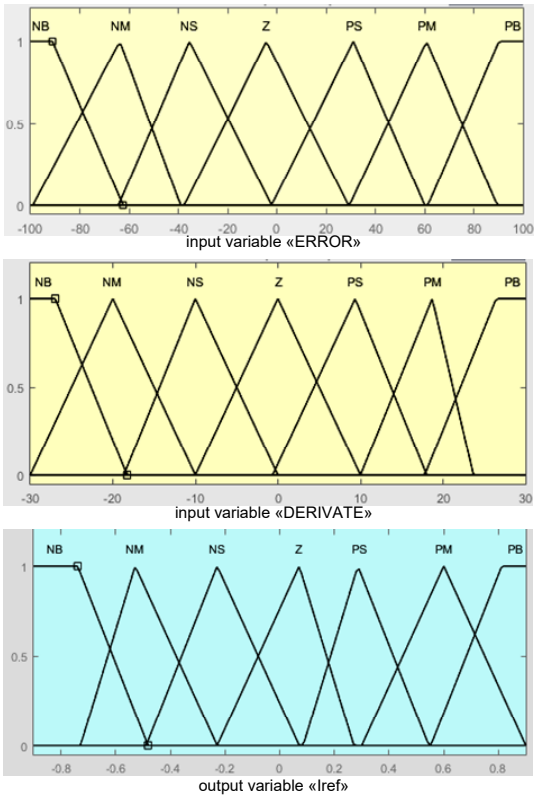

Fig. 9. Membership functions of fuzzy system

The inference engine plays a crucial role in fuzzy logic operations by linking membership functions with fuzzy rules to produce a fuzzy output. Memdani method is employed to execute this process. On the other hand, defuzzification is the opposite of fuzzification, involving the conversion of fuzzy quantities into precise values. In our case, the center of gravity is employed to calculate the output of the FLC, specifically the reference current as outlined in Table 1.

Table 1

Rule base of FLC

de/e	NB	NM	NS	Z	PS	NM	PB
NB	NB	NB	NB	NM	NM	NS	Z
NM	NB	NB	NM	NM	NS	Z	PS
NS	NB	NM	NM	NS	Z	PS	PM
Z	NM	NM	NS	Z	PS	PM	PM
PS	NM	NS	Z	PS	PM	PM	PB
PM	NS	Z	PS	PM	PM	PB	PB
PB	Z	PS	PM	PM	PB	PB	PB

Figure 9 illustrates the membership functions of the input and output variables in the fuzzy system, while Fig. 10 displays the surface of fuzzy rules.

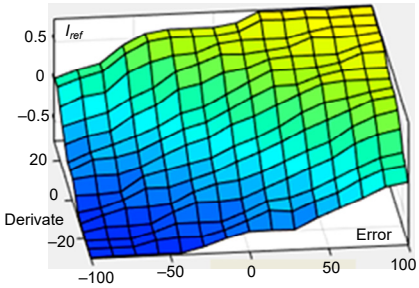

Fig. 10. Fuzzy rules surface

The configuration block of the compensator control system for HB-PRC is shown in Fig. 11.

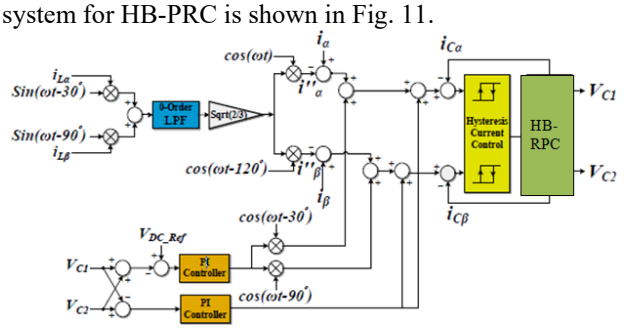

Fig. 11. HB-RPC control system with FLC

PI controller approach. The PI controller's efficiency in limiting steady-state error, as well as its ease of implementation, are the grounds for its extensive application. Figure 12 shows the PI controller principle and the configuration block of the compensator control system for HB-PRC.

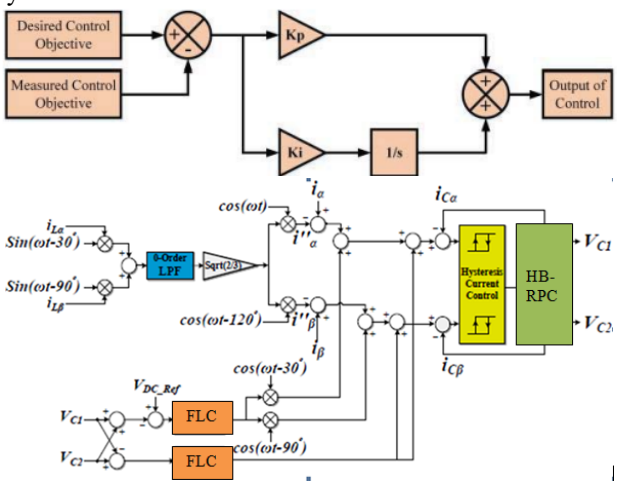

Fig. 12. HB-RPC control system with PI

Results and discussion. The aforementioned test system was created in MATLAB/Simulink. This section is further divided into two scenarios:

- case (1) has HB-RPC in high-speed railway system with 2 trains;
- case (2) has the HB-RPC with 4 trains.

A comparison of the DC-link voltages and simulation results for scenario (1) and (2) is performed, taking into account both scenarios with and without a compensator and controller. The simulations were utilized to verify the effectiveness of the proposed compensator and control method, as well as to evaluate the new transformer's ability to alleviate NSC.

A standard electrical traction system was selected to facilitate an authentic comparative case study between FLC and PI controllers with two scenarios with varying load conditions are examined to analyze the influence of the proposed topology. The assumed values for the public electrical grid voltage are 230 kV, and its secondary side provides a 27.5 kV supply to the traction loads. In the analysis of our electric railway system, electric locomotives are modeled as asynchronous motors, which representing nonlinear loads and providing a suitable basis for result evaluation.

The compensator is linked in parallel with the three-phase power system. The specific parameters of the chosen traction system are outlined in Table 2.

Table 2
Simulation parameters

Transformer (class TPS) ratio	230 kV / 27.5 kV
Ynev transformer ratio	27.5 / 1
Interface inductance, mH	4
DC-link capacitors, mF	40
Nominal power, MW	10
Voltage of DC capacitor Vdc_{ref}, V	2000

The controller is used to correct the error between the reference value of the DC-link voltage Vdc_{ref} and the instantaneous actual value V_{dc}. The HB-RPC's controller should issue instructions for the compensation currents to be injected, followed by the acquisition of sinusoidal and symmetrical currents on the three-phase electrical grid side without the NSC and to transfer active and reactive energy from one segment to another.

The DC-link voltage is displayed in Fig. 13, at t = 0.5 s, the HB-RPC is activated the V_{dc} voltage following to the reference signal Vdc_{ref}. It is clearly observed that the DC-link voltage stable and regulated (reducing the voltage fluctuation) better with the FLC compared to the PI. Fuzzy control demonstrates robustness by efficiently managing variables with distinct fuzzy logic and facilitating the enhancement of fuzzy rules. The utilization of fuzzy control for refining compensation contributes to improved performance in achieving better compensation outcomes.

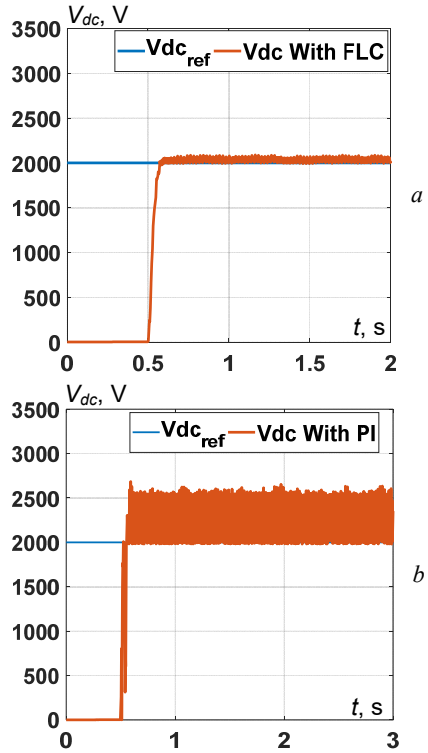

Fig. 13. DC-link voltage with FLC (*a*) and with PI (*b*)

Case I with two trains. The currents of the primary side and the secondary side are shown in Fig. 14; I_A, I_B and I_C are unbalanced and unequal, when the compensator turned off, which contain NSC but after the HB-RPC is turned on at 0.5 s, the currents are more stable (balanced, equal, phase difference 120°). It is clear appeared that the time response of the compensator with the FLC is less than the PI.

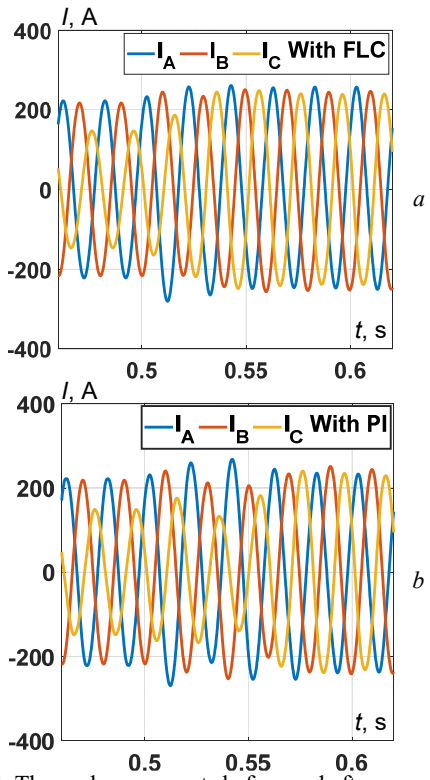

Fig. 14. Three-phase currents before and after compensation with FLC (*a*) and with PI (*b*) for Case I

In Fig. 15, as we can see the secondary current of the transformer I_α, I_β are balanced even before turned on the HB-RPC, which confirms the transformer's ability to reduce the imbalance.

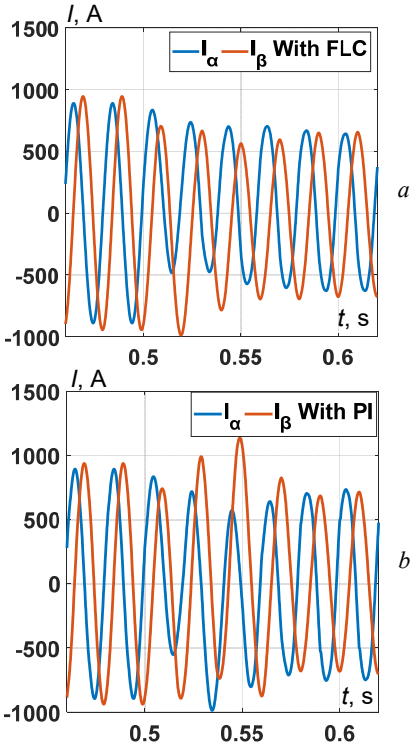

Fig. 15. The secondary side current of the traction transformer with FLC (*a*) and with PI (*b*) for Case I

Figure 16 presents the compensation current $I_{C\alpha}$, $I_{C\beta}$. After 0.5 s the present current is sinusoidal which shows that it includes most effective active current without harmonics, which can induced balanced three-phase currents on the power grid.

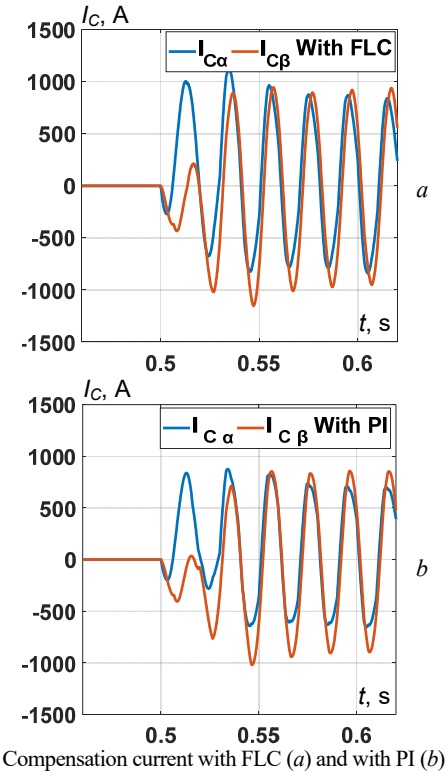

Fig. 16. Compensation current with FLC (*a*) and with PI (*b*) for Case I

According to Fig. 17, which shows the NSC which is reduced to almost zero and explain the symmetrical three-phase current. We called the relationship between the NSC and PSC the current unbalance ration. Table 3 represents the ratio index before and after the HB-RPC start working.

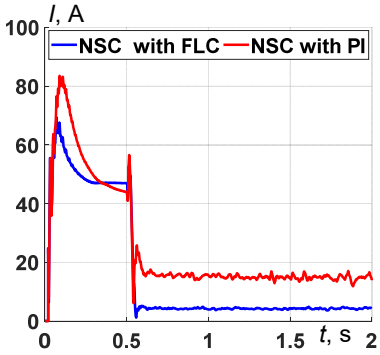

Fig. 17. Negative sequence currents with FLC and PI for Case I

Table 3

NSC ratio in the public electrical grid current with PI and FLC

HB-RPC integrate	Before	After
Time, s	0 – 0.4	0.5 – 2
PI, %	25	2.08
FLC, %		1.17

Table 4 shows the FFT analysis results before and after the compensation of the currents at the phases *A*, *B* and *C*; it is observed that the performance of the HB-PRC and Ynev transformer with the FLC is superior to the PI controller for harmonic elimination.

Table 4

THD compensation results

Cases 2 trains	I_A	I_B	I_C
Without compensation, %	7.88	8.94	13.68
Compensation / FLC, %	1.18	0.92	1.51
Compensation / PI, %	3.16	1.69	2.74

Case II with four trains. The loading situation, which was created by delivering a step load to the system, was simulated in order to stress the system with a high-power variation for a stability test.

Figures 18, 19 illustrate the simulation outcomes corresponding to case II. In this scenario, the absence of a compensator (no HB-RPC) interval is associated with elevated levels of nonlinear signal components and harmonics, necessitating compensation.

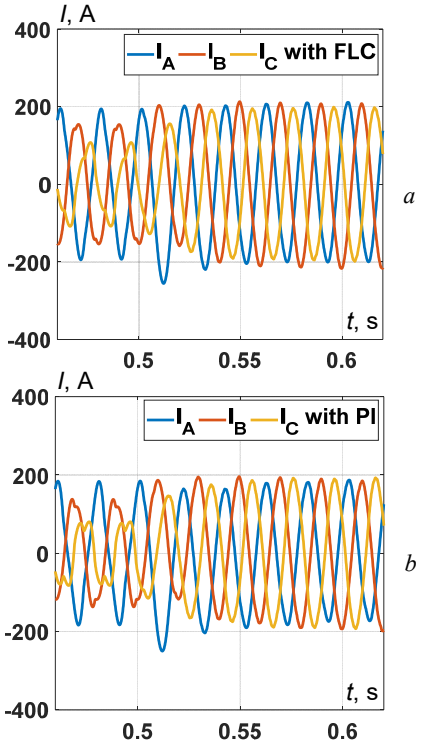

Fig. 18. Three-phase currents before and after compensation with FLC (*a*) and with PI (*b*) for Case II

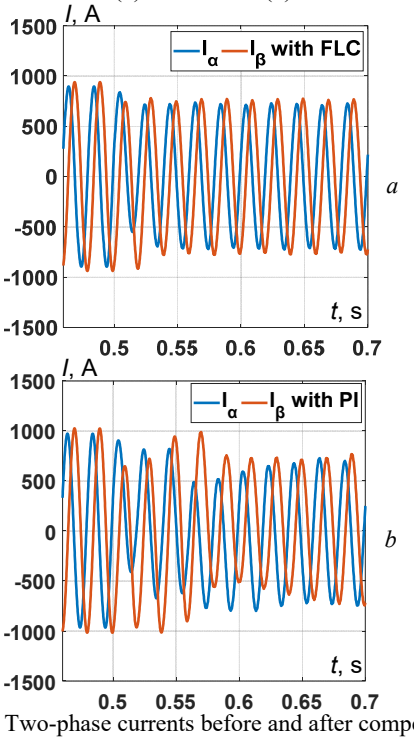

Fig. 19. Two-phase currents before and after compensation with FLC (*a*) and with PI (*b*) for Case II

Figures 18, 19 illustrate the three-phase and two-phase current waveform under HB-RPC-based FLC and PI control in response to variations in traction load. The three-phase side currents maintain stability amid changes in traction load.

Figure 20 shows the compensatory currents of the converter in FLC/HB-RPC and PI/HB-RPC, respectively. Following $t = 0.5$ s, the HB-RPC is activated. As depicted in Fig. 20, all power quality indices show enhancement and comply with the specifications outlined in the IEEE 1159 Standard. Therefore, drawing from the findings of the two cases, the suggested system has effectively mitigated grid-side nonlinear signal component, and current THDs.

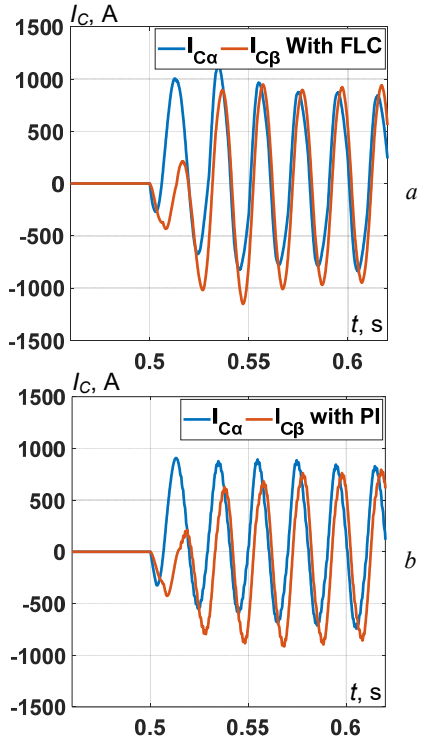

Fig. 20. Compensation current with FLC (*a*) and with PI (*b*) for Case II

NSC values for the FLC/HB-RPC are significantly lower compared to those of the PI/HB-RPC as illustrated in Fig. 21 and Table 5.

Table 6 displays the results of FFT analysis conducted both before and after current compensation for phases *A*, *B*, *C*. The data indicates that the HB-PRC and Ynev transformer, in conjunction with the FLC, outperform the PI controller in terms of harmonic elimination.

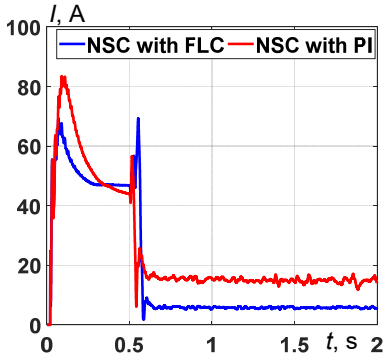

Fig. 21. Negative sequence currents with FLC and PI for Case II

Table 5

NSC ratio in the public electrical grid current with PI and FLC

HB-RPC integrate	Before	After
Time, s	0 – 0.4	0.5 – 2
PI, %	47.4	2.1
FLC, %		1.2

Table 6
THD compensation results

Cases 4 trains	I_A	I_B	I_C
Without compensation, %	25.37	16.05	39.55
Compensation / FLC, %	2.21	1.12	2.81
Compensation / PI, %	5.42	1.88	3.89

Conclusions. Addressing power quality issues in the traction power supply system of a high-speed railway equipped with Ynev wiring transformer. Ynev transformer is characterized by the capability to provide symmetrical two-phase current for traction loads and balanced three-phase current in railway system.

This study introduces a novel power quality control approach centered around half-bridge reactive power railway power conditioner (HB-RPC). The paper initially examines the mathematical model and control strategy of HB-RPC to improve the power quality in high-speed railway system. The use of adaptive fuzzy logic control is demonstrated to offer enhanced stability compared to PI control.

Through an analysis of two traction load scenarios, it is determined that HB-RPC, under adaptive fuzzy logic control, exhibits superior stability. Beyond improved stability, the response times are faster when compared to PI control, both during HB-RPC activation and changes in traction load. The use of fuzzy logic control ensures a combination of swift response and stability, thereby guaranteeing the reliable and efficient operation of HB-RPC. Both scenarios demonstrate that proposed system has superior stability and dynamic performance.

Conflict of interest. The authors declare that they have no conflicts of interest.

REFERENCES

1. Bharule S., Kidokoro T., Seta F. Evolution of High-Speed Rail and its Development Effects: Stylized Facts and Review of Relationships. *ADBI Working Paper Series*, 2019, no. 1040, 28 p. doi: https://doi.org/10.2139/ssrn.3554834.

2. Brenna M., Kaleybar H.J., Foiadelli F., Zaninelli D. Modern Power Quality Improvement Devices Applied to Electric Railway Systems. *2022 20th International Conference on Harmonics & Quality of Power (ICHQP)*, 2022, pp. 1-6. doi: https://doi.org/10.1109/ICHQP53011.2022.9808635.

3. Zare M., Varjani A.Y., Mohammad Dehghan S., Kavehei S. Power Quality Compensation and Power Flow Control in AC Railway Traction Power Systems. *2019 10th International Power Electronics, Drive Systems and Technologies Conference (PEDSTC)*, 2019, pp. 426-432. doi: https://doi.org/10.1109/PEDSTC.2019.8697653.

4. Wu S., Wu M., Wang Y. A Novel Co-Phase Power-Supply System Based on Modular Multilevel Converter for High-Speed Railway AT Traction Power-Supply System. *Energies*, 2021, vol. 14, no. 1, art. no. 253. doi: https://doi.org/10.3390/en14010253.

5. Barros L., Tanta M., Martins A., Afonso J., Pinto J. Evaluation of Static Synchronous Compensator and Rail Power Conditioner in Electrified Railway Systems Using V/V and Scott Power Transformers. *EAI Endorsed Transactions on Energy Web*, 2021, vol. 8, no. 34, art. no. 169164. doi: https://doi.org/10.4108/eai.29-3-2021.169164.

6. Tanta M., Pinto J.G., Monteiro V., Martins A.P., Carvalho A.S., Afonso J.L. Topologies and Operation Modes of Rail Power Conditioners in AC Traction Grids: Review and Comprehensive Comparison. *Energies*, 2020, vol. 13, no. 9, art. no. 2151. doi: https://doi.org/10.3390/en13092151.

7. Kryukov A., Cherepanov A., Avdienko I. Simulation of traction electricity supply systems equipped with unbalance-to-balance transformers. *AIP Conference Proceedings*, 2023, vol. 2700, no. 1, art. no. 040009. doi: https://doi.org/10.1063/5.0124856.

8. Boonlert T., Hongesombut K. Comparison of Voltage Distortion Impacts from High-Speed Railway Systems Connected to Electrical Grid Under Different Special Transformers. *2018 International Electrical Engineering Congress (IEECON)*, 2018, pp. 1-4. doi: https://doi.org/10.1109/IEECON.2018.8712124.

9. Roudsari H.M., Jalilian A., Jamali S. Half-Bridge Power Quality Conditioner for Railway Traction Distribution System Based on a New Balancing Transformer. *2018 Electrical Power Distribution Conference (EPDC)*, 2018, pp. 1-7. doi: https://doi.org/10.1109/EPDC.2018.8536270.

10. Reddy C.V.K., Das G.T.R., Krishna Veni K. Analysis of AC Transmission System Using Fuzzy Logic Controller for Damping of Low Frequency Oscillations with Interline Power Flow Controller. *International Journal of Applied Engineering Research*, 2019, vol. 14, no 9, pp. 2148-2155.

11. Lao K.W., Wong M.C., Santoso S. Recent Advances of FACTS Devices for Power Quality Compensation in Railway Traction Power Supply. *2018 IEEE/PES Transmission and Distribution Conference and Exposition (T&D)*, 2018, pp. 1-5. doi: https://doi.org/10.1109/TDC.2018.8440270.

12. Afonso J.L., Tanta M., Pinto J.G.O., Monteiro L.F.C., Machado L., Sousa T.J.C., Monteiro V. A Review on Power Electronics Technologies for Power Quality Improvement. *Energies*, 2021, vol. 14, no. 24, art. no. 8585. doi: https://doi.org/10.3390/en14248585.

13. Mohamed S.A. Enhancement of power quality for load compensation using three different FACTS devices based on optimized technique. *International Transactions on Electrical Energy Systems*, 2020, vol. 30, no. 3. art. no. e12196. doi: https://doi.org/10.1002/2050-7038.12196.

14. Tasiu I.A., Liu Z., Wu S., Yu W., Al-Barashi M., Ojo J.O. Review of Recent Control Strategies for the Traction Converters in High-Speed Train. *IEEE Transactions on Transportation Electrification*, 2022, vol. 8, no. 2, pp. 2311-2333. doi: https://doi.org/10.1109/TTE.2022.3140470.

15. Sujatha M.S., Sreelakshmi S., Parimalasundar E., Suresh K. Mitigation of harmonics for five level multilevel inverter with fuzzy logic controller. *Electrical Engineering & Electromechanics*, 2023, no. 4, pp. 52-56. doi: https://doi.org/10.20998/2074-272X.2023.4.08.

16. Chaib Ras A., Bouzerara R., Bouzeria H., Aissaoui M., Mammeri I. An Efficient Strategy for Power Quality Conditioner with Half-Bridge for High-Speed Railway. *Lecture Notes in Networks and Systems*, 2021, vol. 174, pp. 894-901. doi: https://doi.org/10.1007/978-3-030-63846-7_87.

17. Cui G., Luo L., Liang C., Hu S., Li Y., Cao Y., Xie B., Xu J., Zhang Z., Liu Y., Wang T. Supercapacitor Integrated Railway Static Power Conditioner for Regenerative Braking Energy Recycling and Power Quality Improvement of High-Speed Railway System. *IEEE Transactions on Transportation Electrification*, 2019, vol. 5, no. 3, pp. 702-714. doi: https://doi.org/10.1109/TTE.2019.2936686.

18. Zhao S., Huang X., Fang Y., Zhang H. DC-Link-Fluctuation-Resistant Predictive Torque Control for Railway Traction Permanent Magnet Synchronous Motor in the Six-Step Operation. *IEEE Transactions on Power Electronics*, 2020, vol. 35, no. 10, pp. 10982-10993. doi: https://doi.org/10.1109/TPEL.2020.2975497.

19. Dai X. Negative Sequence Compensation Method for High-Speed Railway With Integrated Photovoltaic Generation System. *CPSS Transactions on Power Electronics and Applications*, 2022, vol. 7, no. 2, pp. 130-138. doi: https://doi.org/10.24295/CPSSTPEA.2022.00012.

20. Ikhe A., Pahariya Y. Voltage regulation using three phase electric spring by fuzzy logic controller. *Electrical Engineering & Electromechanics*, 2023, no. 4, pp. 14-18. doi: https://doi.org/10.20998/2074-272X.2023.4.02.

21. Gopal Reddy S., Ganapathy S., Manikandan M. Power quality improvement in distribution system based on dynamic voltage restorer using PI tuned fuzzy logic controller. *Electrical Engineering & Electromechanics*, 2022, no. 1, pp. 44-50. doi: https://doi.org/10.20998/2074-272X.2022.1.06.

Received 11.08.2023
Accepted 13.11.2023
Published 02.03.2024

A. Chaib Ras[1], *PhD,*
R. Bouzerara[1], *Professor,*
H. Bouzeria[1], *Doctor, Associate Professor,*
[1] Transportation Engineering Department,
University of Constantine 1,
Route d'Ain ElBey, 25000, Constantine, Algeria,
e-mail: amira.chaibras@student.umc.edu.dz (Corresponding Author);
bouzerara.ramdane@umc.edu.dz; bouzeria.hamza@umc.edu.dz

How to cite this article:
Chaib Ras A., Bouzerara R., Bouzeria H. An adaptive controller for power quality control in high speed railway with electric locomotives with asynchronous traction motors. *Electrical Engineering & Electromechanics*, 2024, no. 2, pp. 23-30. doi: https://doi.org/10.20998/2074-272X.2024.2.04

UDC 621.3.013 https://doi.org/10.20998/2074-272X.2024.2.05

B.I. Kuznetsov, A.S. Kutsenko, T.B. Nikitina, I.V. Bovdui, V.V. Kolomiets, B.B. Kobylianskyi

Method for design of two-level system of active shielding of power frequency magnetic field based on a quasi-static model

Aim. *Development of method for design a two-level active shielding system for an industrial frequency magnetic field based on a quasi-static model of a magnetic field generated by power line wires and compensating windings of an active shielding system, including coarse open and precise closed control.* ***Methodology.*** *At the first level rough control of the magnetic field in open-loop form is carried out based on a quasi-static model of a magnetic field generated by power line wires and compensating windings of an active shielding system. This design calculated based on the finite element calculations system COMSOL Multiphysics. At the second level, a stabilizing accurate control of the magnetic field is implemented in the form of a dynamic closed system containing, in addition plant, also power amplifiers and measuring devices of the system. This design calculated based on the calculations system MATLAB.* ***Results.*** *The results of theoretical and experimental studies of optimal two-level active shielding system of magnetic field in residential building from power transmission line with a «Barrel» type arrangement of wires by means of active canceling with single compensating winding are presented.* ***Originality.*** *For the first time, the method for design a two-level active shielding system for an power frequency magnetic field based on a quasi-static model of a magnetic field generated by power line wires and compensating windings of an active shielding system, including coarse open and precise closed control is developed.* ***Practical value.*** *It is shown the possibility to reduce the level of magnetic field induction in residential building from power transmission line with a «Barrel» type arrangement of wires by means of active canceling with single compensating winding with initial induction of 3.5 μT to a safe level for the population adopted in Europe with an induction of 0.5 μT.* References 53, figures 9.

Key words: **overhead power line, magnetic field, quasi-static model, system of active shielding, computer simulation, experimental research.**

Мета. *Розробка методу проектування дворівневої системи активного екранування для магнітного поля промислової частоти на основі квазістатичної моделі магнітного поля, яке створюється проводами лінії електропередач і компенсаційними обмотками системи активного екранування, включаючи грубе розімкнуте і точне замкнуте управління.* ***Методологія****. На першому рівні програмне керування магнітним полем в розімкнутій формі здійснюється на основі квазістатичної моделі магнітного поля, яке створюється проводами лінії електропередач і компенсаційними обмотками системи активного екранування. Це проектування виконується на основі розрахункової системи скінчених елементів COMSOL Multiphysics. На другому рівні реалізовано стабілізуюче управління магнітним полем в формі динамічної замкнутої системи, що містить, крім об'єкту управління, також підсилювачі потужності та вимірювальні пристрої. Це проектування виконується в розрахунковій системі MATLAB.* ***Результати.*** *Наведено результати теоретичних та експериментальних досліджень оптимальної дворівневої системи активного екранування магнітного поля з однією компенсуючою обмоткою для житлового будинку від дії магнітного поля лінії електропередачі з розташуванням проводів типу «бочка».* ***Оригінальність.*** *Вперше запропоновано метод проектування дворівневої системи активного екранування магнітного поля промислової частоти на основі квазістатичної моделі магнітного поля, яке створюється проводами лінії електропередач і компенсаційними обмотками системи активного екранування, в вигляді грубого розімкненого і точного закинутого управління.* ***Практична цінність****. Показано можливість зниження рівня індукції магнітного поля в житловому будинку від магнітного поля лінії електропередач з розташуванням проводів типу «бочка» за допомогою однієї компенсуючої обмотки, з початкової індукції в 3,5 мкТл до безпечного рівня для населення, який прийнятий в Європі, з індукцією в 0,5 мкТл.* Бібл. 53, рис. 9.

Ключові слова: **повітряна лінія електропередачі, магнітне поле, квазістатична модель, система активного екранування, комп'ютерне моделювання, експериментальні дослідження.**

Introduction. The constantly accelerating technological progress in energy and communications means that our environment is becoming more and more saturated with electromagnetic waves of various spectra, which can threaten human health. The main cause for concern is the possibility that chronic exposure to low-level non-ionizing radiation can lead to long-term effects such as cancer or degenerative diseases of the immune and nervous systems [1-3].

Therefore in recent years, the terms «electromagnetic ecology», «electromagnetic pollution of the environment» have become firmly established in the topics of scientific publications, scientific conferences, and public hearings and in the controversy of social networks. These terms reflect the awareness of the fact that such presence poses a threat to human health. Such risks of prolonged exposure to an electromagnetic field on the human body are assessed by the World Health Organization and the International Agency for Research on Cancer [1-3].

The most negative impact on the residential environment is provided by overhead power lines that cover large residential and populated areas. They are densely distributed in the modern environment of long-term human stay in residential, industrial and public buildings and in the residential area. Overhead power lines generate industrial frequency magnetic field (MF) inside residential buildings located near power lines, the level of which is often 3-5 times higher than the norms for safe living in the level of the magnetic field adopted in Europe [4-6].

Prolonged exposure of the population to even weak levels of the industrial frequency magnetic field leads to an increased level of cancer in the population living in residential buildings near power lines. The creation of methods and means of normalizing the level of the electromagnetic field in existing residential areas near power lines without evicting the population or decommissioning existing electrical networks determines the economic significance of such studies. Therefore, all over the world, methods are being intensively developed to reduce the level of the magnetic field in existing residential buildings located near power lines to a safe level for the population to live in it [7-23].

The magnetic field active shielding system is an automatic control system, with the help of which a compensating magnetic field is automatically formed, directed against the original magnetic field, which needs to be compensated [24-28]. All fundamental results of the theory of automatic control systems are obtained on the basis of mathematical models of controlled processes in the form of systems of ordinary differential equations [29-33]. Analysis and synthesis of control systems for objects, given in the form of systems of differential equations, is a purely mathematical problem based on the structure of solving differential equations in an analytical form, or on numerical integration methods [34-38].

The cornerstone of the theory of automatic control is to obtain the time dependences of the parameters that determine the state of the control object. In the most general case, mathematical models of control objects can consist of a composition of subsystems of ordinary differential equations and partial differential equations [39-43].

Mathematical modeling of an electromagnetic field reduced to solving a boundary value problem for the system of Maxwell's equations [6]. Maxwell's equations are a system of partial differential equations. When modeling the electromagnetic field of power frequency, a quasi-stationary magnetic field is used, which at each moment of time is completely determined by the distribution of electric currents at the same moment of time and can be found from this distribution in the same way as it is done in magnetostatics.

The task of synthesizing a magnetic field control system is usually complicated by significant uncertainties in the mathematical model of the control object [34-37]. Due to objective circumstances, such as the inaccuracy of the first level model, unmeasured external and internal disturbances, the actual values of the output coordinates will differ from the calculated ones [44-47]. In this regard, we will consider design of two-level magnetic field control system.

At the first level, rough control of the magnetic field is carried out on the basis of a mathematical model of the first approximation. At the second level, a stabilizing accurate of the magnetic field is implemented, which aims to eliminate errors in the output coordinates due to the inaccuracy of the mathematical model of the first level.

In this regard, we will consider a two-level system of active shielding of the industrial frequency magnetic field based on a quasi-static model of the industrial frequency magnetic field generated by power line wires and compensating windings of the active shielding system.

The aim of the work is to develop a method for design a two-level active shielding system for an power frequency magnetic field based on a quasi-static model of a magnetic field generated by power line wires and compensating windings of an active shielding system, and including rough open-loop and accurate closed-loop control.

Quasi-static model of a magnetic field. Mathematical modeling of an electromagnetic field in general terms can be reduced to solving a boundary value problem for Maxwell partial differential equations system [6]

$$\mathrm{rot}\,\boldsymbol{H} = \boldsymbol{j} + \partial_t \boldsymbol{D} + \boldsymbol{j}_{ex}; \quad (1)$$

$$\mathrm{rot}\,\boldsymbol{E} = -\partial_t \boldsymbol{B}, \quad (2)$$

where $\boldsymbol{E}$ is the electric field strength, $\boldsymbol{H}$ is the magnetic field strength, $\boldsymbol{D}$ and $\boldsymbol{B}$ are the electric and magnetic induction vectors, $\boldsymbol{j}$ – conduction current density, $\boldsymbol{j}_{ex}$ – density of extraneous currents created by sources outside the area under consideration.

The first equation expresses the generalized Ampere law, which states that the total current density is a vortex of magnetic field strength. The second equation contains a differential formulation of Faraday law that the change in time of magnetic induction generates a vortex electric field.

In particular, the magnetic field induction in the immediate vicinity of the wires depends on two spatial variables and changes harmoniously with time and therefore satisfies the second-order elliptic equation

$$\frac{\partial}{\partial x}\left(\frac{1}{\mu}\frac{\partial \boldsymbol{B}}{\partial x}\right)+\frac{\partial}{\partial y}\left(\frac{1}{\mu}\frac{\partial \boldsymbol{B}}{\partial y}\right)-\left(\mathrm{j}\omega\sigma-\omega^2\varepsilon\right)\boldsymbol{B}=0, \quad (3)$$

where μ – relative magnetic permeability, ω – circular frequency of the electromagnetic field, σ – electrical conductivity, ε – relative dielectric constant.

An intermediate position between a constant field and a rapidly changing field is occupied by the so-called quasi-stationary field, which is of particular importance in technical applications. A quasi-stationary field is such an electromagnetic field, in the study of which displacement currents can be neglected in comparison with conduction currents. Maxwell equations for a quasi-stationary field are

$$\mathrm{rot}\,\boldsymbol{H} = \boldsymbol{j} + \boldsymbol{j}_{ex}; \quad (4)$$

$$\mathrm{rot}\,\boldsymbol{E} = -\partial_t \boldsymbol{B}. \quad (5)$$

It follows from the first equation of this approximation that the quasi-stationary magnetic field at each given moment of time is completely determined by the distribution of electric currents at the same moment of time and can be found from this distribution in exactly the same way as it is done in magnetostatics.

To assess the impact of the magnetic field of power lines on the environment, most calculations were performed [33-41] based on the Biot-Savart-Laplace's law for elementary current

$$\mathrm{d}\boldsymbol{H}(t) = \frac{I(t)}{4\pi \boldsymbol{R}^3}(\mathrm{d}l \times \boldsymbol{R}), \quad (6)$$

where the vector $\boldsymbol{R}$ is directed from an elementary segment dl with a total current $I(t)$ to the observation point $P(x, y, z)$. Then the total field strength vector is equal to:

$$\boldsymbol{H}(P,t) = \frac{I(t)}{4\pi}\int_L \frac{(\mathrm{d}l \times \boldsymbol{R})}{\boldsymbol{R}^3}. \quad (7)$$

This formula is widely used to calculate the magnetic field of air power transmission lines instead of Maxwell equations system.

Thus, the dependence of the magnitude of the MF intensity on the current is static and is described by (7).

In conclusion, we give one more form of writing a quasi-stationary model of an electromagnetic field those changes in time according to a sinusoidal law. The basic equations and methods for their solution can be significantly simplified by excluding from consideration one of the independent variables – time [6]. When analyzing such fields, a symbolic method is used and harmonically changing quantities are written in complex form

$$I(x,t) = A(x)e^{j\omega t}, \quad (8)$$

where $A(x)$ is the field amplitude.

First level control system synthesis. The block diagram of a two-level control system is shown in Fig. 1.

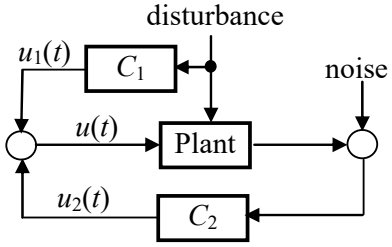

Fig. 1. The block diagram of a two-level control system

At the first level, program controller C_1 in the form of an open loop rough control u_1 is carried out on the basis of a quasi-static mathematical model of the first approximation. At the second level, a stabilizing accurate controller C_2 is implemented in the form of a closed loop control u_2 based on the equations of the dynamics of a closed system, taking into account models of actuating and measuring devices, disturbances and measurement noise, and aimed at eliminating errors in the output coordinates due to the inaccuracy of the mathematical model of the first level.

The magnetic field generated by the power line must be reduced to a safe level. With active shielding with help compensation windings, it is necessary to generate a magnetic field directed against the original MF generated by the power transmission line. The task of the active shielding system design is to calculate the coordinates of the spatial arrangement of the compensating windings, as well as the magnitudes of currents and their phases in the compensating windings.

We set the currents amplitude A_i and phases φ_i of power frequency ω, wires currents power lines. Then we set wires currents in power lines in a complex form

$$I_i(t) = A_i \exp j(\omega t + \varphi_i). \quad (9)$$

The magnitude of the currents of power lines do not remain constant and have daily, weekly, seasonal and annual fluctuations. Moreover, the magnetic field generated by multi-circuit transmission lines and groups of transmission lines, when changing currents, changes not only the intensity, but also the spatio-temporal characteristic. Therefore, we introduce the vector $\boldsymbol{\delta}$ of uncertainties of the mathematical model of the magnetic field. Then, for given currents (9) of the wires of a power transmission line or a group of power lines the vector $\boldsymbol{B}_L(Q_i,\boldsymbol{\delta},t)$ of the magnetic field generated by all power lines wires $\boldsymbol{B}_{Li}(\boldsymbol{Q_i},\boldsymbol{\delta},t)$ in point Q_i of the shielding space calculated based on Biot-Savart's law (8)

$$\boldsymbol{B}_L(Q_i,\boldsymbol{\delta},t) = \sum \boldsymbol{B}_l(Q_i,\boldsymbol{\delta},t). \quad (10)$$

Let's set the vector $\boldsymbol{X}_1$ of initial geometric values of the dimensions of the compensating windings of active shielding, as well as the currents amplitude A_{ai} and phases φ_{ai} in the compensating windings. We set the currents in the compensating windings wires in a complex form

$$I_{ai}(t) = A_{ai} \exp j(\omega t + \varphi_{wi}). \quad (11)$$

Then the vector $\boldsymbol{B}_1(Q_i,\boldsymbol{X}_1,t)$ of the magnetic field generated by all compensating windings wires of active shielding $\boldsymbol{B}_{1i}(Q_i,\boldsymbol{X}_1,t)$ in point Q_i of the shielding space can also calculated based Biot-Savart's law

$$\boldsymbol{B}_1(Q_i,\boldsymbol{X}_1,t) = \sum \boldsymbol{B}_{1i}(Q_i,\boldsymbol{X}_1,t). \quad (12).$$

Then the vector $\boldsymbol{B}_{R1}(Q_i,\boldsymbol{X}_1,\boldsymbol{\delta},t)$ of the resulting magnetic field generated by power lines and only windings of the first level active shielding system calculated as sum

$$\boldsymbol{B}_{R1}(Q_i,\boldsymbol{X}_1,\boldsymbol{\delta},t) = \boldsymbol{B}_L(Q_i,\boldsymbol{\delta},t) + \boldsymbol{B}_1(Q_i,\boldsymbol{X}_1,t). \quad (13)$$

Sanitary norms usually limit the value $\boldsymbol{B}_{R1}(Q_i,\boldsymbol{X}_1,\boldsymbol{\delta})$ of the effective value of the magnetic field induction, which determined by the vector of the instantaneous value $\boldsymbol{B}_{R1}(Q_i,\boldsymbol{X}_1,\boldsymbol{\delta},t)$ of the magnetic field induction

$$\boldsymbol{B}_{R1}(Q_i,\boldsymbol{X}_1,\boldsymbol{\delta}) = \frac{\sqrt{2}}{2}\sqrt{\frac{1}{T}\int_0^T \left|\boldsymbol{B}_{R1}(Q_i,\boldsymbol{X}_1,\boldsymbol{\delta},t)\right|^2 \mathrm{d}t}. \quad (14)$$

Often they also limit the semi-major axis of the ellipsoid of rotation of the magnetic field induction vector

$$\boldsymbol{B}_{R1}(Q_i,\boldsymbol{X}_1,\boldsymbol{\delta}) = \frac{\sqrt{2}}{2}\max_{0\le t\le T}\left|\boldsymbol{B}_{R1}(Q_i,\boldsymbol{X}_1,\boldsymbol{\delta},t)\right|. \quad (15)$$

Then the problem of designing a first level control system is reduced to computing the solution of the vector game

$$\boldsymbol{B}_{R1}(\boldsymbol{X}_1,\boldsymbol{\delta}) = \langle \boldsymbol{B}_{R1}(Q_i,\boldsymbol{X}_1,\boldsymbol{\delta})\rangle \quad (16)$$

The components of the game payoff vector $\boldsymbol{B}_{R1}(\boldsymbol{X}_1,\boldsymbol{\delta})$ are the effective values $\boldsymbol{B}_{R1}(Q_i,\boldsymbol{X}_1,\boldsymbol{\delta})$ of the induction of the resulting magnetic field at all considered points Q_i in the shielding space.

In this vector game it is necessary to find the minimum of the game payoff vector (16) by the vector $\boldsymbol{X}_1$, but the maximum of the same game payoff vector (16) by the vector $\boldsymbol{\delta}$.

At the same time, naturally, it is necessary to take into account constraints on the vector $\boldsymbol{X}$ desired parameters of a combined shield in the form of vector inequality and, possibly, vector equality

$$\boldsymbol{G}(\boldsymbol{X}_1) \le \boldsymbol{G}_{\max}, \quad \boldsymbol{H}(\boldsymbol{X}_1) = 0. \quad (17)$$

Note that the components of the vector game (16) and vector constraints (17) are the nonlinear functions of the vector of the required parameters [5, 6] and calculated based on the finite element calculations system COMSOL Multiphysics.

Second level control system synthesis. Consider the structure of the second level active shielding system in the form of a dynamic closed system containing, in addition plant, also power amplifiers and measuring devices of the system. In the zone of active shielding of the magnetic field, m sources of the magnetic field – magnetic executive bodies – are installed. Let's introduce a n – dimensional control vector $\boldsymbol{u}_P(t)$, the m components of which are the currents $\boldsymbol{I}_w(t)$ in the control windings. Let's introduce an n – dimensional state vector $\boldsymbol{x}_P(t)$ whose components include currents $I_w(t)$ in the windings of magnetic field sources. Then the state equation of such magnetic field sources can be written in the standard form

$$\boldsymbol{x}_p(t+1) = A_p\boldsymbol{x}_p(t) + B_p\boldsymbol{u}_P(t), \quad (18)$$

$$\boldsymbol{I}_w(t) = C_p\boldsymbol{x}_p(t), \quad (19)$$

in which the state A_P, control B_P and output C_P matrices of magnetic field sources as plant.

This differential equation describes the dynamics of only the actual windings and their power sources as plant.

Let's write down the differential equation of state of discrete PID controllers, the input of which is the $\boldsymbol{u}_S(t)$ of measured magnetic field induction components, and the output $\boldsymbol{u}_P(t)$ is the vector of closed-loop control of magnetic executive bodies in the following form

$$\boldsymbol{x}_c(t+1) = A_c\boldsymbol{x}_C(t) + B_C\boldsymbol{u}_S(t); \quad (20)$$

$$\boldsymbol{u}_P(t) = C_C\boldsymbol{x}_C(t), \quad (21)$$

in which the state A_C, control B_C and output C_C matrices of PID controllers.

To design second level active shielding system, it is necessary to have magnetic field measuring devices – magnetometers installed at certain points in space to measure the magnetic field $\boldsymbol{H}_S(t)$ created both by the output transmission line and by the executive windings of the active shielding system. Let's form a vector $\boldsymbol{u}_S(t)$ of measured components at the moment of time t at the points P_j of installation of magnetometers in the following form

$$\boldsymbol{x}_s(t+1) = A_S\boldsymbol{x}_S(t) + B_S\boldsymbol{H}_S(t); \quad (22)$$

$$\boldsymbol{u}_S(t) = C_S\boldsymbol{x}_S(t) + \boldsymbol{w}(t), \quad (23)$$

in which the state A_S, control B_S and output C_S matrices of magnetometers.

Let's introduce the vector $\boldsymbol{X}_2 = \{A_C, B_C, C_C\}$ of sought parameters, the components of which are the sought elements of the state A_C, control B_C and output C_C matrices of PID controllers of second level active shielding system.

Then for the current $I_w(t)$ calculated by (19) in the windings the vector $\boldsymbol{B}_2(Q_i,\boldsymbol{X}_2,t)$ of the magnetic field generated by all compensating windings wires of second level active shielding $\boldsymbol{B}_{2i}(Q_i,\boldsymbol{X}_2,t)$ in point Q_i of the shielding space can also calculated based Biot-Savart's law

$$\boldsymbol{B}_2(Q_i,\boldsymbol{X}_2,t) = \sum \boldsymbol{B}_{2i}(Q_i,\boldsymbol{X}_2,t). \quad (24)$$

Then the vector $\boldsymbol{B}_R(Q_i,\boldsymbol{X}_1,\boldsymbol{X}_2,\boldsymbol{\delta},t)$ of the resulting magnetic field generated by power lines and windings of both first and second level active shielding system calculated as sum

$$\begin{aligned}\boldsymbol{B}_R(Q_i,\boldsymbol{X}_1,\boldsymbol{X}_2,\boldsymbol{\delta},t) = \boldsymbol{B}_L(Q_i,\boldsymbol{\delta},t) + \dots \\ \dots + \boldsymbol{B}_1(Q_i,\boldsymbol{X}_1,t) + \boldsymbol{B}_2(Q_i,\boldsymbol{X}_2,t).\end{aligned} \quad (25)$$

Note that equations (18) – (25) describe the dynamics of a closed second level active shielding system.

Then the problem of designing a second level control system is reduced to computing the solution of the vector game

$$\boldsymbol{B}_R(\boldsymbol{X}_2,\boldsymbol{\delta}) = \langle \boldsymbol{B}_R(Q_i,\boldsymbol{X}_1^*,\boldsymbol{X}_2,\boldsymbol{\delta}) \rangle. \quad (26)$$

The components of the game payoff vector $\boldsymbol{B}_R(\boldsymbol{X}_2,\boldsymbol{\delta},t)$ are the effective values $\boldsymbol{B}_R(Q_i,\boldsymbol{X}_1^*,\boldsymbol{X}_2,\boldsymbol{\delta})$ of the induction of the resulting magnetic field at all considered points Q_i in the shielding space calculated for the optimal value of the vector $\boldsymbol{X}_1^*$ of parameters of first level active shielding system.

Then the synthesis of the two level system of active shielding of the magnetic field, which includes open and closed control circuits, is reduced to finding the $\boldsymbol{X}_1$ and the $\boldsymbol{X}_2$ of the parameters of the controllers.

Problem solving algorithm. A feature of the solution of the considered multi-criteria problem is inconsistency of local criteria to each other, which prevents the simultaneous optimization in general by all criteria at the same time [44]. This is due to the fact that minimizing the induction at one point, for example, located in the center of the screening space, leads to an increase in the induction at the points located closer to the power line due to overcompensation of the original magnetic field, and at the same time leads to an increase in the induction of the resulting magnetic field at points located farther than the power line due to undercompensation of the original magnetic field.

This means that one goal cannot be optimized at the expense of another goal. To solve the problems of multicriteria optimization, various strategies have been developed and each approach has its own pros and cons, and there is no single best option for solutions to multi-criteria optimization in the general case. The simplest method for solving the problem of multi-objective optimization is to form a composite objective function as a weighted sum of goals, where the weight for goals is proportional to the preference for this local criterion. Scalarization of the target vector into one component objective function transforms the multiobjective optimization problem into a single optimization goal.

Usually, the maximum values of partial criteria are known, which makes it possible to perform normalization. In this case, the normalized partial criteria are in the range $0 \le \boldsymbol{B}_{RN}(Q_i,\boldsymbol{X}) \le 1$. Approximation of the normalized value of the i–th particular criterion to unity corresponds to a tense situation. If the value of the normalized value of the particular criterion approaches zero, then this corresponds to a calm situation. To solve this problem of multicriteria optimization, the simplest non-linear trade-off scheme is used, in which the original multi-criteria problem is reduced to a single-criteria

$$\vec{\boldsymbol{X}}^* = \arg\min_{\vec{X}} \sum_{i=1}^{J} \alpha_i \left[1 - \boldsymbol{B}_{RN}(Q_i,\boldsymbol{X})\right]^{-1}, \quad (27)$$

where α_i are weight coefficients that characterize the importance of particular criteria and determine the preference for individual criteria by the decision maker. Naturally, such a formalization of the solution of the problem of multi-criteria optimization by reducing to a single-criteria problem allows one to reasonably choose one single point from the area of compromises – the Pareto area. However, this «single» point can be further tested in order to further improve the trade-off scheme from the point of view of the decision maker.

Note, that such a nonlinear scheme of trade-offs actually corresponds to the penalty function method with an internal point, since when the criterion $\boldsymbol{B}(Q_i,\boldsymbol{X})$ approaches unity, i.e. in a tense situation, scalar optimization is actually performed only according to this tense particular criterion, and the remaining criteria with a calm situation are practically not taken into account during optimization.

Such a non-linear trade-off scheme allows you to choose criteria in accordance with the intensity of the situation. If any criterion comes close to its limit value, then its normalized value approaches one. Then this non-

linear compromise scheme, in fact, with the help of a scalar criterion, reduces the problem of minimizing the sum of criteria to minimizing this one criterion, according to which there is a tense situation. If, according to other criteria, the situation is calm and their relative values are far from unity, then such a non-linear compromise scheme operates similarly to a simple linear compromise scheme.

Thus, with the help of this non-linear scheme of compromises, in fact, the tension of the situation according to individual criteria is a priori introduced into the scalar criterion. It can be shown that this non-linear compromise scheme satisfies the Pareto-optimality condition, i.e. using this scheme, it is possible to determine a point from the region of unimprovable solutions. When such a composite objective function optimized, in most cases you can get one concrete compromise solution. This processing procedure multiobjective optimization problems are simple, but relatively subjective. This procedure is based on preferences multipurpose optimization.

The second approach is to define the entire set solutions that are not dominated with respect to each another. This set is known as the Pareto optimal set. Bye moving from one Pareto solution to another, always a certain number of victims in one or more goals to achieve a certain gain in other(s). Pareto-optimal solution sets are often preferred over single solutions because they can be practical when consideration of real life problems. Pareto set size usually increases with an increase in the number goals. The result obtained preference-based strategy largely depends on the relative a preference vector used in the formation of a composite function. Changing this preference vector leads to another compromise solution. On the other hand, the ideal multipurpose the optimization procedure is less subjective. The main task in this approach is to find as many different compromises as possible solutions as far as possible.

Let's consider the method of solving the formulated problem. In order to correctly solve the problem of multi-criteria optimization, in addition to the vector optimization criterion and constraints, it is also necessary to have information about the binary relations of preference of local solutions to each other. The basis of this formal approach is the construction of areas of Pareto-optimal solutions. This approach makes it possible to significantly narrow the range of possible optimal solutions to the initial multi-criteria optimization problem and, therefore, to reduce the labor intensity of the person making the decision regarding the selection of a single variant of the optimal solution.

The task of finding a local minimum at one point of the considered space is, as a rule, multi-extreme, containing local minima and maxima, therefore, it is advisable to use stochastic multi-agent optimization algorithms for its solution. Consider the algorithm for finding the set of Pareto-optimal solutions of multi-criteria nonlinear programming problems based on stochastic multi-agent optimization.

To date, a large number of Particle Swarm Optimization (PSO) algorithms have been developed – PSO algorithms based on the idea of the collective intelligence of a particle swarm, such as the gbest PSO and lbest PSO algorithms [48-50]. The application of stochastic multi-agent optimization methods for solving multi-criteria problems today causes certain difficulties and this direction continues to develop intensively.

To solve the original multi-criteria problem of nonlinear programming with constraints, we will build a stochastic multi-agent optimization algorithm based on a set of particle swarms, the number of which is equal to the number of components of the vector optimization criterion. In the standard particle swarm optimization algorithm, particle velocities change according to linear laws. In order to increase the speed of finding a global solution, special nonlinear algorithms of stochastic multi-agent optimization have recently become widespread, in which the movement of particle i swarm j is described by the following expressions

$$v_{ij}(t+1) = w_j v_{ij}(t) + c_{1j} r_{1j}(t) H\left(p_{1j} - \varepsilon_{1j}(t)\right) \times \ldots$$
$$\ldots \times \left[y_{ij}(t) - x_{ij}(t)\right] + c_{2j} r_{2j}(t) H\left(p_{2j} - \varepsilon_{2j}(t)\right) \times \ldots \quad (28)$$
$$\ldots \times \left[y_j^*(t) - x_{ij}(t)\right];$$

$$x_{ij}(t+1) = x_{ij}(t) + v_{ij}(t+1), \quad (29)$$

where, are the position $x_{ij}(t)$ and speed $v_{ij}(t)$ of the particle i of the swarm j; c_1 and c_2 – positive constants that determine the weights of the cognitive and social components of the speed of particle movement; $r_{1j}(t)$ and $r_{2j}(t)$ are random numbers from the range [0, 1], which determine the stochastic component of the particle velocity component. Here, $y_{ij}(t)$ and y_j^* – the best local-lbest and global-gbest positions of that particle i are found, respectively, only by one particle i and by all particles i of that swarm j. The use of the inertia coefficient w_j allows to improve the quality of the optimization process.

The Heavyside function H is used as a function of switching the movement of the time-stick in accordance with the local $y_{ij}(t)$ and global $y_j^*(t)$ optimum. Parameters of switching the cognitive p_{1j} and social p_{2j} components of the speed of particle movement in accordance with the local and global optimum; random numbers $\varepsilon_{1j}(t)$ and $\varepsilon_{2j}(t)$ determine the parameters of switching the movement of the particle according to the local and global optimum. If $p_{1j}<\varepsilon_{1j}(t)$ and $p_{2j}<\varepsilon_{2j}(t)$, then the speed of movement of particle i swarm j does not change at the step t and the particle moves in the same direction as in the previous optimization step.

With the help of individual swarms j, optimization problems of scalar criteria $\boldsymbol{B}(\boldsymbol{X},P_j)$, which are components of vector optimization criteria, are solved. To find a global solution to the original multi-criteria problem, individual swarms exchange information among themselves during the search for optimal solutions of local criteria. At the same time, information about the global optimum obtained by the particles of another swarm is used to calculate the speed of movement of the particles of one swarm, which allows all potential Pareto-optimal solutions to be identified [51-53].

For this purpose, at each step t of the movement of particle i swarm j, the functions of advantages of local solutions obtained by all swarms are used. The solution $\boldsymbol{X}_j^*(t)$ obtained during the optimization of the

objective function $\boldsymbol{B}(\boldsymbol{X}(t),P_k)$ using the swarm k is $\boldsymbol{X}_j^*(t) \succ \boldsymbol{X}_k^*(t)$ better in relation to the solution obtained during the optimization of the objective function using the swarm j, i.e., if the condition is fulfilled

$$\max_{i=1,m} \boldsymbol{B}\left(P_i, \boldsymbol{X}_j^*(t)\right) < \max_{i=1,m} \boldsymbol{B}\left(P_i, \boldsymbol{X}_k^*(t)\right). \quad (30)$$

At the same time, the global solution $\boldsymbol{X}_k^*(t)$ obtained by the swarm k is used as the global optimal solution $\boldsymbol{X}_j^*(t)$ of the swarm j, which is better than the global solution $\boldsymbol{X}_k^*(t)$ of the swarm k on the basis of the weight ratio.

In fact, this approach implements the basic idea of the method of successive narrowing of the area of rade-offs – from the initial set of possible solutions, based on information about the relative importance of local solutions, all Pareto-optimal solutions that cannot be chosen according to the available information about the attitude of superiority. The deletion is carried out until a globally optimal solution is obtained. As a result of applying such an approach, no potentially optimal solution will be removed at each narrowing step.

Simulation results. Let us consider the results of the design of a two-level system of active shielding of the magnetic field generated by a double-circuit power line in a residential building, as shown in Fig. 2.

Fig. 2. Residential building closed to double-circuit power line

Figure 3 shows the scheme of the two-level active shielding system design.

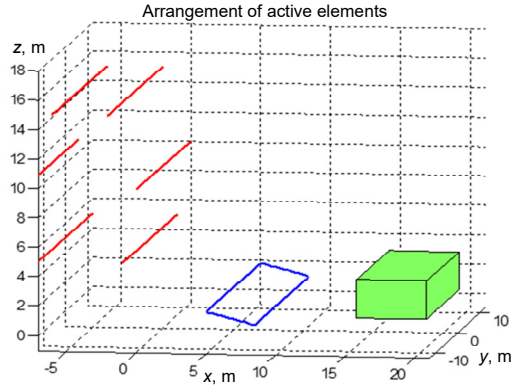

Fig. 3. Scheme of the two-level active shielding system design

Figure 4 shows the dependences of the initial and resulting magnetic field. With the help of the system, the level of the magnetic field does not exceed the level of 0.5 μT, which is accepted as a safe level of the magnetic field in Europe.

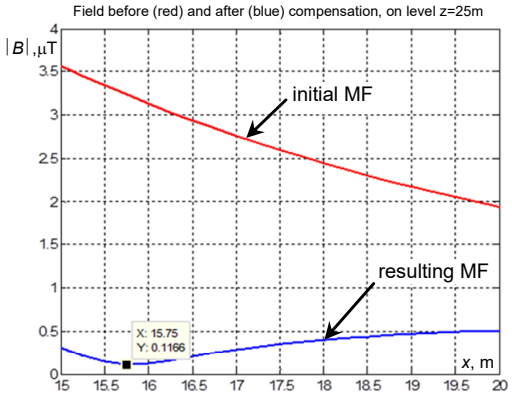

Fig. 4. Dependences of the initial and resulting magnetic field

Figure 5 shows the dependences of the spatio-temporal characteristic of the initial and resulting magnetic field and the magnetic field generated only by the compensation winding.

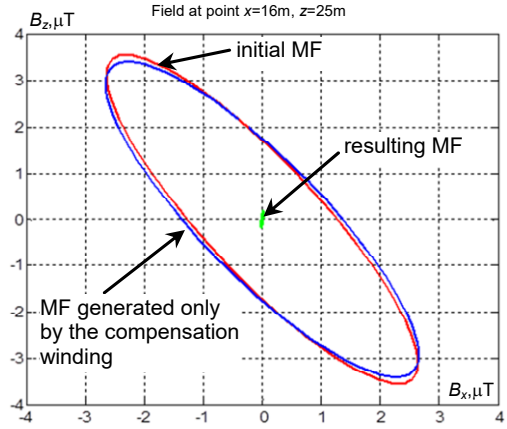

Fig. 5. Dependences of the spatio-temporal characteristic of the initial and resulting magnetic field and the magnetic field generated only by the compensation winding

Results of experimental studies. Let us now consider the results of experimental studies of the system. On Fig. 6 shows the compensation winding of the experimental setup.

Fig. 6. Compensation winding of the experimental setup

On Fig. 7 shows the control system of the experimental setup.

On Fig. 8 shows the experimental spatio-temporal characteristic of the initial magnetic field.

On Fig. 9 shows the experimental spatio-temporal characteristic of the resulting magnetic field. On the basis of experimental studies of the experimental installation of

a two-level active shielding system, it was found that the shielding factor is more than 7 units.

Fig. 7. Active shielding system of the experimental setup

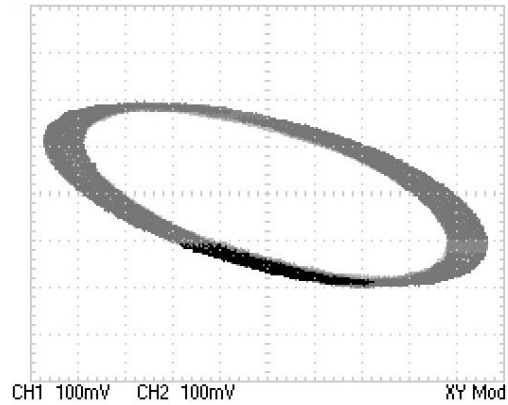

Fig. 8. Experimental spatio-temporal characteristic of the initial magnetic field

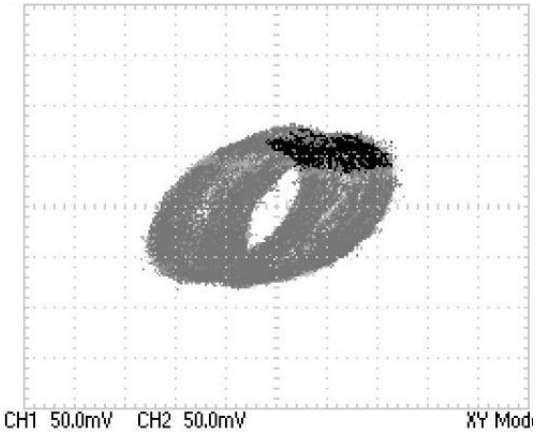

Fig. 9. Experimental spatio-temporal characteristic of the resulting magnetic field

If it is possible to measure the current of the current line of three-phase power lines or to directly measure the induction of the magnetic field near the current line, then an open system of active shielding can be built on the basis of these measurements.

Conclusions.

1. At the first level rough control of the magnetic field in open-loop form is carried out based on a quasi-static model of a magnetic field generated by power line wires and compensating windings of an active shielding system. This design calculated based on the finite element calculations system COMSOL Multiphysics.

2. At the second level, a stabilizing accurate control of the magnetic field is implemented in the form of a dynamic closed system containing, in addition plant, also power amplifiers and measuring devices of the system. This design calculated based on the calculations system MATLAB.

3. Design both first and second level control according to the developed method reduced to computing the solution of vector multi-criteria two-player zero-sum antagonistic game based on binary preference relations. The payoff game vector and constraints calculation based on quasi-static model of a magnetic field. These solutions calculated from sat of Pareto-optimal solutions based on binary preferences based on stochastic nonlinear Archimedes algorithms.

4. Two-level control system under consideration is a system with two degrees of freedom, which combines both open-loop and closed-loop control. However, in contrast to the classical synthesis of robust control of a system with two degrees of freedom, in the developed method, the synthesis of open-loop rough control is performed on the basis of a quasi-static model of the magnetic field. The synthesis of a closed-loop accurate control is carried out on the basis of the equations of the dynamics of a closed system, taking into account models of actuating and measuring devices, disturbances and measurement noise.

5. Using calculated optimal two-level active shielding system made it possible to reduce the level of magnetic field in residential building from power transmission line with a «Barrel» type arrangement of wires by means of active canceling with single compensating winding with initial induction of 3.5 μT to a safe level for the population adopted in Europe with an induction of 0.5 μT.

Acknowledgments. The authors express their gratitude to the engineers A.V. Sokol and A.P. Shevchenko of the Department of Magnetism of Technical Objects of Anatolii Pidhornyi Institute of Mechanical Engineering Problems of the National Academy of Sciences of Ukraine for the creative approach and courage shown during the creation under fire, under martial law, of an experimental installation and successful testing of a laboratory model of the system of active silencing.

Conflict of interest. The authors declare that they have no conflicts of interest.

REFERENCES

1. Sung H., Ferlay J., Siegel R.L., Laversanne M., Soerjomataram I., Jemal A., Bray, F. Global Cancer Statistics 2020: GLOBOCAN Estimates of Incidence and Mortality Worldwide for 36 Cancers in 185 Countries. *CA: A Cancer Journal for Clinicians*, 2021, vol. 71, no. 3, pp. 209-249. doi: https://doi.org/10.3322/caac.21660.

2. *Directive 2013/35/EU of the European Parliament and of the Council of 26 June 2013 on the minimum health and safety requirements regarding the exposure of workers to the risks arising from physical agents (electromagnetic fields)*. Available at: http://data.europa.eu/eli/dir/2013/35/oj (Accessed 25.07.2022).

3. *The International EMF Project. Radiation & Environmental Health Protection of the Human Environment World Health Organization*. Geneva, Switzerland, 1996. 2 p. Available at: https://www.who.int/initiatives/the-international-emf-project (Accessed 25.07.2022).

4. Rozov V.Y., Pelevin D.Y., Levina S.V. Experimental research into indoor static geomagnetic field weakening phenomenon. *Electrical Engineering & Electromechanics*, 2013, no. 6, pp. 72-76. (Rus). doi: https://doi.org/10.20998/2074-272X.2013.6.13.

5. Rozov V.Y., Kvytsynskyi A.A., Dobrodeyev P.N., Grinchenko V.S., Erisov A.V., Tkachenko A.O. Study of the magnetic field of three phase lines of single core power cables with two-end bonding of their shields. *Electrical Engineering & Electromechanics*, 2015,

no. 4, pp. 56-61. (Rus). doi: https://doi.org/10.20998/2074-272X.2015.4.11.
6. Rozov V.Yu., Reutskyi S.Yu., Pelevin D.Ye., Kundius K.D. Approximate method for calculating the magnetic field of 330-750 kV high-voltage power line in maintenance area under voltage. *Electrical Engineering & Electromechanics*, 2022, no. 5, pp. 71-77. doi: https://doi.org/10.20998/2074-272X.2022.5.12.
7. Rozov V.Y., Pelevin D.Y., Kundius K.D. Simulation of the magnetic field in residential buildings with built-in substations based on a two-phase multi-dipole model of a three-phase current conductor. *Electrical Engineering & Electromechanics*, 2023, no. 5, pp. 87-93. doi: https://doi.org/10.20998/2074-272X.2023.5.13.
8. Salceanu A., Paulet M., Alistar B.D., Asiminicesei O. Upon the contribution of image currents on the magnetic fields generated by overhead power lines. *2019 International Conference on Electromechanical and Energy Systems (SIELMEN).* 2019. doi: https://doi.org/10.1109/sielmen.2019.8905880.
9. Del Pino Lopez J.C., Romero P.C. Influence of different types of magnetic shields on the thermal behavior and ampacity of underground power cables. *IEEE Transactions on Power Delivery*, Oct. 2011, vol. 26, no. 4, pp. 2659-2667. doi: https://doi.org/10.1109/tpwrd.2011.2158593.
10. Hasan G.T., Mutlaq A.H., Ali K.J. The Influence of the Mixed Electric Line Poles on the Distribution of Magnetic Field. *Indonesian Journal of Electrical Engineering and Informatics (IJEEI)*, 2022, vol. 10, no. 2, pp. 292-301. doi: https://doi.org/10.52549/ijeei.v10i2.3572.
11. Victoria Mary S., Pugazhendhi Sugumaran C. Investigation on magneto-thermal-structural coupled field effect of nano coated 230 kV busbar. *Physica Scripta*, 2020, vol. 95, no. 4, art. no. 045703. doi: https://doi.org/10.1088/1402-4896/ab6524.
12. Ippolito L., Siano P. Using multi-objective optimal power flow for reducing magnetic fields from power lines. *Electric Power Systems Research*, 2004, vol. 68, no. 2, pp. 93-101. doi: https://doi.org/10.1016/S0378-7796(03)00151-2.
13. Barsali S., Giglioli R., Poli D. Active shielding of overhead line magnetic field: Design and applications. *Electric Power Systems Research*, May 2014, vol. 110, pp. 55-63. doi: https://doi.org/10.1016/j.epsr.2014.01.005.
14. Bavastro D., Canova A., Freschi F., Giaccone L., Manca M. Magnetic field mitigation at power frequency: design principles and case studies. *IEEE Transactions on Industry Applications*, May 2015, vol. 51, no. 3, pp. 2009-2016. doi: https://doi.org/10.1109/tia.2014.2369813.
15. Beltran H., Fuster V., García M. Magnetic field reduction screening system for a magnetic field source used in industrial applications. *9 Congreso Hispano Luso de Ingeniería Eléctrica (9 CHLIE)*, Marbella (Málaga, Spain), 2005, pp. 84-99. Available at: https://www.researchgate.net/publication/229020921_Magnetic_field_reduction_screening_system_for_a_magnetic_field_source_used_in_industrial_applications (Accessed 22.06.2021).
16. Bravo-Rodríguez J., Del-Pino-López J., Cruz-Romero P. A Survey on Optimization Techniques Applied to Magnetic Field Mitigation in Power Systems. *Energies*, 2019, vol. 12, no. 7, p. 1332. doi: https://doi.org/10.3390/en12071332.
17. Canova A., del-Pino-López J.C., Giaccone L., Manca M. Active Shielding System for ELF Magnetic Fields. *IEEE Transactions on Magnetics*, March 2015, vol. 51, no. 3, pp. 1-4. doi: https://doi.org/10.1109/tmag.2014.2354515.
18. Canova A., Giaccone L. Real-time optimization of active loops for the magnetic field minimization. *International Journal of Applied Electromagnetics and Mechanics*, Feb. 2018, vol. 56, pp. 97-106. doi: https://doi.org/10.3233/jae-172286.
19. Canova A., Giaccone L., Cirimele V. Active and passive shield for aerial power lines. *Proc. of the 25th International Conference on Electricity Distribution (CIRED 2019)*, 3-6 June 2019, Madrid, Spain. Paper no. 1096. Available at: https://www.cired-repository.org/handle/20.500.12455/290 (Accessed 28 May 2021).
20. Canova A., Giaccone L. High-performance magnetic shielding solution for extremely low frequency (ELF) sources. *CIRED - Open Access Proceedings Journal*, Oct. 2017, vol. 2017, no. 1, pp. 686-690. doi: https://doi.org/10.1049/oap-cired.2017.1029.
21. Celozzi S. Active compensation and partial shields for the power-frequency magnetic field reduction. *2002 IEEE International Symposium on Electromagnetic Compatibility*, Minneapolis, MN, USA, 2002, vol. 1, pp. 222-226. doi: https://doi.org/10.1109/isemc.2002.1032478.
22. Celozzi S., Garzia F. Active shielding for power-frequency magnetic field reduction using genetic algorithms optimization. *IEE Proceedings - Science, Measurement and Technology*, 2004, vol. 151, no. 1, pp. 2-7. doi: https://doi.org/10.1049/ip-smt:20040002.
23. Celozzi S., Garzia F. Magnetic field reduction by means of active shielding techniques. *WIT Transactions on Biomedicine and Health*, 2003, vol. 7, pp. 79-89. doi: https://doi.org/10.2495/ehr030091.
24. Martynenko G. Analytical Method of the Analysis of Electromagnetic Circuits of Active Magnetic Bearings for Searching Energy and Forces Taking into Account Control Law. *2020 IEEE KhPI Week on Advanced Technology (KhPIWeek)*, 2020, pp. 86-91. doi: https://doi.org/10.1109/KhPIWeek51551.2020.9250138.
25. Martynenko G., Martynenko V. Rotor Dynamics Modeling for Compressor and Generator of the Energy Gas Turbine Unit with Active Magnetic Bearings in Operating Modes. *2020 IEEE Problems of Automated Electrodrive. Theory and Practice (PAEP)*, 2020, pp. 1-4. doi: https://doi.org/10.1109/PAEP49887.2020.9240781.
26. Buriakovskyi S.G., Maslii A.S., Pasko O.V., Smirnov V.V. Mathematical modelling of transients in the electric drive of the switch – the main executive element of railway automation. *Electrical Engineering & Electromechanics*, 2020, no. 4, pp. 17-23. doi: https://doi.org/10.20998/2074-272X.2020.4.03.
27. Ostroverkhov M., Chumack V., Monakhov E., Ponomarev A. Hybrid Excited Synchronous Generator for Microhydropower Unit. *2019 IEEE 6th International Conference on Energy Smart Systems (ESS)*, Kyiv, Ukraine, 2019, pp. 219-222. doi: https://doi.org/10.1109/ess.2019.8764202.
28. Ostroverkhov M., Chumack V., Monakhov E. Ouput Voltage Stabilization Process Simulation in Generator with Hybrid Excitation at Variable Drive Speed. *2019 IEEE 2nd Ukraine Conference on Electrical and Computer Engineering (UKRCON)*, Lviv, Ukraine, 2019, pp. 310-313. doi: https://doi.org/10.1109/ukrcon.2019.8879781.
29. Tytiuk V., Chornyi O., Baranovskaya M., Serhiienko S., Zachepa I., Tsvirkun L., Kuznetsov V., Tryputen N. Synthesis of a fractional-order $PI^{\lambda}D^{\mu}$-controller for a closed system of switched reluctance motor control. *Eastern-European Journal of Enterprise Technologies*, 2019, no. 2 (98), pp. 35-42. doi: https://doi.org/10.15587/1729-4061.2019.160946.
30. Zagirnyak M., Chornyi O., Zachepa I. The autonomous sources of energy supply for the liquidation of technogenic accidents. *Przeglad Elektrotechniczny*, 2019, no. 5, pp. 47-50. doi: https://doi.org/10.15199/48.2019.05.12.
31. Chornyi O., Serhiienko S. A virtual complex with the parametric adjustment to electromechanical system parameters. *Technical Electrodynamics*, 2019, pp. 38-41. doi: https://doi.org/10.15407/techned2019.01.038.
32. Shchur I., Kasha L., Bukavyn M. Efficiency Evaluation of Single and Modular Cascade Machines Operation in Electric Vehicle. *2020 IEEE 15th International Conference on Advanced Trends in Radioelectronics, Telecommunications and Computer Engineering (TCSET)*, Lviv-Slavske, Ukraine, 2020, pp. 156-161. doi: https://doi.org/10.1109/tcset49122.2020.235413.
33. Shchur I., Turkovskyi V. Comparative Study of Brushless DC Motor Drives with Different Configurations of Modular Multilevel Cascaded Converters. *2020 IEEE 15th International Conference on Advanced Trends in Radioelectronics, Telecommunications and Computer Engineering (TCSET)*, Lviv-Slavske, Ukraine, 2020, pp. 447-451. doi: https://doi.org/10.1109/tcset49122.2020.235473.
34. Solomentsev O., Zaliskyi M., Averyanova Y., Ostroumov I., Kuzmenko N., Sushchenko O., Kuznetsov B., Nikitina T., Tserne E., Pavlikov V., Zhyla S., Dergachov K., Havrylenko O., Popov A., Volosyuk V., Ruzhentsev N., Shmatko O. Method of Optimal Threshold Calculation in Case of Radio Equipment Maintenance. *Data Science and Security. Lecture Notes in Networks and Systems*, 2022, vol. 462, pp. 69-79. doi: https://doi.org/10.1007/978-981-19-2211-4_6.
35. Ruzhentsev N., Zhyla S., Pavlikov V., Volosyuk V., Tserne E., Popov A., Shmatko O., Ostroumov I., Kuzmenko N., Dergachov K., Sushchenko O., Averyanova Y., Zaliskyi M., Solomentsev O., Havrylenko O., Kuznetsov B., Nikitina T. Radio-Heat Contrasts of UAVs and Their Weather Variability at 12 GHz, 20 GHz, 34 GHz,

and 94 GHz Frequencies. *ECTI Transactions on Electrical Engineering, Electronics, and Communications*, 2022, vol. 20, no. 2, pp. 163-173. doi: https://doi.org/10.37936/ecti-eec.2022202.246878.
36. Havrylenko O., Dergachov K., Pavlikov V., Zhyla S., Shmatko O., Ruzhentsev N., Popov A., Volosyuk V., Tserne E., Zaliskyi M., Solomentsev O., Ostroumov I., Sushchenko O., Averyanova Y., Kuzmenko N., Nikitina T., Kuznetsov B. Decision Support System Based on the ELECTRE Method. *Data Science and Security. Lecture Notes in Networks and Systems*, 2022, vol. 462, pp. 295-304. doi: https://doi.org/10.1007/978-981-19-2211-4_26.
37. Shmatko O., Volosyuk V., Zhyla S., Pavlikov V., Ruzhentsev N., Tserne E., Popov A., Ostroumov I., Kuzmenko N., Dergachov K., Sushchenko O., Averyanova Y., Zaliskyi M., Solomentsev O., Havrylenko O., Kuznetsov B., Nikitina T. Synthesis of the optimal algorithm and structure of contactless optical device for estimating the parameters of statistically uneven surfaces. *Radioelectronic and Computer Systems*, 2021, no. 4, pp. 199-213. doi: https://doi.org/10.32620/reks.2021.4.16.
38. Volosyuk V., Zhyla S., Pavlikov V., Ruzhentsev N., Tserne E., Popov A., Shmatko O., Dergachov K., Havrylenko O., Ostroumov I., Kuzmenko N., Sushchenko O., Averyanova Yu., Zaliskyi M., Solomentsev O., Kuznetsov B., Nikitina T. Optimal Method for Polarization Selection of Stationary Objects Against the Background of the Earth's Surface. *International Journal of Electronics and Telecommunications*, 2022, vol. 68, no. 1, pp. 83-89. doi: https://doi.org/10.24425/ijet.2022.139852.
39. Halchenko V., Trembovetska R., Tychkov V., Storchak A. Nonlinear surrogate synthesis of the surface circular eddy current probes. *Przegląd Elektrotechniczny*, 2019, vol. 95, no. 9, pp. 76-82. doi: https://doi.org/10.15199/48.2019.09.15.
40. Halchenko V.Ya., Storchak A.V., Trembovetska R.V., Tychkov V.V. The creation of a surrogate model for restoring surface profiles of the electrophysical characteristics of cylindrical objects. *Ukrainian Metrological Journal*, 2020, no. 3, pp. 27-35. doi: https://doi.org/10.24027/2306-7039.3.2020.216824.
41. Sushchenko O., Averyanova Y., Ostroumov I., Kuzmenko N., Zaliskyi M., Solomentsev O., Kuznetsov B., Nikitina T., Havrylenko O., Popov A., Volosyuk V., Shmatko O., Ruzhentsev N., Zhyla S., Pavlikov V., Dergachov K., Tserne E. Algorithms for Design of Robust Stabilization Systems. *Computational Science and Its Applications – ICCSA 2022. ICCSA 2022. Lecture Notes in Computer Science*, 2022, vol. 13375, pp. 198-213. doi: https://doi.org/10.1007/978-3-031-10522-7_15.
42. Chystiakov P., Chornyi O., Zhautikov B., Sivyakova G. Remote control of electromechanical systems based on computer simulators. *2017 International Conference on Modern Electrical and Energy Systems (MEES)*, Kremenchuk, Ukraine, 2017, pp. 364-367. doi: https://doi.org/10.1109/mees.2017.8248934.
43. Zagirnyak M., Bisikalo O., Chorna O., Chornyi O. A Model of the Assessment of an Induction Motor Condition and Operation Life, Based on the Measurement of the External Magnetic Field. *2018 IEEE 3rd International Conference on Intelligent Energy and Power Systems (IEPS)*, Kharkiv, 2018, pp. 316-321. doi: https://doi.org/10.1109/ieps.2018.8559564.
44. Maksymenko-Sheiko K.V., Sheiko T.I., Lisin D.O., Petrenko N.D. Mathematical and Computer Modeling of the Forms of Multi-Zone Fuel Elements with Plates. *Journal of Mechanical Engineering*, 2022, vol. 25, no. 4, pp. 32-38. doi: https://doi.org/10.15407/pmach2022.04.032.
45. Hontarovskyi P.P., Smetankina N.V., Ugrimov S.V., Garmash N.H., Melezhyk I.I. Computational Studies of the Thermal Stress State of Multilayer Glazing with Electric Heating. *Journal of Mechanical Engineering*, 2022, vol. 25, no. 1, pp. 14-21. doi: https://doi.org/10.15407/pmach2022.02.014.
46. Kostikov A.O., Zevin L.I., Krol H.H., Vorontsova A.L. The Optimal Correcting the Power Value of a Nuclear Power Plant Power Unit Reactor in the Event of Equipment Failures. *Journal of Mechanical Engineering*, 2022, vol. 25, no. 3, pp. 40-45. doi: https://doi.org/10.15407/pmach2022.03.040.
47. Rusanov A.V., Subotin V.H., Khoryev O.M., Bykov Y.A., Korotaiev P.O., Ahibalov Y.S. Effect of 3D Shape of Pump-Turbine Runner Blade on Flow Characteristics in Turbine Mode. *Journal of Mechanical Engineering*, 2022, vol. 25, no. 4, pp. 6-14. doi: https://doi.org/10.15407/pmach2022.04.006.
48. Ummels M. *Stochastic Multiplayer Games Theory and Algorithms*. Amsterdam University Press, 2010. 174 p.
49. Ray T., Liew K.M. A Swarm Metaphor for Multiobjective Design Optimization. *Engineering Optimization*, 2002, vol. 34, no. 2, pp. 141-153. doi: https://doi.org/10.1080/03052150210915.
50. Xiaohui Hu, Eberhart R.C., Yuhui Shi. Particle swarm with extended memory for multiobjective optimization. *Proceedings of the 2003 IEEE Swarm Intelligence Symposium*. SIS'03 (Cat. No.03EX706), Indianapolis, IN, USA, 2003, pp. 193-197. doi: https://doi.org/10.1109/sis.2003.1202267.
51. Zhyla S., Volosyuk V., Pavlikov V., Ruzhentsev N., Tserne E., Popov A., Shmatko O., Havrylenko O., Kuzmenko N., Dergachov K., Averyanova Y., Sushchenko O., Zaliskyi M., Solomentsev O., Ostroumov I., Kuznetsov B., Nikitina T. Practical imaging algorithms in ultra-wideband radar systems using active aperture synthesis and stochastic probing signals. *Radioelectronic and Computer Systems*, 2023, no. 1, pp. 55-76. doi: https://doi.org/10.32620/reks.2023.1.05.
52. Zhyla S., Volosyuk V., Pavlikov V., Ruzhentsev N., Tserne E., Popov A., Shmatko O., Havrylenko O., Kuzmenko N., Dergachov K., Averyanova Y., Sushchenko O., Zaliskyi M., Solomentsev O., Ostroumov I., Kuznetsov B., Nikitina T. Statistical synthesis of aerospace radars structure with optimal spatio-temporal signal processing, extended observation area and high spatial resolution. *Radioelectronic and Computer Systems*, 2022, no. 1, pp. 178-194. doi: https://doi.org/10.32620/reks.2022.1.14.
53. Hashim F.A., Hussain K., Houssein E.H., Mabrouk M.S., Al-Atabany W. Archimedes optimization algorithm: a new metaheuristic algorithm for solving optimization problems. *Applied Intelligence*, 2021, vol. 51, no. 3, pp. 1531-1551. doi: https://doi.org/10.1007/s10489-020-01893-z.

Received 18.08.2023
Accepted 09.11.2023
Published 02.03.2024

B.I. Kuznetsov[1], *Doctor of Technical Science, Professor,*
A.S. Kutsenko[1], *Doctor of Technical Science, Professor,*
T.B. Nikitina[2], *Doctor of Technical Science, Professor,*
I.V. Bovdui[1], *PhD, Senior Research Scientist,*
V.V. Kolomiets[2], *PhD, Assistant Professor,*
B.B. Kobylianskyi[2], *PhD, Associate Professor,*
[1] Anatolii Pidhornyi Institute of Mechanical Engineering Problems of the National Academy of Sciences of Ukraine,
2/10, Pozharskogo Str., Kharkiv, 61046, Ukraine,
e-mail: kuznetsov.boris.i@gmail.com (Corresponding Author)
[2] Educational scientific professional pedagogical Institute of Ukrainian Engineering Pedagogical Academy,
9a, Nosakov Str., Bakhmut, Donetsk Region, 84511, Ukraine,
e-mail: nnppiuipa@ukr.net

How to cite this article:
Kuznetsov B.I., Kutsenko A.S., Nikitina T.B., Bovdui I.V., Kolomiets V.V., Kobylianskyi B.B. Method for design of two-level system of active shielding of power frequency magnetic field based on a quasi-static model. *Electrical Engineering & Electromechanics*, 2024, no. 2, pp. 31-39. doi: https://doi.org/10.20998/2074-272X.2024.2.05

UDC 621.314 https://doi.org/10.20998/2074-272X.2024.2.06

H.K.E. Zine, K. Abed

Smart current control of the wind energy conversion system based permanent magnet synchronous generator using predictive and hysteresis model

Introduction. *Given the increasing demand for performance and efficiency of converters and power drives, the development of new control systems must take into account the real nature of these types of systems. Converters and dimmers power are nonlinear systems of a hybrid nature, including elements linear and nonlinear and a finite number of switching devices. Signals input for power converters are discrete signals that control the 'opening and closing' transitions of each component.* ***Problem.*** *In the multilevel inverters connected to grid, the switching frequency is the principal cause of harmonics and switching losses, which by nature, reduces the inverter's efficiency.* ***Purpose.*** *For guarantee the satisfying quality of power transmitted to the electrical grid, while ensuring reduction of current ripples and output voltage harmonics.* ***Novelty.*** *This work proposes a new smart control, based on a predictive current control of the three level neutral point clamped inverter, used in Wind Energy Conversion System (WECS) connected to grid, based permanent magnet synchronous generator, powered by a hysteresis current control for the rectifier. This new formula guarantees handling with the influence of harmonics disturbances (similar current total harmonic distortion), voltage stress, switching losses, rise time, over or undershoot and settling time in WECS.* ***Methods.*** *The basic idea of this control is to choose the best switching state, of the power switches, which ameliorates the quality function, selected from order predictive current control of WECS.* ***Results. Practical value.*** *Several advantages in this intelligent method, such as the fast dynamic answer, the easy implementation of nonlinearities and it requires fewer calculations to choose the best switching state. In addition, an innovative algorithm is proposed to adjust the current ripples and output voltage harmonics of the WECS. The performances of the system were analyzed by simulation using MATLAB/Simulink.* References 33, table 3, figures 11.

Key words: **hysteresis current control, permanent magnet synchronous generator, predictive current control, wind energy conversion system, three level neutral point clamped inverter.**

Вступ. *Зважаючи на зростаючі вимоги до продуктивності та ефективності перетворювачів та силових приводів, при розробці нових систем керування необхідно враховувати реальну природу систем такого типу. Перетворювачі та регулятори потужності являють собою нелінійні системи гібридної природи, що включають лінійні та нелінійні елементи та кінцеве число комутаційних пристроїв. Вхідні сигнали для силових перетворювачів є дискретними сигналами, які керують переходами «відкриття та закриття» кожного компонента.* ***Проблема***. *У багаторівневих інверторах, підключених до мережі, частота перемикання є основною причиною гармонік та втрат перемикання, що за своєю природою знижує ефективність інвертора.* ***Мета***. *Гарантувати задовільну якість електроенергії, що передається в електричну мережу, при одночасному зниженні пульсацій струму та гармонік вихідної напруги.* ***Новизна***. *У цій роботі пропонується новий інтелектуальний контроль, заснований на прогнозуючому керуванні струмом трирівневого інвертора з фіксованою нейтральною точкою, що використовується в системі перетворення енергії вітру (WECS), підключеної до мережі, на основі синхронного генератора з постійними магнітами, що живиться від керування струмом . Ця нова формула гарантує обробку з урахуванням впливу гармонічних перешкод (аналогічні загальні гармонічні спотворення струму), перенапруги, втрат перемикання, часу наростання, пере- чи недорегулювання, а також часу стабілізації WECS.* ***Методи***. *Основна ідея цього управління полягає у виборі найкращого стану перемикання силових перемикачів, що покращує функцію якості, обрану з порядку прогнозуючого керування струмом WECS.* ***Результати***. ***Практична цінність***. *Цей інтелектуальний метод має кілька переваг, таких як швидка динамічна відповідь, простота реалізації нелінійностей і необхідність меншої кількості обчислень для вибору найкращого стану перемикання. Крім того, запропоновано інноваційний алгоритм регулювання пульсацій струму та гармонік вихідної напруги WECS. Характеристики системи проаналізовано шляхом моделювання з використанням MATLAB/Simulink.* Бібл. 33, табл. 3, рис. 11.

Ключові слова: **управління струмом з гістерезисом, синхронний генератор з постійними магнітами, прогностичне управління струмом, система перетворення енергії вітру, інвертор з трирівневим фіксуванням нейтральної точки.**

Introduction. The increasing use in the industrial sector of powered systems electronically and controllable, motivated by the improvement of their performance, has led to a proliferation of static converters. Among these most common structures and the most attractive are the Pulse Width Modulation (PWM) voltage rectifier [1].

Participation in system services must be on an alternative grid three-phase. It is then necessary to use an electronic converter for the DC-AC and/or AC-DC conversion in the conversion chain wind energy [1, 2].

The advent of power electronics has a major impact on the world of industry in recent decades. This advent occurred through the arrival on the market for power electronic components such as thyristors, triacs, GTO, IGBT or high-power transistors.

The constant growth of energy consumption in all its forms and the associated polluting effects, mainly caused by the combustion of fossil fuels, are at the heart of the issue of sustainable development and care of the environment in a discussion for the future of the planet.

Wind energy is clean and renewable energy, unlike conventional energy which presents the constraints of distance from the electricity network and the constraints of fuel transport, as well as the periodic maintenance of the installations [3].

In recent literatures, authors have investigated the potential technical impacts in voltage regulation, active and reactive power variations, transformers loading, current and voltage harmonics causes with renewable energy integration [4-6].

In the resolution of harmonics disturbances problems, many researchers used the sinusoidal PWM approach and implement it in Wind Energy Conversion System (WECS) to ameliorate the harmonic content on the output voltage waveform [7]. Space vector modulation technique possesses remarkable performance in 3-level PWM topologies [8]. Other techniques involving modulation methods at a low switching frequency that have attained more demand in a broader field of function are staircase

modulation, space vector control [9, 10], selective harmonic elimination [10, 11] and sliding mode control for Permanent Magnet Synchronous Generator (PMSG) [12].

System for application generator. In the studied system, we are interested in the wound rotor PMSG and its use for the production of electrical energy from wind power. The variable speed configuration is represented in Fig. 1.

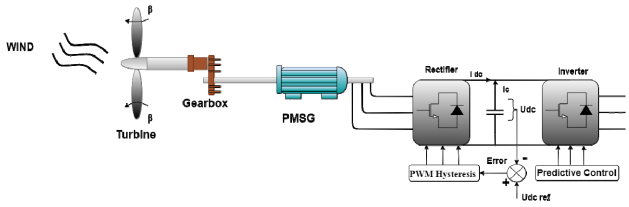

Fig. 1. PMSG-based WECS

The rotor is connected to a rectifier (rotor side converter). A predictive control applied to Three Level Neutral Point Clamped (3L-NPC) inverter (grid side converter), which is placed in the output of the rectifier controlled by PWM hysteresis.

1. The modeling of the turbine. The turbine rotate speed is depending on wind speed; this makes it possible to know the wind torque applied to the wind turbine. This modeling is based on bibliographic cross-checking or additional information from brochures from different manufacturers [13]:

$$P_{aer} = \frac{1}{2} c_p(\lambda, \beta) \rho S V_v^3 = \frac{1}{2} \rho \pi R_t^2 V_v^3, \qquad (1)$$

where

$$\lambda = \frac{\Omega_t R_t}{V_v}, \qquad (2)$$

where P_{aer} is the aerodynamic power; c_p indicates the performance coefficient of the wind generator; λ is the speed ratio (rad); β is the inclination angle of the blade, which depicts the orientation angle of the blades; Ω_t is the turbine rotation speed; R_t is the blade radius; V_v is the wind speed; ρ is the air density (1.22 kg/m^3 at atmospheric pressure at 15 °C); the Betz limit is that the coefficient $c_p(\lambda, \beta)$ does not exceed the value 16/17=0.59 [13, 14].

2. Modeling of the multiplier. The multiplier adapts the turbine rotation speed to the PMSG rotation speed. For this we grant a multiplier between the turbine and the PMSG, the latter is mathematically modelled by the following equations:

$$C_g = C_t / G \quad (3) \quad \text{and} \quad \Omega_t = \Omega_{mech} / G. \quad (4)$$

The mechanical equations:

$$\frac{C_t}{G} - C_g = \left(\frac{J_t}{G^2} + J_g\right) \frac{d\Omega_{mech}}{dt} + \left(\frac{f_t}{G^2} + f_g\right) \Omega_{mech}; \quad (5)$$

$$\frac{J_t}{G^2} + J_g = J \quad (6) \quad \text{and} \quad \frac{f_t}{G^2} + f_g = f. \quad (7)$$

So, the mechanical equations are:

$$C_{mech} = J \frac{d\Omega_{mech}}{dt}; \qquad (8)$$

$$C_{mech} = C_g - C_{em} - C_{vis}; \qquad (9)$$

$$C_{vis} = f \Omega_{mech}, \qquad (10)$$

where C_{mech}, C_t, C_g, C_{vis} are the mechanical, wind, electromagnetic and viscous torques, respectively; J, J_t, J_g are the total, turbine and generator inertias; f, f_t, f_g are the coefficient of total friction, viscous friction of the turbine and of the generator; G is the ratio of the speed multiplier; Ω_{mech} is the generator rotation speed (fast axis).

3. PMSG modeling. By choosing a *d-q* reference frame synchronized with the stator flux [3, 14, 15] are next.

The equations of tensions:

$$\begin{cases} V_{sd} = R_s I_{sd} + \dfrac{d\varphi_{sd}}{dt} - \omega_s \varphi_{sq}; \\ V_{sq} = R_s I_{sq} + \dfrac{d\varphi_{sq}}{dt} - \omega_s \varphi_{sd}; \\ V_{rd} = R_r I_{rd} + \dfrac{d\varphi_{rd}}{dt} - (\omega_s - \omega)\varphi_{rq}; \\ V_{rq} = R_r I_{rq} + \dfrac{d\varphi_{rq}}{dt} - (\omega_s - \omega)\varphi_{rd}; \\ J \dfrac{d\Omega_t}{dt} = C_{em} - C_r - f_r \Omega_r, \end{cases} \qquad (11)$$

The equations of the flux:

$$\begin{cases} \varphi_{sd} = L_s I_{sd} + M I_{rd}; \\ \varphi_{sq} = L_s I_{sq} + M I_{rq}; \\ \varphi_{rd} = L_r I_{rd} + M I_{sd}; \\ \varphi_{rq} = L_r I_{rq} + M I_{sq}, \end{cases} \qquad (12)$$

$$C_{em} = \frac{M}{L_r} p\left(\varphi_{dr} I_{qs} - \varphi_{qr} I_{ds}\right). \qquad (13)$$

The electromagnetic torque becomes:

$$C_{em} = \frac{3}{2} \frac{M}{L_s} p\left(\varphi_{qs} I_{dr} - \varphi_{ds} I_{qr}\right). \qquad (14)$$

The stator and rotor active and reactive powers are expressed by:

$$\begin{cases} P_s = \dfrac{3}{2}\left(V_{sd} I_{sd} + V_{sq} I_{sq}\right); \\ Q_s = \dfrac{3}{2}\left(V_{sq} I_{sd} + V_{sd} I_{sq}\right); \\ P_r = \dfrac{3}{2}\left(V_{rd} I_{rd} + V_{rq} I_{rq}\right); \\ Q_r = \dfrac{3}{2}\left(V_{rq} I_{rd} + V_{rd} I_{rq}\right), \end{cases} \qquad (15)$$

where R_s, R_r are the stator and rotor resistances; L_s, L_r, M are the stator, rotor, mutual inductances, respectively; I_{sd}, I_{sq}, I_{rd}, I_{rq} are the stator and rotor currents in the *d-q* frame; φ_{sd}, φ_{sq}, φ_{rd}, φ_{rq} are the stator and rotor flux in the *d-q* frame; p is the number of pairs of poles; P_s, Q_s, P_r, Q_r are the stator and rotor active and reactive powers; V_{sd}, V_{sq}, V_{rd}, V_{rq} are the stator and rotor voltage components in the *d-q* frame; ω_s is the speed of stator magnetic field; $\omega_r = \omega_s - \omega$ is the angular speed of rotor; ω is the mechanical angular speed.

PMSG and turbine parameters are shown in Table 1.

Table 1

PMSG and turbine parameters

PMSG parameters		Turbine parameters
P_n = 1680 W	L_l = 0.6 mH	R = 1.8 m
V_s = 110 V	L_s = 5.25 mH	J = 0.07 kg·m^2
f = 50 Hz	ω_r = 0.1827 rad/s	G = 1
R_s = 0.9585 Ω	C = 8 N·m	ρ = 1.25 kg/m^3
R_l = 0.5 Ω	p = 4	

Hysteresis current control.

1. Modeling of the rectifier. The rectifier bridge consists of three arms with six bipolar transistors antiparallel with diodes. These switches are controlled by closing and opening (pulse time closing «0» and opening «1»). And in the same arm the switches operate in a complementary way ($K_a = \overline{K'_a}$) to avoid the short circuit [16]. The model of bridge rectifier is depicted in Fig. 2.

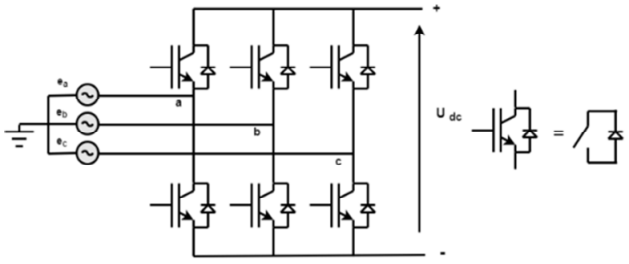

Fig. 2. Bridge rectifier

The different switching and combination states of the PWM rectifier switches are shown in Table 2.

Table 2

8 possible states of the switches

K	S_a	S_b	S_c	V_{ab}	V_{bc}	V_{ac}
0	1	0	0	U_{dc}	0	$-U_{dc}$
1	1	1	0	0	U_{dc}	$-U_{dc}$
2	0	1	1	$-U_{dc}$	U_{dc}	0
3	0	1	0	$-U_{dc}$	0	U_{dc}
4	0	0	1	0	$-U_{dc}$	U_{dc}
5	1	0	1	U_{dc}	$-U_{dc}$	0
6	0	0	0	0	0	0
7	1	1	1	0	0	0

From Table 1 we can represent the rectifier input voltages in general as follows [17-19]:

$$V_{ab} = (S_a - S_b)U_{dc}; \tag{16}$$

$$V_{bc} = (S_b - S_c)U_{dc}; \tag{17}$$

$$V_{ca} = (S_c - S_a)U_{dc}. \tag{18}$$

So we can deduce the phase-to-neutral voltages:

$$V_b = f_b U_{dc}; \tag{19}$$

$$V_c = f_c U_{dc}, \tag{20}$$

where:

$$f_a = \frac{2S_a - (S_b + S_c)}{3}; \tag{21}$$

$$f_b = \frac{2S_b - (S_a + S_c)}{3}; \tag{22}$$

$$f_c = \frac{2S_c - (S_a + S_b)}{3}. \tag{23}$$

8 possible states of the input voltage V in a complex plane α-β [20]:

$$V_{k+1} = \begin{cases} \frac{2}{3}U_{dc}e^{\frac{jk\pi}{3}} & \text{for } k = 0...5; \\ V_7 = V_0 = 0. \end{cases} \tag{24}$$

8 voltage vectors noted as $V_0(0\ 0\ 0)$ – $V_7(1\ 1\ 1)$ are presented in Fig. 3, where V_{ab}, V_{bc}, V_{ca} are the complex voltages; f_a, f_b, f_c are the rectifier switching function; U_{dc} is the rectified voltage; S_a, S_b, S_c are the switching states of the rectifier; V_a, V_b, V_c are the simple voltages.

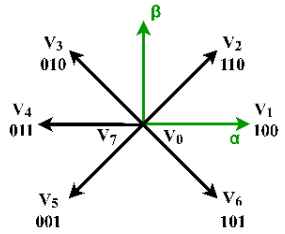

Fig. 3. Presentation of voltage vector V_k

2. Functional representation of the PWM rectifier in the three-phase reference. The voltage equations for the balanced three-phase system without neutral can be written as (Fig. 3):

$$\bar{e} = \overline{V_1} + \overline{V}; \tag{25}$$

$$\bar{e} = R\bar{i} + L\frac{\mathrm{d}\bar{i}}{\mathrm{d}t} + \overline{V}; \tag{26}$$

$$\begin{bmatrix} e_a \\ e_b \\ e_c \end{bmatrix} = R\begin{bmatrix} i_a \\ i_b \\ i_c \end{bmatrix} + L\frac{\mathrm{d}}{\mathrm{d}t}\begin{bmatrix} i_a \\ i_b \\ i_c \end{bmatrix} + \begin{bmatrix} V_a \\ V_b \\ V_c \end{bmatrix}; \tag{27}$$

The rectifier input voltage can be written as:

$$V_n = U_{dc}\left(S_n \cdot \frac{1}{3} \cdot \sum_{n=a}^{c} S_n\right), \tag{28}$$

where S_n = 0 or 1 are the state of the switches, where ($n = a, b, c$). In addition, we can write the DC bus current as:

$$C\frac{\mathrm{d}U_{dc}}{\mathrm{d}t} = i_c. \tag{29}$$

The current in the capacitor can also write:

$$i_c = i_{dc} - i_{ch}; \tag{30}$$

$$C\frac{\mathrm{d}U_{dc}}{\mathrm{d}t} = S_a i_a + S_b i_b + S_c i_c - i_{dc}. \tag{31}$$

Also, the current i_c is the sum of the currents of each phase by the state of its switch [16]:

$$C\frac{\mathrm{d}U_{dc}}{\mathrm{d}t} = S_a i_a + S_b i_b + S_c i_c - i_{ch}. \tag{32}$$

So, the AC side of the rectifier:

$$L\frac{\mathrm{d}i_a}{\mathrm{d}t} + Ri_a = e_a - U_{dc}\left(S_a - \frac{1}{3}\cdot\sum_{n=a}^{c} S_n\right) = e_a - U_{dc}\left(S_a - \frac{1}{3}(S_a + S_b + S_c)\right); \tag{33}$$

$$L\frac{\mathrm{d}i_b}{\mathrm{d}t} + Ri_b = e_b - U_{dc}\left(S_b - \frac{1}{3}\cdot\sum_{n=a}^{c} S_n\right) = e_b - U_{dc}\left(S_b - \frac{1}{3}(S_a + S_b + S_c)\right); \tag{34}$$

$$L\frac{\mathrm{d}i_c}{\mathrm{d}t} + Ri_c = e_c - U_{dc}\left(S_c - \frac{1}{3}\cdot\sum_{n=a}^{c} S_n\right) = e_c - U_{dc}\left(S_c - \frac{1}{3}(S_a + S_b + S_c)\right), \tag{35}$$

where the network voltages are expressed by:

$$e_a = E_m\sin(\omega t); \tag{36}$$

$$e_b = E_m\sin(\omega t - 2\pi/3); \tag{37}$$

$$e_c = E_m\sin(\omega t + 2\pi/3). \tag{38}$$

The above equation can be summarized as:

$$L\frac{\mathrm{d}i_n}{\mathrm{d}t}+Ri_n=e_n-U_{dc}\left(S_n-\frac{1}{3}\cdot\sum_{n=a}^{c}S_n\right);\qquad(39)$$

$$C\frac{\mathrm{d}U_{dc}}{\mathrm{d}t}=\sum_{n=a}^{c}i_nS_n-i_{ch}\,,\qquad(40)$$

where e_a, e_b, e_c are the network voltages; V_n are the instantaneous phase voltages; S_n are the switching states; i_c is the capacitor current; i_{dc} is the rectifier output current; i_{ch} is the load current; E_m is the maximum phase voltage.

3. PWM to hysteresis band. The purpose of hysteresis controller is to force the actual current to follow the predefined reference current. In conventional hysteresis controller, the comparators switch between the fixed bandwidths, this technique only requires a hysteresis comparator per phase [21, 22].

The principle of hysteresis used in this system is expressed in Fig. 4. The switch opens if the error becomes less than $-H/2$, it closes if the latter is greater than $+H/2$, where H is the range (or width) of hysteresis. If the error is now between $-H/2$, and $+H/2$, (it varies within the hysteresis range), the switch does not switch [21, 23].

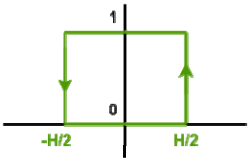

Fig. 4. Diagram of proposed hysteresis controller

The topology of hysteresis current control PWM technique using in this configuration is shown in Fig. 5.

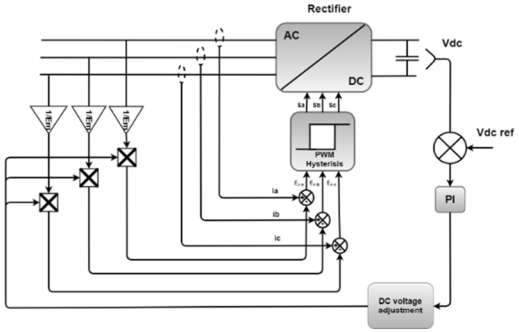

Fig. 5. Control diagram of the hysteresis current control rectifier connected to the inverter

Implementation predictive current control 3L-NPC inverter.

1. Modeling inverter 3L-NPC. The power and control circuit of a 3L-NPC inverter connected to grid is shown in Fig. 6, each phase of three-phase 3L-NPC inverter consists of 3 arms constituted of 4 switches (S1, S2, S3, S4) connected in series and 2 median diodes (D1 and D2). The midpoints of switches (S2 and S3) of each phase are connected to the load and the midpoints of diodes (D1 and D2) are connected to the neutral point [24, 25].

In the same arm the switches operate in a complementary way connection functions of the arm switches k (a complementary way) will be given by:

$$\overbrace{\begin{cases}S_{a1}=\overline{S_{a2}}\\S_{a3}=\overline{S_{a4}}\end{cases}\quad\begin{cases}S_{a1}=\overline{S_{a3}}\\S_{a2}=\overline{S_{a4}}\end{cases}\quad\begin{cases}S_{a1}=\overline{S_{a4}}\\S_{a2}=\overline{S_{a3}}\end{cases}}.\qquad(41)$$

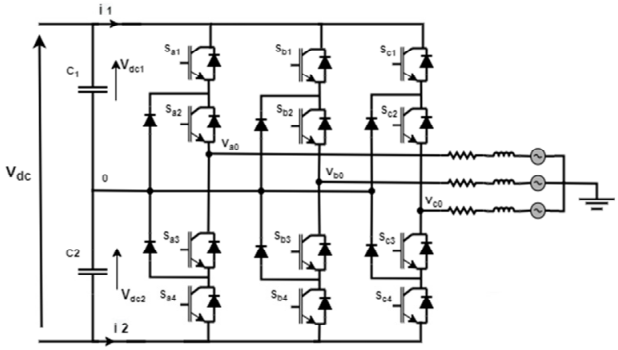

Fig. 6. The power circuit model of a 3L-NPC inverter connected to the grid

The switching function on A, B, and C phase can be defined as follows:

$$\overbrace{\begin{cases}S_{k1}=\overline{S_{k3}}\\S_{k2}=\overline{S_{k4}}\end{cases}\quad\begin{cases}S_{k1}=1-S_{k3}\\S_{k2}=1-S_{k4}\end{cases}}.\qquad(42)$$

The equations of voltages (a), (b), (c) of the three-level inverter, with respect to the midpoint «0» of the input voltage source is expressed as [26, 27]:

$$\begin{cases}V_{a0}=\left(S_{a1}S_{a2}-S_{a3}S_{a4}\right)V_{dc};\\V_{b0}=\left(S_{b1}S_{b2}-S_{b3}S_{b4}\right)V_{dc};\\V_{c0}=\left(S_{c1}S_{c2}-S_{c3}S_{c4}\right)V_{dc}.\end{cases}\qquad(43)$$

The compound voltages in matrix form are:

$$\begin{bmatrix}V_{ab}\\V_{bc}\\V_{ac}\end{bmatrix}=\begin{bmatrix}v_{a0}-v_{b0}\\v_{b0}-v_{c0}\\v_{a0}-v_{c0}\end{bmatrix}=\\=\begin{bmatrix}1&-1&0\\0&1&-1\\-1&0&1\end{bmatrix}\cdot\begin{bmatrix}S_{a1}S_{a2}-S_{a3}S_{a4}\\S_{b1}S_{b2}-S_{b3}S_{b4}\\S_{c1}S_{c2}-S_{c3}S_{c4}\end{bmatrix}\cdot V_{dc}.\qquad(44)$$

We can define the simple voltages (v_a, v_b, v_c) with respect to the neutral point n:

$$\begin{cases}v_a=v_{an}=v_{a0}-v_{n0};\\v_b=v_{bn}=v_{b0}-v_{n0};\\v_c=v_{cn}=v_{c0}-v_{n0}.\end{cases}\qquad(45)$$

The voltage equation between the midpoint of the DC power supply of the inverter and the point load neutral which is written as follows:

$$v_{n0}=\frac{1}{3}\left(v_{a0}+v_{b0}+v_{c0}\right).\qquad(46)$$

Finally, the system in the matrix form is:

$$\begin{bmatrix}v_a\\v_b\\v_c\end{bmatrix}=\frac{1}{3}\begin{bmatrix}2&-1&-1\\-1&2&-1\\-1&-1&2\end{bmatrix}\cdot\begin{bmatrix}S_{a1}S_{a2}-S_{a3}S_{a4}\\S_{b1}S_{b2}-S_{b3}S_{b4}\\S_{c1}S_{c2}-S_{c3}S_{c4}\end{bmatrix}V_{dc}\,,\qquad(47)$$

where S_{k1}, S_{k2}, S_{k3}, S_{k4} are the switching states of the inverter power switches; v_{a0}, v_{b0}, v_{c0} are the phase-to-neutral voltages at the output of the inverter between the phases of the load and the midpoint «0»; v_{n0} is the voltage between the midpoint of the inverter DC supply and the neutral point of the load; v_{an}, v_{bn}, v_{cn} are the phase-to-neutral voltages with respect to the neutral point n.

Depending on the states of the inverter, this vector can take several positions in; these positions are

designated on the vector diagram or switch hexagon shown in Fig. 7 [24, 26].

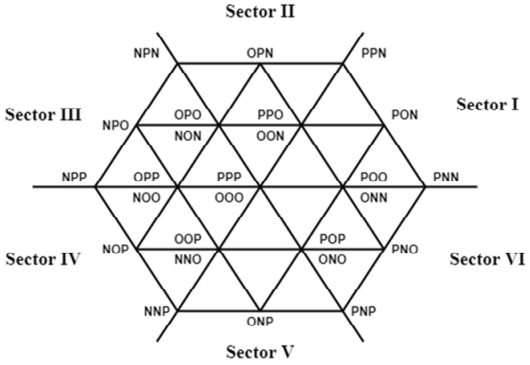

Fig. 7. Space vector diagram of a 3-L NPC inverter

2. Implementation predictive current control. The proposed predictive control strategy is based on the fact that only a finite number of possible switching states can be generated by a power converter static and that models of the system can be used to predict behavior variables for each switching state. For switching selection appropriate to apply, a selection criterion must be defined. This selection criterion is expressed as a quality function that will be evaluated for the predicted values variables to control. The prediction of the future value of these variables is calculated for each possible switching state. The switching state that minimizes the quality function is selected [28, 29]. This approximation is considered in Fig. 8.

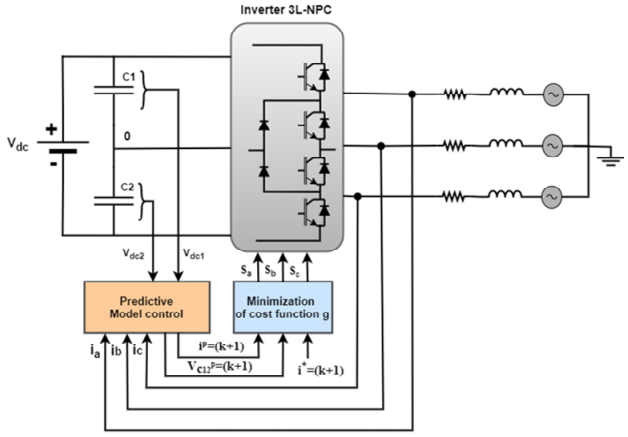

Fig. 8. Block diagram of predictive current control for a 3L-NPC inverter connected to grid

The system model equations are given as follows:

$$\begin{cases} v_{an} = Ri_a + L\dfrac{\mathrm{d}i_a}{\mathrm{d}t} - e_a; \\ v_{bn} = Ri_b + L\dfrac{\mathrm{d}i_b}{\mathrm{d}t} - e_b; \\ v_{cn} = Ri_c + L\dfrac{\mathrm{d}i_c}{\mathrm{d}t} - e_c. \end{cases} \tag{48}$$

After the Clarke transformation and with the use of Euler's method to obtain a discrete-time model of the current, the current equations are expressed as follows:

$$\frac{\mathrm{d}i}{\mathrm{d}t} = \frac{i(k+1) - i(k)}{T_s}, \tag{49}$$

where T_s is the sampling period and k shows sampling time.

$$\begin{cases} i_\alpha^p(k+1) = \left(1 - T_s\dfrac{R}{L}\right) i_\alpha(k) + \dfrac{T_s}{L}\left(v_\alpha - e_\alpha(k)\right); \\ i_\beta^p(k+1) = \left(1 - T_s\dfrac{R}{L}\right) i_\beta(k) + \dfrac{T_s}{L}\left(v_\beta - e_\beta(k)\right). \end{cases} \tag{50}$$

The currents i_{c1}, i_{c2} supplied by each capacitor C_1, C_2 are represented by the following equations:

$$\begin{cases} i_{c1}(k) = i_{dc}(k) - H_{1a}i_a(k) - H_{1b}i_b(k) - H_{1c}i_c(k); \\ i_{c2}(k) = i_{dc}(k) - H_{2a}i_a(k) - H_{2b}i_b(k) - H_{2c}i_c(k). \end{cases} \tag{51}$$

The switch states function of the 3L-NPC calculates the variables (H_{1x}, H_{2x}) and is given by:

$$\begin{cases} H_{1x} = \begin{cases} 1 & \text{if} \quad S_x = \text{"+"}; \\ 0 & \text{other}; \end{cases} \\ H_{2x} = \begin{cases} 1 & \text{if} \quad S_x = \text{"–"}; \\ 0 & \text{other}. \end{cases} \end{cases} \tag{52}$$

We use the Euler method to obtain the equations in discrete time which allows the prediction of DC bus voltages as follows:

$$\begin{cases} v_{c1}^p(k+1) = v_{c1}(k) + \dfrac{1}{C} i_{c1}(k) T_s; \\ v_{c2}^p(k+1) = v_{c2}(k) + \dfrac{1}{C} i_{c2}(k) T_s, \end{cases} \tag{53}$$

where $i(k)$ is i_α^p, i_β^p and represents the current vector in stationary frame α-β; i_{c1}, i_{c2} are the currents flowing respectively through the capacitors C_1, C_2; variables H_{1x}, H_{2x} depend on the switching states; v_{c1}, v_{c2} are the voltages across DC-link capacitors C_1, C_2.

3. Cost function. The objective of the current control scheme is to minimize the error between the currents measured and reference values. This requirement can be written as a cost function. The cost function is expressed in orthogonal coordinates and measures the error between the references and the predicted currents:

$$g = \left|i_\alpha^* - i_\alpha^p\right| + \left|i_\beta^* - i_\beta^p\right| + \lambda_{dc}\left|v_{c1}^p - v_{c2}^p\right|, \tag{54}$$

where g is the cost function; λ_{dc} is the weighting factor.

The evaluation of the precomputed results and the determination of future optimal control actions are made by the cost function [30-33].

4. Diagram smart current control. Predictive model algorithm applied to control the centralized 3L-NPC inverter in WECS is shown in Fig. 9. To make the necessary calculation of the equations of the predictive command Fig. 9 presents the algorithm of the deferent step of this smart control [28, 29].

Results. This section is to validate the results obtained from the model smart predictive current control of 3L-NPC inverter algorithm of WECS through eigenvalues analysis and also the comparative studies between the proposed model and the exist solution already used for PMSG connected to grid. In the first part, the results obtained after rotor side converter are illustrated in Fig. 8.

Figures 10,*a*,*d* show the applied variable change of wind profile for the studied system. Figure 10,*c* presents the form of the DC link voltage. The DC link voltage reference is set to 540 V, the measured voltage perfectly follows the reference signal.

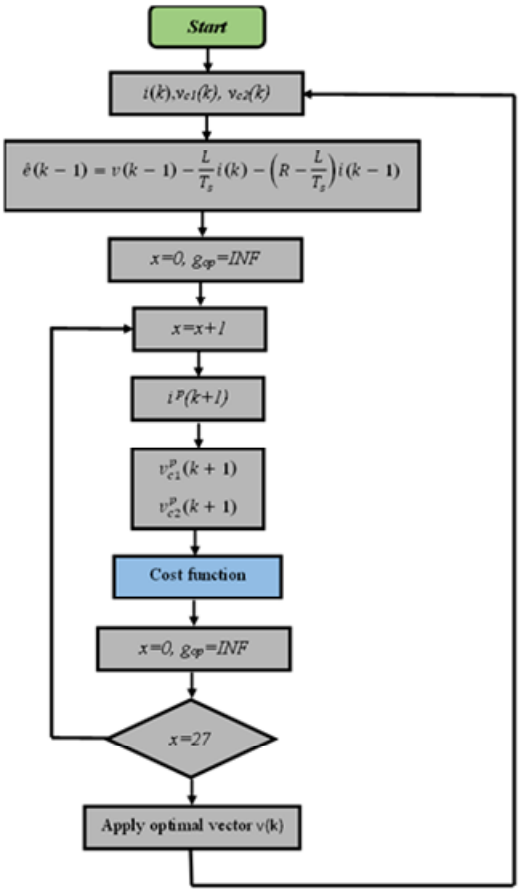

Fig. 9. Smart current control algorithm

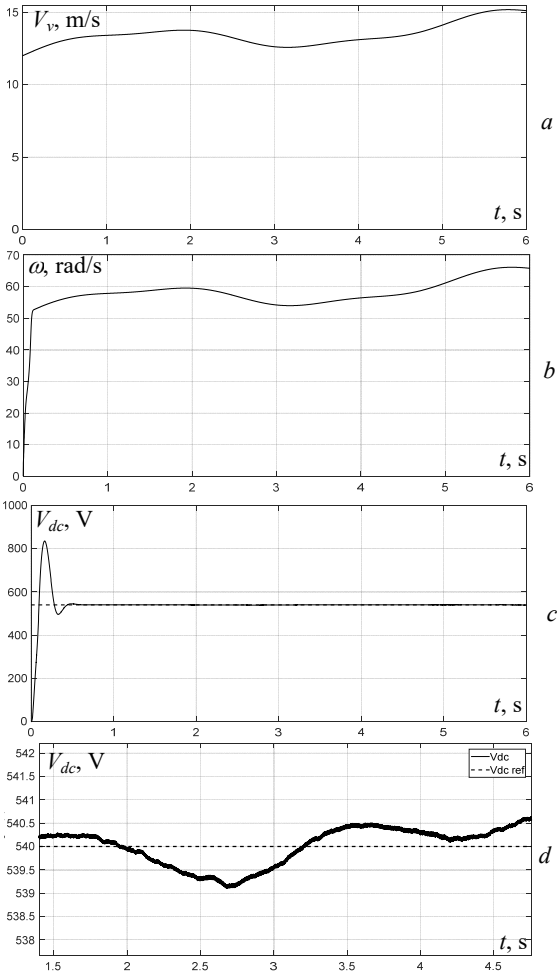

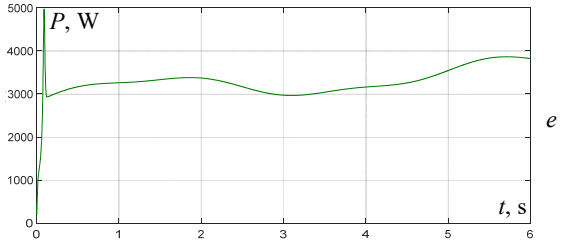

Fig. 10. Simulation results of the rotor side converter: *a* – wind speed; *b* – mechanical speed; *c* – DC-link voltage; *d* – zoom DC-link voltage; *e* – PMSG power

The second part shows the results after grid side converter and is illustrated in Fig. 11.

Figure 11,*a* clearly shows the proper tracking of the converter reference currents with small currents ripples.

It can be seen in Fig. 9,*b* waveform of the controlled currents i_α and i_β is smooth and stable.

Figure 11,*c* illustrates the DC voltage ripples are low enough. The spectral analysis of the modulated voltage signal is presented in Fig. 11,*g*, where we noticed a drop in Total Harmonic Distortion (THD).

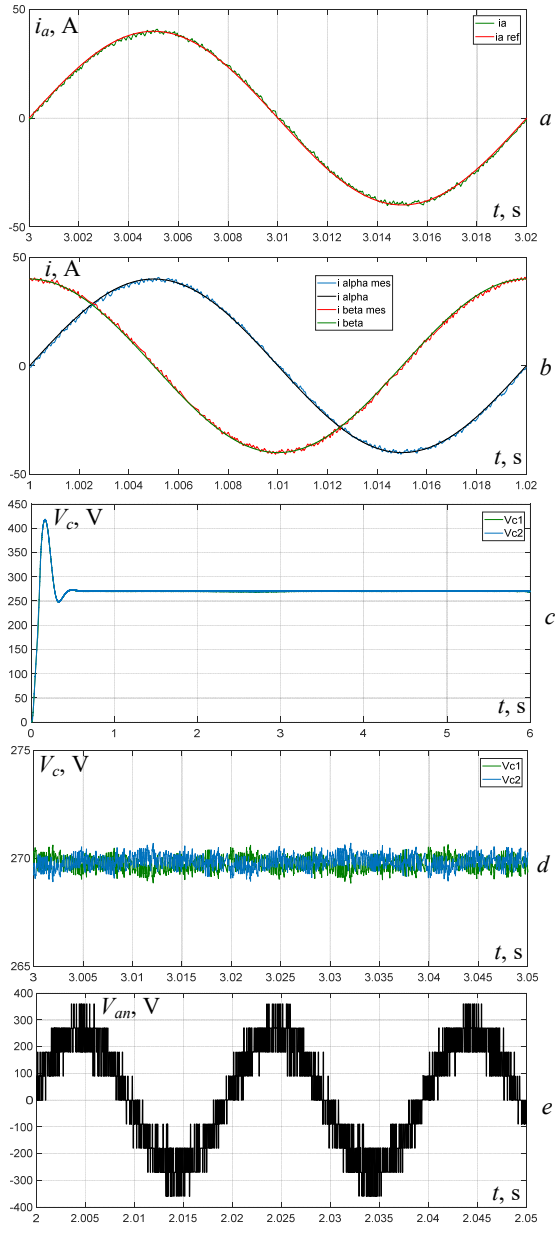

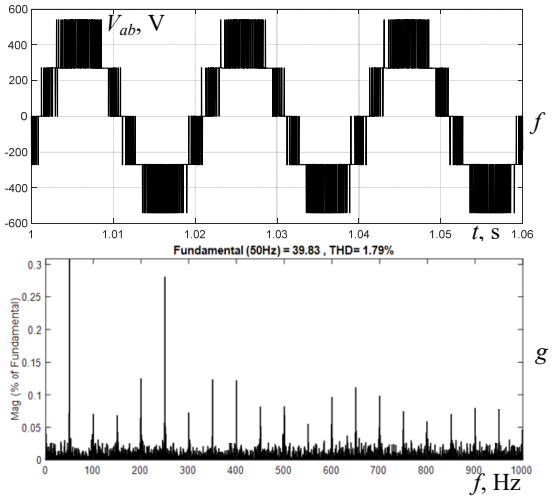

Fig. 11. Simulation results of the grid side converter: a – output current i_a; *b* – controlled currents i_a, i_β and their references; *c* – DC voltages across the two capacitors V_{dc1}, V_{dc2}; *d* – zoom of the DC voltages across the two capacitors V_{dc1}, V_{dc2}; *e* – simple voltage at inverter output V_{an}; *f* – output line-to-line voltage V_{ab}; *g* – spectrum of current i_a

Comparison to state-of-the-art. The purpose of this part a comparative study between the smart current control of the WECS and exist solution using in [11]. Table 3 summarizes the principal differences between exist solution and the new smart current control of the WECS.

These results and comparison showed high stability, fast response, low disturbance, eases of implementation and strong the robustness of this smart current control.

Table 3

Comparison of smart current control and exist solution

Parameter	Exist solution [11]	Smart current control
Answer dynamic	Stable	Stable
The behavior of current in regime const THD, %	5.3	1.38
Frequency of switching, Hz	2500	2500
Response time, ms	>40	40
Robustness, %	45	80
Complexity of implantation, %	35	10

Conclusions.

1. In this paper, a new design and intelligent control has been proposed and implemented for wind energy conversion system based PMSG.

2. All presented results have validated the capability and effectiveness of the proposed intelligent control strategy and showed a high performance and dynamic behavior even at high power. Also, the measured DC voltage follows the reference voltage closely (transitory response 30 ms) and this proves its robustness. The control of three level neutral point clamped inverter is guarantied by smart advanced current control, which gives good results regarding THD (1.38 %) in the both of simulation and experimentation results.

3. Optimizing using metaheuristic algorithms are more precise for THD optimization and switching loss mitigation.

4. Experimental validation is the focus of future work: using DC machine for creating mechanical speed of the turbine, multiplier, PMSG, PWM rectifier, board Dspace1104, current sensors, voltage sensors, DC voltage stabilizer, control interface, three level neutral point clamped inverter, MATLAB/Simulink and control desk.

Conflict of interest. The authors of the article declare that there is no conflict of interest.

REFERENCES

1. Sathish C., Chidambaram I.A., Manikandan M. Intelligent cascaded adaptive neuro fuzzy interface system controller fed KY converter for hybrid energy based microgrid applications. *Electrical Engineering & Electromechanics*, 2023, no. 1, pp. 63-70. doi: https://doi.org/10.20998/2074-272X.2023.1.09.

2. Chen R., Ke D., Sun Y., Chung Y.C., Wu H., Liao S., Xu J., Wei C. Hierarchical Frequency-dependent Chance Constrained Unit Commitment for Bulk AC/DC Hybrid Power Systems with Wind Power Generation. *Journal of Modern Power Systems and Clean Energy*, 2023, vol. 11, no. 4, pp. 1053-1064. doi: https://doi.org/10.35833/MPCE.2022.000138.

3. Kamel Eddine Z.H., Dib R., Abed K. New Intelligent Power Adjustment of the Wind Energy Conversion System Extended Virtual Flux based Direct Power Control Using New Fuzzy-PI Controller. *Proceedings of the 9th International Workshop on Simulation for Energy, Sustainable Development & Environment (SESDE 2021)*, 2021, pp. 27-37. doi: https://doi.org/10.46354/i3m.2021.sesde.004.

4. Bhattacherjee H., Mukherjee D., Chakraborty C. Three-level Vienna Rectifier with a Brushless and Permanent Magnetless Generator for Wind Energy Conversion Systems. *Power Electronics and Drives*, 2022, vol. 7, no. 1, pp. 84-102. doi: https://doi.org/10.2478/pead-2022-0007.

5. Choudhury S., Bajaj M., Dash T., Kamel S., Jurado F. Multilevel Inverter: A Survey on Classical and Advanced Topologies, Control Schemes, Applications to Power System and Future Prospects. *Energies*, 2021, vol. 14, no. 18, art. no. 5773. doi: https://doi.org/10.3390/en14185773.

6. Devineni G.K., Ganesh A. Problem Formulations, Solving Strategies, Implementation Methods & Applications of Selective Harmonic Elimination for Multilevel Converters. *Journal Européen Des Systèmes Automatisés*, 2020, vol. 53, no. 6, pp. 939-952. doi: https://doi.org/10.18280/jesa.530620.

7. Eroğlu H., Cuce E., Mert Cuce P., Gul F., Iskenderoğlu A. Harmonic problems in renewable and sustainable energy systems: A comprehensive review. *Sustainable Energy Technologies and Assessments*, 2021, vol. 48, art. no. 101566. doi: https://doi.org/10.1016/j.seta.2021.101566.

8. Sarker R., Datta A., Debnath S. FPGA-Based High-Definition SPWM Generation With Harmonic Mitigation Property for Voltage Source Inverter Applications. *IEEE Transactions on Industrial Informatics*, 2021, vol. 17, no. 2, pp. 1352-1362. doi: https://doi.org/10.1109/TII.2020.2983844.

9. Jayakumar V., Chokkalingam B., Munda J.L. A Comprehensive Review on Space Vector Modulation Techniques for Neutral Point Clamped Multi-Level Inverters. *IEEE Access*, 2021, vol. 9, pp. 112104-112144. doi: https://doi.org/10.1109/ACCESS.2021.3100346.

10. Wu M., Li Y.W., Konstantinou G. A Comprehensive Review of Capacitor Voltage Balancing Strategies for Multilevel Converters Under Selective Harmonic Elimination PWM. *IEEE Transactions on Power Electronics*, 2021, vol. 36, no. 3, pp. 2748-2767. doi: https://doi.org/10.1109/TPEL.2020.3012915.

11. Alakkad M.A.M., Rasin Z., Rasheed M., Abd Halim W., Omar R. Real-time switching thirteen-level modified CHB-Multilevel inverter using artificial neural network technique based on selective harmonic elimination. *Indonesian Journal of Electrical Engineering and Computer Science*, 2020, vol. 20, no. 3, pp. 1642-1652. doi: https://doi.org/10.11591/ijeecs.v20.i3.pp1642-1652.

12. Sami I., Ullah S., Ali Z., Ullah N., Ro J.-S. A Super Twisting Fractional Order Terminal Sliding Mode Control for DFIG-Based Wind Energy Conversion System. *Energies*, 2020, vol. 13, no. 9, art. no. 2158. doi: https://doi.org/10.3390/en13092158.

13. Boukadoum A., Bouguerne A., Bahi T. Direct power control using space vector modulation strategy control for wind energy conversion system using three-phase matrix converter. *Electrical Engineering & Electromechanics*, 2023, no. 3, pp. 40-46. doi: https://doi.org/10.20998/2074-272X.2023.3.06.
14. Bouraghda S., Sebaa K., Bechouat M., Sedraoui M. An improved sliding mode control for reduction of harmonic currents in grid system connected with a wind turbine equipped by a doubly-fed induction generator. *Electrical Engineering & Electromechanics*, 2022, no. 2, pp. 47-55. doi: https://doi.org/10.20998/2074-272X.2022.2.08.
15. Cheikh R., Boualem B., Belmili H. Improved Fuzzy Logic MPPT Controller of Stand-alone WECS-based PMSG under Stochastic Wind Environment. *Journal of Renewable Energies*, 2023, vol. 1, no. 1, pp. 31-42. doi: https://doi.org/10.54966/jreen.v1i1.1096.
16. Ghanem S., Fandi G., Kyncl J., Müller Z. A novel scheme for control by active and reactive power utilized in gearless variable speed wind turbine system with PMSG connected to the grid. *Electrical Engineering & Electromechanics*, 2022, no. 2, pp. 56-68. doi: https://doi.org/10.20998/2074-272X.2022.2.09.
17. Babu A., Shivaleelavathi B.G., Yatnalli V. Efficiency Analysis and Design Considerations of a Hysteretic Current Controlled Parallel Hybrid Envelope Tracking Power Supply. *Engineering, Technology & Applied Science Research*, 2023, vol. 13, no. 1, pp. 9812-9818. doi: https://doi.org/10.48084/etasr.5414.
18. Sakri D., Laib H., Farhi S.E., Golea N. Sliding mode approach for control and observation of a three phase AC-DC pulse-width modulation rectifier. *Electrical Engineering & Electromechanics*, 2023, no. 2, pp. 49-56. doi: https://doi.org/10.20998/2074-272X.2023.2.08.
19. Malinowski M. *Sensorless Control Strategies for Three-Phase PWM Rectifiers*. Ph.D. Thesis, Faculty of Electrical Engineering Institute of Control and Industrial Electronics, Warsaw University of Technology, 2001. 128 p.
20. Deng Q., Gou B., Ge X., Lin C., Xie D., Feng X. A High-Accuracy-Light-AI Data-Driven Diagnosis Method for Open-Circuit Faults in Single-Phase PWM Rectifiers. *IEEE Transactions on Transportation Electrification*, 2023, vol. 9, no. 3, pp. 4352-4365. doi: https://doi.org/10.1109/TTE.2023.3238009.
21. Zhou Z., Song J., Yu Y., Xu Q., Zhou X. Research on High-Quality Control Technology for Three-Phase PWM Rectifier. *Electronics*, 2023, vol. 12, no. 11, art. no. 2417. doi: https://doi.org/10.3390/electronics12112417.
22. Kendouli F., Nabti K., Labed K., Benalla H. Modélisation, simulation et contrôle d'une turbine éolienne à vitesse variable basée sur la génératrice asynchrone à double alimentation. *Journal of Renewable Energies*, 2023, vol. 14, no. 1, pp. 109-120. (Fra). doi: https://doi.org/10.54966/jreen.v14i1.245.
23. Adjie A.P., Hamid M.I. Harmonics Analysis of Input Current of 3-Phase PWM Rectifier. *Andalas Journal of Electrical and Electronic Engineering Technology*, 2021, vol. 1, no. 1, pp. 31-40. doi: https://doi.org/10.25077/ajeeet.v1i1.6.
24. Yaramasu V. *Predictive control of multilevel converters for megawatt wind energy conversion systems*. PhD Thesis, Ryerson University, Toronto, ON, Canada, 2014. 259 p. doi: https://doi.org/10.32920/ryerson.14655330.v1.
25. Abid M., Laribi S., Larbi M., Allaoui T. Diagnosis and localization of fault for a neutral point clamped inverter in wind energy conversion system using artificial neural network technique. *Electrical Engineering & Electromechanics*, 2022, no. 5, pp. 55-59. doi: https://doi.org/10.20998/2074-272X.2022.5.09.
26. Guo F., Ma Z., Diao F., Zhao Y., Wheeler P. Hybrid Virtual Coordinate-Driven CBPWM Strategy of Three-Level T-Type NPC Converters for Electric Aircraft Propulsion Applications. *IEEE Transactions on Industrial Electronics*, 2024, vol. 71, no. 3, pp. 2309-2319. doi: https://doi.org/10.1109/TIE.2023.3266552.
27. Lyu J., Yan H., Ding J., Wu Q., Lyu X., Sun Z. Optimal switching sequence model predictive control for three-level NPC grid-connected inverters. *IET Power Electronics*, 2021, vol. 14, no. 3, pp. 626-639. doi: https://doi.org/10.1049/pel2.12050.
28. Gu X., Xu W., Zhang G., Chen W., Jin X. Three-Level Inverter-PMSM Model Predictive Current Control Based on the Extended Control Set. *Electronics*, 2023, vol. 12, no. 3, art. no. 557. doi: https://doi.org/10.3390/electronics12030557.
29. Vargas R., Cortes P., Ammann U., Rodriguez J., Pontt J. Predictive Control of a Three-Phase Neutral-Point-Clamped Inverter. *IEEE Transactions on Industrial Electronics*, 2007, vol. 54, no. 5, pp. 2697-2705. doi: https://doi.org/10.1109/TIE.2007.899854.
30. Rodriguez J., Pontt J., Silva C.A., Correa P., Lezana P., Cortes P., Ammann U. Predictive Current Control of a Voltage Source Inverter. *IEEE Transactions on Industrial Electronics*, 2007, vol. 54, no. 1, pp. 495-503. doi: https://doi.org/10.1109/TIE.2006.888802.
31. Rojas D., Rivera M., Munoz J., Baier C., Wheeler P. Predictive Current Control Applied to a 3L-NPC Inverter. *2021 IEEE International Conference on Automation/XXIV Congress of the Chilean Association of Automatic Control (ICA-ACCA)*, 2021, pp. 1-7. doi: https://doi.org/10.1109/ICAACCA51523.2021.9465309.
32. Babes B., Hamouda N., Kahla S., Amar H., Ghoneim S.S.M. Fuzzy model based multivariable predictive control design for rapid and efficient speed-sensorless maximum power extraction of renewable wind generators. *Electrical Engineering & Electromechanics*, 2022, no. 3, pp. 51-62. doi: https://doi.org/10.20998/2074-272X.2022.3.08.
33. Katkout A., Nasser T., Essadki A. An Efficient Model Predictive Current Control Algorithm for Grid-Connected Multi-Level Inverter with Computational Delay Compensation. *2020 International Conference on Electrical and Information Technologies (ICEIT)*, 2020, pp. 1-6. doi: https://doi.org/10.1109/ICEIT48248.2020.9113234.

Received 25.07.2023
Accepted 10.11.2023
Published 02.03.2024

Hamed Kamel Eddine Zine[1]*, PhD Student,*
Khoudir Abed[1]*, PhD, Master of Computer Application,*
[1] Department of Electrical Engineering,
Faculty of Engineering Sciences,
Laboratory of Electrical Engineering of Constantine (LGEC),
Mentouri University, Road Ain El Bey, Constantine, Algeria,
e-mail: kamel-eddine.zine-hamed@lec-umc.org,
khoudir.abed@laposte.net (Corresponding Author)

How to cite this article:
Zine H.K.E., Abed K. Smart current control of the wind energy conversion system based permanent magnet synchronous generator using predictive and hysteresis model. *Electrical Engineering & Electromechanics*, 2024, no. 2, pp. 40-47. doi: https://doi.org/10.20998/2074-272X.2024.2.06

UDC 621.3.022: 621.396.6: 533.93 https://doi.org/10.20998/2074-272X.2024.2.07

M.I. Baranov

Calculation and experimental determination of the speed of advancement of the plasma leader channel of a pulse spark discharge in atmospheric air

Goal. *Calculation and experimental determination of middle speed v_L of advancement of plasma leader channel of a pulse spark discharge in the long air interval of the double-electrode discharge system (DEDS) «tip-plane».* ***Methodology.*** *Bases of the theoretical electrical engineering and electrophysics, electrophysics bases of technique of ultra- and high-voltage and high pulse currents, bases of high-voltage pulse technique and measuring technique.* ***Results.*** *The close calculation and experimental method of determination of middle speed v_L of advancement of plasma leader channel of an electric pulse spark discharge is offered in the long air interval of DEDS «tip-plane». This method is based on the offered calculation empiric formula for finding of the indicated speed v_L and results of decoding of oscillograms of process of cut of in-use standard interconnect aperiodic pulse of over- and high-voltage of temporal shape of T_m/T_d≈200 μs/1990 μs of positive polarity at an electric hasp in indicated DEDS of long air intervals with their minimum length of l_{min}, numeral making 1,5 m (first case) and 3 m (second case). It is shown that middle speed v_L of advancement in atmospheric air of front of plasma channel of positive leader of an electric pulse spark discharge in probed DEDS «tip-plane» for two considered applied cases at l_{min}=1,5 m of l_{min}=3 m numeral makes approximately v_L≈(1±0,03)·10^5 m/s. The found numeral value of this speed v_L well coincides with the known experimental information for speed of advancement of v_L≈10^5 m/s in atmospheric air of plasma channel of negative leader for a long storm spark discharge in DEDS «charged cloud-earth». It is set that for the standard interconnect aperiodic pulse of high- and ultra- voltage of temporal shape of T_m/T_d≈200 μs/1990 μs of positive polarity middle value of aggressive strength E_d of high pulse electric field in the air interval of probed DEDS «tip-plane» numeral makes minimum length of l_{min}=1,5 m near E_{d1}≈360,8 kV/m, and for his minimum length of l_{min}=3 m of − E_{d2}≈313,4 kV/m.* ***Originality.*** *The comfortable is developed in the use and reliable in practical realization technicians-and-engineers calculation and experimental method of research in the conditions of high-voltage electrophysics laboratory of difficult electro-discharge processes of development of leader hasp of long air intervals and determination of minimum electric durability of air insulation of electrical power engineering and electrophysics equipment on working voltage of classes of 330-1150 kV.* ***Practical value.*** *Application in area of industrial electrical power engineering and high-voltage pulse technique of the got numeral electrophysics results and offered calculation and experimental method of determination of middle speed v_L of advancement in atmospheric air of plasma channel of leader of a long spark discharge will allow, from one side, to deepen our scientific knowledges about a long electric pulse spark discharge in an air dielectric, and, from other side, to develop high-voltage electrical power engineering and electrophysics devices with enhanceable reliability of their work both in normal operation and malfunctions.* References 20, figures 5.

Key words: **plasma leader channel, electric pulse spark discharge, air dielectric, advance speed of a spark discharge front, calculation, experiment.**

Надані результати розрахунково-експериментального визначення усередненої швидкості v_L просування плазмового лідерного каналу електричного імпульсного іскрового розряду в довгому повітряному проміжку двоелектродної розрядної системи «вістря-площина» (для двох прикладних випадків при l_{min}=1,5 м і l_{min}=3 м), яка випробовує дію стандартного комутаційного аперіодичного імпульсу високої і надвисокої напруги часової форми T_m/T_d≈200 мкс/1990 мкс позитивної полярності. Запропонований метод чисельної оцінки величини v_L в даній розрядній системі базується на використанні отриманої емпіричної формули та отриманні осцилограм процесу зрізу застосованих імпульсів над- і високої напруги при електричному пробої в ній довгих повітряних проміжків вказаної мінімальної довжини l_{min}. На основі запропонованої наближеної розрахункової формули і виконаних за допомогою потужного надвисоковольтного випробувального обладнання сильнострумових експериментів показано, що вказана швидкість v_L розповсюдження в атмосферному повітрі переднього фронту позитивного лідера імпульсного іскрового розряду чисельно складає v_L≈(1±0,03)·10^5 м/с. Отримані розрахунково-експериментальні дані для усередненої швидкості v_L просування в повітрі лідерного каналу імпульсного іскрового розряду добре узгоджуються з її прийнятими для грозових іскрових розрядів в атмосферному повітрі чисельними показниками. Бібл. 20, рис. 5.

Ключові слова: **плазмовий лідерний канал, електричний імпульсний іскровий розряд, повітряний діелектрик, швидкість просування фронту іскрового розряду, розрахунок, експеримент.**

State-of-the-art and relevance of the problem. In the technique of high (ultra-high) electrical voltages, the real danger for the used electrical equipment is an electrical breakdown of its vacuum, gas, liquid or solid insulation, which is accompanied by the occurrence of a short circuit in the electrical circuit, the formation of a highly conductive spark (arc) channel at the breakdown site and discharge through it of a high pulse current. Air insulation has found a sufficiently wide practical application both in industrial electricity and in the field of high-voltage pulse technology (HPT) intended for scientific and technological purposes [1-6].

It is known that in long air gaps (with lengths of 1 m or more), their electrical breakdown is carried out by the growth from one electrode (for example, from the potential anode) of a high-voltage device to another (for example, to the grounded cathode) of the leader of the electric gas discharge – a thin plasma conductive channel, the degree of ionization of gas molecules (atoms) in which is much higher than in the initial discharge streamer channel [3, 7]. After the head of the leader of the electric discharge, which glows brightly, reaches the opposite electrode-cathode and propagates along the leader channel towards the anode with speed of about v_E≈10^7 m/s, first the return wave of a high electric field (electric potential wave) and then the return wave of the conduction current on site of the leading channel, a strongly ionized discharge spark channel is formed, which glows brightly [3, 7]. Due to the flow of a large pulse

current through this highly conductive channel and intense energy release on its ohmic resistance, the temperature and pressure in it increase sharply, which leads to the expansion of the spark discharge channel with the rapid radial spread of its low-temperature plasma and the formation of a powerful shock wave in the surrounding air environment. Despite the presence of well-known theories of streamer and leader breakdown of air insulation, which have been tested many times in scientific laboratories around the world [1, 3, 7], those related to taking into account the peculiarities of the physics of pulse spark discharge in atmospheric air remain poorly studied issues today regarding its flow in the conditions of action of sharply heterogeneous high pulse electric fields, characteristic for electrotechnical practice, and determination of the speed v_L of the advancement of its plasma leader channel, which is the first to short out the air gaps of electrical discharge systems that are part of various high-voltage devices at breakdown.

The results of mathematical and computer modelling of complex electric discharge processes in various types of dielectrics [1, 3, 8-14], which are aimed at increasing the electrical strength of gas, liquid and solid insulation of high-voltage electrical equipment used in the electric power industry and HPT, do not allow to give answers to the specified above are relevant issues in the field of gas spark discharge electrophysics. The deepening of our scientific knowledge about electric pulse spark discharge in gas insulation (in particular, in long air gaps), which is a complex and complicated electrophysical phenomenon of nature, allows to more rationally develop the designs of many high-voltage electrical engineering and electric power devices with increased reliability of their operation in normal and emergency modes, as well as means of lightning protection both for various aircraft and strategic industrial and technical facilities of ground infrastructure.

The goal of the article is to calculate and experimentally determine the average speed v_L of the advancement of the plasma leader channel of an electrical pulse spark discharge in the long air gap of a two-electrode discharge system «tip-plane».

1. Problem definition. A typical example in the field of HPT of the electric discharge systems with a sharply inhomogeneous high pulsed electric field is a double-electrode discharge system (DEDS) «tip-plane», containing a vertically placed potential electrode in the form of a metal rod 1 with radius r_0 with a pointed lower edge with radius of its curvature $r_c << r_0$ and the grounded electrode in the form of a horizontally located metal plane 2 of unlimited dimensions (Fig. 1). Let the electric potentials of these electrodes 1 and 2 be equal to φ_1 and $\varphi_2=0$, respectively, and homogeneous atmospheric air is placed between them in the interelectrode insulating gap of minimum length $l_{\min}$, equal to the length of the straight line drawn from the tip of the potential electrode 1 along the normal to the flat surface of the grounded electrode 2 under the following physical conditions [15]: gas pressure $P_a \approx (1.013 \pm 0.005) \cdot 10^5$ Pa; absolute gas temperature $T_a \approx (293.15 \pm 5)$ K; relative humidity of gas $\gamma_a \approx (45 \pm 15)$ %.

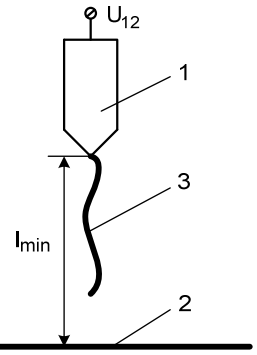

Fig. 1. Schematic representation of the investigated air DEDS, on the example of which the electrophysical process of propagation of the plasma leader channel of a puls spark discharge in atmospheric air is considered (1, 2 − potential and grounded metal electrodes, respectively; 3 − zigzag-shaped leader channel of the spark discharge in the DEDS)

Let's assume that the electrical strength of the interelectrode air gap in the DEDS in relation to the average level of its breakdown voltage E_d of a high pulse electric field for an ultra- and high-voltage pulse supplied to the DEDS is E_{d1} for $l_{\min}=1.5$ m and E_{d2} for $l_{\min}=3$ m. In these two practical cases, the electric potential φ_1 at the edge of the rod with a DEDS tip will acquire critical values equal to φ_{1d1} and φ_{1d2}, respectively. We will limit ourselves to considering the case when the amplitude-time parameters (ATPs) of the electric pulse voltage $U_{12}(t)=(\varphi_1-\varphi_2)$ in the interelectrode air gap of the DEDS change in time t according to the law of the standard switching aperiodic voltage pulse of the time shape $T_m/T_d \approx (250 \pm 50)$ μs/(2500±750) μs of positive polarity with appropriate tolerances [16-18]. Let us point out that it is this temporal shape of high (ultra-high) pulse voltage that is usually used in industrial power engineering and HPT when determining the electrical strength of the internal and external insulation of various high-voltage electrical equipment. On the basis of calculation and experimental data, which relate to the flow of electrophysical processes in the discharge long air gap of the DEDS (see Fig. 1), it is necessary to numerically determine the average speed v_L of the advancement of the positive leader in the plasma channel of the electric pulse spark discharge in the air gap of the investigated DEDS «tip-plane» with the specified two numerical values of its minimum length ($l_{\min}=1.5$ m and $l_{\min}=3$ m).

2. Calculation and experimental estimation of the speed v_L of the advancement of the plasma leader channel of a pulse spark discharge in atmospheric air. The research results of research in the field of electrical breakdown of long air gaps in DEDS «tip-plane» using a standard switching pulse voltage of the time shape $T_m/T_d \approx 200$ μs/1990 μs of positive polarity indicate that the development in them of the plasma leader channel of high-voltage pulse of a spark discharge occurs along a zigzag path, the length of which l_c always exceeds their minimum length $l_{\min}$ with the obligatory fulfillment of the inequality of the form $l_c \geq 1.1 l_{\min}$ [1, 3, 17-19]. When the minimum length $l_{\min}$ of their discharge intervals is changed in the indicated air DEDS in the range

l_{min} ≈(1−4) m, the given difference between the lengths l_c and l_{min} is from 10 to 15 % [17-19]. For the certainty of further calculation estimations of the averaged value of the sought parameter v_L, let's focus on the case in which this difference between the lengths l_c and l_{min} turns out to be approximately 13 % on average, and the ratio l_c/l_{min} is numerically close to l_c/l_{min}≈1.13. Taking into account this research result, the formula for an approximate estimation of the average speed v_L of the advancement of the plasma leader channel of a high-voltage electrical pulse spark discharge in the atmospheric air of the adopted DEDS «tip-plane» at l_{min}≈(1−4) m takes the following empirical form:

$$v_L \approx 1{,}13 l_{min} / T_{dc}, \quad (1)$$

where T_{dc} is the duration of the cut of the voltage pulse, which causes an electrical breakdown of a long air gap in the DEDS «tip-plane» under study, the minimum length of which is numerically l_{min}≥1 m.

In (1), the numerical value of the parameter l_{min}≥1 m for the «tip-plane» aerial DEDS is selected by the personnel of the test team and fixed by the appropriate measuring instrument (a long metric ruler) experimentally, and the numerical value of the duration of the cut T_{dc} of the voltage pulse is determined by deciphering its oscillograms in the process of electrical breakdown of the air gap in the DEDS with length l_{min} using a digital storage oscilloscope and an ultra-high-voltage ohmic voltage divider (OVD). The use of this type of ultra-high voltage divider in the case under consideration by us is due to the relative simplicity of its manufacture and the relatively low cost of the electrical components included in its composition [18, 20].

The use of the T_{dc} value in (1) is explained by the physical condition that this duration of the cut T_{dc} of the pulse of high (ultra-high) pulse voltage applied to the air DEDS characterizes the time of shortening along the air path of the real length l_c by the conducting plasma leader channel of the selected electric pulse spark discharge air gap in this DEDS with its minimum length l_{min} and, accordingly, the time of equalization of electric potentials (φ_1≈φ_2≈0) on the electrodes of the DEDS we are investigating.

Figure 2 shows the general view of the investigated DEDS «tip-plane» with a long discharge air gap of length l_{min}=3 m, which was galvanically connected to a high-current discharge electric circuit of an ultra-high-voltage generator of standard switching aperiodic voltage pulses of the time shape T_m/T_d≈200 μs/1990 μs of positive (negative) polarity, developed and created at the Research and Design Institute «Molniya» of National Technical University «Kharkiv Polytechnic Institute» [17, 18].

Figure 3 shows an experimental oscillogram of a complete standard switching aperiodic voltage pulse of the time shape T_m/T_d ≈200 μs/1990 μs of positive polarity, which acts in the discharge circuit of the specified ultra-high-voltage test generator [17, 18] on the air DEDS «tip-plane» we are investigating without an electrical breakdown of its long air space of length l_{min}=3 m.

Fig. 2. General view of the ultra-high-voltage air DEDS «tip-plane» (l_{min}=3 m), in which to the potential upper steel rod electrode pointed at the lower edge with radius r_0≈15 mm, placed in the center of its grounded lower flat electrode made of galvanized steel with overall dimensions of 5×5 m, OPN-2,5 for nominal electrical pulse voltage of 2.5 MV with the division coefficient K_d≈53650 is connected [18]

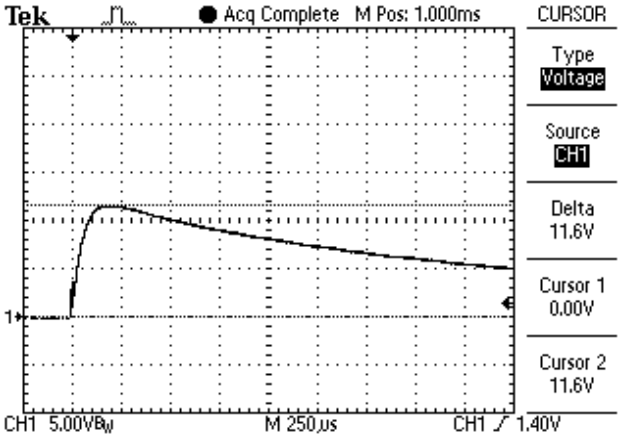

Fig. 3. Oscillogram of a complete switching aperiodic high-voltage pulse of the time shape T_m/T_d ≈200 μs/1990 μs of positive polarity without electrical breakdown of a long air gap of length l_{min}=3 m in the DEDS «tip-plane» (U_{mc}≈11.6 V × 53650≈622.3 kV – high voltage pulse amplitude; T_m≈200 μs – time of rise of the voltage pulse to U_{mc} amplitude; T_d≈1990 μs – duration of the voltage pulse at the level of 0.5 U_{mc}; vertical scale – 268.2 kV/div; horizontal scale – 250 μs/div)

Figure 4 shows the experimental oscillogram of the standard switching aperiodic high-voltage pulse T_m/T_d≈200 μs/1990 μs used in the experiments cut off on the rising part with an electrical breakdown of a long air discharge gap in the DEDS «tip-plane» with minimum length l_{min}=1.5 m, ATPs of which was determined according to the requirements of the current Standard [16].

Using obtained according to Fig. 4 research numerical data for the cut-off duration T_{dc}≈17 μs of the corresponding high-voltage pulse (for the case where U_{mcd}≈611.6 kV) in the considered air DEDS (l_{min}=1.5 m) from (1) for the averaged speed v_L of the advancement of the plasma leader channel of a pulse spark discharge in the atmospheric air of its specified long discharge interval results that v_L≈0.997·10^5 m/s. At a given speed v_L of

propagation in the atmospheric air of the positive leader of a pulse spark discharge, the actual path length l_c through it in the interelectrode air gap of the DEDS (l_{min}=1.5 m) at its electrical breakdown (T_{dc}≈17 μs) by the applied high-voltage pulse is numerically $l_c \approx v_L T_{dc} \approx 1.695$ m. We can see that in this case, the real length l_c of the development path of the leader channel of the spark discharge in the studied DEDS exceeds the minimum length l_{min}=1.5 m of its discharge air gap by approximately 13 %.

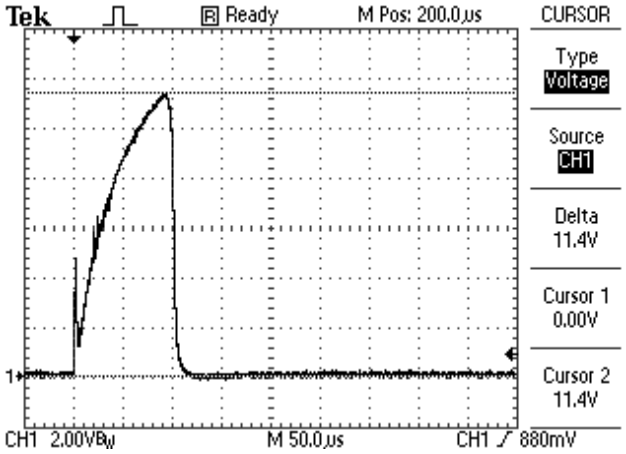

Fig. 4. Oscillogram of a truncated standard high-voltage switching aperiodic pulse of the time shape T_m/T_d ≈200 μs/1990 μs of positive polarity at electrical breakdown of a long air gap of length l_{min} =1.5 m in the DEDS «tip-plane» (U_{mcd}≈11.4 V × 53650≈611.6 kV – pulse cut-off voltage level; T_c ≈95 μs – cut-off time of the voltage pulse; T_{dc}≈17 μs – duration of the cut (commutation) of the voltage pulse; vertical scale – 107.3 kV/div; horizontal scale – 50 μs/div)

Note that at the rate of increase of the pulse voltage $U_{12}(t)$, which is applied to the discharge gap of the air DEDS, equal to $dU_{12}(t)/dt \geq 5$ kV/μs (as in our electrophysical cases), the development of the positive leader in atmospheric air occurs continuously (without stepwise formation of separate plasma leader channels in DEDS) [3]. With this process of advancement of the positive discharge leader in the air, the length l_c of its plasma channel in this DEDS will monotonically increase (see Fig. 1).

To compare the numerical result obtained above for the average speed v_L of the positive leader, which is characteristic of the electric discharge processes that occur under laboratory conditions in the air DEDS «tip-plane» with its long discharge gap (l_{min}=1.5 m), we note that according to [7], the smallest average speed v_L of the advance in the atmospheric air of the front of the negative leader of a long spark discharge between the thundercloud and the surface of the earth (lightning) is quantitatively about $v_L \approx 10^5$ m/s. As we can see, the experimental result obtained in laboratory conditions using this DEDS at l_{min} = 1.5 m and a standard switching aperiodic ultra-high voltage pulse of the time shape T_m/T_d ≈200 μs/1990 μs of positive polarity approximated taking into account (1) the calculated and experimental result for the averaged the speed $v_L \approx 0.997 \cdot 10^5$ m/s of advancement in atmospheric air of the plasma leader channel of a pulse spark discharge is practically equal to its quantitative value accepted in the field of physics of atmospheric electricity (lightning) and electrophysics of ultra-high voltages ($v_L \approx 10^5$ m/s [7]).

It should be noted that when performing ultra- and high-voltage experiments using the «tip-plane» air DEDS under investigation (see Fig. 2) and the results obtained by us for long discharge air gaps (l_{min}=1.5 m and l_{min}=3 m) experimental results according to Fig. 4, 5, both an ohmic voltage divider of the OPN-2,5 type (K_d ≈53650) [18] and a Tektronix TDS 1012B digital oscilloscope certified by the State Metrological Service, which stores useful electrical signals (calibration certificate UA01 No. 1312 dated 29.06. 2023) were used.

Figure 5 shows an oscillogram of an ultra-high-voltage standard switching aperiodic voltage pulse T_m/T_d ≈200 μs/1990 μs cut off on the frontal part used in the laboratory high-current experiments performed by us with an electrical breakdown of a long air discharge gap in the studied DEDS «tip-plane» with minimum length l_{min}=3 m.

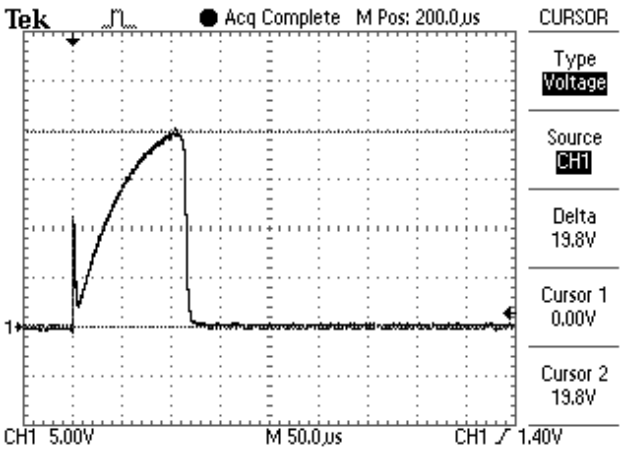

Fig. 5. Oscillogram of a truncated standard switching aperiodic ultra-high voltage pulse of the time shape T_m/T_d ≈200 μs/1990 μs of positive polarity during an electrical breakdown of a long air gap of length l_{min}=3 m in a «tip-plane» DEDS (U_{mcd}≈19.8 V × 53650 ≈1062.3 kV – voltage pulse cut-off level; T_c≈104 μs – voltage pulse cut-off time; T_{dc}≈33 μs – voltage pulse cut-off (commutation) duration; vertical scale – 268.2 kV/div; horizontal scale – 50 μs/div)

Let us point out that the presence of peak-like bursts shown in presented in Fig. 4, 5 oscillograms of truncated voltage pulses (at first their frontal parts) are related to the structural features of the construction of the ultra-high-voltage generator of the GIN-4 type [17, 18] used in the circuit for the formation of aperiodic voltage pulses used by us, which has a massive steel screen-roof with an area of about 60 m^2. The rapid charge and discharge of the electric capacity of this screen-roof GIN-4 causes the appearance of the indicated voltage peaks. These peak-like voltage surges cannot affect the development of electric discharge processes in our DEDS.

According to the research data (Fig. 5), in the case of an electrical breakdown of a long air gap in the investigated DEDS «tip-plane» (l_{min}=3 m), the duration of the cut-off T_{dc} at the front of the ultra-high-voltage (U_{mcd}≈1062.3 kV) standard switching aperiodic voltage

pulse T_m/T_d ≈200 μs/1990 μs of positive polarity takes a numerical value equal to approximately T_{dc}≈33 μs. We see that with a doubling (from 1.5 m to 3 m) of the minimum length $l_{\min}$ of the air discharge gap in the «tip-plane» DEDS, the duration of the cut-off T_{dc} on the rising part of the used test voltage pulse $U_{12}(t)$ almost doubles (approximately from 17 μs to 33 μs according to the data of experimental oscillograms in Fig. 4, 5). These experimental results indicate that the average speed v_L of the advancement of the plasma leader channel of a pulsed spark discharge in the atmospheric air of the studied DEDS «tip-plane» with a sharply inhomogeneous high pulse electric field when the minimum length $l_{\min}$ in it changes in the range of $l_{\min}$=(1.5–3) m practically does not depend on the length of the long air gap electrically broken in this DEDS by a high or ultra-high pulse voltage $U_{12}(t)=(\varphi_1-\varphi_2)$, which at $l_{\min}$=1.5 m takes a numerical value of about U_{mcd} ≈611.6 kV (see Fig. 4), and at $l_{\min}$=3 m – approximately U_{mcd}≈1062.3 kV (see Fig. 5). Concrete confirmation of this is the fact that in the used air DEDS «tip-plane» ($l_{\min}$=3 m), which tests the effect of a standard switching aperiodic voltage pulse of the time shape T_m/T_d≈200 μs/1990 μs, the average speed v_L of advancement in atmospheric air of the plasma channel of the positive leader of a pulsed spark discharge taking into account the empirical formula (1) at $l_{\min}$=3 m and T_{dc}≈33 μs is numerically about v_L≈1.03·10^5 m/s. This quantitative value for v_L (at $l_{\min}$=3 m in air DEDS) differs by no more than 3 % from the one previously obtained by us on the basis of the calculation and experimental method proposed here for the quantitative determination of the average speed v_L of the advancement in air of the positive leader of a long spark discharge during electrical breakdown in the same DEDS of the discharge air gap with a minimum length $l_{\min}$=1.5 m of the numerical value for v_L, which is approximately v_L≈0.997·10^5 m/s. The actual path length l_c of advancement in the interelectrode gap of the air DEDS of the positive leader of the spark discharge in this case ($l_{\min}$=3 m; T_{dc}≈33 μs; v_L≈1.03·10^5 m/s) will be numerically equal to about $l_c\approx v_L T_{dc}$≈3.399 m, which is approximately 13 % higher than the specified minimum length $l_{\min}$=3 m of the discharge air gap in the «tip-plane» DEDS under study. At a significantly lower speed v_L of the advancement of the positive leader of the discharge in the air, the «tip-plane» DEDS (for example, at v_L≈1.5·10^4 m/s, see Fig. 5.36 in [3]), in which the electrical breakdown of its discharge gaps ($l_{\min}$=1.5 m and $l_{\min}$=3 m) is also determined by the supply to its corresponding electrodes of a standard high (U_{mcd}≈611.6 kV) or ultra-high (U_{mcd}≈1062.3 kV) switching aperiodic pulse voltages of the time shape T_m/T_d ≈200 μs/1990 μs of positive polarity, for the actual numerical values of the duration of their cut-off T_{dc} recorded by us (respectively equal to ~17 μs and ~33 μs according to the data of Fig. 4, 5) passing through it (a similar positive leader of the charge) of the indicated real paths of length $l_c\approx v_L T_{dc}$ (in the first case for l_c≈1.695 m, and in the second one l_c≈3.399 m) becomes fundamentally impossible. At the specified speed v_L≈1.5·10^4 m/s [3], for the passage by such a discharge leader of the used lengths $l_c>l_{\min}$, T_{dc} values will be required, which should numerically be at least (110-220) μs, which will contradict the conditions and realities of our ultra-high-voltage experiments. In this regard, the known experimental data given in [7] (see Table 17.2) for the lowest average speed v_L≈10^5 m/s of the advancement of the negative lightning leader in the atmospheric air are more reliable. The physics of the development of leader breakdown of long air gaps in both natural and laboratory conditions, despite the significant difference in the levels of ultra-high voltage $U_{12}(t)$, at $dU_{12}(t)/dt\geq 5$ kV/μs should remain the same. The data obtained with the help of the proposed calculationl and experimental method for the average speed v_L of advancement in the atmospheric air of the positive leader of the pulse spark discharge in the DEDS «tip-plane» at $l_{\min}$=(1.5–3) m complement and clarify the little-studied electrophysical features of the mechanisms of manifestation in the world of leader breakdown of long air gaps in the used DEDS «tip-plane» with a sharply inhomogeneous high pulse electric field.

Taking into account the approximate numerical data for v_L presented in this work and the minimum measurement error of the ATPs used in the conducted experiments with the air DEDS «tip-plane» of standard switching aperiodic pulses of ultra- and high-voltage of the time shape T_m/T_d≈200 μs/1990 μs of positive polarity, which is at least 3 % [16, 17, 20], it can be assumed that the average speed v_L of the advancement in the atmospheric air of this DEDS of the leading front of the positive leader in the plasma channel of the pulse spark discharge is numerically about v_L≈(1±0.03)·10^5 m/s.

3. Calculation and experimental estimation of the short-term electrical strength of long air gaps. Here it is important to emphasize that the electrical strength of air insulation in the power industry and HPT is determined and selected based on the effect on it of the following two forms of ultra- and high-voltage pulses [1, 3, 16]: first, a standard switching aperiodic pulse; secondly, a standard oscillating decaying sinusoidal pulse. Obtaining similar data for long air gaps (for $l_{\min}$=(1–10) m) at pulse voltage level $U_{12}(t)$=(1–5) MV is associated with great technical difficulties and material costs. In this case, it is necessary to reliably protect both the main electrical devices of the ultra-high-voltage test electrical equipment itself and the external power supply devices connected to it from electrical surges [1, 2]. In addition, at the same time, it is necessary to provide for special measures both for safety and to prevent possible electrical breakdowns in the insulation of used electrical devices [1, 3, 17]. In this regard, the calculation and experimental results, which are presented above for the ultra-high-voltage air DEDS «tip-plane», which belongs to one of the main basic discharge systems [1, 3], may have a certain applied value when choosing in the field of industrial electric power and HPT of the minimum levels of discharge electric voltages and breakdown field strengths E_d of a strong pulse electric field for long air gaps.

Taking into account the empirical formula (1), for the averaged value of the breakdown field strengths E_d of a high electric field in the long air gaps of the investigated «tip-plane» DEDS, the following calculation relationship can be written:

$$E_d \approx \varphi_{1d}/(1{,}13 l_{\min}), \qquad (2)$$

where φ_{1d} is the electric potential at the edge of the upper electrode in the studied DEDS in case of electrical breakdown of its discharge air gap, which is characterized by its minimum length l_{min}.

In the applied case 1, when l_{min}=1.5 m, from (2) at $\varphi_{1d}\approx\varphi_{1d1}\approx U_{mcd}\approx$611.6 kV (see Fig. 4) for the average breakdown field strength level $E_d=E_{d1}$ of a high pulse electric field in the indicated long air gap of the DEDS «tip-plane» we get a numerical value approximately equal to $E_{d1}\approx$360.8 kV/m. For the applied case 2 with l_{min}=3 m and $\varphi_{1d}\approx\varphi_{1d2}\approx U_{mcd}\approx$1062.3 kV (see Fig. 5) from (2), we find that the average value of the breakdown field strength $E_d=E_{d2}$ of a high pulse electric field in this long air gap of this DEDS is numerically close to $E_{d2}\approx$313.4 kV/m. As we can see, with an increase (by a factor of 2 from 1.5 m to 3 m) in the studied DEDS with a sharply inhomogeneous high pulse electric field of the minimum length l_{min} of its discharge air gap, the average value of the breakdown field strength E_d in it decreases (by approximately 13.1 % from 360.8 kV/m to 313.4 kV/m). These calculation and experimental results for the averaged breakdown field strength E_d of a high pulse electric field in the air DEDS «tip-plane» at l_{min}=(1.5–3) m are in good agreement with the data known in the field of electric power, which relate to the minimum electrical strength of air gaps of length l_{min}=(1–4) m [1-3].

Conclusions.

1. An approximate calculation and experimental method for determining the average speed v_L of the advancement of the plasma leader channel of an electrical pulse spark discharge in the long air gap of the «tip-plane» DEDS is proposed. This method is based on the proposed empirical formula and experimental data for the duration of the cut (commutation) T_{dc} of the breakdown voltage pulses, obtained from the results of deciphering the oscillograms of the process of the cut of the standard switching aperiodic ultra- and high-voltage pulse of the time shape $T_m/T_d\approx$200 μs/1990 μs of positive polarity in the event of an electrical breakdown in the specified DEDS of long air gaps with their minimum length l_{min}, which varies discretely in the range l_{min}=(1.5-3) m.

2. It is shown that the average speed v_L of the advancement in the atmospheric air of the front of the plasma channel of the positive leader of the electric pulse spark discharge in the investigated DEDS «tip-plane» for the two considered applied cases at l_{min}=1.5 m and l_{min}=3 m is numerically approximately equal to $v_L\approx(1\pm0.03)\cdot10^5$ m/s. Our numerical result for v_L is in good agreement with the known experimental data for the speed $v_L\approx10^5$ m/s in the atmospheric air of the plasma channel of the negative leader for a long thunderstorm spark discharge in the «charged cloud-to-ground» DEDS.

3. It was established by calculation and experiment that for a standard switching aperiodic pulse of high- and ultra-high voltage of the time shape $T_m/T_d\approx$200 μs/1990 μs of positive polarity, the average value of the breakdown field strength E_d of a high pulse electric field in the long air gap of the studied DEDS «tip-plane» with minimum length l_{min}=1.5 m is numerically about $E_{d1}\approx$360.8 kV/m, and for its minimum length l_{min}=3 m − $E_{d2}\approx$313.4 kV/m. The obtained results for E_d correlate well with the known data for the minimum electrical strength of air gaps of length l_{min}=(1–4) m in the studied air DEDS «tip-plane».

Acknowledgment. The work was carried out with the support of the Ministry of Education and Science of Ukraine (project DB No. 0123U101704).

Conflict of interest. The author declares no conflict of interest.

REFERENCES

1. Brzhezitsky V.O., Biliy I.V., Boiko M.I., Gul' V.I., Gurin A.G., Il'enko O.S., Isakova A.V., Kondra B.M., Kopshin V.O., Kravchenko V.I., Naboka B.G., Protsenko O.R., Rudakov V.V., Khymenko L.T., Khominich V.I., Shostak V.O., Yanishevsky V.I. *Technique and Electrophysics of High Voltages*. Kharkiv, NTU «KhPI», Tornado Publ., 2005. 930 p. (Ukr).

2. Knopfel' G. *Ultra strong pulsed magnetic fields*. Moscow, Mir Publ., 1972. 391 p. (Rus).

3. Bortnik I.M., Beloglovskiy A.A., Vereshchagin I.P., Vershinin Yu.N., Kalinin A.V., Kuchinskiy G.S., Larionov V.P., Monastyrskiy A.E., Orlov A.V., Temnikov A.G., Pintal' Yu.S., Sergeev Yu.G., Sokolova M.V. *Electrophysics bases of HV technique*. Moscow, Publ. House of MEI, 2010. 704 p. (Rus).

4. Baranov M.I. A choice of sections of electric wires and cables in circuits of devices of high-voltage high-current impulse technique. *Electrical Engineering & Electromechanics*, 2018, no. 6, pp. 56-62. doi: https://doi.org/10.20998/2074-272X.2018.6.08.

5. Baranov M.I., Rudakov S.V. Electrothermal Action of the Pulse of the Current of a Short Artificial-Lightning Stroke on Test Specimens of Wires and Cables of Electric Power Objects. *Journal of Engineering Physics and Thermophysics*, 2018, vol. 91, no. 2, pp. 544-555. doi: https://doi.org/10.1007/s10891-018-1775-2.

6. Vovchenko A.I., Bohuslavsky L.Z., Myroshnychenko L.N. Trends in development of high-powered high-voltage pulse current generators in the Institute of Pulse Processes and Technology of Ukraine (review). *Technical electrodynamics*, 2010, no. 5, pp. 69-74. (Rus).

7. Rayzer Yu.P. *Physics of gas discharge*. Moscow, Nauka Publ., 1987. 592 p. (Rus).

8. Niemeyer L., Pietronero L., Wiesmann H.J. Fractal Dimension of Dielectric Breakdown. *Physical Review Letters*, 1984, vol. 52, no. 12, pp. 1033-1036. doi: https://doi.org/10.1103/PhysRevLett.52.1033.

9. Wiesmann H.J., Zeller H.R. A fractal model of dielectric breakdown and prebreakdown in solid dielectrics. *Journal of Applied Physics*, 1986, vol. 60, no. 5, pp. 1770-1773. doi: https://doi.org/10.1063/1.337219.

10. Hussein A.M., Janischewskyj W., Chang J.-S., Shostak V., Chisholm W.A., Dzurevych P., Kawasaki Z.-I. Simultaneous measurement of lightning parameters for strokes to the Toronto Canadian National Tower. *Journal of Geophysical Research: Atmospheres*, 1995, vol. 100, no. D5, pp. 8853-8861. doi: https://doi.org/10.1029/95JD00543.

11. Xia Y., Liu D., Wang W., Bi Z., Wang X., Niu J., Ji L., Song Y., Qi Z. Effects of previous ionization and excitation on the ionization wave propagation along the dielectric tube. *Journal of Physics D: Applied Physics*, 2016, vol. 49, no. 16, art. no. 165202. doi: https://doi.org/10.1088/0022-3727/49/16/165202.

12. Kebbabi L., Beroual A. Fractal analysis of creeping discharge patterns propagating at solid/liquid interfaces: influence of the nature and geometry of solid insulators. *Journal of Physics D: Applied Physics*, 2006, vol. 39, no. 1, pp. 177-183. doi: https://doi.org/10.1088/0022-3727/39/1/026.

13. Hu H.M., Yang Y., Lu W., Zhao G.P. Electrical Tree Simulation Based on the Self-Organization Criticality. *Energy*

and Power Engineering, 2013, vol. 5, no. 4, pp. 1273-1276. doi: https://doi.org/10.4236/epe.2013.54B241.
14. Xiong Z., Robert E., Sarron V., Pouvesle J.-M., Kushner M. J. Dynamics of ionization wave splitting and merging of atmospheric-pressure plasmas in branched dielectric tubes and channels. *Journal of Physics D: Applied Physics*, 2012, vol. 45, no. 27, art. no. 275201. doi: https://doi.org/10.1088/0022-3727/45/27/275201.
15. Kuhling H. *Handbook of Physics*. Moscow, Mir Publ., 1982. 520 p. (Rus).
16. *Standard GOST 1516.2-97. Electrical equipment and installations for a.c. voltages 3 kV and higher. General methods of dielectric tests*. Minsk, Intergovernmental Council of Standardization, Measuring and Certification Publ., 1997. 31 p. (Rus).
17. Baranov M.I., Koliushko G.M., Kravchenko V.I. A switching aperiodic superhigh-voltage pulse generator for testing the electric strength of insulation of technical objects. *Instruments and Experimental Techniques*, 2013, vol. 56, no. 6, pp. 653-658. doi: https://doi.org/10.1134/S0020441213050126.
18. Baranov M.I., Koliushko G.M., Kravchenko V.I. Generation of standard switching aperiodic impulses of high and superhigh voltage for full-scale tests of electrical power objects. *Electrical Engineering & Electromechanics*, 2013, no. 2, pp. 52-56. (Rus). doi: https://doi.org/10.20998/2074-272X.2013.2.10.
19. Baranov M.I. *Selected topics of Electrophysics. Monograph in 4 Vols. Vol. 4. Effects of interaction of physical bodies with fields and currents*. Kharkiv, FOP Panov A.N. Publ., 2023. 552 p. (Ukr).
20. Baranov M.I., Buriakovskyi S.G., Rudakov S.V. The metrology support in Ukraine of tests of objects of energy, aviation and space-rocket engineering on resistibility to action of pulses of current (voltage) of artificial lightning and commutation pulses of voltage. *Electrical Engineering & Electromechanics*, 2018, no. 5, pp. 44-53. doi: https://doi.org/10.20998/2074-272X.2018.5.08.

Received 30.09.2023
Accepted 16.11.2023
Published 02.03.2024

M.I. Baranov[1], *Doctor of Technical Science*, *Chief Researcher,*
[1] Research and Design Institute «Molniya»
of National Technical University «Kharkiv Polytechnic Institute»,
47, Shevchenko Str., Kharkiv, 61013, Ukraine,
e-mail: baranovmi49@gmail.com (Corresponding Author)

How to cite this article:
Baranov M.I. Calculation and experimental determination of the speed of advancement of the plasma leader channel of a pulse spark discharge in atmospheric air. *Electrical Engineering & Electromechanics*, 2024, no. 2, pp. 48-54. doi: https://doi.org/10.20998/2074-272X.2024.2.07

UDC 621.318: 539.3 https://doi.org/10.20998/2074-272X.2024.2.08

D.V. Lavinsky, Yu.I. Zaitsev

Computational studies of electromagnetic field propagation and deforming of structural elements for a thin-walled curved workpiece and an inductor

Introduction. *At the present stage of industrial development, the electromagnetic field is widely used in various technological processes. The force effect of an electromagnetic field on conductive materials is used in a class of technological operations called electromagnetic forming.* ***Problem.*** *Under the conditions of electromagnetic forming, the main element of the technological equipment – the inductor – is simultaneously subjected to the force impact with the workpiece. At certain levels of the electromagnetic field, the deformation of the inductor becomes so significant that it can lead to a loss of its efficiency.* ***Goal.*** *Computational analysis of a thin-walled curved workpiece and a two-turn inductor under the conditions of electromagnetic processing of the workpiece corner zone. Determining the distribution of quantitative characteristics of the electromagnetic field and the stress-strain state and conducting assessments based on them regarding the efficiency of the technological operation.* ***Methodology.*** *Computational modeling using the finite element method as a method of numerical analysis. The* ***results*** *on the distribution of quantitative characteristics of the electromagnetic field and components of the stress-strain state for a thin-walled workpiece and an inductor are obtained. It is shown that for the specified characteristics of the technological operation, the inductor remains operational, and plastic deformations occur in the workpiece. A series of calculations were carried out, in which some parameters of the technological system were varied.* ***Originality.*** *For the first time, the results of the calculation analysis of the quantitative characteristics distribution of the electromagnetic field of the deformation process for the «inductor – thin-walled curved workpiece» system are presented.* ***Practical value.*** *The presented design scheme of a curved thin-walled workpiece and a two-turn inductor, the method of calculation analysis and some obtained results can be used in the analysis of electromagnetic processing of thin-walled structures that contain curved elements.* References 16, table 1, figures 6.

Key words: **computational analysis, electromagnetic field, electromagnetic forming, deformation, finite element method.**

Вступ. *Електромагнітне поле на сучасному етапі розвитку промисловості широко використовують у різних технологічних процесах. Силовий вплив електромагнітного поля на провідникові матеріали використовується в класі технологічних операцій, що називається електромагнітним формуванням.* ***Проблема.*** *За умов електромагнітного формування силовому впливу одночасно із заготовкою піддається і основний елемент технологічного обладнання – індуктор. При певних рівнях електромагнітного поля деформування індуктора стає настільки значним, що може приводити до втрати його працездатності.* ***Мета.*** *Проведення розрахункового аналізу тонкостінної вигнутої заготовки та двовиткового індуктора за умов електромагнітної обробки кутової зони заготовки. Визначення розподілу кількісних характеристик електромагнітного поля і напружено-деформованого стану та проведення на їх основі оцінок стосовно ефективності технологічної операції.* ***Методологія.*** *Розрахункове моделювання із використанням методу скінченних елементів в якості методу чисельного аналізу. Одержані* ***результати*** *з розподілу кількісних характеристик електромагнітного поля та компонентів напружено-деформованого стану для тонкостінної заготовки та індуктора. Показано, що для заданих характеристик технологічної операції індуктор залишається працездатним, а у заготовці виникають пластичні деформації. Проведено серію розрахунків, у яких варіювалися деякі параметри технологічної системи.* ***Оригінальність.*** *Вперше представлено результати розрахункового аналізу з розподілу кількісних характеристик електромагнітного поля процесу деформування для системи «індуктор – тонкостінна вигнута заготовка».* ***Практичне значення.*** *Представлена розрахункова схема вигнутої тонкостінної заготовки та двовиткового індуктора, використаний метод розрахункового аналізу та деякі отримані результати можуть використовуватися при аналізі електромагнітної обробки тонкостінних конструкцій, які містять вигнуті елементи.* Бібл. 16, табл. 1, рис. 6.

Ключові слова: **розрахунковий аналіз, електромагнітне поле, електромагнітна обробка, деформування, метод скінченних елементів.**

Introduction. Electromagnetic field (EM-field) energy is widely used in various modern technological operations. The force effect of the EM-field is used in a class of technological operations traditionally called electromagnetic forming (EMF). A fairly complete overview of the current state of issues related to the classification of various technological operations of the EMF is presented in works [1, 2]. In general, the standard EMF technological operation can be characterized as follows: the using of the EM-field energy to influence a conductive workpiece with the aim of plastically changing its shape. It should be noted that non-traditional directions of the EMF are currently being developed. The basic questions of some modern trends in the development of EMF technologies are presented in articles [3-5].

Currently, thin-walled structural elements are widely used in various branches of mechanical engineering. Very often such structural elements have a pre-produced curvature. Usually, the necessary curved structural elements are manufactured in two stages: in the first stage, they reach the required general (overall) dimensions and shape, in the second stage they achieve the required quality directly in the corner zone. Part of the technological operations of EMF is aimed at creating conditions for the occurrence of residual deformations in curved thin-walled metal workpieces directly in the corner zone. This zone can be called the «target zone» of the technological operation. This group of technological operations was named technological operations of «filling corners». In practice, it means the reduction of rounding radii to acceptable values in the bending zones of thin-walled workpieces. From the point of view of the conditions of the technological operation, it is necessary to exert the maximum force around the «target zone». In works [6, 7], it is proposed to use an inductor with two turns, which have one common current line directed along the bend, to «fill the corners» on thin-walled curved

workpieces, each of the turns is a plane that makes an angle of up to 15° with the wall of the workpiece.

At the modern stage of development, the design of new technological operations of the EMF and the improvement of existing ones is impossible without computer modeling and computational studies. Creating calculation models that are closest to reality is impossible without the use of numerical methods. The most popular is the finite element method (FEM), which allows, within the same design model, to perform a computational analysis of various physical processes. This is especially important in the case of analyzing EMF technological systems, since here it is very important to study the processes of workpiece deforming. As an example of a computational analysis of EMF processes using FEM, works [8-12] can be considered.

Note that in most cases, the object of study when analyzing deforming is the workpiece. At the same time, the main element generating the EM-field, the inductor, is also subject to intense force action. Under certain conditions, the deforming of the inductor can become quite intense and lead to its destruction. Therefore, from our point of view, analysis of the inductors deforming under the conditions of technological operations of the EMF is also an important task.

The goal of the paper is the computational analysis of the EM-field distribution under the conditions of the «filling corners» technological operation of a thin-walled curved workpiece and determination of the stress-strain state (SSS) components of the inductor and the workpiece for the assess the effectiveness of this technological operation.

Mathematical formulation of the problem. The effectiveness of the EMF technological operation can be considered achieved if, on the one hand, the inductor remains operational, and on the other hand, an irreversible change in the shape of the workpiece is achieved. If we conduct a computational analysis, then we must determine the presence or absence of plastic deformation zones in the inductor and the workpiece. Thus, it is necessary to obtain the distribution of quantitative characteristics of the EM-field and then solve the problem of elastic-plastic deformation.

The solution to this problem must be based on a correct mathematical formulation. The complete mathematical formulation of the problem of the EM-field quantitative characteristics distribution and further elastic-plastic deforming of systems of conductive bodies is presented in work [13].

Figure 1 shows a design diagram of a curved thin-walled workpiece and a two-turn inductor designed to concentrate the force in the rounding zone (this is where plastic deformations should occur).

The problem of numerical EMF calculation was considered under the assumption of a plane-parallel distribution of the field. Physically, this assumption is valid for the case when the length of the workpiece and the inductor along the z coordinate is significantly (several times) larger than the dimensions along the other two coordinates. The formulation of the problem in this assumption allows not paying attention to specific ways of closing the turns of the current conductor of the inductor.

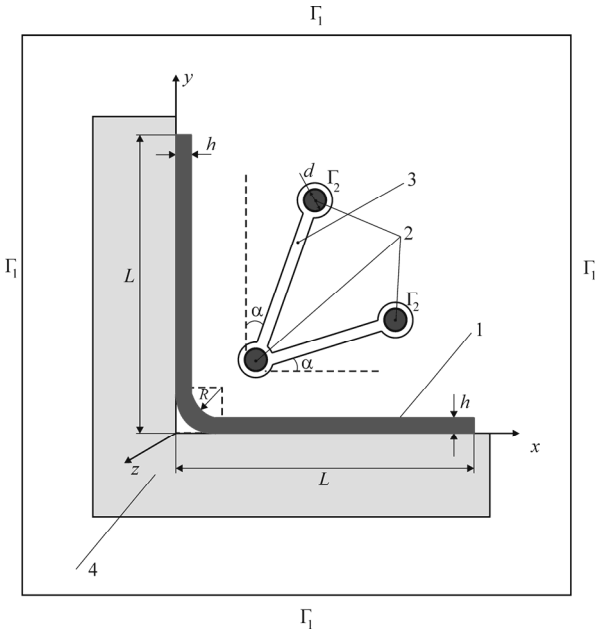

Fig. 1. Design diagram of a curved workpiece together with a two-turn inductor and a dielectric mold: 1 – workpiece; 2 – turns of the current conductor of the inductor; 3 – inductor insulation; 4 – dielectric mold

As in work [13], the resolving equation for the EM-field is formulated with respect to the vector magnetic potential $\vec{A}$. In the setting of the plane-parallel distribution, the vector magnetic potential has only one non-zero component: $\vec{A} = (0, 0, A_Z)$; $A_Z = A$. This also applies to the current density vector $\vec{j}$. The magnetic field intensity and magnetic induction instead have two non-zero components, in the chosen coordinate system: $\vec{H} = (H_x, H_y, 0)$; $\vec{B} = (B_x, B_y, 0)$; $\vec{B} = \mu_a \vec{H}$, where $\mu_a = \mu_0\mu_r$, $\mu_0 = 4\pi\cdot10^{-7}$ H/m is the magnetic constant, μ_r is the relative magnetic permeability of the system elements material. The defining equation for the non-zero component of the vector magnetic potential in this case takes the form (in the case of a material with constant magnetic permeability μ_a and constant specific electrical conductivity γ):

$$\frac{\partial^2 A}{\partial x^2}+\frac{\partial^2 A}{\partial y^2}-\mu_a\gamma\frac{\partial A}{\partial t}=-\mu_a j(t). \qquad (1)$$

At the same time, the components of the magnetic induction vector can be found as follows:

$$B_x=\frac{\partial A}{\partial y};\ B_y=-\frac{\partial A}{\partial x}.$$

We use initial and boundary conditions:

$$A(0)=0;\ A\big|_{\Gamma_1}=0, \qquad (2)$$

where Γ_1 is the boundary of the calculation area, on which the EM-field attenuation conditions must be met.

The variational formulation of the problem requires the determination of the stationarity of the functional, which has the form:

$$MAG=\int_S\left[\frac{1}{2}\left\{\left(\frac{\partial A}{\partial x}\right)^2+\left(\frac{\partial A}{\partial y}\right)^2\right\}+\mu_a\gamma\frac{\partial A}{\partial t}A-\mu_a jA\right]\mathrm{d}S, \qquad (3)$$

where S is the area occupied by the design scheme.

An electric current evenly distributed over the cross-section of the current conductor turns of the inductor is considered as a source of EM-field. The magnitude of the non-zero component of the current density vector varied over time t according to the next law:

$$j(t) = j_m e^{-\delta_0 \omega t} \sin(2\pi\nu t), \quad (4)$$

where $j_m \approx \frac{4I_m}{\pi d^2}$ is the current density amplitude; $I_m = 40$ kA is the amplitude of the current in the inductor, $\nu = 2$ kHz is the pulse current frequency, $\omega = 2\pi\nu$ is the cyclic frequency of the current change, $\delta_0 = \delta/\omega = 0{,}3$ is the relative coefficient of the inductor current attenuation δ.

The second and main stage of the analysis is the study of the elements deforming of the inductor and workpiece, which are presented within the framework of a single scheme. In this case, the bodies system deforming is considered within the framework of plane deformation. The distribution of the main tensor-vector components that describe the deforming process of the inductor elements and the workpiece is subjected to the following group of equations. Equilibrium equation:

$$\begin{cases} \frac{\partial \sigma_x}{\partial x} + \frac{\partial \tau_{xy}}{\partial y} + f_x = 0 \\ \frac{\partial \tau_{xy}}{\partial x} + \frac{\partial \sigma_y}{\partial y} + f_y = 0 \end{cases}, \quad (5)$$

where σ_x, σ_y, τ_{xy} are non-zero components of the stress tensor; $f_x = -jB_y$, $f_y = -jB_x$ are the components of the volumetric electromagnetic force vector.

Geometric dependences in the Cauchy form:

$$\varepsilon_x = \frac{\partial u_x}{\partial x};\ \varepsilon_y = \frac{\partial u_y}{\partial y};\ \gamma_{xy} = \frac{\partial u_x}{\partial y} + \frac{\partial u_y}{\partial x}, \quad (6)$$

where ε_x, ε_y, γ_{xy} are the non-zero components of the deformation tensor; u_x, u_y are the non-zero components of the displacement vector.

The relationship between stresses and deformations is accepted according to the elastic model:

$$\{\varepsilon\} = [A]\{\sigma\}, \quad [A_{ij}] = \frac{(1+\nu)}{E}\begin{bmatrix} 1+\nu & -\nu & 0 \\ -\nu & 1+\nu & 0 \\ 0 & 0 & 2 \end{bmatrix}, \quad (7)$$

where E is the modulus of elasticity, ν is the Poisson ratio.

The following can be stated regarding the fixing conditions: the conductive workpiece must be freely located on the dielectric mold; its edges must not be fixed in any way (article [14] shows that in the case of fixed edges of the workpiece, the highest stress levels occur around them). In turn, since the force effect on the mold in this case is not of interest to us, we will not dwell on the specific method of its fastening, we will assume that the its lower outer border is fastened.

In the case when the workpiece is freely located on the mold (see Fig. 1), the conditions of one-sided contact between them must be taken into account. In this case, during the numerical solution, the contact was modeled by introducing a layer of special contact elements (similar to how it was done in [15]). Also, layers of contact elements are introduced between the turns of the inductor and the insulation. The inductor was considered fixed on the boundaries indicated in Fig. 1 as Γ_2:

$$u_x\Big|_{\substack{x\in\Gamma_2 \\ y\in\Gamma_2}} = 0, \quad u_y\Big|_{\substack{x\in\Gamma_2 \\ y\in\Gamma_2}} = 0. \quad (8)$$

The solution was based on finite element modeling. The defining equations for which in similar problems are generally given in [16]. A three-node finite element (FE) with a linear approximation of the non-zero component of the vector magnetic potential and displacements is used as the basis. At the first stage of the analysis, the spatio-temporal distributions of the main quantitative characteristics of EM-field were found. Here, a series of calculations was carried out, in which the rational parameters of the calculation model were determined: the dimensions of the environment, the number of FEs, and the time integration step. All this was done in order to satisfy the boundary conditions (2) and prove the reliability of the obtained results.

During calculations, the following values of geometric dimensions were considered: d = 10 mm, L = 100 mm, h = 2 mm, α = 15°.

The physical and mechanical parameters of the system elements, which were used in all subsequent calculations, are given in Table 1.

Table 1

Physical and mechanical parameters of system elements

The elements characteristics name	The inductor current conductor parameters, copper	The workpiece parameters, aluminum alloy	The insulation parameters, kaprolon	The data of the dielectric mold, fiberglass
μ_r	1	1	1	1
γ, $(\Omega m)^{-1}$	$7{\cdot}10^7$	$4{,}6{\cdot}10^7$	0	0
E, GPa	120	71	2,5	200
ν	0,33	0,29	0,3	0,27
σ_y, MPa	380	190	–	–
σ_B^+, MPa	–	–	70	100
σ_B^-, MPa	–	–	90	120

In Table 1 adopt the following designations: σ_y is the yield strength of the material; σ_B^+ is the tensile strength limit; σ_B^- is the compressive strength limit.

The dimensions of the surrounding environment were characterized by the distance from the vertical and horizontal walls of the workpiece. Based on the results of the calculations, the maximum values of the tangential component of the magnetic field intensity on the inner surfaces of the workpiece around the corner were compared. The first calculation was carried out at a distance of $L/10$ (see Fig. 1). The subsequent calculations were carried out with an increase in the distance by the same amount of $L/10$. It turned out that when the distance goes from $L/2$ to $3L/5$, the difference in the values of the tangential component of the magnetic field intensity around the corner does not exceed 2,32 %. Therefore, all subsequent calculations were carried out under the condition that the boundaries of the surrounding medium are at a distance of $L/2$ from the walls of the workpiece.

To establish the reliability of the finite element modeling results, studies were conducted in which the number of FEs was changed by increasing them. It should be noted that since the main object of consideration was the workpiece and the inductor, the FE concentration was

carried out precisely in the areas of the calculation scheme corresponding to these elements. The initial FE mesh consisted of 1650 elements. Further calculations were carried out by doubling the number of elements, while comparing the maximum values of the magnetic field strength in the vicinity of the rounding. When moving from 13200 FEs to 26400 FEs, it turned out that the value of the maximum magnetic field strength changes slightly – by 1,214 %. Therefore, all further calculations were carried out for a finite element mesh containing 13200 FEs.

Regarding the variation of the integration step over time, it was found that the reduction of the time step does not lead to significant changes in the results of the distribution of EM-field components. All calculations were performed for a step of 0.1 ms.

Analysis of the calculation results. Let us consider some calculation results. At the first stage, the spatio-temporal distributions of the main quantitative characteristics of EM-field were obtained. In Fig. 2 shows the distribution of the H_y-component of the magnetic field intensity corresponding to it maximum in the time interval.

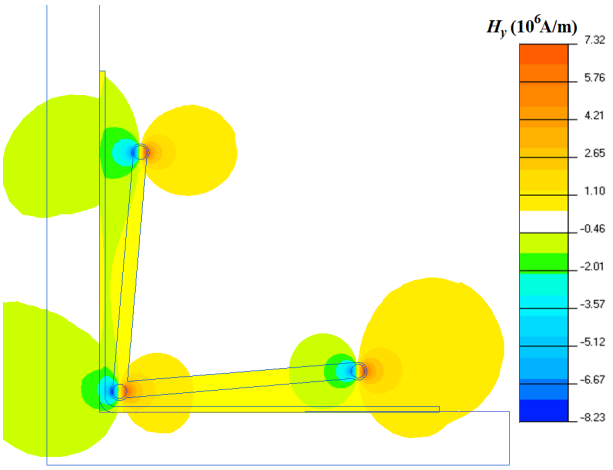

Fig. 2. Distribution of the H_y-component of the magnetic field intensity

From the data of Fig. 2 is seen that the maximum values of intensity H_y are observed around the turns of the inductor current conductor and it is here that the maximum force impact on the workpiece should be expected.

Let's consider in more detail the results of SSS calculations of the workpiece, mold and inductor. Calculations were performed in a quasi-stationary setting, for EM-field components that have maximum values from the considered time interval.

The found distributions of the tensor components of the SSS make it possible to carry out quantitative assessments of the strength of the workpiece and the elements of the inductor, which in turn allows drawing conclusions about the efficiency of the technological operation. When carrying out the relevant assessments, we used the approach given in article [16], when the equivalent stresses were determined and compared with the material strength characteristics. The stress intensity was calculated for the elements of the calculation scheme made of conductive materials (workpiece, inductor conductor), and the equivalent stress was calculated for dielectrics (inductor insulation) according to Mohr's criterion.

Figures 3 and 4 show the spatial distributions of stress intensity σ_i and equivalent stresses according to Mohr's criterion σ_{Mo} in the workpiece.

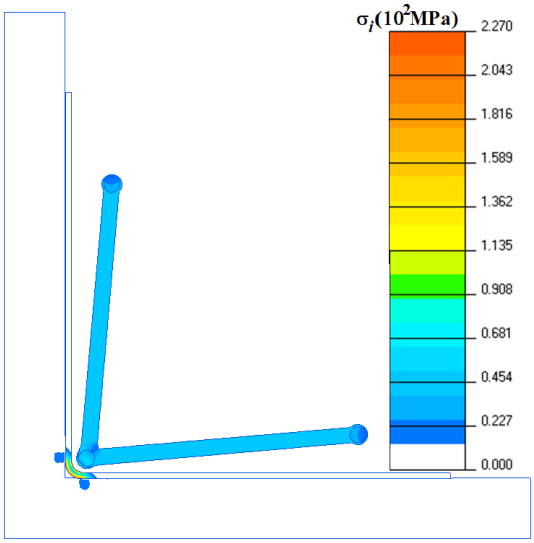

Fig. 3. Distribution of stress intensity

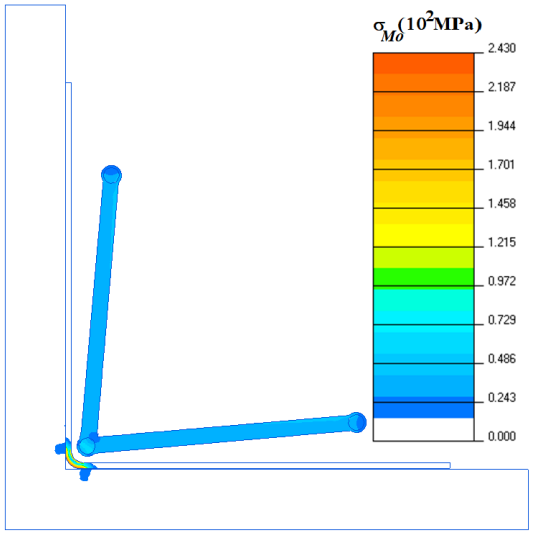

Fig. 4. Distribution of equivalent stresses according to Mohr's criterion

The given distributions of equivalent stresses allow us to conclude that the most loaded are: the workpiece zone around the rounding («target zone» of the technological operation), the current conductor and the insulation zones bordering the current conductor.

The maximum value of the stress intensity in the workpiece, which is observed on the workpiece surface (directly in the vicinity of rounding – in the «target zone» of the technological operation), is 227 MPa, which is greater than the yield strength of the aluminum alloy. Thus it can be stated that from the point of view of the plastic deformations possibility in the workpiece, the technological operation is efficient. The maximum intensity of stress in the current conductor of the inductor is approximately 60 MPa, which does not exceed the yield strength of it material. The maximum value of the equivalent stress according to Mohr's criterion in the insulation of the inductor is 52 MPa, which also does not exceed the limit of the tensile strength of the material. So, it can be concluded that in this case the inductor remains operational.

Next, a series of calculations was carried out in order to determine the influence of the design and operational parameters of the technological operation on the process of elastic-plastic deformation of the workpiece. The purpose of these calculations was to determine the inductor application limits of this type and size, as well as to determine the rational values of some design and operational parameters of the technological system.

One of the series of calculations was aimed at finding out the degree of influence of the distance between the inductor and the workpiece on the distribution of SSS components in it. Here, the value of the distance between the coil of the inductor, which is close to the workpiece, and the workpiece varied, while other parameters of the technological operation (the dimensions of the workpiece, the values of the characteristics of the external EM-field) remained constant. The analysis of the results shows that when the inductor is moved away from the workpiece, the value of the maximum stress intensity in it decreases (Fig. 5), at a distance of 14 mm, the maximum stress intensity in the workpiece is approximately equal to the yield point of the aluminum alloy, i.e., with further distance, the workpiece will deform elastically. Thus, the most rational option is when the inductor touches the workpiece, and the largest distance between the inductor and the workpiece should not exceed 14 mm.

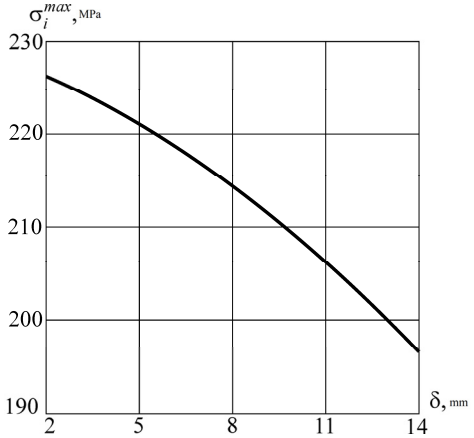

Fig. 5. Dependence of the maximum stress intensity in the workpiece on the distance between the inductor and the workpiece

Another series of calculations was aimed at finding out the influence degree of the current amplitude in the inductor on the distribution of SSS components in the elements of the technological system. Calculations were performed for the case of contact between the inductor and the workpiece. Five calculations were carried out, in which the amplitude of the current I_m was assumed to be equal to 40, 45, 50, 55 and 60 kA.

As the current strength increases, the qualitative patterns of distribution of SSS components in the workpiece are preserved, and the stress values increase. Figure 6 shows graphs illustrating the growth of the maximum stress intensity in the workpiece and in the current conductor, as well as the maximum equivalent stress according to Mohr's criterion in the dielectric insulation with increasing current magnitude in the inductor.

It can be seen that when the amplitude of the current I_m exceeds the level of 50 kA, the values of the equivalent stresses in the insulation of the calculated system reach dangerous values: at the same time ($\sigma_{Mo} > \sigma_B^+$).

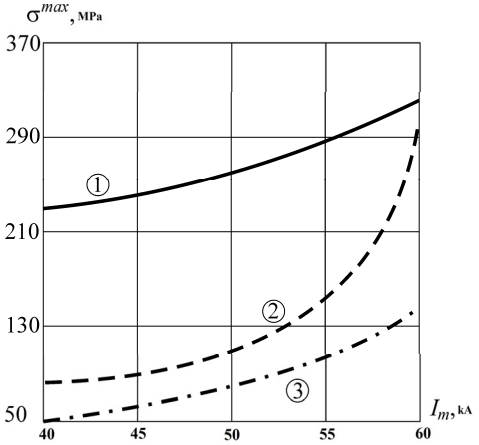

Fig. 6. Dependence of the equivalent stresses on the magnitude of the current amplitude: 1 – in the workpiece (stress intensity); 2 – in the inductor coil (stress intensity); 3 – in insulation (equivalent stress according to Mohr's criterion)

Thus, with the considered design parameters, the amplitude of the current I_m in the inductor should not exceed 50 kA, because with its further increase, there is a possibility of operability loss of the used inductor due to the destruction of the dielectric insulation.

Conclusions.

1. The design scheme of the technological operation of «filling corners», which includes a curved thin-walled workpiece and a two-turn inductor, is considered. A mathematical formulation of the problem of electromagnetic field propagation and deformation is presented. The finite element method was used as a numerical method. Numerical studies were carried out to substantiate the parameters of the design scheme.

The results of calculations on the distribution of the electromagnetic field quantitative characteristics and the deformation process are given. The spatial distribution of the H_y-component of the magnetic field intensity, which corresponds to it maximum in the time interval, is presented, from which a forecast can be made regarding the zones of maximum force impact on the workpiece. Spatial distributions in the elements of the calculation system of equivalent strength indicators are also given: stress intensity and equivalent stress according to Mohr's criterion.

2. It is shown that the maximum force impact occurs directly in the area of the workpiece rounding. In this case, with the considered parameters of influence, plastic deformation begins in the workpiece, and the inductor remains operational.

A series of calculations of the electromagnetic field and the stress-strain state of the calculation system were carried out, in which the values of the distance between the inductor and the workpiece, as well as the amplitude of the inductor current, varied. Rational values of the specified parameters were found, at which the used inductor remains operational, and plastic deformations occur in the workpiece material.

3. The further development of this work consists in carrying out calculation studies of the workpiece deforming in the region beyond the yield strength of it material.

Conflict of interest. The authors of the article declare that there is no conflict of interest.

REFERENCES

1. Psyk V., Risch D., Kinsey B.L., Tekkayaa A.E., Kleiner M. Electromagnetic forming – a review. *Journal of Materials Processing Technology*, 2011, vol. 211, no. 5, pp. 787-829. doi: https://doi.org/10.1016/j.jmatprotec.2010.12.012.

2. Gayakwad D., Dargar M.K., Sharma P.K., Purohit R., Rana R.S. A Review on Electromagnetic Forming Process. *Procedia Materials Science*, 2014, vol. 6, pp. 520-527. doi: https://doi.org/10.1016/j.mspro.2014.07.066.

3. Batygin Yu.V., Chaplygin E.A., Shinderuk S.A., Strelnikova V.A. The main inventions for technologies of the magnetic pulsed attraction of the sheet metals. A brief review. *Electrical Engineering & Electromechanics*, 2018, no. 3, pp. 43-52. doi: https://doi.org/10.20998/2074-272X.2018.3.06.

4. Batygin Y.V., Chaplygin E.A. Vortical currents in flat metallic sheet. *Electrical Engineering & Electromechanics*, 2006, no. 5, pp. 54-59. (Rus).

5. Batygin Yu., Barbashova M., Sabokar O. *Electromagnetic Metal Forming for Advanced Processing Technologies*. Cham, Springer International Publ. AG., 2018. 93 p. doi: https://doi.org/10.1007/978-3-319-74570-1.

6. Batygin Y.V., Golovashchenko S.F., Gnatov A.V., Smirnov D.O. Magnetic field and pressures excited by four pairwise coplanar solenoids in the cavity of a rectangular tube. *Electrical Engineering & Electromechanics*, 2010, no. 2, pp. 46-49. (Rus).

7. Batygin Y.V., Serikov G.S. Magnetic field and pressures excited by a single-turn inductor in a corner bend of a sheet worpiece. *Electrical Engineering & Electromechanics,* 2006, no. 6, pp. 66-70. (Rus).

8. Unger J., Stiemer M., Schwarze M., Svendsen B., Blum H., Reese S. Strategies for 3D simulation of electromagnetic forming processes. *Journal of Materials Processing Technology*, 2008, vol. 199, no. 1-3, pp. 341-362. doi: https://doi.org/10.1016/j.jmatprotec.2007.08.028.

9. Stiemer M., Unger J., Svendsen B., Blum H. An arbitrary Lagrangian Eulerian approach to the three-dimensional simulation of electromagnetic forming. *Computer Methods in Applied Mechanics and Engineering*, 2009, vol. 198, no. 17-20, pp. 1535-1547. doi: https://doi.org/10.1016/j.cma.2009.01.014.

10. Mamalis A.G., Manolakos D.E., Kladas A.G., Koumoutsos A.K. Electromagnetic Forming Tools and Processing Conditions: Numerical Simulation. *Materials and Manufacturing Processes*, 2006, vol. 21, no. 4, pp. 411-423. doi: https://doi.org/10.1080/10426910500411785.

11. Yu H., Chen J., Liu W., Yin H., Li C. Electromagnetic forming of aluminum circular tubes into square tubes: Experiment and numerical simulation. *Journal of Manufacturing Processes*, 2018, vol. 31, pp. 613-623. doi: https://doi.org/10.1016/j.jmapro.2017.12.019.

12. Doley J.K., Kore S.D. Fully Coupled Numerical Simulation of Electromagnetic Forming. *Key Engineering Materials*, 2012, vol. 504-506, pp. 1201-1206. doi: https://doi.org/10.4028/www.scientific.net/KEM.504-506.1201.

13. Altenbach H., Morachkovsky O., Naumenko K., Lavinsky D. Inelastic deformation of conductive bodies in electromagnetic fields. *Continuum Mechanics and Thermodynamics*, 2016, vol. 28, no. 5, pp. 1421-1433. doi: https://doi.org/10.1007/s00161-015-0484-8.

14. Lavinsky D.V. Analysis of elastic-plastic deformation when modeling the «corner filling» operation. Part 1. *Bulletin of the National Technical University «KhPI» Series: Dynamics and Strength of Machines*, 2010, no. 37, pp. 100-104. (Rus).

15. Lavinsky D.V., Zaitsev Yu.I. Computational analysis method of the electromagnetic field propagation and deformation of conductive bodies. *Electrical Engineering & Electromechanics*, 2023, no. 5, pp. 77-82. doi: https://doi.org/10.20998/2074-272X.2023.5.11.

16. Lavinskii D.V., Morachkovskii O. K. Elastoplastic Deformation of Bodies Interacting Through Contact Under the Action of Pulsed Electromagnetic Field. *Strength of Materials*, 2016, vol. 48, no. 6, pp. 760-767. doi: https://doi.org/10.1007/s11223-017-9822-3.

Received 14.10.2023
Accepted 07.12.2023
Published 02.03.2024

D.V. Lavinsky[1], *Doctor of Technical Science, Associate Professor,*
Yu.I. Zaitsev[1], *Candidate of Technical Science, Professor,*
[1] National Technical University «Kharkiv Polytechnic Institute», 2, Kyrpychova Str., Kharkiv, Ukraine, 61002,
e-mail: Denys.Lavinskiy@khpi.edu.ua (Corresponding Author); yurii.zaitsev@khpi.edu.ua

How to cite this article:
Lavinsky D.V., Zaitsev Yu.I. Computational studies of electromagnetic field propagation and deforming of structural elements for a thin-walled curved workpiece and an inductor. *Electrical Engineering & Electromechanics*, 2024, no. 2, pp. 55-60. doi: https://doi.org/10.20998/2074-272X.2024.2.08

UDC 621.314 https://doi.org/10.20998/2074-272X.2024.2.09

M. Kaddache, S. Drid, A. Khemis, D. Rahem, L. Chrifi-Alaoui

Maximum power point tracking improvement using type-2 fuzzy controller for wind system based on the double fed induction generator

Introduction. *In this paper, to maximize energy transmission in wind power system, various Maximum Power Point Tracking (MPPT) approaches are available. Among these techniques, we have proposed the one based on typical fuzzy logic. Despite the somewhat reduced performance of fuzzy MPPT. For a number of reasons, fuzzy MPPT can replace conventional optimization techniques. In practice, the effectiveness of conventional MPPT methods depends mainly on the accuracy of the information given and the wind speed or knowledge of the aerodynamic properties of the wind system.* ***Novelty.*** *Our new MPPT for monitoring the maximum power point has been proposed. We developed an algorithm to improve control performance and govern the stator's developed active and reactive power using the typical fuzzy logic 2 and enable robust control of a grid-connected, doubly fed induction generator.* ***Purpose.*** *MPPT which implies the wind turbine's rotating speed should be modified in real time to capture the most wind energy, is necessary to achieve high efficiency for wind energy conversion, according to the aerodynamic characteristics of the wind turbine.* ***Methods.*** *Developing a mathematical model for a wind energy production system is complex, can be strongly affected by wind variation and is a non-linear problem. Thanks to these characteristics, thus, the Lyapunov technique is combined with a sliding mode control to ensure overall asymptotic stability and robustness with regard to parametric fluctuations in order to accomplish this goal. We contrasted our fuzzy type-2 algorithm's performance with that of the fuzzy type-1 and Perturbation & Observation (P&O) suggested in the literature.* ***Practical value****. The simulation results demonstrate that the control performance is satisfactory when using the fuzzy logic technique. From these results, it can be said for the optimization of energy conversion in wind systems, the fuzzy type-2 technique may offer a workable option. Since it presents a great possibility to avoid problems either technical or economics linked to conventional strategies.* References 21, figures 15.

Key words: **wind turbine, doubly fed induction machine, Lyapunov function, maximum power point tracking, fuzzy logic type-2, fuzzy logic type-1.**

Вступ*. У цій статті для максимізації передачі енергії у вітроенергетичній системі наведені різні підходи відстеження точки максимальної потужності (MPPT). Серед цих методів ми запропонували той, що базується на типовій нечіткій логіці. Незважаючи на дещо знижену продуктивність нечіткого MPPT. З ряду причин нечіткий MPPT може замінити звичайні методи оптимізації. На практиці ефективність звичайних методів MPPT залежить головним чином від точності наданої інформації та швидкості вітру або знання аеродинамічних властивостей вітрової системи.* ***Новизна****. Було запропоновано наш новий MPPT для моніторингу точки максимальної потужності. Ми розробили алгоритм для покращення продуктивності керування та керування розвиненою активною та реактивною потужністю статора за допомогою типової нечіткої логіки 2 та забезпечення надійного керування підключеним до мережі індукційним генератором із подвійним живленням.* ***Мета****. MPPT, який означає, що швидкість обертання вітряної турбіни має бути змінена в режимі реального часу, щоб отримувати найбільшу кількість енергії вітру, необхідна для досягнення високої ефективності перетворення енергії вітру відповідно до аеродинамічних характеристик вітрової турбіни.* ***Методи****. Розробка математичної моделі для системи виробництва вітрової енергії є складною, на неї можуть сильно впливати коливання вітру, яка є нелінійною задачею. Завдяки цим характеристикам, таким чином, метод Ляпунова поєднується з керуванням ковзним режимом для забезпечення загальної асимптотичної стабільності та стійкості щодо параметричних флуктуацій для досягнення цієї мети. Ми порівняли продуктивність нашого алгоритму нечіткого типу 2 з показниками алгоритмів нечіткого типу 1 і збурення та спостереження (P&O), запропонованих у літературі.* ***Практична цінність****. Результати моделювання демонструють, що ефективність керування є задовільною при використанні методу нечіткої логіки. З цих результатів можна сказати, що для оптимізації перетворення енергії у вітряних системах метод нечіткого типу 2 може запропонувати працездатний варіант, оскільки це чудова можливість уникнути технічних або економічних проблем, пов'язаних зі звичайними стратегіями.* Бібл. 21, рис. 15.

Ключові слова: **вітряна турбіна, асинхронна машина з подвійним живленням, функція Ляпунова, відстеження точки максимальної потужності, нечітка логіка типу 2, нечітка логіка типу 1.**

Introduction. Despite the use of windmills since antiquity, wind energy has long been forgotten. It was only after the oil crisis of 1973 that alerted the energy producing states fossil that it has known for more than 40 years an exceptional development. Indeed, from the year 2000 and in the same context of the fossil fuel market disruption, the increase electricity demand in the world and the awareness of environmental issues, these are reasons that have accentuated the need to exploit the clean energies where wind power takes a privileged place [1]. The rapid development of this technology has given rise to increasingly powerful wind turbines, whose operation increases energy efficiency, reduces mechanical efforts and improves the quality of the electrical energy produced [2]. Algeria having good wind potential, whose wind regime is moderate between 2 and 6 m/s (for 10 m from the ground) according to the wind map established by the Center for the Development of Renewable Energies (CDER) [3, 4] (Fig. 1).

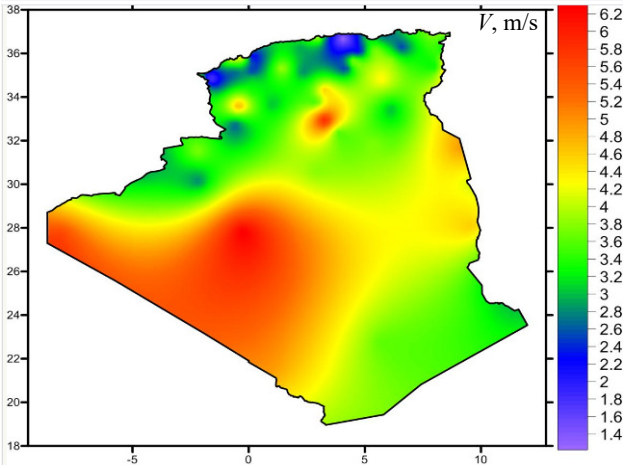

Fig. 1. Wind potential map of Algeria for 10 m from the ground, CDER [3]

The In-Salah site has an average wind speed of 6.4 m/s next to Adrar which 6.3 m/s. The Hassi-R'Mel site has fairly high average speeds reaching 6.5 m/s, whereas the province of Illizi shows speeds above 5 m/s at roughly 10 locations. As for the north of the country from west to east, various microclimates are also found. In the case of the Hauts-Plateaux, we observe that the regions of Mecheria and Tiaret have a particularly interesting average speed of 5.6 m/s. While 5.1 m/s and 5.3 m/s are recorded respectively in Djelfa and M'sila. Algeria plans to reach nearly 40 % of national electricity production from renewable sources by 2030. In addition to the installation of several photovoltaic plants in the Hauts Plateaux and the south, large wind farm projects should be built before 2024. In fact, in 2014 Algeria took delivery of the pilot Kabertène wind farm in Adrar (10 MW) and studies have been carried out to detect favorable locations in order to carry out other projects over the period 2017-2030 for a power of approximately 22 GW. Currently, variable speed wind systems based on the Doubly Fed Induction Generator (DFIG) are increasingly used on wind farms. The main advantage is the use of low power rated converters to control the slip power which is a small part of the machine rated power. By the way, the grid-connected DFIG ensures that the converters will be less in size since it permits operation across a speed range of ±30 % or less around the synchronization speed [1, 2, 5, 6]. In fact, it is a considerable economic benefit over alternative approaches (for example, the permanent magnet synchronous generator). The studied system is shown in Fig. 2. The C_p coefficient can be considered as part of the available wind power. It depends on the type and dimensions of the turbine. Generally, it is a function of the tip speed ratio λ (Fig. 3). In order to optimise the wind system, it is important to maximize C_p. To do that, we should keep the tip speed ratio at its optimal value with controlling the speed. In recent years, many researchers have focused on improving control strategy of Maximum Power Point Tracking (MPPT) based on fuzzy algorithm [7, 8].

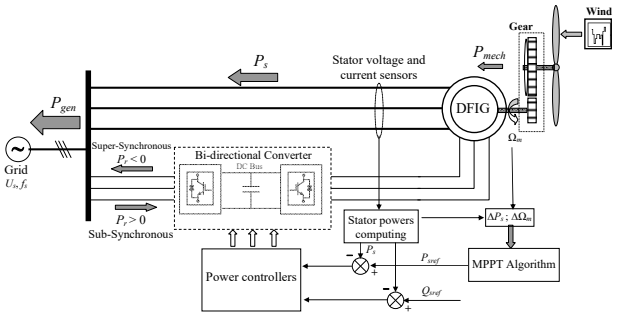

Fig. 2. Control system of the DFIG

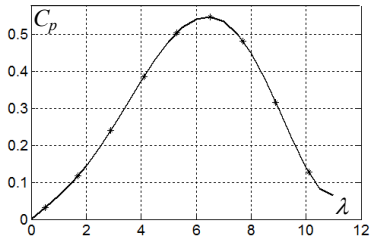

Fig. 3. Function $C_p = f(\lambda)$

The goal of the paper. In this paper, we propose a type-2 fuzzy MPPT controller. This controller will be compared with others MPPT's previously developed to demonstrate the efficiency of the proposed technique.

Modeling of wind. Turbines considering a tool for wind energy recovery on a surface S and assuming that the wind speed is identical at every point on this surface, the volume of air passing through this surface is equal to ρ, S. Consequently, the wind's incident power is kinetic and depends on the surface area that the wind sensor offers to the wind. This power P_w is defined as [9]:

$$P_w = 0.5 \cdot C_p \cdot S \cdot \rho \cdot V^3, \tag{1}$$

where P_w is the wind power; C_p is the power coefficient; S is the blades surface; ρ is the air density; V is the wind speed.

The relationship between the gear ratio is the product of the blades' linear speed and the wind speed:

$$\lambda = \Omega_t \cdot R / V, \tag{2}$$

where λ is the tip speed ratio; Ω_t is the mechanical angular speed of the wind turbine; R is the wind turbine radius.

Replacing (2) in (1), we have

$$P_w = 0.5 \cdot C_p(\lambda) \cdot S \cdot \rho \cdot \left(\frac{R}{\lambda}\right)^3 \cdot \Omega_t^3 \cdot \tag{3}$$

The following equation is used to compute the electromagnetic torque T of the turbine:

$$T = 0.5 \cdot C_p \cdot S \cdot \rho \cdot V \cdot \frac{1}{\lambda}. \tag{4}$$

The schematic diagram of the dynamic turbine model based on these equations is given in Fig. 4.

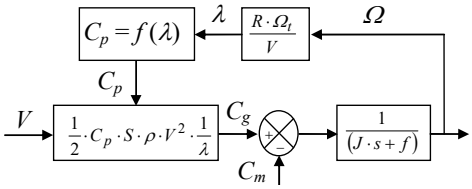

Fig. 4. Diagram of the turbine model

The DFIG model is represented by the ensuing equations in the synchronous reference frame [10]:

$$\begin{cases} \vec{V}_s = R_s \vec{I}_s + \dfrac{\mathrm{d}\vec{\phi}_s}{\mathrm{d}t} + J\omega_s \vec{\phi}_s; \\ \vec{V}_r = R_r \vec{I}_r + \dfrac{\mathrm{d}\vec{\phi}_r}{\mathrm{d}t} + J\omega_r \vec{\phi}_r, \end{cases} \tag{5}$$

where V_s, V_r, R_s, R_r, I_s, I_r, ϕ_s, ϕ_r, ω_s, ω_r are the stator and rotor voltages, resistances, currents, fluxes and current frequencies, respectively; J is the inertia moment.

The equation for current and flux is:

$$\begin{cases} \vec{I}_s = \gamma \vec{\phi}_s + \lambda \vec{\phi}_r; \\ \vec{I}_r = \lambda \vec{\phi}_s + \chi \vec{\phi}_r, \end{cases} \tag{6}$$

where

$$\gamma = 1/\sigma L_s; \quad \lambda = -M/\sigma L_s \cdot L_r; \quad \chi = 1/\sigma L_r.$$

The following equations result from equalizing the real and imaginary components of (5):

$$\begin{cases} V_{sd} = \gamma_1 \phi_{sd} - \gamma_2 \phi_{rd} + \dfrac{\mathrm{d}\phi_{sd}}{\mathrm{d}t} - \omega_s \phi_{sq} = -f_1 + \dfrac{\mathrm{d}\phi_{sd}}{\mathrm{d}t}; \\ V_{sq} = \gamma_2 \phi_{sq} - \gamma_2 \phi_{rq} + \dfrac{\mathrm{d}\phi_{sq}}{\mathrm{d}t} + \omega_s \phi_{sd} = -f_2 + \dfrac{\mathrm{d}\phi_{sq}}{\mathrm{d}t}; \\ V_{rd} = \gamma_3 \phi_{sd} + \gamma_4 \phi_{rd} + \dfrac{\mathrm{d}\phi_{rd}}{\mathrm{d}t} - \omega_r \phi_{rq} = -f_3 + \dfrac{\mathrm{d}\phi_{rd}}{\mathrm{d}t}; \\ V_{rq} = \gamma_3 \phi_{sq} + \gamma_4 \phi_{rq} + \dfrac{\mathrm{d}\phi_{rq}}{\mathrm{d}t} + \omega_r \phi_{rd} = -f_4 + \dfrac{\mathrm{d}\phi_{rq}}{\mathrm{d}t}, \end{cases} \tag{7}$$

where «*s*» and «*r*» mean stator and rotor; «*d*» and «*q*» are the direct and quadratic indicators for orthogonal component parts; and:

$$\gamma_1 = 1/\sigma\cdot\tau_s;\quad \gamma_2 = M/\sigma\cdot\tau_s\cdot L_r;\quad \gamma_3 = M/\sigma\cdot\tau_r\cdot L_s;\quad \gamma_4 = 1/\sigma\cdot\tau_r,$$

where M is the mutual inductance; σ is the leakage flux total coefficient; τ_s, τ_r are the stator and rotor time constants; L_s, L_r are the stator and rotor inductances; and:

$$\begin{cases} -f_1 = \gamma_1\phi_{sd} - \gamma_2\phi_{rd} - \omega_s\phi_{sq};\\ -f_2 = \gamma_1\phi_{sq} - \gamma_2\phi_{rq} + \omega_s\phi_{sd};\\ -f_3 = \gamma_3\phi_{sd} + \gamma_4\phi_{rd} - \omega_r\phi_{rq};\\ -f_4 = \gamma_3\phi_{sq} + \gamma_4\phi_{rq} + \omega_r\phi_{rd}. \end{cases} \quad (8)$$

The rewrite of (7) gives

$$\begin{cases} \dfrac{\mathrm{d}\phi_{sd}}{\mathrm{d}t} = f_1 + V_{sd};\\ \dfrac{\mathrm{d}\phi_{sq}}{\mathrm{d}t} = f_2 + V_{sq};\\ \dfrac{\mathrm{d}\phi_{rd}}{\mathrm{d}t} = f_3 + V_{rd};\\ \dfrac{\mathrm{d}\phi_{rq}}{\mathrm{d}t} = f_4 + V_{rq}. \end{cases} \quad (9)$$

Vector control strategy of the DFIG considers the stator voltage shown as follows in the *d-q* axis [10]:

$$\begin{cases} V_{sd} = 0;\\ V_{sq} = V_s. \end{cases} \quad (10)$$

The power expressions become

$$\begin{cases} P_s = V_s\left(\lambda\phi_{rq} + \gamma\phi_{sq}\right);\\ Q_s = V_s\left(\lambda\phi_{rd} + \gamma\phi_{sd}\right), \end{cases} \quad (11)$$

where P_s, Q_s are the stator active and reactive power.

Choosing a Lyapunov function

$$V_1 = \frac{1}{2}\left(P_s - P_{sref}\right)^2 + \frac{1}{2}\left(Q_s - Q_{sref}\right)^2 > 0. \quad (12)$$

The functions derivate is

$$V_1 = \left(P_s - P_{sref}\right)\left(P_s - P_{sref}\right) + \left(Q_s - Q_{sref}\right)\left(Q_s - Q_{sref}\right). \quad (13)$$

Substituting (9) and (12) in (13) it results in

$$\begin{aligned} V_1 = &\left(P_s - P_{sref}\right)\left(\alpha_1 + \lambda V_s V_{rq} - P_{sref}\right) + \\ &+ \left(Q_s - Q_{sref}\right)\left(\alpha_2 + \lambda V_s V_{rd} - Q_{sref}\right), \end{aligned} \quad (14)$$

with

$$\begin{cases} \alpha_1 = \lambda V_s f_4 + \gamma\left(f_2 + V_s\right);\\ \alpha_2 = \lambda V_s f_3 + \gamma f_1. \end{cases} \quad (15)$$

Equation (14) can be clearly negative, if the control law described below is established

$$\begin{cases} V_{rd} = \dfrac{1}{\lambda V_s}\left(\alpha_2 + Q_{sref} - K_2\left(Q_s - Q_{sref}\right)\right);\\ V_{rq} = \dfrac{1}{\lambda V_s}\left(\alpha_1 + P_{sref} - K_1\left(P_s - P_{sref}\right)\right). \end{cases} \quad (16)$$

Replacing (15) in (14) can be obtained

$$V_1 = -K_1\left(P_s - P_{sref}\right)^2 - K_2\left(Q_s - Q_{sref}\right)^2 < 0. \quad (17)$$

So (16) is stable, if K_i (i = 1, 2) were, of course, are all positive [11], in other words

$$\begin{cases} \lim\limits_{t\to\infty}\left(Q_s - Q_{sref}\right) = 0;\\ \lim\limits_{t\to\infty}\left(P_s - P_{sref}\right) = 0. \end{cases}$$

Robust control. The robust non-linear state return control law based on Lyapunov theory is designed to address the problems of model uncertainties related to the variation of machine parameters and measurement noise [12, 13]. Model uncertainties in this type of control are generally non-linear functions [14]. Generally, the functions (f_i, α_i) are written as:

$$\begin{cases} f_i = \hat{f}_i + \Delta f_i;\\ \alpha_i = \hat{\alpha}_i + \Delta\alpha_i. \end{cases} \quad (18)$$

Replacing (18) in (9), can be obtained:

$$\begin{cases} \dfrac{\mathrm{d}\phi_{sd}}{\mathrm{d}t} = \hat{f}_1 + \Delta f + V_{sd};\\ \dfrac{\mathrm{d}\phi_{sq}}{\mathrm{d}t} = \hat{f}_2 + \Delta f + V_{sq};\\ \dfrac{\mathrm{d}\phi_{rd}}{\mathrm{d}t} = \hat{f}_3 + \Delta f + V_{rd};\\ \dfrac{\mathrm{d}\phi_{rq}}{\mathrm{d}t} = \hat{f}_4 + \Delta f + V_{rq}. \end{cases} \quad (19)$$

The new law control can be selected by taking into account Δf_i as follows:

$$\begin{cases} V_{rd} = \dfrac{1}{\lambda V_s}\begin{pmatrix} -\alpha_2 + Q_{sref} - K_2\left(Q_s - Q_{sref}\right) - \\ - K_{22}\,\mathrm{sgn}\left(Q_s - Q_{sref}\right) \end{pmatrix};\\ V_{rq} = \dfrac{1}{\lambda V_s}\begin{pmatrix} \alpha_1 + P_{sref} - K_1\left(P_s - P_{sref}\right) - \\ - K_{22}\,\mathrm{sgn}\left(P_s - P_{sref}\right) \end{pmatrix}. \end{cases} \quad (20)$$

where $K_{ii} \ge \beta_i$, $K_{ii} \ge 0$, K_i (i = 1, 2).

Equations (19), (20) were used to build the Lyapunov function analog from (14)

$$\begin{aligned} V_2^{\bullet} = &\left(P_s - P_{sref}\right)\left(\Delta\alpha_1 - K_{11}\,\mathrm{sgn}\left(P_s - P_{sref}\right)\right) + \\ &+ \left(Q_s - Q_{sref}\right)\left(\Delta\alpha_2 - K_{22}\,\mathrm{sgn}\left(Q_s - Q_{sref}\right)\right) < 0. \end{aligned} \quad (21)$$

Therefore, if chosen, the f_i with enhanced system stability, variances can be absorbed:

$$\begin{cases} K_{11} = \left|\Delta\alpha_1\right|;\\ K_{22} = \left|\Delta\alpha_2\right|. \end{cases} \quad (22)$$

Finely, we can resume:

$$\dot{V}_1 < \dot{V}_2 < 0. \quad (23)$$

For the convergent processes stability, the control law given by (20) is applied for any α_i. The design of robust controllers is illustrated in Fig. 5.

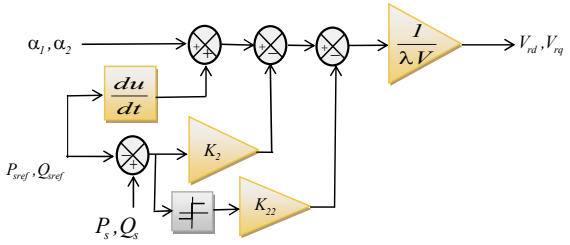

Fig. 5. Diagram design of robust controllers

New MPPT. In order to maximize the generated power, a new MPPT has been developed based on the

relationship of the aerodynamic power P, turbine speed Ω_t and electromagnetic torque T of the DFIG (Fig. 6):

$$\lambda = \Omega_t \cdot R / V , \quad (24)$$

$$P = 0.5 \cdot \rho \cdot R^2 \cdot V^3 ; \quad (25)$$

$$C_p = \omega \cdot T / P . \quad (26)$$

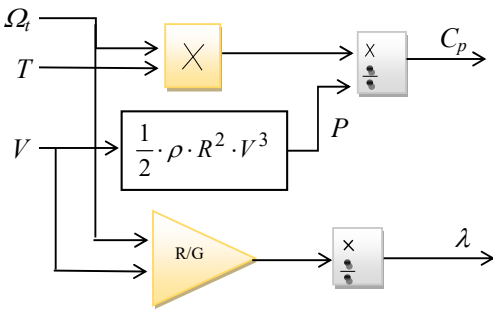

Fig. 6. New MPPT

In this research, a nonlinear empirical interpolation to represent the C_p is shown in Fig. 7.

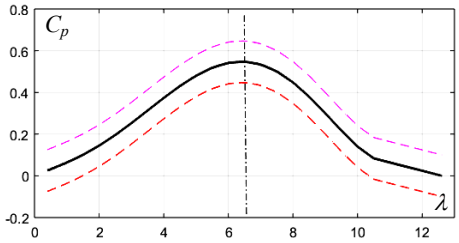

Fig. 7. Coefficient various tip speed ratio characteristic

MPPT using fuzzy logic type-2. Stator power active and speed turbine variation are the fuzzy controller's two inputs (Fig. 8).

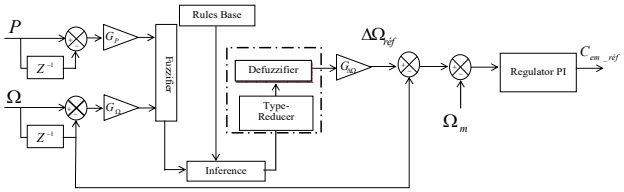

Fig. 8. Proposed fuzzy controller type-2

The definitions of error variation ΔP and $\Delta\Omega$ are [15]:

$$\begin{cases} \Delta P_s = P_s(t) - P_g(t-\Delta t) = P_g(k) - P_g(k-1); \\ \Delta\Omega_g = \Omega_m(t) - \Omega_m(t-\Delta t) = \Omega_m(k) - \Omega_m(k-1), \end{cases} \quad (27)$$

where Δt is the time step; k is the time step number.

The output of the regulator is corresponding to the coefficient variation $\Delta\dot{\Omega}_m$. The three quantities ΔP, $\Delta\Omega_m$ and $\Delta\dot{\Omega}_m$, are standardized as:

$$\begin{cases} \Delta P_g = G_p P_g ; \\ \Delta\Omega_m = G_\Omega \Delta\Omega_m ; \\ \Delta\dot{\Omega}_m = G_{\Delta\Omega} \Delta\dot{\Omega}_m , \end{cases} \quad (28)$$

where G_p, G_Ω, $G_{\Delta\Omega}$ are the scale factors or normalization, and they have a significant impact on both the control's static and dynamic performance.

The fuzzy logic type-2 membership functions for the stator active power and speed turbine variation are selected to be the same as Gaussian forms, with ΔP defined on the interval [0, 1] in Fig. 9,*a* and $\Delta\Omega_m$ is defined on the interval [–1, 1] in Fig. 9,*b*. The fuzzy logic type-2 membership functions of the variation $\Delta\dot{\Omega}_m$ are chosen with intervals formed on the interval [0, 1.2] (Fig. 9,*c*).

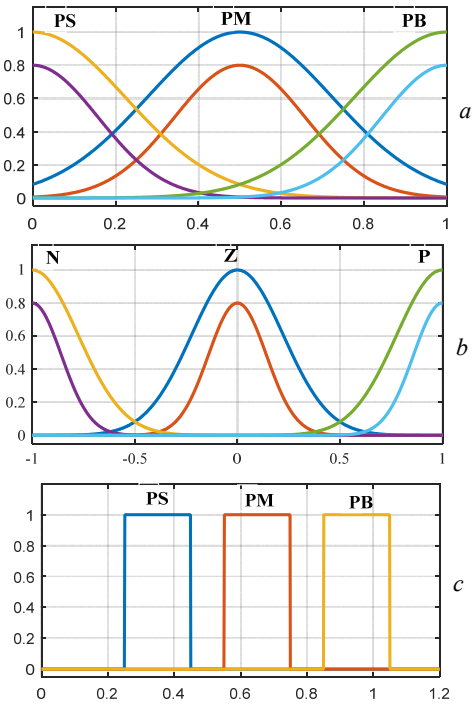

Fig. 9. Fuzzy type-2 membership functions for the variation of ΔP (*a*); $\Delta\Omega_m$ (*b*); $\Delta\dot{\Omega}_m$ (*c*)

Comparative study with fuzzy type-1 and Perturbation and Observation (P&O) algorithm. In order to show the performance of our approach based on fuzzy logic type-2, a comparison with the approach based on fuzzy logic type-1 and the P&O algorithm has been carried out [16-21].

P&O algorithm stands out because it does not need a database or training. This guarantees more versatility to this algorithm, with direct application in the system, without the need for previous information or wind speed sensors or understanding of the curve of the aerodynamic characteristics.

Figure 10 shows the P&O algorithm flow chart as it should be implemented in the control microprocessor.

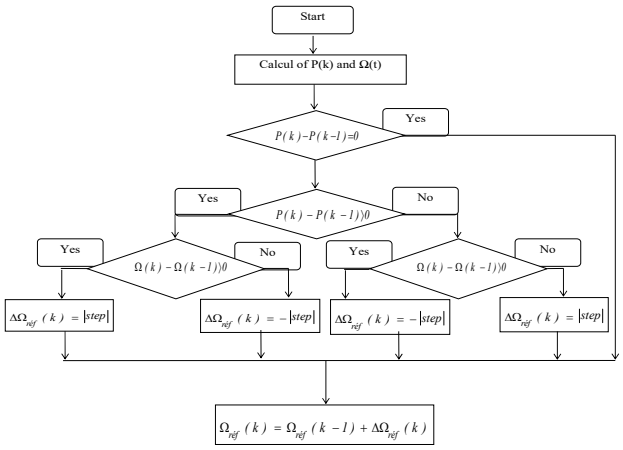

Fig. 10. P&O algorithm flow chart

Fuzzy logic type-1. For the variation of the active power of the stator ΔP and the speed of the turbine Ω_m,

their membership functions have been chosen with triangular forms and is defined on the interval [–1, 1] (Fig. 11,*a*,*b*). The membership functions type-1 of the variation of $\Delta\dot{\Omega}_m$ chosen from triangular shapes over the interval [–1, 1] (Fig. 11,*c*).

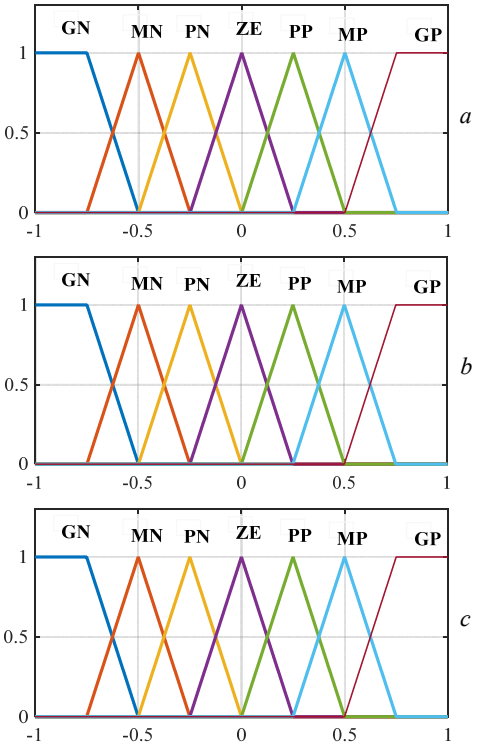

Fig. 11. Fuzzy type-1 membership functions for the variation of ΔP (*a*); $\Delta\Omega_m$ (*b*); $\Delta\dot{\Omega}_m$ (*c*)

Results. The results are arranged in accordance with the following criteria, respectively:

- simulated system with a variable wind speed with an average value of 5.8 m/s (Fig. 12);
- turbine speed (Fig. 13) fixed at 140 rad/s;
- power coefficient C_p (Fig. 14);
- stator active power (Fig. 15).

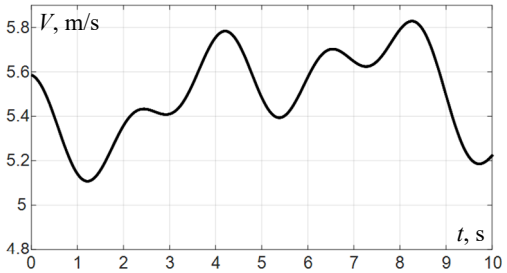

Fig. 12. Wind speed

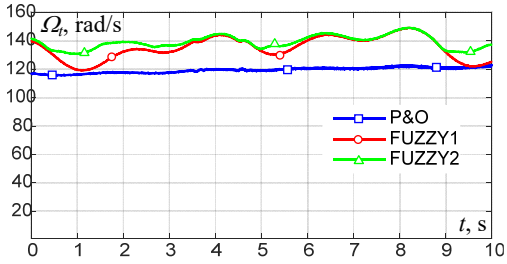

Fig. 13. Turbine speed

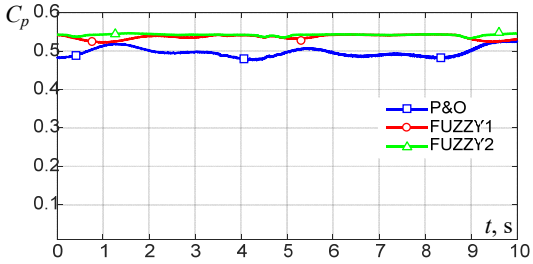

Fig. 14. Power coefficient C_p

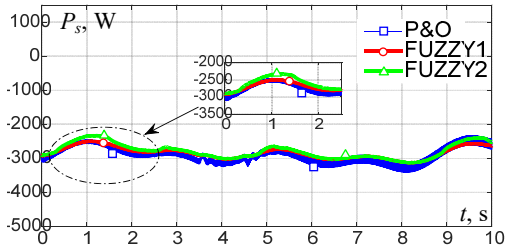

Fig. 15. Stator active power

The active power varied between –5 kW to 1 kW while the reactive power is fixed at 0 VAr. After seeing the correct follow-up of the proposed instructions it is necessary to assess the structure's robustness to parameter uncertainty. Therefore, the next step is to assess the resistance to stator and rotor change.

Finally, the results evince that the method based on fuzzy logic type-2 is superior in terms of effectiveness, robustness, and response time.

Conclusions. The results obtained show the performance of our type-2 fuzzy maximum power point tracking (MPPT) compared to two other techniques (Perturbation and Observation) and type-1 fuzzy. For several reasons, the latter technique can replace conventional optimization techniques. In practice, the effectiveness of conventional MPPT methods depends mainly on the accuracy of the information given and the wind speed or the knowledge of the aerodynamic properties of the wind system. However, this need an anemometer, which raises the systems cost. Thus, knowledge of aerodynamic properties requires the manufacturer to carry out tests that are a bit complex and expensive. In addition, these characteristics change from turbine to turbine. They also vary with climatic conditions, which decrease the reliability of the system. It is better to choose the command strategies that do not depend on these parameters.

Conflict of interest. The authors of the article declare that there is no conflict of interest.

REFERENCES

1. Belkacem Y., Drid S., Makouf A., Chrifi-Alaoui L. Multi-agent energy management and fault tolerant control of the micro-grid powered with doubly fed induction generator wind farm. *International Journal of System Assurance Engineering and Management*, 2022, vol. 13, no. 1, pp. 267-277. doi: https://doi.org/10.1007/s13198-021-01228-2.

2. Slimane W., Benchouia M.T., Golea A., Drid S. Second order sliding mode maximum power point tracking of wind turbine systems based on double fed induction generator. *International Journal of System Assurance Engineering and Management*, 2020, vol. 11, no. 3, pp. 716-727. doi: https://doi.org/10.1007/s13198-020-00987-8.

3. Guezgouz M., Jurasz J., Chouai M., Bloomfield H., Bekkouche B. Assessment of solar and wind energy

complementarity in Algeria. *Energy Conversion and Management*, 2021, vol. 238, art. no. 114170. doi: https://doi.org/10.1016/j.enconman.2021.114170.
4. Daaou Nedjari H., Haddouche S.K., Balehouane A., Guerri O. Optimal windy sites in Algeria: Potential and perspectives. *Energy*, 2018, vol. 147, pp. 1240-1255. https://doi.org/10.1016/j.energy.2017.12.046.
5. Galdi V., Piccolo A., Siano P. Exploiting maximum energy from variable speed wind power generation systems by using an adaptive Takagi–Sugeno–Kang fuzzy model. *Energy Conversion and Management*, 2009, vol. 50, no. 2, pp. 413-421. doi: https://doi.org/10.1016/j.enconman.2008.09.004.
6. Abdeddaim S., Betka A., Drid S., Becherif M. Implementation of MRAC controller of a DFIG based variable speed grid connected wind turbine. *Energy Conversion and Management*, 2014, vol. 79, pp. 281-288. doi: https://doi.org/10.1016/j.enconman.2013.12.003.
7. Hemeyine A., Abbou A., Tidjani N., Mokhlis M., Bakouri A. Robust Takagi Sugeno Fuzzy Models control for a Variable Speed Wind Turbine Based a DFI-Generator. *International Journal of Intelligent Engineering and Systems*, 2020, vol. 13, no. 3, pp. 90-100. doi: https://doi.org/10.22266/ijies2020.0630.09.
8. Hemeyine A.V., Abbou A., Bakouri A., Labbadi M., El Moustapha S.M.o.M. Power Control for Wind Turbine Driving a Doubly Fed Induction Generator using Type-2 Fuzzy Logic Controller. *2019 7th International Renewable and Sustainable Energy Conference (IRSEC)*, 2019, pp. 1-6. doi: https://doi.org/10.1109/IRSEC48032.2019.9078146.
9. Lei Y., Mullane A., Lightbody G., Yacamini R. Modeling of the Wind Turbine With a Doubly Fed Induction Generator for Grid Integration Studies. *IEEE Transactions on Energy Conversion*, 2006, vol. 21, no. 1, pp. 257-264. doi: https://doi.org/10.1109/TEC.2005.847958.
10. Cheikh R., Menacer A., Drid S. Robust control based on the Lyapunov theory of a grid-connected doubly fed induction generator. *Frontiers in Energy*, 2013, vol. 7, no. 2, pp. 191-196. doi: https://doi.org/10.1007/s11708-013-0245-y.
11. Bodson M., Chiasson J. Differential-geometric methods for control of electric motors. *International Journal of Robust and Nonlinear Control*, 1998, vol. 8, no. 11, pp. 923-954. doi: https://doi.org/10.1002/(SICI)1099-1239(199809)8:11<923::AID-RNC369>3.0.CO;2-S.
12. Mahboub M.A., Drid S., Sid M.A., Cheikh R. Robust direct power control based on the Lyapunov theory of a grid-connected brushless doubly fed induction generator. *Frontiers in Energy*, 2016, vol. 10, no. 3, pp. 298-307. doi: https://doi.org/10.1007/s11708-016-0411-0.
13. Khalil H.K. Adaptive output feedback control of nonlinear systems represented by input-output models. *IEEE Transactions on Automatic Control*, 1996, vol. 41, no. 2, pp. 177-188. doi: https://doi.org/10.1109/9.481517.
14. Drid S., Makouf A., Nait-Said M.S, Tadjine M. The doubly fed induction generator robust vector control based on Lyapunov Method. *Transactions on Systems, Signals & Devices*, 2009, vol. 4, no. 2, pp. 237-249.
15. Kaddache M., Drid S., Khemis A., Rahem D., Chrifi-Alaoui L., Drid M.D. Fuzzy-type-2 maximum power tracking controller of the double fed wind generator. *2022 IEEE 21st International Conference on Sciences and Techniques of Automatic Control and Computer Engineering (STA)*, 2022, pp. 512-515. doi: https://doi.org/10.1109/STA56120.2022.10019178.
16. Kim I.-S., Kim M.-B., Youn M.-J. New Maximum Power Point Tracker Using Sliding-Mode Observer for Estimation of Solar Array Current in the Grid-Connected Photovoltaic System. *IEEE Transactions on Industrial Electronics*, 2006, vol. 53, no. 4, pp. 1027-1035. doi: https://doi.org/10.1109/TIE.2006.878331.
17. Hessad M.A., Bouchama Z., Benaggoune S., Behih K. Cascade sliding mode maximum power point tracking controller for photovoltaic systems. *Electrical Engineering & Electromechanics*, 2023, no. 1, pp. 51-56. doi: https://doi.org/10.20998/2074-272X.2023.1.07.
18. Abid M., Laribi S., Larbi M., Allaoui T. Diagnosis and localization of fault for a neutral point clamped inverter in wind energy conversion system using artificial neural network technique. *Electrical Engineering & Electromechanics*, 2022, no. 5, pp. 55-59. doi: https://doi.org/10.20998/2074-272X.2022.5.09.
19. Akkouchi K., Rahmani L., Lebied R. New application of artificial neural network-based direct power control for permanent magnet synchronous generator. *Electrical Engineering & Electromechanics*, 2021, no. 6, pp. 18-24. doi: https://doi.org/10.20998/2074-272X.2021.6.03.
20. Khemis A., Boutabba T., Drid S. Model reference adaptive system speed estimator based on type-1 and type-2 fuzzy logic sensorless control of electrical vehicle with electrical differential. *Electrical Engineering & Electromechanics*, 2023, no. 4, pp. 19-25. doi: https://doi.org/10.20998/2074-272X.2023.4.03.
21. Sahraoui H., Mellah H., Drid S., Chrifi-Alaoui L. Adaptive maximum power point tracking using neural networks for a photovoltaic systems according grid. *Electrical Engineering & Electromechanics*, 2021, no. 5, pp. 57-66. doi: https://doi.org/10.20998/2074-272X.2021.5.08.

Received 20.07.2023
Accepted 03.10.2023
Published 02.03.2024

M. Kaddache[1], *PhD Student*,
S. Drid[2], *PhD*, *Professor*,
A. Khemis[3], *Doctor of Technical Science*, *Associate Professor*,
D. Rahem[1], *PhD*, *Professor*,
L. Chrifi-Alaoui[4], *PhD*, *Professor*,
[1] Laboratoire de Génie Electrique et Automatique (LGEA),
University of Oum El Bouaghi,
B.P 358 Route de Constantine, Oum El Bouaghi, 04000, Algeria,
e-mail: kaddache.mouna@gmail.com; rahem_djamel@yahoo.fr
[2] Higher National School of Renewable Energies, Environment and Sustainable Development,
53, Constantine Road, Fesdis, Batna, 05078, Algeria,
e-mail: s.drid@hns-re2sd.dz (Corresponding Author)
[3] University of Khenchela,
El-Hamma, BP 1252 Road of Batna, Khenchela, 40004, Algeria,
e-mail: khemis05@yahoo.fr
[4] Laboratoire des Technologies Innovantes (LTI),
University of Picardie Jules Verne, Amiens, 80000, France,
e-mail: larbi.alaoui@u-picardie.fr

How to cite this article:
Kaddache M., Drid S., Khemis A., Rahem D., Chrifi-Alaoui L. Maximum power point tracking improvement using type-2 fuzzy controller for wind system based on the double fed induction generator. *Electrical Engineering & Electromechanics*, 2024, no. 2, pp. 61-66. doi: https://doi.org/10.20998/2074-272X.2024.2.09

UDC 621.313.332 https://doi.org/10.20998/2074-272X.2024.2.10

L.I. Mazurenko, O.V. Dzhura, M.O. Shykhnenko

Steady-state analysis of a hybrid power supply system using an induction generator with a shunt AC/DC converter

Hybrid power supply systems (HPSSs) are considered as a good option for electric power supply of remotely located from the grid consumers due to significant fuel savings compared to diesel sets. Quick development and improvement of HPSSs may be achieved using specialized methodologies and programs. In the paper a schematic diagram is proposed and operation principles of a 400 V / 50 Hz HPSS were developed. The system's main component is the master generating unit of the hydropower plant using a 250 kW induction generator (IG). The voltage of the system is controlled by the controller of the AC/DC power converter. The electrical frequency of the system is controlled by the speed controller of the hydropower turbine. A wind turbine, an energy storage system and a regulated dump load are connected to the IG through the AC/DC converter. ***Goal.*** *The paper aims to develop a methodology for steady state performance analysis of the hydraulic turbine driven isolated IG operating in parallel through an AC/DC power converter with additional sources and consumers of active power.* ***Methodology.*** *The methodology for evaluation of performance characteristics of the IG operating in the proposed system has been developed. The methodology is based on the equivalent circuit of the system, equations of active and reactive power balance in the system and the superposition method.* ***Results.*** *The equations of frequency, voltage and power regulators of the system are given. The performance characteristics of the IG operating in the system supplying resistive and RL load in «constant voltage – constant frequency» mode are obtained.* ***Novelty.*** *The developed methodology is innovative in taking into account the control algorithms of the system. The comparative analysis of the IG's performance operating in the stand-alone generating unit and in the generating unit connected to the proposed system is performed.* ***Practical value.*** *The developed methodology can be used for development and performance improvement of hybrid AC power systems.* References 19, table 1, figures 4.
Key words: **hybrid power system, induction generator, superposition method, equivalent circuit.**

Гібридні системи електропостачання (ГСЕ) розглядаються як хороший варіант для електропостачання віддалених від мережі споживачів завдяки значній економії палива порівняно з дизель-агрегатами. Швидка розробка і вдосконалення ГСЕ можуть бути досягнуті за допомогою спеціалізованих методик і програм. В статті запропоновано схемне рішення та розроблено принципи роботи ГСЕ промислової напруги і частоти 400 В / 50 Гц. Система побудована на основі ведучого гідроелектроагрегата з асинхронним генератором (АГ) потужністю 250 кВт. Стабілізація напруги системи забезпечується силовим AC/DC перетворювачем, а стабілізація електричної частоти системи – регулятором частоти обертання гідротурбіни. Вітроустановка, накопичувач енергії і регульоване баластне навантаження підключаються до АГ через AC/DC перетворювач. ***Метою*** *роботи є розробка методики розрахунку характеристик автономного АГ з гідротурбінним приводом, що працює паралельно через AC/DC перетворювач з додатковими джерелами та споживачами активної потужності. Розроблено* ***методику*** *розрахунку характеристик АГ запропонованої системи. Розроблена методика базується на основі еквівалентної схеми заміщення системи, рівнянь балансу активної і реактивної потужності та методу накладання. Наведено рівняння регуляторів частоти, напруги і потужності системи. З допомогою розробленої методики виконано розрахунки характеристик АГ за активного і активно-індуктивного навантаження споживачів при умові підтримання постійного значення напруги АГ і електричної частоти в системі. Створена методика має* ***новизну*** *в частині врахування алгоритмів керування системою. Проведено аналіз і співставлення характеристик АГ отриманих за його роботи в складі гідроелектроагрегата працюючого автономно і в складі запропонованої системи.* ***Отримані результати*** *можуть бути використані при розробці та для покращення технічних характеристик гібридних систем електропостачання змінного струму.* Бібл. 19, табл. 1, рис. 4.
Ключові слова: **гібридна система електропостачання, асинхронний генератор, метод накладання, схема заміщення.**

Introduction. Isolated power supply systems and modern distributed generation systems are capable to operate off-grid thus ensuring elimination of interruptions in power supply during grid outages and blackouts. These systems can reduce the cost of construction and losses of both power transmission and distribution lines caused by power transmission to local consumers located remotely from power transmission lines [1-4]. Photovoltaic systems, wind turbines (WTs), hydropower turbine equipped generating units (HTGUs), geothermal power plants, etc. are often combined with each other in distributed generation and isolated power supply systems to improve their performance. Electric power generating systems using different renewable primary energy sources are called hybrid power supply systems (HPSSs). When necessarily to provide a more reliable power supply, diesel power sets may be integrated in the HPSSs.

Today's power ratings of HTGUs, WTs and diesel power sets used in HPSSs are generally in the range 3-4 MW. WTs and HTGUs of this power range may be designed using permanent magnet generators, synchronous generators, doubly-fed and squirrel cage IGs [5-7]. The efficiencies of permanent magnet generators and synchronous generators are somewhat higher comparing to IGs, but IGs are simpler to service and repair. Moreover, due to lower price and lower maintenance costs, IGs are paid off sooner.

The solution of problems related to the performance analysis and evaluation of indicators of efficiency of energy conversion of IGs driven by regulated prime movers, such as hydraulic turbines (HTs) and diesel engines (DEs), has been successfully carried out and reported in the literature [8-10]. At the same time it should be noted, that methodologies developed for the steady-state analysis of stand-alone IGs using IG equivalent circuit are not adapted for performance analysis of IGs operating in parallel with various electric power sources within off-grid HPSSs. The study of the performance characteristics of IGs interconnected to electromechanical systems is a more complex objective requiring the development of complex mathematical

models [11, 12]. Complex dynamic models are a powerful tool for scientific investigations but they require a lot of computational efforts and time for debugging. Therefore, development of static mathematical models and new universal methodologies suitable for performing such studies or revision of existing ones is up to date.

The purpose of the article is to develop and test a methodology for steady state performance analysis of the induction generator driven by a hydraulic turbine of the master hydropower turbine equipped generating unit and operating in «constant voltage – constant frequency» mode in parallel through an electronic AC/DC power converter with sources and consumers of active power in the hydro-wind-battery hybrid power supply system supplying a three phase load.

Configuration and operating principles of the HPSS. The proposed HPSS (Fig. 1) consist of a master-HTGU with IG, a variable speed WT, an energy storage system (ESS) and a regulated dump load (RDL). The G2 generator of the WT is connected to the IG G1 through AC/DC voltage source converters VSC1 and VSC2. Both RDL and ESS are connected to the IG G1 through the VSC1. Power VSCs allow performing smooth power control of the sources of electric energy [13, 14]. The ESS can be of different types: flywheel ESS, battery ESS, supercapacitor based, etc. [15, 16]. The HPSS of Fig. 1 can operate both on-grid and off-grid. The HTGU consists of the IG G1, a regulated HT, the VSC1 converter and a bank of compensation capacitors (BCC) for self-excitation of the IG when the HPSS is off-grid. If hydro energy is unavailable in the region, diesel engines (DEs) may be used instead of HTs. Regulation of the electrical frequency in the system is carried out by the speed controller of the HT or DE. The controller of the WT uses wind speed and rotational speed of the WT for output power control of the wind generator. The ESS is provided to reduce frequency overshoot in transient modes and to limit the active power of the IG G1 during short-term peak demand. The RDL is intended mainly to consume active power excess in the system when the ESS is fully charged. It can also be used for «frequency-responsive» spinning reserve regulation [17, 18].

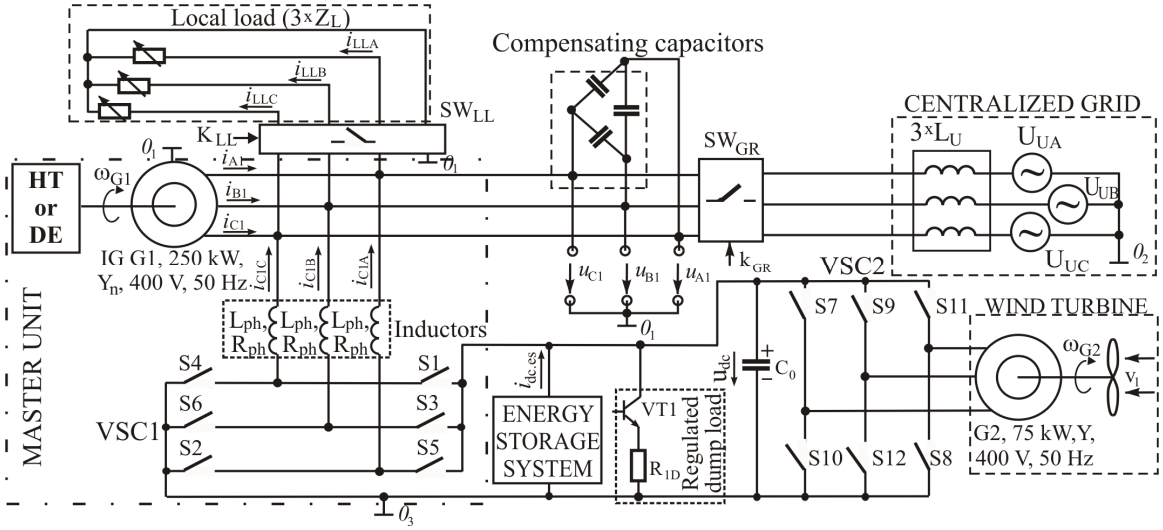

Fig. 1. Schematic diagram of the hybrid power supply system

Equations of frequency, voltage and power controllers are as follows.

- AC voltage, DC voltage and HTGU speed controllers

$$U_g^* = \text{const}; \quad (1)$$

$$U_{dc}^* = \text{const}; \quad (2)$$

$$\omega_e^* = \text{const}. \quad (3)$$

- RDL controller

$$P_{DL}^* = P_{EX}^* + \Delta P_{DL}^*, \quad (4)$$

where

$$\Delta P_{DL}^* = \begin{cases} -\Delta P_{EL}^*, \ \Delta P_{EL}^* < 0 \text{ and } \omega_{\min}^* < \omega_e < \omega_{\max}^*; \\ \Delta P_{DL1}^*, \text{ ESS is charged and } \omega_e > \omega_{\max}^*; \\ \Delta P_{DL2}^*, \text{ ESS is discharged and } \omega_e < \omega_{\min}^*; \\ 0, \text{ else}; \end{cases}$$

$$\Delta P_{EL}^* = P_L + P_{EX}^* - P_{WG} - P_{ES};$$

$$\Delta P_{DL1}^* = \max\left(0, \tilde{\omega}_{\max} k_{p1} + \int \tilde{\omega}_{\max} k_{i1}\right);$$

$$\Delta P_{DL2}^* = \max\left(-P_{EX}^*, \tilde{\omega}_{\min} k_{p1} + \int \tilde{\omega}_{\min} k_{i1}\right);$$

$$\tilde{\omega}_{\min} = \omega_e - \left(\omega_{\min}^* + \omega_h^*\right), \ \tilde{\omega}_{\max} = \omega_e - \left(\omega_{\max}^* - \omega_h^*\right).$$

- ESS controller

$$P_{ES}^* = \begin{cases} P_{ES1}^*, \text{ ESS is charged and } \omega_e > \omega_{\min}^*; \\ P_{ES2}^*, \text{ ESS is charged and } \omega_e < \omega_{\min}^*; \\ P_{ES3}^*, \text{ ESS is discharged, } \omega_e > \omega_{\min}^* \\ \quad \text{and } I_g < k_{gI} I_{gN}; \\ P_{ES4}^*, \text{ ESS is discharged and } \omega_e > \omega_{\max}^*; \\ 0, \text{ else}, \end{cases} \quad (5)$$

where

$$P_{ES1}^* = \max\left(0, \tilde{I}_{g.\max} k_{p2} + \int \tilde{I}_{g.\max} k_{i2}\right);$$

$$P_{ES2}^* = \max\left(0, -\tilde{\omega}_{\min} k_{p2} - \int \tilde{\omega}_{\min} k_{i2}\right);$$

$$P_{ES3}^* = -I_{dc.es}^* U_{dc};$$

$$P_{ES4}^* = \min\left(0, -\tilde{\omega}_{\max} k_{p2} - \int \tilde{\omega}_{\max} k_{i2}\right);$$

$$\tilde{I}_{g.\max} = I_g - I_{g.\max}^*.$$

The WT speed control is described in [17].

In the above equations U_g^* is the RMS reference value of phase voltage of the IG; ω_e^* is the angular electrical frequency reference in the system; U_{dc}^* is the DC-side voltage reference of the VSC1; P_{EX}^* is the «frequency-responsive» spinning reserve reference regulated with the RDL controller; P_L – is the active power demand; P_{WG} is the output active power of the WT; P_{ES}^* is the output power of the ESS assumed to be of positive sign while discharging of the ESS; P_{DL}^* is the active power reference of the RDL; I_g, $I_{g.\max}^*$, I_{gN} are values of actual, maximum reference and nominal RMS phase current of the IG; k_{p1}, k_{i1}, k_{p2}, k_{i2}, k_{gI} are positive constants; $\omega_{\max}^*$, $\omega_{\min}^*$, ω_e are values of maximum frequency reference, minimum frequency reference and actual angular electrical frequency in the system; $0 < \omega_h^* << \left(\omega_{\max}^* - \omega_{\min}^*\right) \cdot 0{,}5$; $I_{dc.es}^*$ is the input current reference of the ESS.

It is clear from (4), that when the sum of the active power demand of the local load and spinning reserve reference $P_L + P_{EX}^*$ is greater than the total output power of the WT and ESS and $\omega_{\min}^* < \omega_e < \omega_{\max}^*$, then $P_{DL} = P_{EX}^*$. When $P_{EX}^* < P_{WG} + P_{ES} - P_L$, we have an excess of active power in the system. In this case, if $\omega_{\min}^* < \omega_e < \omega_{\max}^*$, the power of the RDL is equal to $P_{DL}^* = P_{WG} + P_{ES} - P_L$ and the output active power of the IG is zero. If the electrical frequency in the system exceeds $\left(\omega_{\min}^* ... \omega_{\max}^*\right)$ limits and with current state of charge the ESS cannot perform frequency regulation, then the RDL performs this objective within the limits of its functional capabilities.

When the ESS is charged, as can be seen from (5), if $\omega_{\min}^* < \omega_e$, the ESS controller limits the current value of the generator to the $I_{g.\max}^*$ value level or, if the ω_e value falls below $\omega_{\min}^*$, it adjusts the ω_e value to the $\omega_{\min}^* + \omega_h^*$ level. At the same time, in accordance with (3), the frequency of the HPSS of Fig. 1 is regulated by the speed controller of the HTGU.

When the ESS is discharged and the output active power of the IG is sufficiently lower than its rated output and $\omega_{\min}^* < \omega_e$, then the ESS is being charged. At the same time, the value of the ESS power consumed is regulated by adjusting the value of the current $I_{dc.es}^*$. If there is a frequency error such that $\omega_e > \omega_{\max}^*$, and the ESS is discharged, then the controller of the ESS adjusts the ω_e value to the $\omega_{\max}^* - \omega_h^*$ level.

The methodology for performance analysis of the IG operating in the HPSS. To obtain performance characteristics of the HPSS, we will use shown in Fig. 2 proposed equivalent circuit (EC) of the system where all components of the system of Fig. 1 are represented by equivalent impedances.

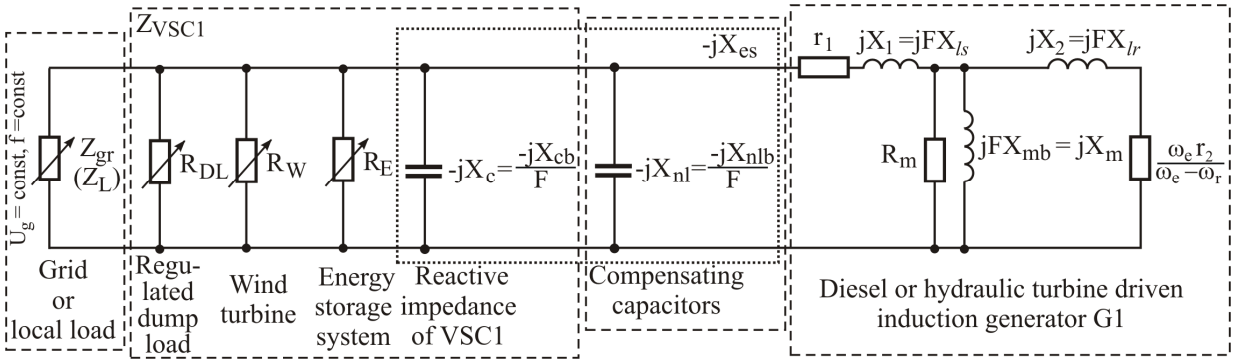

Fig. 2. Equivalent circuit of the hybrid power supply system

In Fig. 2 r_1, r_2, X_1, X_2 are the stator and rotor resistance and leakage reactance; ω_r is the electrical angular speed of the rotor of the IG; R_m is the core loss resistance; $F = \omega_e/\omega_{eN}$ is the per unit stator frequency of the IG; ω_{eN} is the nominal angular frequency of the stator; X_m is the magnetizing reactance; R_{DL}, R_W, R_E are equivalent resistances of RDL, WT and ESS. The values of reactances X_{ls}, X_{lr}, X_{cb}, X_{nlb}, X_{mb} refer to the base (rated) frequency of 50 Hz.

If we assume U_g = const and ω_e = const the EC of Fig. 2 can be used for performance analysis of the IG operating both in the off-grid HPSS supplying local load with Z_L impedance and on-grid with Z_{gr} input impedance of the grid.

To maintain the balance between power supply and demand for active and reactive power in the EC of Fig. 2, both real and imaginary part of the sum of admittances Y_S, Y_m and Y_R must be zero

$$\mathrm{Re}\left(Y_S + Y_m + Y_R\right) = 0; \quad (6)$$

$$\mathrm{Im}\left(Y_S + Y_m + Y_R\right) = 0, \quad (7)$$

where

$$Y_S = \left(r_1 + jX_1 - \frac{jX_{es}Z_{eq}}{Z_{eq} - jX_{es}} \right)^{-1};$$

$$Y_m = \frac{1}{jX_m} + \frac{1}{R_m}; \quad Y_R = \frac{1}{jX_2 + r_2/s};$$

$$X_{es} = X_c + X_{nl}; \quad Z_L = R_L + jX_L = z_l e^{j\varphi_L};$$

$$Z_{eq} = 1/\left(\left(Z_L\right)^{-1} + \left(R_{DL}\right)^{-1} + \left(R_W\right)^{-1} + \left(R_E\right)^{-1}\right) =$$

$$= z_{eq} e^{j\varphi_{eq}} = R_{eq} + jX_{eq};$$

$$s = (\omega_e - \omega_r)/\omega_e .$$

Let F = 1. Then from (6) the slip of the IG can be given by

$$s = r_2\left(\sqrt{1-4a_0X_{lr}^2}-1\right)/\left(2a_0X_{lr}^2\right), \quad (8)$$

and from (7) the magnetizing reactance of the IG can be obtained as

$$X_m = X_{mb} = b_0\left(r_2^2 + X_{lr}^2 s^2\right)/\left(\left(b_1X_{lr}^2 - b_0X_{lr}\right)s^2 + b_1r_2^2\right), \quad (9)$$

where

$$a_0 = \frac{a_1R_m + \left(a_1^2 + a_2^2\right)}{\left(a_1^2 + a_2^2\right)R_m}; \quad a_1 = r_1 + \frac{X_{es}^2R_{eq}}{a_3};$$

$$a_2 = X_{ls} - \frac{R_{eq}^2X_{es}}{a_3} - \frac{X_{eq}X_{es}\left(X_{eq} - X_{es}\right)}{a_3};$$

$$a_3 = R_{eq}^2 + \left(X_{eq} - X_{es}\right)^2; \quad b_0 = a_1^2 + a_2^2; \quad b_1 = -a_2 .$$

The air gap voltage of the IG U_m can be determined from the $X_m = U_{mb}(X_{mb})$ curve obtained from the synchronous speed test at rated speed.

The rotor electrical speed, phase current, phase voltage and per-phase input admittance of the IG are computed using the following equations

$$\omega_r = (1-s)\omega_e ; \quad (10)$$

$$I_{ph} = U_mY_S ; \quad (11)$$

$$U_{ph} = -jI_{ph}X_{es}z_{eq}e^{j\varphi_{eq}}/\left(z_{eq}e^{j\varphi_{eq}} - jX_{es}\right); \quad (12)$$

$$y_1 = \left(r_1 + jX_{ls} + \left(Y_m + Y_R\right)^{-1}\right)^{-1} = 0 . \quad (13)$$

It should be noted that the EC of Fig. 2 allows us to analyze not all the operating modes of the HPSS of Fig. 1, but only those in which the condition ω_e = const or ω_r = const is valid.

The methodology for performance analysis of the IG driven by the HT of the master-HTGU and operating in the proposed system of Fig. 1 is outlined as follows.

At first, we will obtain the performance characteristics of the stand-alone IG.

1. Set up the power factor of the load $\cos\varphi_L$, a $k1\times1$ column vector of the impedance of the local load $\boldsymbol{Z_L}$ and a $h1\times1$ column vector of trial values of the total reactive impedance of the BCC and VSC1 $\boldsymbol{X_{es}^{ig}}$

$$\boldsymbol{Z_L} = \left(z_{k,h}\right)_{k1\times1}, \quad \boldsymbol{X_{es}^{ig}} = \left(x_{h,k}\right)_{h1\times1} . \quad (14)$$

2. Find the elements of the air gap voltage matrix using magnetization characteristic of the IG and (9), phase current and voltage matrixes according to (11), (12), slip and input admittance matrixes of the IG according to (8), (13) using all combinations of elements of $\boldsymbol{Z_L}$ and $\boldsymbol{X_{es}^{ig}}$ vectors

$$\boldsymbol{U_m^{ig}} = \left(um_{k,h}\right)_{k1\times h1}, \quad \boldsymbol{I_{ph}^{ig}} = \left(iph_{k,h}\right)_{k1\times h1},$$

$$\boldsymbol{U_{ph}^{ig}} = \left(uph_{k,h}\right)_{k1\times h1}, \quad \boldsymbol{SI^{ig}} = \left(s_{k,h}\right)_{k1\times h1}, \quad (15)$$

$$\boldsymbol{YI^{ig}} = \left(y1_{k,h}\right)_{k1\times h1}.$$

3. Set the phase voltage reference of the IG and in each row of the $\boldsymbol{U_m^{ig}}$ (k = const, h = var) array determine the number of the column corresponding to the minimum deviation of the actual voltage from the reference $U_g^* = \text{const}$. Save the found column numbers into a one-dimensional array. Further, from the matrices (15), we form $k1\times1$ column vectors of the air gap voltage $\boldsymbol{U_m^{ig,uc}}$, phase current $\boldsymbol{I_{ph}^{ig,uc}}$, phase voltage $\boldsymbol{U_{ph}^{ig,uc}}$, input admittance of the IG $\boldsymbol{YI^{ig,uc}}$, slip $\boldsymbol{SI^{ig,uc}}$, electrical angular speed of the rotor $\boldsymbol{W_r^{ig,co}}$ and the total reactive impedance of the BCC and VSC1 $\boldsymbol{X_{es}^{ig,uc}}$ ensuring the performance with the least voltage error for each load value .

4. From the $\boldsymbol{X_{es}^{ig,uc}}$ vector we find the reactive impedance of the BCC $X_{nl} = X_{es}^{ig,uc}[i1]$, where the index $i1$ corresponds to the element with maximum impedance of the local load array $Z_L[i1] = \max\left(z_{k,h}\right)_{k1\times1}$.

5. Find the elements of the per-phase reactance, the phase current and the apparent power of the VSC1 arrays $\boldsymbol{X_{VSC1}^{ig,uc}}$, $\boldsymbol{I_{VSC1}^{ig,uc}}$, $\boldsymbol{S_{VSC1}^{ig,uc}}$, the power factor array and efficiency array $\boldsymbol{PF_{IG}^{ig,uc}}$, $\boldsymbol{EF_{IG}^{ig,uc}}$ of the IG

$$X_{VSC1}^{ig,uc}[k] = \left(\frac{1}{X_{es}^{ig,uc}[k]} - \frac{1}{X_{nl}}\right)^{-1}; \quad (16)$$

$$I_{VSC1}^{ig,uc}[k] = \frac{U_{ph}^{ig,uc}[k]}{X_{VSC1}^{ig,uc}[k]}; \quad (17)$$

$$S_{VSC1}^{ig,uc}[k] = Q_{VSC1}^{ig,uc}[k] = 3\frac{\left|U_{ph}^{ig,uc}[k]\right|^2}{X_{VSC1}^{ig,uc}[k]}; \quad (18)$$

$$PF_{IG}^{ig,uc}[k] = \frac{\mathrm{Re}\left(Y1^{ig,uc}[k]\right)}{\left|Y1^{ig,uc}[k]\right|}; \quad (19)$$

$$EF_{IG}^{ig,uc}[k] = \frac{P_L^{ig,uc}[k]}{P_L^{ig,uc}[k] + P_{Cu}^{ig,uc}[k] + P_{Fe}^{ig,uc}[k] + P_{Fr}^{ig,uc}[k]}, \quad (20)$$

where $P_{Cu}^{ig,uc}[k] = P_{Cu1}^{ig,uc}[k] + P_{Cu2}^{ig,uc}[k]$; $\boldsymbol{P_L^{ig,uc}}$, $\boldsymbol{P_{Cu1}^{ig,uc}}$, $\boldsymbol{P_{Cu2}^{ig,uc}}$, $\boldsymbol{P_{Fe}^{ig,uc}}$, $\boldsymbol{P_{Fr}^{ig,uc}}$ are column vectors of real power of the load, stator copper losses, rotor copper losses, core losses and friction losses;

$$P_L^{ig,uc}[k] = 3\frac{\left(U_{ph}^{ig,uc}[k]\right)^2}{\left|Z_L[k]\right|}\cos\varphi_L ;$$

$$P_{Cu1}^{ig,uc}[k] = 3\left(I_{ph}^{ig,uc}[k]\right)^2 r_1 ;$$

$$P_{Cu2}^{ig,uc}[k] = 3\left|\frac{U_m^{ig,uc}[k]}{jX_{lr} + r_2/S1^{ig,uc}[k]}\right|^2 r_2 ;$$

$$P_{Fe}^{ig,uc}[k] = 3R_m\left|\frac{U_m^{ig,uc}[k]}{R_m}\right|^2; \quad P_{Fr}^{ig,uc}[k] = k_{Fr}FP_{gN} ;$$

k_{Fr} – friction coefficient; P_{gN} – nominal power of the IG.

Next, we will use the principle of superposition and compute the performance characteristics of the IG operating in the system of Fig. 1 by superposition of power curves of other elements and power curves of the stand-alone IG. The principle and method of superposition are applied to determine currents and voltages in linear circuits and sometimes for obtaining performance characteristics of AC systems with parallel power sources [19]. For the off-grid mode of the HPSS of Fig. 1 when the Fig. 2 EC is used, the relation between the active power of the IG and the active power of the load due to the power transmission losses neglected is linear. Other elements such as WT, RDL and ESS are represented in the EC by linear resistances. Therefore, the principle of superposition can be applied in this case.

Assume the ESS is charged and the output power of the WT P_{WG} is constant. First, let's add WT and RDL to the stand-alone HTGU with IG, assuming that ESS has no influence on the control of the RDL. Accordingly to (4) and (5) if $\omega^*_{\min} < \omega_e < \omega^*_{\max}$, this is possible under the condition that the ESS is not used or the ESS controller limits the current value of the IG when $\Delta P^*_{EL} \ge 0$, i.e. when there is no excess of active power in the system. The said condition in the system of Fig. 1 will be satisfied if the charged ESS will not be discharged in the no load mode of the IG, that is, practically always in steady state. Taking into account the above assumptions, in the absence of a steady state power error, the power of the RDL will be given by

$$P_{DL}[k] = P^*_{EX} + \Delta P^*_{DL}[k], \quad (21)$$

where

$$\Delta P^*_{DL}[k] = \begin{cases} 0, P_{WG} - P^{ig,uc}_L[k] < P^*_{EX} \\ P_{WG} - P^{ig,uc}_L[k] - P^*_{EX}, P_{WG} - P^{ig,uc}_L[k] \ge P^*_{EX} \end{cases}.$$

6. Determine the active power of the IG when the RDL and WT are connected (ON) and the ESS is disconnected (OFF) from the HPSS

$$P^{WD}_{IG}[k] = P^{ig,uc}_L[k] + P_{DL}[k] - P_{WG}. \quad (22)$$

7. The phase current of the IG when the RDL and WT are ON and the ESS is OFF can be obtained by interpolation of the relation between values of elements of the array of the real power of the load $\boldsymbol{P^{ig,uc}_L}$ and the array of the phase current values $\boldsymbol{I^{ig,uc}_{ph}}$ of the stand-alone IG

$$I^{WD}_{ph}[k] = \text{inter}\left(\boldsymbol{P^{ig,uc}_L}, \boldsymbol{I^{ig,uc}_{ph}}, P^{WD}_{IG}[k]\right). \quad (23)$$

The next step is to add the ESS to the system and determine the following values.

8. The ESS power provided there is no steady state power error

$$P_{ES}[k] = \begin{cases} 0, I^{WD}_{ph}[k] < I^*_{g.\max}; \\ P^{WD}_{IG}[k] - P^*_{g.\max}, I^{WD}_{ph}[k] \ge I^*_{g.\max}, \end{cases} \quad (24)$$

where $P^*_{g.\max} = \text{inter}\left(\boldsymbol{I^{WD}_{ph}}, \boldsymbol{P^{WD}_{IG}}, I^*_{g.\max}\right)$ is real power of the IG with ESS is OFF and $I_{ph} = I^*_{g.\max}$.

9. Real power of the IG when RDL ,WT and ESS are ON

$$P^{WDE}_{IG}[k] = P^{ig,uc}_L[k] + P_{DL}[k] - P_{WG} - P_{ES}[k]. \quad (25)$$

10. Equivalent impedance of the per-phase load of the IG when RDL ,WT and ESS are ON

$$Z^{WDE}_L[k] = \left(\frac{1}{Z_L[k]} + \frac{P_{DL}[k] - P_{WG} - P_{ES}[k]}{3\left(U^*_g\right)^2} \right)^{-1} = \quad (26)$$

$$= \left(1/Z_L[k] + 1/R^{WDE}_{VSC1}[k]\right)^{-1},$$

where $\boldsymbol{R^{WDE}_{VSC1}}$ is the column vector of the per-phase equivalent resistances of the VSC1

11. Repeat steps 2–5 using the $\boldsymbol{Z^{WDE}_L}$ array instead of the $\boldsymbol{Z_L}$ array. As a result, we get new $k1\times1$ air gap voltage array $\boldsymbol{U^{WDE}_m}$, phase current array $\boldsymbol{I^{WDE}_{ph}}$, phase voltage array $\boldsymbol{U^{WDE}_{ph}}$, input admittance array of the IG $\boldsymbol{Y1^{WDE}}$, slip array $\boldsymbol{S1^{WDE}}$, electrical angular speed array of the rotor $\boldsymbol{W^{WDE}_r}$, total per phase reactance of the BCC and VSC1 array $\boldsymbol{X^{WDE}_{es}}$, and reactance array of the VSC1 when RDL ,WT and ESS are ON $\boldsymbol{X^{WDE}_{VSC1}}$.

Compute the elements of the following arrays for the «full» HPSS (RDL ,WT and ESS are ON).

12. The per phase impedance array and phase current array of the VSC1

$$Z^{WDE}_{VSC1}[k] = -jX^{WDE}_{VSC1}[k] + R^{WDE}_{VSC1}[k]; \quad (27)$$

$$I^{WDE}_{VSC1}[k] = U^{WDE}_{ph}[k] / Z^{WDE}_{VSC1}[k]. \quad (28)$$

13. The real power array, reactive power array and apparent (total) power array of the VSC1

$$P^{WDE}_{VSC1}[k] = -3\left|U^{WDE}_{ph}[k]\right|^2 / R^{WDE}_{VSC1}[k]; \quad (29)$$

$$Q^{WDE}_{VSC1}[k] = 3\left|U^{WDE}_{ph}[k]\right|^2 / X^{WDE}_{VSC1}[k]; \quad (30)$$

$$S^{WDE}_{VSC1}[k] = \sqrt{\left(P^{WDE}_{VSC1}[k]\right)^2 + \left(Q^{WDE}_{VSC1}[k]\right)^2}. \quad (31)$$

14. The power factor array $\boldsymbol{PF^{WDE}_{IG}}$ and efficiency array $\boldsymbol{EF^{WDE}_{IG}}$ of the IG are determined from (19), (20) using $\boldsymbol{Y1^{WDE}}$, $\boldsymbol{I^{WDE}_{ph}}$, $\boldsymbol{U^{WDE}_{ph}}$, $\boldsymbol{U^{WDE}_m}$, $\boldsymbol{S1^{WDE}}$ arrays instead of $\boldsymbol{Y1^{ig,uc}}$, $\boldsymbol{I^{ig,uc}_{ph}}$, $\boldsymbol{U^{ig,uc}_{ph}}$, $\boldsymbol{U^{ig,uc}_m}$, $\boldsymbol{S1^{ig,uc}}$ arrays.

Results. The performance analysis of the 250 kW IG operating both in the stand-alone HTGU and in the HTGU of the HPSS of Fig. 1 was carried out using the explained above methodology with values of the power factor of the load 1 (Fig. 3) and 0.9 (Fig. 4). It was set $P^*_{EX} = 0.1$ p.u., P_{WG} = 0.3 p.u., $U^*_g = 1$ p.u. and $I^*_{g.\max} = 1$ p.u.

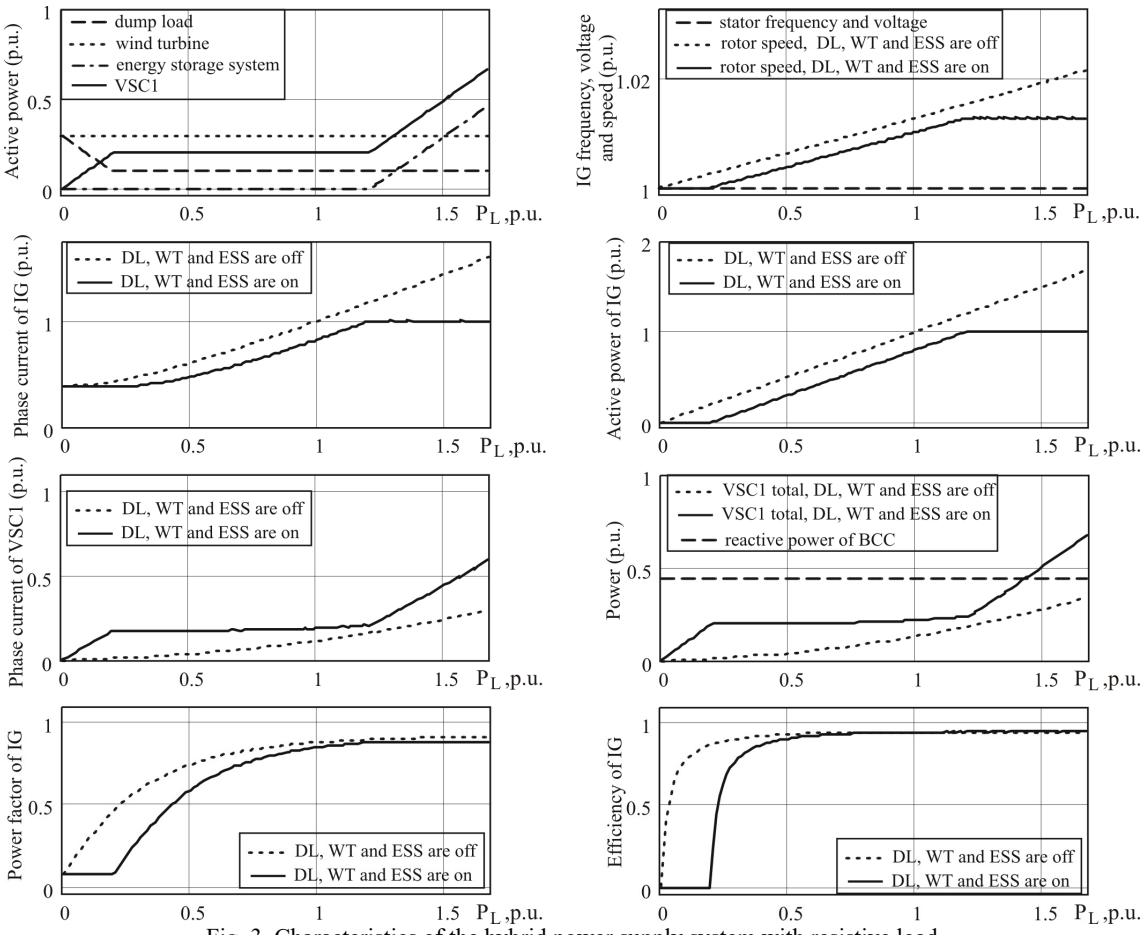

Fig. 3. Characteristics of the hybrid power supply system with resistive load

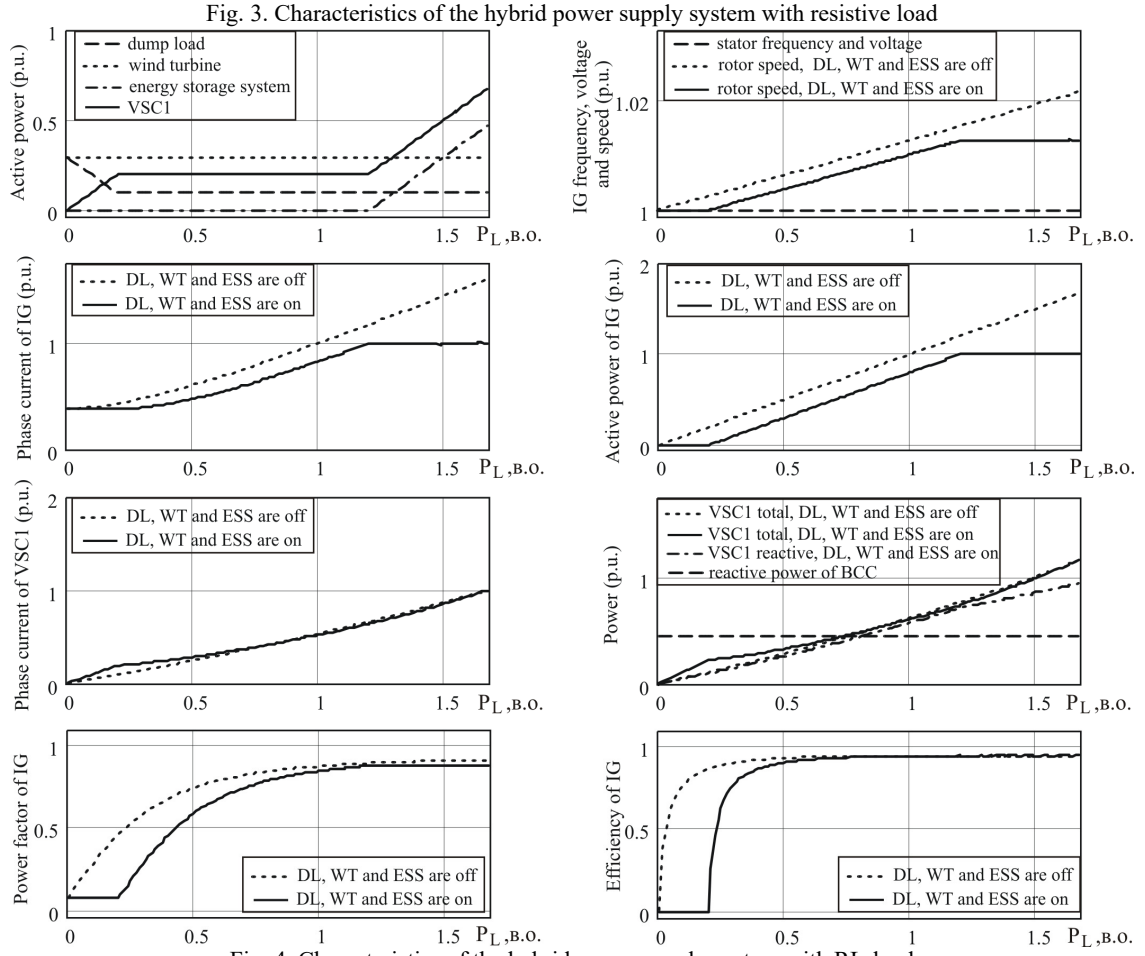

Fig. 4. Characteristics of the hybrid power supply system with RL-load

As can be seen from Fig. 3 and Fig. 4, the characteristics of the IG under resistive and RL local load are much similar. Since $P_{WG} > P_{EX}^{*}$, then during operation of the HTGU with IG in the HPSS running on low (0…0.2 p.u.) load, there is excess of active power generated in the system, which is consumed by the RDL, the real power of the IG G1 is zero, and the electrical rotor speed is near to the synchronous speed. When the IG current value reaches 1 p.u., the linear increasing in power of the ESS is observed and due to this the current and active power values of the IG stay at the nominal level. The power factor and efficiency values of the IG remain unchanged while there is excess of active power generated. The rotor speed within the load power range corresponding to 1 p.u. IG current value is constant as well.

Differences between Fig. 3 and Fig. 4 refer only to the characteristics of the VSC1 converter. Since the VSC1 converter for voltage control of the IG load, in addition to the compensation of the reactive power of the IG, must compensate under RL local load its reactive power, accordingly the values of the phase current and apparent power of the VSC1 are much greater than while supplying the resistive load. As can be seen from Fig. 3 and Fig. 4, when the value of the real power component of the load P_L is 1 p.u. and the IG is operating in the stand-alone HTGU, then the ratio of currents and apparent powers of the VSC1 obtained under resistive and RL-load is 1:4.7. When the IG is operating in the HPSS of Fig. 1, this ratio is 1:2.8.

At the same time, the values of the current and apparent power of the VSC1 during the operation of the IG in the «full» HPSS running under P_L = 1 p.u. load power when the load is resistive are 1.7 greater than during stand-alone operation of the HTGU and approximate to each other under RL-load. The power factor of the IG operating in the stand-alone HTGU in the entire load range, except for no load point, is greater than the power factor of the IG operating in the HPSS of Fig. 1. The maximum efficiency value of the IG operating in the stand-alone HTGU and in the HPSS of Fig. 1 was 0.947, and the maximum power factor value of the IG was 0.91 and 0.88 in stand-alone mode and for in system operation, respectively. These values correlate well with specifications of serial induction machines.

Simulation parameters and characteristics.

IG G1. Rated power / voltage / frequency / poles / (connection) – 250 kW / 400 V / 50 Hz / 4 / (Y); resistance of the stator / rotor winding, mΩ – 7.7 / 7.7; stator / rotor leakage reactance, mΩ – 33 / 33; core loss resistance, Ω – 42.3; friction coefficient, N·m·s/rad – 0.015. The magnetization characteristic of the IG is given in the Table 1.

Table 1

Magnetization characteristic of the IG G1

Phase current, A	20	27	54	105	141	191	290	421	592	836
Phase voltage, V	99	110	154	201	221	243	265	287	310	331

WT, RDL, ESS, VSC1, load, BCC, inductors. The output power of the WT is 0.3 p.u.; P_{EX}^{*} = 0.1 p.u.; the ESS is charged and limits the current value of the generator to the 1 p.u. value; losses in the VSC1 converter and inductors are neglected; the local load is symmetrical resistive or RL with a power factor of 0.9; the per phase capacity of the BCC is 2.2 mF.

Base quantities of power, voltage, current, speed and frequency for Fig. 3, 4 data. 250 kW = 1 p.u. of power; 230 V = 1 p.u. of voltage; 418 A = 1 p.u. of current; 1500 rpm = 1 p.u. of rotational speed; 50 Hz = 1 p.u. of frequency.

Conclusions. The methodology for steady state performance analysis of the induction generator driven by a hydraulic turbine of the master hydropower turbine equipped generating unit and operating in «constant voltage – constant frequency» mode in parallel through an electronic AC/DC power converter with sources and consumers of active power in the hydro-wind-battery hybrid power supply system supplying a three phase load has been developed.

Known methodologies for steady state performance analysis of isolated hybrid power systems using induction generators and regulated static energy converters are dynamic model based and thus are quite complex in use and modification. In contrast to known methodologies of steady state performance analysis of self-excited induction generator and parallel operated induction generators, superposition method and interpolation of characteristics are used to take into account additional power sources and consumers with preset control algorithms in the developed methodology. With the developed methodology it is possible to calculate performance of the system under study for an arbitrary output voltage reference thanks to the parametric analysis of this system provided in the methodology.

Approbation of the developed methodology was carried out on the isolated power system using a 250 kW induction generator. The obtained characteristics of the induction generator operating in the system differ from the characteristics of the stand-alone hydropower turbine equipped generating unit and depend on the characteristics and control algorithms of the additional sources and consumers of active power of the system. It was shown that, when the system supplied a local load with nominal real power component, the reduction of the power factor of the load from 1 to 0.9 led to an increase in the values of the apparent power and input currents of the AC/DC converter by 4.7 times in the stand-alone mode of operation of the hydropower turbine equipped generating unit and 2.8 times when the unit operated in the system. Due to this a significant increase in the installed capacity of the AC/DC converter both for stand-alone operation mode of the hydropower turbine equipped generating unit, and for its operation in the system supplying RL-load, is required in contrast to operation with resistive load. The obtained values of the maximum power factor and efficiency of the induction generator correlate well with the technical characteristics of serial asynchronous machines.

Further improvement and development of the outlined methodology can be carried out thanks to a more accurate calculation of losses and consideration of new modes of operation and circuit solutions of hybrid power systems.

Conflict of interest. The authors declare that they do not have conflicts of interest.

REFERENCES

1. Vita V., Alimardan T., Ekonomou L. The Impact of Distributed Generation in the Distribution Networks' Voltage Profile and Energy Losses. *IEEE European Modelling Symposium (EMS)*, Madrid, Spain, 2015, pp. 260-265. doi: https://doi.org/10.1109/EMS.2015.46.

2. Zharkin A., Novskyi V., Palachov S., Pazieiev A., Malakhatka D. Means of Electromagnetic Compatibility Providing In Local Electricity Networks Under Distributed Generation Development. *2020 IEEE 4th International Conference on Intelligent Energy and Power Systems (IEPS)*, Istanbul, Turkey, 2020, pp. 57-62. doi: https://doi.org/10.1109/IEPS51250.2020.9263199.

3. Tebbakh N., Labed D., Labed M.A. Optimal size and location of distributed generations in distribution networks using bald eagle search algorithm. *Electrical Engineering & Electromechanics*, 2022, no. 6, pp. 75-80. doi: https://doi.org/10.20998/2074-272X.2022.6.11.

4. Shavelkin A.A., Gerlici J., Shvedchykova I.O., Kravchenko K., Kruhliak H.V. Management of power consumption in a photovoltaic system with a storage battery connected to the network with multi-zone electricity pricing to supply the local facility own needs. *Electrical Engineering & Electromechanics*, 2021, no. 2, pp. 36-42. doi: https://doi.org/10.20998/2074-272X.2021.2.06.

5. Bhutto D.K., Ansari J.A., Bukhari S.S.H., Chachar F.A. Wind Energy Conversion Systems (WECS) Generators: a Review. *2nd International Conference on Computing, Mathematics and Engineering Technologies (iCoMET)*, Sukkur, Pakistan, 2019, pp. 1-6. doi: https://doi.org/10.1109/ICOMET.2019.8673429.

6. Mazurenko L.I., Kotsiuruba A.V., Dzhura O.V., Shykhnenko M.O. Voltage and Power Regulation of an Induction Generator-Based Hydroelectric Power Plant. *IEEE International Conference on Modern Electrical and Energy Systems (MEES)*, Kremenchuk, Ukraine, 21-24 September 2021, pp. 1-6. doi: https://doi.org/10.1109/MEES52427.2021.9598549.

7. Boukadoum A., Bouguerne A., Bahi T. Direct power control using space vector modulation strategy control for wind energy conversion system using three-phase matrix converter. *Electrical Engineering & Electromechanics*, 2023, no. 3, pp. 40-46. doi: https://doi.org/10.20998/2074-272X.2023.3.06.

8. Singh B., Murthy S.S., Gupta S. Analysis and design of electronic load controller for self-excited induction Generators. *IEEE Transactions on Energy Conversion*, 2006, vol. 21, no. 1, pp. 285-293. doi: https://doi.org/10.1109/TEC.2005.847950.

9. Alghuwainem S.M. Steady-state analysis of self-excited induction generator using real and reactive power balances. *IEEE 27th Canadian Conference on Electrical and Computer Engineering (CCECE)*, Toronto, ON, Canada, 2014, pp. 1-4. doi: https://doi.org/10.1109/CCECE.2014.6900964.

10. Wang L., Yang Y.-F., Kuo S.-C. Analysis of grid-connected induction generators under three-phase balanced conditions. *IEEE Power Engineering Society Winter Meeting. Conference Proceedings (Cat. No.02CH37309)*, New York, NY, USA, 2002, vol. 1, pp. 413-417. doi: https://doi.org/10.1109/PESW.2002.985033.

11. Popovych O., Golovan I., Shevchuk S., Listovshchyk L. Means of Complex Design of the Electromechanical System of the Gravity Energy Storage of the WindPower Plant. *2022 IEEE 8th International Conference on Energy Smart Systems (ESS)*, Kyiv, Ukraine, 2022, pp. 149-152. doi: https://doi.org/10.1109/ESS57819.2022.9969243.

12. Vanfretti L., Li W., Bogodorova T., Panciatici P. Unambiguous power system dynamic modeling and simulation using modelica tools. *2013 IEEE Power & Energy Society General Meeting*, Vancouver, BC, Canada, 2013, pp. 1-5. doi: https://doi.org/10.1109/PESMG.2013.6672476.

13. Hernández-Mayoral E., Dueñas-Reyes E., Iracheta-Cortez R., Campos-Mercado E., Torres-García V., Uriza-Gosebruch R. Modeling and Validation of the Switching Techniques Applied to Back-to-Back Power Converter Connected to a DFIG-Based Wind Turbine for Harmonic Analysis. *Electronics*, 2021, vol. 10, no. 23, art. no. 3046. doi: https://doi.org/10.3390/electronics10233046.

14. Louze L., Abdessemad O., Nemmour A., Khezzar A. An Effective Control of an Isolated Induction Generator Supplying DC Load for Wind Power Converting Applications. *Electrical Engineering & Electromechanics*, 2020, no. 3, pp. 65-69. doi: https://doi.org/10.20998/2074-272X.2020.3.10.

15. Sobczyński D., Pawłowski P. Energy storage systems for renewable energy sources. *2021 Selected Issues of Electrical Engineering and Electronics (WZEE),* Rzeszow, Poland, 2021, pp. 1-4, doi: https://doi.org/10.1109/WZEE54157.2021.9576964.

16. Yang P., Nehorai A. Joint Optimization of Hybrid Energy Storage and Generation Capacity With Renewable Energy. *IEEE Transactions on Smart Grid*, 2014, vol. 5, no. 4, pp. 1566-1574. doi: https://doi.org/10.1109/TSG.2014.2313724.

17. Mazurenko L.I., Dzhura O.V., Kotsiuruba A.V., Shykhnenko M.O. A Wind-Hydro Power System Using a Back-to-Back PWM Converter and Parallel Operated Induction Generators. *IEEE Problems of Automated Electrodrive. Theory and Practice (PAEP)*, Kremenchuk, Ukraine, September 21-25, 2020, pp. 1-5. doi: https://doi.org/10.1109/PAEP49887.2020.9240777.

18. Xie J., Zheng Y., Pan X., Zheng Y., Zhang L., Zhan Y. A Short-Term Optimal Scheduling Model for Wind-Solar-Hydro Hybrid Generation System With Cascade Hydropower Considering Regulation Reserve and Spinning Reserve Requirements. *IEEE Access*, 2021, vol. 9, pp. 10765-10777. doi: https://doi.org/10.1109/ACCESS.2021.3049280.

19. Engler A., Hardt C., Strauss P., Vandenbergh M. Parallel Operation of Generators for Stand-Alone Single-Phase Hybrid Systems-First Implementation of a new control Technology. 2001. Available at: https://www.researchgate.net/publication/228944407_Parallel_Operation_of_Generators_for_Stand-Alone_Single-Phase_Hybrid_Systems-First_Implementation_of_a_new_control_Technology (accessed 31.03.2023).

Received 30.08.2023
Accepted 02.10.2023
Published 02.03.2024

L.I. Mazurenko[1], *Doctor of Technical Science, Professor,*
O.V. Dzhura[1], *PhD, Senior Research Scientist,*
M.O. Shykhnenko[1], *PhD, Research Scientist,*
[1] Institute of Electrodynamics National Academy of Sciences of Ukraine,
56, Prospect Beresteiskyi, Kyiv-57, 03057, Ukraine,
e-mail: mlins@ied.org.ua;
suoma1715@gmail.com (Corresponding Author);
s.maxim@email.ua

How to cite this article:
Mazurenko L.I., Dzhura O.V., Shykhnenko M.O. Steady-state analysis of a hybrid power supply system using an induction generator with a shunt AC/DC converter. *Electrical Engineering & Electromechanics*, 2024, no. 2, pp. 67-74. doi: https://doi.org/10.20998/2074-272X.2024.2.10

UDC 621.314 https://doi.org/10.20998/2074-272X.2024.2.11

V.G. Yagup, K.V. Yagup

Analytical method of determining conditions for full compensation of reactive power in the power supply system

Goal. *The purpose of the article is the development of an analytical method for determining the conditions for achieving full compensation in the generalized power supply system based on the use of substitute circuits, which are obtained using equivalent transformations of the topology of the original circuit.* ***Methodology.*** *The article proposes a methodology for replacing series reactive power compensation in high-voltage paths of the power supply system with parallel reactive power compensation in a low-voltage load node.* ***Results***. *An algorithm for successive transformations of the power supply circuit has been developed, which makes it possible to estimate the values of the capacitances of compensating capacitors, at which full compensation of reactive power in the system is achieved.* ***Originality.*** *The proposed analytical method for calculating the parameters of the compensation unit makes it possible to dispense with complex optimization computer methods and makes it possible to estimate the compensation capacities that fall on the share of the load and the network.* ***Practical value.*** *The proposed technique allows, using a simple algorithm, to determine with high accuracy the necessary parameters of the compensating device, which provide the optimal mode in the power supply system. The proposed algorithm can easily be implemented in a microcontroller system for automatic control of the modes of the power supply system.* References 15, table 1, figures 6.

Key words: **electrical system, reactive power, full compensation, search optimization, power factor, equivalent transformations, substitute circuit.**

Мета. *Метою статті є розробка аналітичного методу визначення умов досягнення повної компенсації в узагальненій системі електропостачання, на основі використання замінних схем, які отримані за допомогою еквівалентних перетворень топології вихідної схеми.* ***Методологія***. *У статті запропоновано методику заміни послідовної компенсації реактивної потужності у високовольтних трактах системи електропостачання на паралельну компенсацію реактивної потужності у вузлі навантаження низької напруги.* ***Результати***. *Розроблено алгоритм послідовних перетворень схеми живлення, що дає змогу оцінити значення ємностей компенсувальних конденсаторів, при яких досягається повна компенсація реактивної потужності в системі.* ***Оригінальність***. *Запропонована аналітична методика розрахунку параметрів вузла компенсації дозволяє відмовитися від складних комп'ютерних методів оптимізації та дає можливість оцінити компенсаційні можливості, які припадають на частку навантаження та мережі.* ***Практична цінність***. *Запропонована методика дозволяє за простим алгоритмом з високою точністю визначити необхідні параметри компенсаційного пристрою, які забезпечують оптимальний режим в системі електропостачання. Запропонований алгоритм легко реалізується в мікроконтролерній системі автоматичного керування режимами системи електропостачання.* Бібл. 15, табл. 1, рис. 6.

Ключові слова: **електрична система, реактивна потужність, повна компенсація, пошукова оптимізація, коефіцієнт потужності, еквівалентні перетворення, заступна схема.**

Introduction and problem definition. Reactive power compensation remains one of the main means of increasing the energy efficiency of power supply systems [1-6]. In Ukraine, under the current conditions of martial law, these issues should become one of the main factors in increasing the possibilities of emergency-free electricity supply, in particular, the compensation of reactive power will allow to relieve the load on electric networks and increase the efficiency of the systems as a whole [4, 5]. Along with the traditional approach of partial compensation of reactive power of loads, the mode of full compensation of reactive power deserves attention, in which in three-phase networks the inverse and zero symmetrical components are compensated [7-11], as well as the reactive power of the load directly and, in addition, the reactive power in the electrical network itself [12-14]. The latter are traditionally compensated by the so-called longitudinal compensation, in which compensating capacitors are connected in series in the power transmission line [1, 2]. But, as shown in [14], the compensation of the components caused by the inductances of the power transmission lines can be achieved by increasing the capacities of the transverse compensation capacitors, which shunt the load in the electricity collection nodes. In the general case, the determination of full compensation can be carried out with the help of search optimization [12, 13] by approximate numerical methods, since in essence it is necessary to solve a system of nonlinear equations, which contain both system parameters and currents with voltages, and they are interconnected by multiplication and division operations. This is characteristic, as will be shown below, for the variant of the single-line generalized circuit, which can be applied even when considering branched electrical networks. However, numerical methods are able to conduct research for specific numerical values that characterize the mode of full compensation. Analytical symbolic methods allow to conduct a qualitative analysis and obtain generalized results, recommendations and conclusions.

The goal of the article is to create an analytical method for determining the conditions for achieving full compensation in a generalized power supply system in order to simplify the methodology for determining the parameters of compensating devices and achieving results without using relatively complex procedures based on optimization algorithms.

The main part of the study. We consider the traditional power supply system with transverse compensation of reactive power [1-3, 5, 6, 10], which is shown in Fig. 1 in the generally accepted form for the electric power industry.

This system should be called a generalized power supply system, as it highlights the main components of the power supply system in compliance with the generally

accepted conditions in the power industry. These conditions are, first of all, the assumption that a three-phase power supply system usually operates in a symmetrical mode, and therefore it is sufficient to analyze it in terms of only one of the three phases, and thanks to this, it is possible to consider the so-called single-line version of the system, i.e., a single-phase substitute circuit with one source voltage. Secondly, the parameters of the substitute circuit are redived to one side – either to the generator side, or to the load side, as is done, for example, when calculating short-circuit modes. Thirdly, the network, which can have a branched topology, is replaced by one complex active-inductive resistance based on the theorem on the equivalent active bipolar.

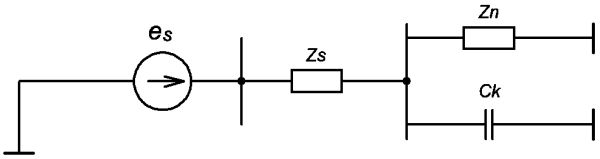

Fig. 1. Generalized single-line power supply system with reactive power compensator

In this circuit, e_s is the voltage source that generates and supplies electricity; Z_s is the complex active-inductive resistance that reflects the power transmission line and takes into account the internal resistance of the generator itself; Z_n is the complex active-inductive load; C_k is the capacity of a battery of capacitors that compensate for reactive power in the power supply system. Usually, quite approximate estimates of the value of this capacity are traditionally used in the electric power industry. It is determined as such that it is capable of compensating a certain given part of the reactive power of the load. This is due to the constant change in loads, for example, in the electricity supply networks of utility consumers.In addition, it is impossible to set the exact value of the capacity of the capacitor battery even when this value is determined, because it affects the discreteness of the values of the capacities of the individual capacitors that make up the battery. However, the development of semiconductor power electronics and means of automatic control of electrotechnical systems have trends in the digitalization of electronics and the transition to intelligent power supply systems [11], which will make it possible to solve these problems in general and provide an opportunity to achieve accurate parameters of compensating devices even in conditions of load variations. This refers to the use of controlled inductances with counter-switched thyristors, as well as power active filters with pulse width modulation.

Figure 2 shows a substitute circuit of a generalized power supply system with a compensator.

In this circuit, R_s and L_s are the active resistance and inductance of the power transmission line, which also include the corresponding parameters of the real generator; R_n and L_n are the active resistance and inductance of the load when the load is represented by a series equivalent.

The system of equations by the method of complex amplitudes describing this equivalent substitute circuit looks as follows in the basis of variables $\dot{I}_s, \dot{I}_n, \dot{U}_c$:

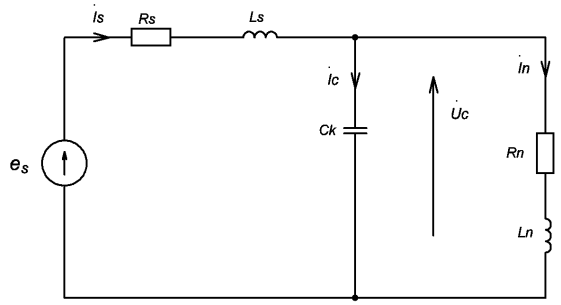

Fig. 2. Substitute circuit of the generalized power supply system with compensator

$$(R_s + j\omega L_s)\dot{I}_s + \dot{U}_c = \dot{e}_s\,; \tag{1}$$

$$(R_n + j\omega L_n)\dot{I}_n - \dot{U}_c = 0\,; \tag{2}$$

$$\dot{I}_s - \dot{I}_n - j\omega C_k\,\dot{U}_c = 0\,. \tag{3}$$

It should be noted that the system of these equations contains unknown currents $\dot{I}_s$, $\dot{I}_n$ and voltage $\dot{U}_c$, and in addition, the unknown quantity is the capacity C_k, which together with U_c forms the product $C\dot{U}_c$. This, in turn, leaves the system (1) – (3) linear, and in addition, three equations are no longer enough to uniquely determine $\dot{I}_s$, $\dot{I}_n$, $\dot{U}_c$ and C_k. In the search optimization method, this problem is solved by imposing additional conditions for reactive power compensation with the subsequent use of numerical algorithms using Newtonian methods or the algorithm optimization method, for example, a deformed polyhedron [12, 13].

We will apply the following stages of equivalent transformations of substitute circuits of the generalized power supply system.

Stage 1. Convert the series equivalent of the load with complex resistance $R_n + j\omega L_n$ into the parallel equivalent with complex conductivity $G_{n1} - jY_{n1}$:

$$G_{n1} - jY_{n1} = \frac{1}{R_n + j\omega L_n} = \frac{R_n}{R_n^2 + \omega^2 L_n^2} -$$

$$- j\frac{\omega L_n}{R_n^2 + \omega^2 L_n^2} = \frac{R_n}{R_n^2 + X_n^2} - j\frac{X_n}{R_n^2 + X_n^2}.$$

In addition, the capacitor C_k is replaced by two capacitors $C_k = C_1 + C_2$, where C_1 is designed to compensate the reactance of the purely load, and C_2 complements the compensation process to the level when the source e_s will not be connected to the reactive power, that is, the voltage and current phases of the sources will coincide and thereby complete compensation of the reactive power in the system will be achieved. The substitute obtained after stage 1 is shown in Fig. 3.

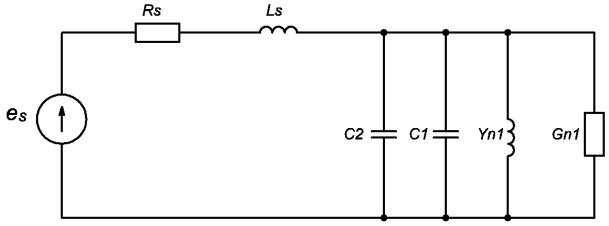

Fig. 3. Substitute circuit of the system with a parallel load equivalent and a distributed compensator

Stage 2. We determine the capacity of the capacitor C_1, which must compensate for the inductance of the parallel equivalent of the load:

$$j\omega C_1 - jY_{n1} = 0 \quad \text{or} \quad \omega C_1 = \frac{X_n}{R_n^2 + X_n^2},$$

where:

$$C_1 = \frac{X_n / \omega}{R_n^2 + X_n^2} = \frac{L_n}{R_n^2 + X_n^2}. \qquad (4)$$

At the same stage, we can also get rid of two reactive elements in the substitute circuit (Fig. 3). We mean the inductance of the parallel equivalent of the load with conductivity Y_{n1} and the capacitor C_1, which fully compensates for this inductance. The sum of the conductances of these elements is zero, therefore, from the point of view of the method of complex amplitudes used here for analysis, these elements can simply be excluded from the circuit in Fig. 3. As a result, we get a substitute circuit without the specified elements, which is presented in Fig. 4.

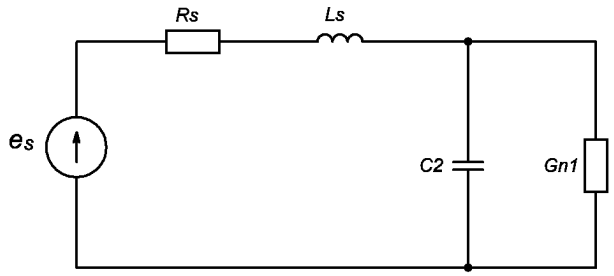

Fig. 4. Substitute circuit of the system with a compensator of the reactive component of the power transmission line

Stage 3. Now it is necessary to determine the capacity of the capacitor C_2, which is connected in parallel with the conductivity G_{n1} and must compensate for the reactive power of the inductance L_s of the power line. Next, let's turn the parallel circuit $G_{n1} - C_2$ into a series connection of the equivalent resistor R_3 and capacitor C_3 (Fig. 5).

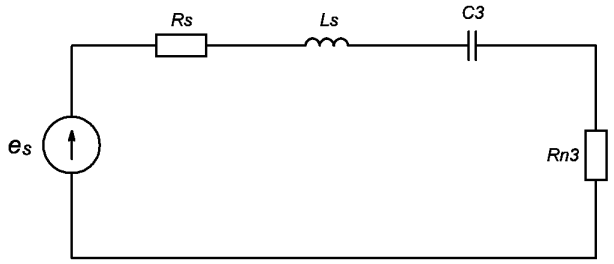

Fig. 5. Substitute circuit of the system at the stage of determining the capacity of the compensator for the power transmission line

We denote: $X_s = \omega L_s$, $Y_{C2} = \omega C_2$, $X_{C3} = 1/Y_{C3}$, $Y_{C3} = \omega C_3$. Then the parameters of the new load circuit will be obtained from the obvious relationships:

$$R_3 - jX_{C3} = \frac{1}{G_{n1} + jY_{C2}} = \frac{G_{n1} - jY_{C2}}{G_{n1}^2 + Y_{C2}^2}. \qquad (5)$$

From here it is clear that

$$R_{n3} = \frac{G_{n1}}{G_{n1}^2 + Y_{C2}^2}; \qquad (6)$$

$$X_{C3} = \frac{Y_{C2}}{G_{n1}^2 + Y_{C2}^2}. \qquad (7)$$

In the circuit in Fig. 5 reactive elements are connected in series, and the conditions for the longitudinal compensation of the reactive power are to fulfill the condition $X_s = X_{C3}$, that is

$$X_S = Y_{C2} / (G_{n1}^2 + Y_{C2}^2), \qquad (8)$$

which leads to the solution of the algebraic quadratic equation

$$Y_{C2}^2 - \frac{1}{X_S} Y_{C2} + G_{n1}^2 = 0. \qquad (9)$$

From here we can determine the conductivity of the capacitor C_2:

$$Y_{C2} = \frac{1}{2X_S} \pm \sqrt{\frac{1}{4X_S^2} - G_{n1}^2}. \qquad (10)$$

As can be seen from the obtained expression, the solution has two roots, from which, for the real case, the equation with the "minus" mark beforethe root should be chosen. The second value confirms the existence of two modes of full compensation of reactive power in the power supply system, which was indicated in previous works [14, 15], where the parameters of the second mode were obtained by a numerical method during optimization using the deformed polyhedron method. The second root corresponds to an overestimated compensation capacity and a significant increase in the current consumed from the source. Capacitance of capacitor C_2: $C_2 = Y_{02} / \omega$. Total capacity required for full compensation: $C_k = C_1 + C_2$.

Conditions for achieving the mode of full compensation. From expression (10), we can obtain the condition for achieving the full compensation mode, which consists in the fact that the radical

$$\frac{1}{4X_S^2} - G_{n1}^2 > 0. \qquad (11)$$

This leads to the expression:

$$X_S < \frac{1}{2G_{n1}}. \qquad (12)$$

Taking into account that

$$G_{n1} = \frac{R_n}{R_n^2 + X_n^2},$$

we obtain:

$$X_S < \frac{1}{2}(R_n + \frac{X_n}{R_n^2}). \qquad (13)$$

Thus, **the method of using** the calculation relationships obtained above can be described as follows:

- We calculate the parallel load equivalent.
- Using the inductive component of the parallel equivalent, we find the capacity of the compensator, which compensates the purely reactive component of the load according to the relationship (4).
- We exclude the inductive component of the parallel equivalent of the load together with its capacitive compensator from the substitute circuit, since their total

conductivity is zero. We introduce into the substitute circuit the capacity C_2, which is designed to compensate for the reactive component of the power transmission line.

- According to relationipшз (13), we check the conditions for achieving full compensation of reactive power in the system.
- If full compensation can be achieved, we form equation (9) and solve it according to relationship (10), which allows us to determine the conductivity of compensator C_2.
- We calculate the capacity C_2 and the total capacity of the compensator, which ensures full compensation of the reactive power in the system.

Results of numerical analysis and modeling. Consider the generalized power supply system (Fig. 2) with the following parameters: $e_s(t) = 100\sin(\omega t)$, where $\omega = 100\pi$; $R_s = 3\ \Omega$; $L_s = 0.03$ H; $R_n = 7\ \Omega$; $L_n = 0.05$ H. Complex load resistance $Z_n = 7 + j15.708$.

The complex conductance of parallel equivalent of the load

$$G_{n1} - jY_{n1} = \frac{1}{7 + j15{,}708} = 0{,}0237 - j0{,}05311.$$

Conductivity of the capacitor C_1, which compensates for the reactance of the load $Y_{C1} = 0.053119$ S.

Capacitor C_1 capacity:

$$C_1 = \frac{Y_{C1}}{\omega} = \frac{0{,}05311}{100\pi} = 169{,}07\ \mu\text{F}.$$

Quadratic equation for finding conductivity Y_{C2}:

$$Y_{C2}^2 - 0{,}1061 \cdot Y_{C2} + 5{,}6024 \cdot 10^{-4} = 0,$$

where

$$Y_{C2} = 0{,}05305 - \sqrt{0{,}0028 - 5{,}24 \cdot 10^{-4}} = 0{,}0055728\ \text{S}.$$

The capacity of the capacitor C_2, which compensates for the inductance of the power transmission line:

$$C_2 = \frac{Y_{C2}}{100\pi} = 17{,}739\ \mu\text{F}.$$

Capacity that provides full compensation of reactive power in the system

$$C_k = C_1 + C_2 = 186{,}81\ \mu\text{F}.$$

According to the obtained results, the system was modeled for three options:

I – without compensating capacitor;

II – with capacity $C_k = C_1$, when partial compensation of only load reactivity is provided;

III – with capacity $C_k = C_1 + C_2$, which ensures full compensation of reactive power in the system.

For simulation, a visual model was created in the MATLAB/Simulink/SimPowerSystem system.

The configuration of the model actually repeats the circuit shown in Fig. 2, and therefore is not given. The complex values of the voltage on the capacitor $\dot{U}_C$, that is, the voltage on the load, is measured; as well as power source current $\dot{I}_S$; capacitor's C_k current $\dot{I}_C$; current $\dot{I}_{Zn}$ through the load. The simulation results are given in Table 1.

Table 1

Simulation results

Parameters	Option I	Option II	Option III
C_k	0	C_1	$C_1 + C_2$
$\dot{U}_C$	63,8∠–2,32°	91,41∠–11,77°	95,57∠–13,25°
$\dot{I}_S$	3,7∠–68,3°	2,16∠–11,77°	2,32∠0°
$\dot{I}_C$	0	4,86∠78,23°	5,61∠76,75°
$\dot{I}_{Zn}$	3,7∠–68,3°	5,33∠–77,75°	5,56∠–79,23°

Analyzing the given results, it is worth noting that in the absence of a compensating capacitor, the mode is characterized by an extremely low level of voltage supplied to the load. A relatively large current is consumed from the source, which creates a sufficiently large voltage drop on the complex resistance of the power transmission line, the amplitude of which reaches more than 30 % of the voltage of the source itself. Calculation of the value of the power factor gives a very low value of cos(68,30°) = 0.369. Application of partial compensation at $C_k = C_1$ fully compensates the reactive power of the load. This is evidenced by the same phase shifts of the load voltage $\dot{U}_C$ and current $\dot{I}_S$, i.e. the load behaves like an active resistor in conjunction with the capacitor C_1. This, in turn, confirms the effectiveness of the substitute circuit shown in Fig. 4 at $C_2 = 0$. Indeed, by dividing the current $\dot{I}_S$ by the voltage $\dot{U}_C$, we obtain the conductivity of the load equivalent

$$G_{eq2} = \frac{2{,}16\angle -11{,}77°}{91{,}41\angle -11{,}77°} = 0{,}02363\ \Omega^{-1}.$$

which coincides with G_{n1} of the substitute circuit in Fig. 4. Equivalent resistance $R_{n1} = 1 / G_{n1} = 42.319\ \Omega$. Without compensation, the load module was

$$|Z_n| = \sqrt{7^2 + 15{,}708^2} = 17{,}971\ \Omega.$$

Thus, the connection of the capacitor C_1, which compensates for the reactance of the load, can be interpreted as a significant increase in the equivalent resistance of the load. Due to this, the current consumed from the source is reduced. At the same time, the share of the source voltage, which goes directly to the load nodes, increases. Although the voltage drop on the power transmission line is reduced by almost three times and is now about 10 % of the source voltage, the voltage at the load still does not reach 5 % of the permissible deviation. In the third option, $C_k = C_1 + C_2$, and here full compensation of the reactive power in the system is achieved. This is evidenced by the coincidence of the phase of the current $\dot{I}_S$ of the source with the phase of its voltage $e_s(t)$. Thanks to the additional compensation of the inductance of the power transmission line, the load voltage $\dot{U}_C$ increases and reaches 5 % of the permissible deviation from the source voltage. The current consumed from the source increases slightly. This can be explained by the substitute circuit shown in Fig. 5, if we take into account that the sum of the reactances of the inductance L_s and the capacitor C_3 is zero. Therefore, these elements can be removed from the circuit by replacing them with a short-circuited conductor. We get a simple substitute circuit with

serial connection of resistors R_s and R_{n3}. Let's calculate the resistance of the last resistor according to (6):

$$R_{n3} = \frac{G_{n1}}{G_{n1}^2 + Y_{C2}^2} = \frac{0{,}0237}{0{,}0237^2 + 0{,}0055728^2} = 39{,}983\ \Omega.$$

As can be seen, the resistance R_{n3} slightly decreases compared to R_{n1}. Current $\dot{I}_S$ calculated taking into account R_s and R_{n3}:

$$\dot{I}_S = \frac{100}{3 + 39{,}9834} = 2{,}326\ \text{A},$$

which coincides with the simulation results in Table 1.

The voltage on the load is calculated as the geometric sum of the voltages on R_{n3} and C_3:

$$U_{n3} = \left[(I_s R_{n3})^2 + \left(\frac{1}{\omega C_3} \cdot I_s\right)^2 \right]^{1/2} = 95{,}59\ \text{V},$$

which also coincides with the simulation results.

A visual model in the MATLAB/SimPowerSystem system was used for modeling in time space (Fig. 6). Virtual devices allow to determine the amplitudes of currents and voltages, as well as active and reactive power on system elements.

Shown in Fig. 6 results correspond to the mode of full compensation. It can be seen here that the source gives only active power P_e = 116.2 W, active load power is P_n = 108.1 W, active losses on the power transmission line and generator resistance is P_s = 8.102 W. The reactive power associated with the power source is zero, and therefore the power factor cosφ = 1. The efficiency of the system is η = 108.1 / 116.2 = 0.93. At the same time, for the uncompensated mode, these values are P_e = 68.34 W, P_n = 47.84 W, P_s = 20.5 W, η =47.84 / 68.34 = 0.7. The reactive power given by the source in this case is Q_e = 171.8 VAr, which causes a low value of the power factor cosφ = 0.37. These results clearly show in favor of the full compensation mode, thanks to which the load consumes a voltage close to the nominal one, which in turn ensures the appropriate level of power consumption, losses on the power transmission line are reduced by 2.5 times, and the efficiency is increased by 23 %. Thus, when full compensation is implemented, the energy indicators of the power supply system are significantly increased and normal power supply of the load is ensured, which in the absence of compensation overloads the network and thereby unacceptably lowers the voltage at the point of connection of this load.

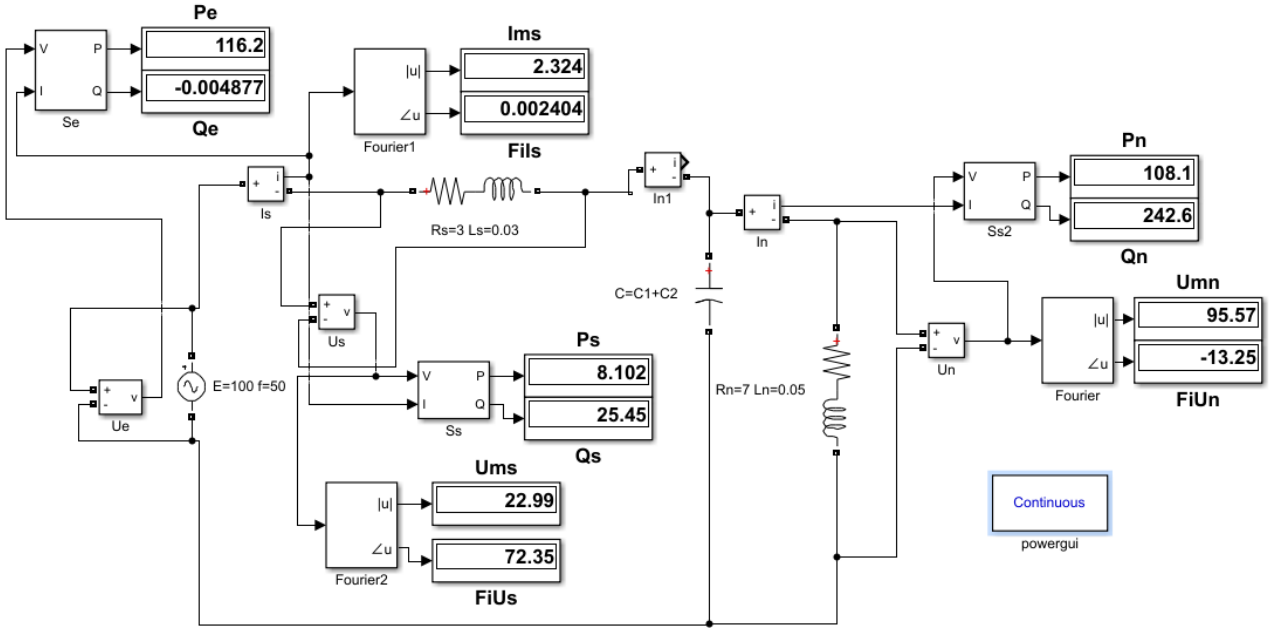

Fig. 6. Visual model of the system for verification of the full compensation mode

Conclusions.

1. An analytical method for determining the conditions for achieving full compensation of reactive power in a generalized power supply system is proposed, which is based on equivalent transformations of the topology of the power supply system and allows not to apply complex methods of solving nonlinear equations by iterative and optimization methods.

2. On the basis of the proposed method, an analytical technique for calculating the parameters of the compensating device and the mode parameters of the system was developed, and its verification was performed, which confirmed the coincidence of the obtained results with known examples of the implementation of full compensation of reactive power.

3. It follows from the conducted analysis that the generally accepted partial compensation of the load reactance may not ensure a proper increase in the load voltage, at the same time, the use of full reactive power compensation ensures a further increase in the load voltage.

4. It is shown that the processes of increasing the load voltage and decreasing the source current can be interpreted as an increase in the equivalent resistance of the load.

5. The proposed method and calculation methodology based on it have the prospect of being applied in the analysis of reactive power compensation processes in electrical networks with many loads and several sources of electricity supply.

6. The results of modeling the mode in the system on the model compiled in the MATLAB/Simulink/SimPowerSysten package with the specified initial parameters and the found parameters of the compensator show an absolute coincidence with the results of mode calculations obtained using the developed methodology.

Conflict of interest. The authors declare that they have no conflicts of interest.

REFERENCES

1. Kyrylenko O., Zharkin A., Butkevych O., Blinov I., Zaitsev I., Zaporozhets A. Power Systems Research and Operation. *Studies in Systems, Decision and Control*, 2022, vol. 388. 174 p. doi: https://doi.org/10.1007/978-3-030-82926-1.

2. Kundur P. *Power system stability and control*. McGraw-Hill Inc., 1994. 1176 p.

3. Wang H., Li Q., Wang S., Song D., Jia Y., Peng X., Deng X., Huang Y. Modeling and Control Strategy of Reactive Power Coordination in the Combined System of New Energy Plant and Energy Storage Station. *2023 9th International Conference on Electrical Engineering, Control and Robotics (EECR)*, 2023, pp. 235-239. doi: https://doi.org/10.1109/EECR56827.2023.10149982.

4. Wang A., Zhang J. A novel reactive power control strategy in virtual flux droop control. *2017 18th International Symposium on Electromagnetic Fields in Mechatronics, Electrical and Electronic Engineering (ISEF) Book of Abstracts*, 2017, pp. 1-2. doi: https://doi.org/10.1109/ISEF.2017.8090711.

5. Qu S., Zhaohui Q., Zhaowei L., MingMing S., Yuchen H., Zhenhua L. Energy Storage Active and Reactive Power Coordinated Control Considering DC Commutation Failue Voltage Recovery and Restraining AC Line Active Power Fluctuation. *2022 7th Asia Conference on Power and Electrical Engineering (ACPEE)*, 2022, pp. 1163-1168. doi: https://doi.org/10.1109/ACPEE53904.2022.9783988.

6. Miller J.E. *Reactive power controlled in electric systems*. John Willey & Sons, 1982. 416 p.

7. Yaoyun L. Research on Voltage and Reactive Power Control Strategy Based on Intelligent Detection of Abnormal Data and Coordinated Control of Dynamic Reactive Power. *2022 IEEE 5th International Conference on Automation, Electronics and Electrical Engineering (AUTEEE)*, 2022, pp. 71-76. doi: https://doi.org/10.1109/AUTEEE56487.2022.9994561.

8. Srinivasan G., Mahesh Kumar Reddy V., Venkatesh P., Parimalasundar E. Reactive power optimization in distribution systems considering load levels for economic benefit maximization. *Electrical Engineering & Electromechanics*, 2023, no. 3, pp. 83-89. doi: https://doi.org/10.20998/2074-272X.2023.3.12.

9. Kobayashi H., Hatta H. Reactive power control method between DG using ICT for proper voltage control of utility distribution system. *2011 IEEE Power and Energy Society General Meeting*, 2011, pp. 1-6. doi: https://doi.org/10.1109/PES.2011.6039569.

10. Yang K., Gong Y., Zhang P., Liu Z. A reactive power compensation method based on tracing the power flow and loss function of power system. *2015 5th International Conference on Electric Utility Deregulation and Restructuring and Power Technologies (DRPT)*, 2015, pp. 615-619. doi: https://doi.org/10.1109/DRPT.2015.7432309.

11. *European Smart Grids Technology Platform: Vision and Strategy for Europe's Electricity Networks of the Future*. European Commission, 2006. 44 p.

12. Miron A., Cziker A.C., Ungureanu S., Beleiu H.G., Darab C.P. Reactive Power Compensation at Industrial Consumers: Romanian Study Case. *2022 International Conference and Exposition on Electrical And Power Engineering (EPE)*, 2022, pp. 101-106. doi: https://doi.org/10.1109/EPE56121.2022.9959800.

13. Yagup V.G., Yagup K.V. Calculating the parameters of symmetry-compensating device for three-phase electrical power system based on the system decomposition. *Technical Electrodynamics*, 2016, no. 6, pp. 20-26. (Rus). doi: https://doi.org/10.15407/techned2016.06.020.

14. Yagup V.G., Yagup K.V. Power compensation modes research in generalized electrical supply system. *Technical Electrodynamics*, 2022, no. 6, pp. 63-71. (Ukr). doi: https://doi.org/10.15407/techned2022.06.063.

15. Yagup V.G., Yagup E.V. Research of the modes of full compensation of reactive power in a three-phase power supply system. *Electrical Engineering & Electromechanics*, 2019, no. 2, pp. 61-65. doi: https://doi.org/10.20998/2074-272X.2019.2.09.

Received 05.08.2023
Accepted 25.09.2023
Published 02.03.2024

V.G. Yagup[1], *Doctor of Technical Science, Professor,*
K.V. Yagup[2], *Doctor of Technical Science, Professor,*
[1] Kharkiv National Automobile and Highway University,
25, Yaroslava Mudrogo Str., Kharkiv, 61002, Ukraine,
e-mail: yagup.walery@gmail.com (Corresponding Author)
[2] National Technical University «Kharkiv Polytechnic Institute»,
2, Kyrpychova Str., Kharkiv, 61002, Ukraine.

How to cite this article:
Yagup V.G., Yagup K.V. Analytical method of determining conditions for full compensation of reactive power in the power supply system. *Electrical Engineering & Electromechanics*, 2024, no. 2, pp. 75-80. doi: https://doi.org/10.20998/2074-272X.2024.2.11

Матеріали приймаються за адресою:
Кафедра "Електричні апарати", НТУ "ХПІ", вул. Кирпичева, 2, м. Харків, 61002, Україна
Електронні варіанти матеріалів по e-mail: a.m.grechko@gmail.com

Довідки за телефонами: +38 067 359 46 96 Гречко Олександр Михайлович

Передплатний індекс: 01216